Loads on Structures due to Extreme Wave Crests

by

Kuang-An Chang, Hamn-Ching Chen, Kai Yu, Yonguk Ryu, Kusalika Ariyarathne, and Richard Mercier

Ocean Engineering Program
Zachry Department of Civil Engineering
Texas A&M University

Final Project Report
Prepared for the Minerals Management Service
Under the MMS/OTRC Cooperative Research Agreement
1435-01-04-CA-35515
Task Order 39807
MMS Project Number 571

June 2008

OTRC Library Number: 6/08A189

"The views and conclusions contained in this document are those of the authors and should not be interpreted as representing the opinions or policies of the U.S. Government. Mention of trade names or commercial products does not constitute their endorsement by the U. S. Government".

For more information contact:

Offshore Technology Research Center
Texas A&M University
1200 Mariner Drive
College Station, Texas 77845-3400
(979) 845-6000

or

Offshore Technology Research Center
The University of Texas at Austin
1 University Station C3700
Austin, Texas 78712-0318
(512) 471-6989

A National Science Foundation Graduated Engineering Research Center

TABLE OF CONTENTS

Page

LIST OF TABLES AND FIGURES

Tables

Figures

EXECUTIVE SUMMARY

In approximately one year from September 2004 to September 2005, three Category 5 hurricanes (Ivan, Katrina, Rita) hit the Gulf of Mexico. Well over 80% of the 4,000 oil and gas production platforms in the Gulf were directly impacted by the hurricanes. The hurricanes destroyed or caused extensive damage to 190 platforms. In most cases the platform damage was caused by green water wave loading on the deck. Green water damage to floating structures results from high pressures and dynamic loads that occur when wave crests inundate the structure far above the waterline in areas not designed to withstand such pressures. In situations where one must consider the possibility of wave overtopping and green water rushing onto the deck, the mechanics of wave loading become very complex and are poorly understood. One of the major sources of uncertainty is the velocity field of the green water flow itself.

The objective of this research is to develop a robust procedure to estimate local and global green water loads on structures due to extreme wave crests. Through the combined efforts of laboratory measurements and numerical simulation, the results will allow designers to avoid or minimize the impact of green water on new floating structures through design, and help the industry and regulators to develop associated design guidance. This research is a continued effort after the successful formulation of green water over a 2D platform through laboratory measurement, and a continuation on the development of a 3D computational fluid dynamics (CFD) code for the simulation of green water. The prior study has shown that the traditional prediction method often used in design, i.e., the dam breaking model, results in significant discrepancy between the model and the laboratory measurements. Since the more realistic 3D prediction model is not yet established, the continuation of the research is critical for the prediction of green water and subsequently its mitigation. The study considers 3D structure geometries such as TLP’s, spars, and ship-shaped FPSO's.

In the experimental approach, we first use laboratory measurements to investigate the void fraction as well as the flow volume, flow rate, water velocity, water elevation and momentum flux of an overtopping flow on a 2D structure. The flow

structure on a 3D model was then measured with preliminary results presented. Green water was generated by the impingement of a plunging breaking wave on the structure following the Froude similarity of an extreme hurricane wave and a simplified offshore structure. The flow is multi-phased and turbulent with significant aeration. A fiber optic reflectometer (FOR) and bubble image velocimetry (BIV) were employed to measure the void fraction and velocity in the flow, respectively, and to determine the water level on the deck. Mean properties of void fraction and velocity were obtained by ensemble-averaging and time-averaging the repeated instantaneous measurements. The temporal and spatial distributions of void fraction reveal that the flow is very highly aerated near the front of green water and has relatively low aeration near the deck surface. The mean void fraction and velocity distributions were also depth-averaged for simplicity and potential use in engineering applications. Using the measured data, similarity profiles for depth-averaged void fraction, depth-averaged velocity, and water level were found. The study suggests that using only the velocity data is insufficient if the flow momentum or the flow rate is to be determined. The accuracy of the void fraction measurements was validated by comparing the directly measured water volume of the overtopping flow with the calculated water volume based on the measured velocity and void fraction.

In the numerical approach, an interface-preserving level set method was incorporated into the Reynolds-Averaged Navier-Stokes (RANS) method for the simulation of the green water effect. In the method, free surface flows are modeled as immiscible air-water two-phase flows and the free surface itself is represented by the zero level set function. Calculations were performed for several benchmark free surface flows including dam break flows, free jets, solitary wave propagation and the impingement of dam break flow on a fixed structure. After some validation, the method is applied to simulate sloshing flows in an LNG tank and green water over an offshore platform. The good agreement between numerical and experimental results prove the level set RANS method is a powerful and accurate CFD methodology in free surface flow simulations.

PART I: NUMERICAL APPROACH - LEVEL-SET RANS METHOD FOR SLOSHING AND GREEN WATER SIMULATIONS[1]

1 This is essentially the PhD dissertation of Dr. Kai Yu

1 INTRODUCTION

1.1 Background

The objective of this study is to develop a general, accurate and robust computational fluid dynamics (CFD) methodology which is capable of predicting the large deforming free surface flows such as green water over an offshore structure and sloshing flow in a Liquefied Natural Gas (LNG) tank.

Engineering applications often involve multi-phase flows. Liquid-gas interfaces occur in a wide variety of natural phenomena and technical processes. In the most common cases, the free surface is an air-water boundary. Free surface flows feature most prominently in the marine environment, and are characterized by air-water interactions and unsteady waves. Figure 1.1 shows the classic curl of a breaking wave as a wave approaches shore. The interaction between the extreme waves and floating structures is a primary concern in the design of offshore structure. Impact pressure due to sloshing flow is also a critical concern for the ship owners, designers and builders of the LNG carriers.

Figure 1.1 A typical breaking wave near shore

This study mainly focuses on the immiscible fluid flow, typically air-water flows. The numerical simulations of free surface flows are difficult due to moving boundaries. The position of the boundary is known only at the initial time; its location at later times has to be determined as part of the solution. The requirements for a good numerical multi-phase prediction method include generality, high accuracy, and minimal memory usage and CPU time.

Prior works on CFD methodologies that are capable of predicting free surface flow can be tracked as far back as the early 1960s. Since then there have been numerous developments in the field, but there are still limitations for each of them. The next section gives an overview of these developments, their advantages and disadvantages. It is then followed by a section which outlines the contribution of this dissertation. The chapter is closed with the structure of the dissertation.

1.2 Literature Review

Green water loads on an offshore platform occur when an incoming wave significantly exceeds the free board and water runs onto the deck. The main problem in the numerical simulation is the accuracy in tracking the air-water interface. Many methods have been proposed to predict the interface between two different fluids. They could be classified into two different categories: the interface-tracking methods and the interface-capturing methods (Ferziger and Peric, 1999). The interface-tracking methods follow the free surface motions and use boundary-fitted grids which are re-adjusted at each time step whenever the free surface moves. The interface-capturing methods do not define a sharp free surface boundary. Instead, the computation is performed on a fixed grid, which is extended beyond the free surface. The geometry of the free surface is determined by a certain numerical variable, which is part of the numerical solutions. A variety of methods in this interface-capturing approach have been developed over the past several decades. Three typical methods from this category are the Marker and Cell

(MAC) scheme (Harlow and Welch, 1965), the volume of fluid (VOF) scheme (Nichols et al., 1980; Hirt and Nichols, 1981) and the level set method (Osher and Sethian, 1988). The methods are summarized in the following section.

1.2.1 Surface Tracking

The surface tracking methods are expressed in a Lagrangian view point which describes fluid motions as we follow a fluid particle along its trajectory. The surface tracking methods are characterized by an explicit representation of the surface. The Lagrangian method treats the free surface as a sharp interface whose motion is exactly followed. This is normally done by adapting boundary-fitted grids to the free surface and updating grids at each time step to track the new location of the free surface by using a height function to describe the vertical height of the free surface location.

Chen, Liu, Chang and Huang (2002) used a Chimera Reynolds-Averaged Navier-Stokes method, which is a kind of Lagrangian approach, for time-domain simulation of turbulent flows around a rectangular barge under large amplitude waves. A flexible chimera grid system was developed to handle partial hull submergence with green water on the barge deck. The grid is adjusted every time step to follow the free surface motion. The same method was applied in Chen, Liu and Huang (2001). The surface tracking methods were also applied in time-domain simulation of floating pier and multiple-vessel interactions, Chen and Huang (2004).

The surface tracking methods can describe the free surface flow accurately especially when small deformation occurs. Figure 1.2 illustrates chimera grids in the simulation of wave runup around multiple cylinders. The wake flows behind cylinders were captured accurately. The drawback of the surface tracking methods is the inability to handle complex surface geometries, such as breaking wave, bubbles in water and droplets in air. This makes the surface tracking methods unable to model sloshing flows

in LNG tanks and green water effects on offshore structures, in which overturning or breaking waves are expected to happen frequently.

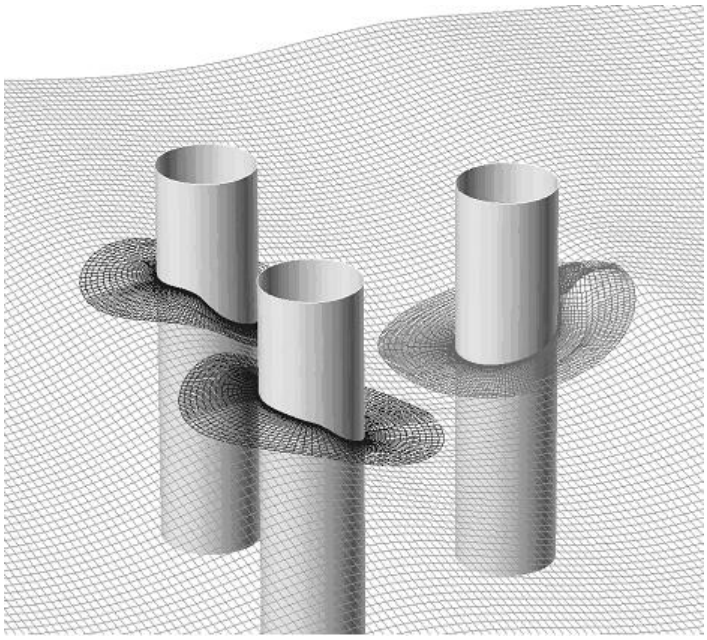

Figure 1.2 Chimera grids around vertical cylinders

1.2.2 Surface Capturing

The surface capturing methods use a different approach based on the so-called Eulerian view point which describes the fluid motion at a fixed point. The computation is performed on a fixed grid, which extends beyond the free surface. Instead of being defined as a sharp boundary, the free surface is determined only after the solution in the whole domain is finished. A number of schemes are available, and all of them use an implicit representation of the interface which is then captured as part of the solution. The most common schemes for surface capturing are the Marker-And-Cell method (MAC) which was first proposed by Harlow and Welch in 1965, the Volume-Of-Fluid method (VOF) which was originally developed by Hirt and Nichols in 1981 and the Level-Set

method which was first studied by Osher and Sethian in 1988. For the last two schemes, the shape of the free surface is determined by computing the fraction of each near-interface cell that is partially filled. The details about these schemes are discussed in the following part.

In the MAC scheme, the free surface is captured by introducing massless particles at the free surface at the initial time and following their motion. Figure 1.3 shows an example of the surface marker applications. These markers capture the details of interface motions on scales much smaller than the grid spacing. The free surface geometry is then defined by all the segments which are connections between adjacent markers.

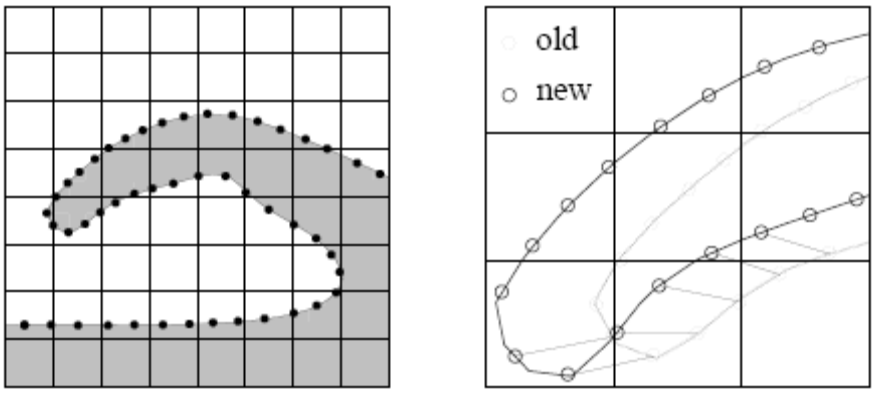

Figure 1.3 MAC method

MAC methods have been used extensively by many groups. Chan and Street (1969) introduced the Stanford University Modified MAC (SUMMAC) code which was shown to be a valid tool for analyzing incompressible flows with a free surface under transient conditions. The Miyata group (1986) developed the TUMMAC method (Tokyo University Modified Marker-And-Cell method) for particular engineering problems related to water wave dynamics. A modified MAC method (SIMAC; Semi-Implicit

Marker-And-Cell) was proposed by Armenio (1997) which accurately treats unsteady high-Reynolds number free surface problems. The MAC methods are favored because they can treat complex free surface phenomena, including wave breaking. The higher degree of accuracy may be achieved by representing the interface through higher order interpolation polynomials. However, intensive computational effort is needed for these methods, especially in three-dimensional problems with violent free surface motions. In addition to solving the equations governing the fluid flow, one has to follow the motion of a large number of particles. This leads to high computation time and cost.

The VOF method introduces a scalar, which is usually named the volume fraction or color function, which defines the filling degree of each cell. Figure 1.4 shows the definition of the VOF function. A cell with a volume fraction value of 0 is empty, and a volume fraction value of 1 means a full cell. For those partially filled cells, *f* is the volume fraction of the fluid in the cell. Here, in addition to the conservation equations for mass and momentum, one has to introduce and solve an equation for the filled fraction of each control volume, that is,

$$\frac{\partial f}{\partial t} + \vec{V} \cdot \nabla f = 0 \tag{1.1}$$

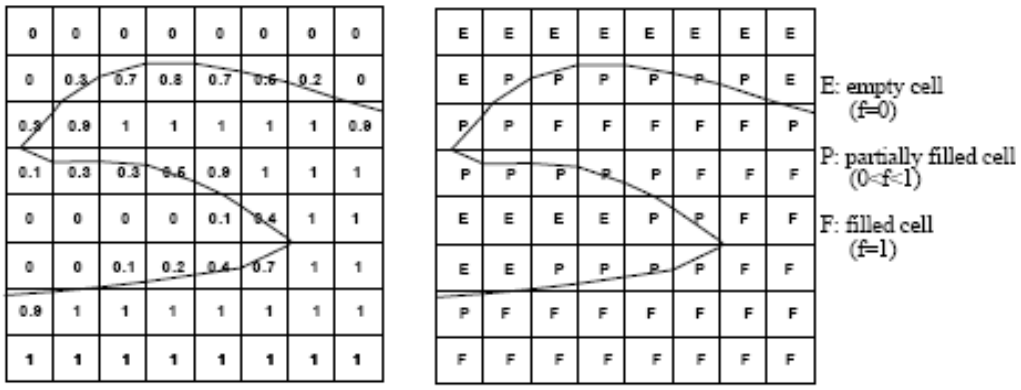

Figure 1.4 The definition of volumn fraction

The VOF method has been known for several decades and has been developed and improved continuously by many research groups. Kothe and Rider (1995) and Scardovelli and Zaleski (1999) provided good reviews for the development of the VOF method in past decades. Now the VOF method has been proven as a popular, useful and robust tool for interface tracking. There are many commercial codes which use this method to represent interfaces, for example, SOLA-VOF (Nichols et al., 1980), NASA-VOF3D (Torrey et al., 1987), RIPPLE (Kothe and Mjolsness, 1992) and FLOW3D (Hirt and Nichols, 1988).

The widespread applications of the VOF method are based on its essential advantages. The algorithm is based on a discrete representation of the conservation law. For this reason, the VOF method preserves mass in a natural way and it conserves mass well in calculations. Another advantage is the VOF method can be relatively simply extended from two-dimensional domains to three-dimensional domains. However, there is an obvious shortcoming for the VOF method. It must locate the interface in order to advect volume fraction per Equation (1.1). A low order reconstruction scheme may cause significant errors in simulation. A lot of work had been done to develop different interface reconstruction procedures.

The most typical reconstruction schemes are known as simple line interface calculation (SLIC) and piecewise linear interface construction (PLIC). The SLIC scheme was widely used in the 1980s' (Hirt and Nichols, 1981) and early 1990s' (Lafauries et al., 1994). This is a first order approach, $O(h)$, which forces the reconstruction to align with one of the mesh coordinates. Figure 1.5 (a) compares the actual interface with the much coarser interface constructed by SLIC. The PLIC scheme is much more accurate in fitting the interface through piecewise linear segments. In Figure 1.5 (b) the interface constructed by the PLIC scheme is much closer to the actual surface.

The VOF scheme is widely used to simulate breaking waves (Biausser et al., 2004), vigorous sloshing in tanks (Yang and Lohner, 2005), and flows around ships and

submerged bodies (Huijsmans and van Groesen, 2004). Nevertheless, in most of these simulations of complex three-dimensional free surface flows problems were encountered in building an accurate and smooth free surface.

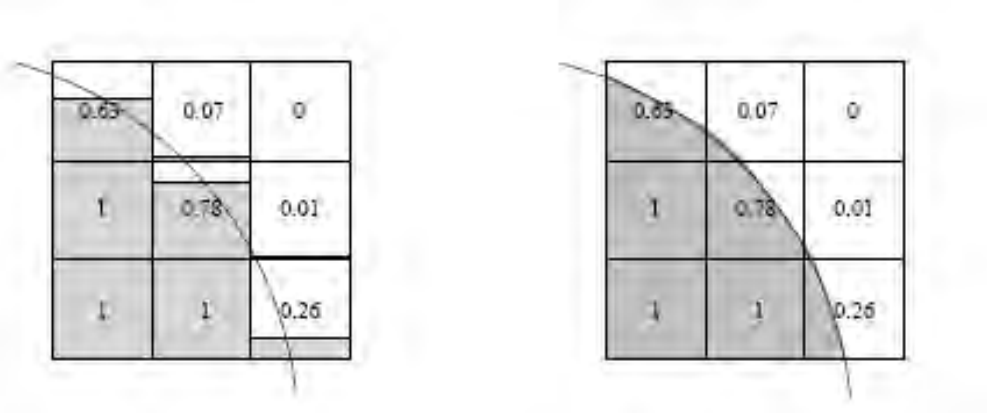

(a) SLIC (b) PLIC

Figure 1.5 The interface reconstruction in VOF methods

Another class of interface capturing methods is based on the level set function introduced by Osher and Sethian (1988). The level set function ϕ, which is defined in the whole domain, is typically initialized as the signed distance from the interface, that is, its value at any point is the physical distance from the nearest point on the interface and its sign is positive on one side of the interface and negative on the other side. The interface is located where the level-set function $\phi = 0$ while other values of this function have no significance. The level set function varies smoothly across the interface and is advected by the local velocity field using the advection equation

$$\frac{\partial \phi}{\partial t} + \vec{V} \cdot \nabla \phi = 0 \tag{1.2}$$

The interface can be captured at any time during the solution by locating the zero level set. In general the computed ϕ may not remain the signed distance from the

interface due to accumulated numerical errors, therefore it needs to be reinitialized for every time step. Sussman et al. (1994) proposed that this can be done by solving the following equation until the steady state is reached:

$$\frac{\partial \phi}{\partial \tau} = sign(\phi_0) \cdot \left(1 - \left| \nabla \phi \right|\right) \tag{1.3}$$

Equation (1.3) guarantees that ϕ has the same sign and zero level as ϕ_0 and satisfies the condition that $\left| \nabla \phi \right| = 1$.

Sethian and Smereka (2003) provided an overview of the level set method for computing the solution to fluid-interface problems. Osher and Fedkiw (2001) discussed not only recent variants and extensions of the level set method but also a user's guide to the level set dictionary and technology. Compared to VOF methods, the level set method seems to be an extremely promising method. Because it is not necessary to do the reconstruction procedure, the level set method handles the complex interface geometries in a simple way. Surface tension effects can also be easily incorporated with this method. The biggest concern with the level set method is the issue of loss of mass.

In order to improve mass conservation, many research groups expanded the original level set method. Sussman et al. (1998) first introduced a new constraint term in the re-distancing scheme to improve accuracy and efficiency. A coupled level set and VOF method was developed recently by Sussman and Puckett (2000). It seems to conserve mass as well as VOF methods. A similar method, which is known as the mass conserving level set method (MCLS), is presented by Van der Pijl et al. (2005). Takahira et al. (2004) improved the re-initialization procedure of the level set function by adding a multiplier of the order of one to the constraint term in order to recover the mass. Enright et al. (2002) proposed a new numerical method to improve the mass conservation by using Lagrangian marker particles to rebuild the level set function in regions that are under-resolved. The particle level set method has proved to be an effective way for

handling problems due to topological merging, breaking and even self-intersection of interfaces. Predictable improvement in mass conservation is also obtained.

The level set method is widely used in many areas other than incompressible fluid flows. Gibou et al. (2003) presented a level set approach for the modeling of dendritic solidification. Pitsch and Lageneste (2002) employed the level set formulation to treat the instantaneous flame front as an interface. Asethian and Adalsteinsson (1996) used the level set method for etching, deposition, and lithography development. More details of the level set methods can be found in Sethian (1996).

1.3 Method of Present Study

In the present study, both the interface-tracking and interface-capturing methods are used in conjunction with a Chimera Reynolds-Averaged Navier-Stokes (RANS) method for time-domain simulation of nonlinear waves around offshore structures. For the interface-tracking method, it is convenient to use separate body-fitted numerical grids for the structures and the ambient wave field. In the chimera domain decomposition approach, the numerical grids around the offshore structures remain fixed while the free surface grids are adjusted every time step to conform to the exact free surface. Since the submerged portion of the structures change continuously at different time instants, the interpolation between different chimera grid blocks is updated every time step to enforce conservation of mass and momentum across block boundaries over the entire simulation. In addition, an effective damping beach approach proposed by Chen and Huang (2004) is implemented on the wave maker boundary to prevent the reflected waves from reaching the wave maker boundary. This enables performance of long-duration simulations without significantly increasing the size of the computational domain. In the present study, the chimera RANS method of Chen et al. (2000, 2001, 2002) has been generalized for time-domain simulation of fully nonlinear wave runup around two- and three-dimensional offshore structures.

The present interface-tracking method was used with considerable success by Chen et al. (2002) for time-domain simulation of barge capsizing. However, the interface-tracking method is not suitable for the simulation of more complex green water problems with the presence of water spray and air bubbles. In view of these limitations, we have also developed an interface-capturing method based on the level set method. The level set method has been incorporated into the chimera RANS method of Chen and Chen (1998) for the prediction of sloshing flows in LNG tanks and green water on offshore platforms. The governing equations are formulated in a curvilinear coordinate system and discretized using the finite-analytic method of Chen et al. (1990) on a non-staggered grid. For the additional level set equations of evolution and re-initialization, we use the 3rd order TVD (total variation diminishing) Runge-Kutta scheme (Yu et al, 2003b) for time derivatives, and the 3rd order ENO (essentially non-oscillatory) scheme for spatial derivatives.

The present interface-capturing method is validated first for several benchmark cases including a stationary circle, Zalesak's problem, and the stretching of a circular fluid element under prescribed free motion. The level set method was then incorporated into the chimera RANS method of Chen and Chen (1998) for complex free surface flow simulations. Calculations were performed first for dam breaking and free jet problems in single-block rectangular grids. The feasibility of using the chimera domain decomposition approach in level set method was also evaluated for the dam breaking problem using two different embedding grid systems. Finally, the new chimera RANS method was used for the simulation of a traveling solitary wave and green water on offshore platforms. These test cases clearly demonstrated that the level set method is capable of simulating violent free surface flows encountered in the wave run up on offshore platforms.

1.4 Organization

In Part I of this report, a numerical method that couples the level set method with the chimera RANS method together is presented. After validation by some benchmark cases, such as dam breaking flow, solitary wave propagation and dam breaking flow with an obstacle, this new method is applied in some typical free surface flows. Simulations of green water over an offshore structure and impact pressure in sloshing flow are provided to show the advantages of this method.

Chapter 2 describes the mathematical formulation of the Level-Set RANS method. The general equation of the level set function and the Reynolds-Averaged Navier-Stokes (RANS) equations are given in both the physical plane and the transformed plane. A large eddy approximation is used for the modeling of turbulent flows. Chapter 3 presents the finite different scheme for both the level set equation and the RANS equations. The third order ENO scheme and TVD scheme are used to discretize the level set equation.

Chapter 4 gives several validations of the Level-Set RANS method. The comparison between numerical simulations and experimental results shows the Level-Set RANS method can capture the free surface accurately.

Chapter 5 presents predictions of impact pressures acting on the wall of an LNG tank during sloshing flow. Six cases of both transverse and longitudinal motions are described in detail. All results demonstrate the Level-Set RANS method can capture the impact pressure accurately.

Chapter 6 presents simulations of green water over an offshore structure. Both two-dimensional and three-dimensional simulations are shown in this chapter. The comparison between numerical and experimental results is good.

Chapter 7 presents a summary and conclusions of the study.

2 MATHEMATICAL MODEL

2.1 Introduction

This chapter describes the mathematical formulation of the Level-Set RANS method. The general equation of the level set function and the Reynolds-Averaged Navier-Stokes (RANS) equations are given in both the physical plane and the transformed plane. A large eddy approximation is used for the modeling of turbulent flows.

2.2 Level Set Equation

As discussed in Chapter 1, the level set function ϕ is typically defined as the signed distance from an interface, and in this study we are concerned with the air-water interface. In the present algorithm, the interface is the zero level set of ϕ:

$$\Gamma = \left\{ \vec{x} \,|\, \phi(\vec{x}, t) = 0 \right\} \tag{2.1}$$

By defining $\phi < 0$ for the air region and $\phi > 0$ for the water region:

$$\phi(\vec{x}, t) \begin{cases} > 0 & if \ \ \vec{x} \in water \\ = 0 & if \ \ \vec{x} \in \Gamma \\ < 0 & if \ \ \vec{x} \in air \end{cases} \tag{2.2}$$

the evolution of ϕ is given by the advection equation as follows:

$$\frac{\partial \phi}{\partial t} + \vec{V} \cdot \nabla \phi = 0 \tag{2.3}$$

The transition zone is defined by $|\phi| \le \varepsilon$, where ε is the half thickness of the interface. In the transition zone, the fluid properties are smoothed by the Heaviside function $H(\phi)$:

$$H(\phi) = \begin{cases} 0 & if\ \phi < -\varepsilon \\ \frac{1}{2}\left[1 + \frac{\phi}{\varepsilon} + \frac{1}{\pi}\sin\left(\frac{\pi\phi}{\varepsilon}\right)\right] & if\ -\varepsilon \le \phi \le \varepsilon \\ 1 & if\ \phi > \varepsilon \end{cases} \tag{2.4}$$

More specifically, the density ρ and viscosity μ are calculated in the following way:

$$\begin{aligned} \rho(\phi) &= \rho_a + (\rho_w - \rho_a)\cdot H(\phi) \\ \mu(\phi) &= \mu_a + (\mu_w - \mu_a)\cdot H(\phi) \end{aligned} \tag{2.5}$$

where the subscripts `*a*' and `*w*' represent air and water, respectively. After a new level set value ϕ_0 is obtained in each time step, it is necessary to solve the re-distancing Equation 2.6 in order to ensure that the level set value remains as a real distance.

$$L(\phi_0, \phi) = sign(\phi_0)\left(1 - |\nabla\phi|\right) \tag{2.6}$$

However, it is well known that numerical errors may accumulate due to repeated re-distance operations on a level set function. In order to prevent the straying of the zero level set from the initial position even after many iterations, a mass constraint term proposed by Sussman and Fatemi (1999) is added to Equation 2.6 as follows:

$$\frac{\partial\phi}{\partial\tau} = L(\phi_0, \phi) + \lambda_{ij} f(\phi) \tag{2.7}$$

where

$$\begin{aligned} L(\phi_0, \phi) &= sign(\phi_0)\left(1 - |\nabla\phi|\right) \\ f(\phi) &\equiv H'(\phi)\,|\nabla\phi| \end{aligned} \tag{2.8}$$

The coefficient λ is determined by

$$\lambda_{ij} = \frac{-\int_{\Omega_{ij}} H'(\phi)\, L(\phi_0, \phi)}{\int_{\Omega_{ij}} H'(\phi)\, f(\phi)} \tag{2.9}$$

for every grid cell $\Omega_{ij} = \left\{ (x,y) \middle| x_{i-1/2} < x < x_{i+1/2} \quad and \quad y_{j-1/2} < y < y_{j+1/2} \right\}$. A more detailed description of the mass constraint term is given in Sussman and Fatemi (1999).

2.3 RANS Equations

The Navier-Stokes equations are rewritten in the level set formulation. Both the density and viscosity at air-water interfaces depend on the level set function being a distance function. The fluid properties are assumed to vary smoothly across a narrow transition zone around the free surface. This enables us to obtain accurate and stable numerical results for violent free surface motions encountered in the simulation of green water on offshore platforms.

It is assumed that both water and air are governed by the incompressible Navier-Stokes equations:

$$\begin{aligned} \rho_w \left(\frac{\partial \vec{V}'}{\partial t'} + \vec{V}' \cdot \nabla \vec{V} \right) &= \rho_w \vec{g} + \mu_w \nabla^2 \vec{V}' - \nabla p' \\ \rho_a \left(\frac{\partial \vec{V}'}{\partial t'} + \vec{V}' \cdot \nabla \vec{V} \right) &= \rho_a \vec{g} + \mu_a \nabla^2 \vec{V}' - \nabla p' \end{aligned} \tag{2.10}$$

The above equations are normalized using the following three dimensionless variables:

$$\vec{V} = \frac{\vec{V}'}{U_0}, \qquad t = \frac{t'}{t_0} = \frac{U_0}{L} t', \qquad p = \frac{p'}{\rho_w U_0^2}$$

After dividing by $\frac{\rho_w U_0^2}{L}$ and combining the two equations together by using the non-dimensional density $\rho(\phi)$ and the non-dimensional viscosity , $\nu(\phi) = \mu(\phi)/\rho(\phi)$ as the following equation which is similar to Equation 2.5,

$$\begin{aligned}\rho(\phi) &= \frac{\rho}{\rho_W} + \left(1 - \frac{\rho}{\rho_W}\right)\cdot H(\phi) \\ \mu(\phi) &= \frac{\mu}{\mu_W} + \left(1 - \frac{\mu}{\mu_W}\right)\cdot H(\phi)\end{aligned} \tag{2.11}$$

Equations 2.10 will be

$$\frac{\partial \vec{V}}{\partial t} + \vec{V}\cdot\nabla\vec{V} = -\frac{\delta_{i,3}}{Fr^2} + \frac{\nu(\phi)}{\mathrm{Re}}\nabla^2\vec{V} - \frac{1}{\rho(\phi)}\nabla p \tag{2.12}$$

where the Froude number $Fr^2 = \frac{U_0^2}{gL}$ and the Reynolds number $\mathrm{Re} = \frac{\rho_w U_0 L}{\mu_w}$.

Then continuity and momentum equations are then transformed to a curvilinear coordinate system,

$$\sum_{i=1}^{3} \frac{\partial U_i}{\partial x^i} = 0 \tag{2.13}$$

$$\frac{\partial U_i}{\partial t} + \sum_{j=1}^{3}\left(U_j\frac{\partial U_i}{\partial x^j} + \frac{\partial \overline{u_i u_j}}{\partial x^j}\right) + \frac{1}{\rho(\phi)}\frac{\partial p}{\partial x^i} - \frac{\nu(\phi)}{\mathrm{Re}}\nabla^2 U_i + \frac{\delta_{i,3}}{Fr^2} = 0 \tag{2.14}$$

with $\nabla^2 = \sum_{j=1}^{3}\frac{\partial^2}{\partial x^j \partial x^j}$.

The Reynolds stresses $\overline{u_i u_j}$ are related to the corresponding mean rate of strain through an isotropic eddy viscosity ν_t according to

$$-\overline{u_i u_j} = \nu_t \left(\frac{\partial U_i}{\partial x^j} + \frac{\partial U_j}{\partial x^i} \right) - \frac{2}{3} \delta_{ij} k \tag{2.15}$$

where $k = (\overline{uu} + \overline{vv} + \overline{ww})/2$ is the turbulent kinetic energy. The substitution of Reynolds stresses into the momentum equations yields:

$$\frac{\partial U_i}{\partial t} + \sum_{j=1}^{3} \left[\left(U_i - \frac{\partial \nu_t}{\partial x^j} \right) \frac{\partial U_i}{\partial x^j} - \frac{\partial \nu_t}{\partial x^j} \frac{\partial U_j}{\partial x^i} \right] = -\frac{\delta_{i,3}}{Fr^2} + \left(\frac{\nu(\phi)}{\mathrm{Re}} + \nu_t \right) \nabla^2 U_i - \left(\frac{1}{\rho(\phi)} \frac{\partial p}{\partial x^i} + \frac{\partial \left(\frac{2}{3} k \right)}{\partial x^i} \right) \tag{2.16}$$

Let $\varphi = U_i$ and rearrange the momentum equations as follows:

$$\nabla^2 \varphi = R_\varphi \cdot \left[\sum_{j=1}^{3} \left(U_j - \frac{\partial \nu_t}{\partial x^j} \right) \frac{\partial \varphi}{\partial x^j} + \frac{\partial \varphi}{\partial t} \right] + s_\varphi \tag{2.17}$$

where the effective viscosity is $R_\varphi = \left(\frac{\nu(\phi)}{\mathrm{Re}} + \nu_t \right)^{-1}$ and the source terms are given by

$$s_\varphi = R_\varphi \left[\frac{1}{\rho(\phi)} \frac{\partial p}{\partial x^i} + \frac{\partial \left(\frac{2}{3} k \right)}{\partial x^i} - \sum_{j=1}^{3} \frac{\partial \nu_t}{\partial x^j} \frac{\partial U_j}{\partial x^i} + \frac{\delta_{i,3}}{Fr^2} \right] \tag{2.18}$$

In the curvilinear coordinate system, the terms in Equation 2.17 can be rewritten in the transformed plane as follows:

$$
\begin{aligned}
\nabla^2\varphi &= \sum_i \sum_j g^{ij} \frac{\partial^2 \varphi}{\partial \xi^i \partial \xi^j} + \sum_j f^j \frac{\partial \varphi}{\partial \xi^j} \\
\frac{\partial \varphi}{\partial t} &= \frac{\partial \varphi}{\partial \tau} - \frac{1}{J} \sum_i \sum_j b_i^j \frac{\partial x^i}{\partial \tau} \frac{\partial \varphi}{\partial \xi^j} \\
\sum_j U_j \frac{\partial \varphi}{\partial x^j} &= \sum_i U_i \left(\frac{1}{J} \sum_j b_i^j \frac{\partial \varphi}{\partial \xi^j} \right) \\
-\frac{\partial \nu_t}{\partial x^j} \frac{\partial \varphi}{\partial x^j} &= -\sum_n \left[\frac{1}{J} \sum_m b_n^m \frac{\partial \nu_t}{\partial \xi^m} \cdot \frac{1}{J} \sum_j b_n^j \frac{\partial \varphi}{\partial \xi^j} \right]
\end{aligned}
\tag{2.19}
$$

where, b_i^j, g^{ij}, f^j and the Jacobian J are geometric coefficients in the curvilinear coordinate system whose values can be readily evaluated in the transformed plane. Substituting these terms into Equation 2.17 yields:

$$
\sum_i \sum_j g^{ij} \frac{\partial^2 \varphi}{\partial \xi^i \partial \xi^j} - \sum_j 2a_\varphi^j \frac{\partial \varphi}{\partial \xi^j} = R_\varphi \frac{\partial \varphi}{\partial \tau} + s_\varphi \tag{2.20}
$$

where

$$
2a_\varphi^j = \frac{R_\varphi}{J} \sum_n b_n^j \left[U_n - \frac{\partial x_i}{\partial \tau} - \sum_m \frac{1}{J} b_n^m \frac{\partial \nu_t}{\partial \xi^m} \right] - f^j \tag{2.21}
$$

Note that

$$
\begin{aligned}
\sum_i \sum_j g^{ij} \frac{\partial^2 \varphi}{\partial \xi^i \partial \xi^j} &= g^{11} \frac{\partial^2 \varphi}{\partial \xi^1 \partial \xi^1} + g^{22} \frac{\partial^2 \varphi}{\partial \xi^2 \partial \xi^2} + g^{33} \frac{\partial^2 \varphi}{\partial \xi^3 \partial \xi^3} \\
&\quad + 2\left(g^{12} \frac{\partial^2 \varphi}{\partial \xi^1 \partial \xi^2} + g^{23} \frac{\partial^2 \varphi}{\partial \xi^2 \partial \xi^3} + g^{13} \frac{\partial^2 \varphi}{\partial \xi^1 \partial \xi^3} \right)
\end{aligned}
\tag{2.22}
$$

Substituting Equation 2.22 into Equation 2.20 yields

$$
\sum_j \left(g^{jj} \frac{\partial^2 \varphi}{\partial \xi^j \partial \xi^j} - 2a_\varphi^j \frac{\partial \varphi}{\partial \xi^j} \right) = R_\varphi \frac{\partial \varphi}{\partial \tau} + S_\varphi \tag{2.23}
$$

$$S_{\varphi} = s_{\varphi} - 2\left(g^{12} \frac{\partial^2 \varphi}{\partial \xi^1 \partial \xi^2} + g^{23} \frac{\partial^2 \varphi}{\partial \xi^2 \partial \xi^3} + g^{13} \frac{\partial^2 \varphi}{\partial \xi^1 \partial \xi^3} \right) \tag{2.24}$$

The momentum equations (Equation 2.23) and the continuity equation (Equation 2.13) are the Reynolds-Averaged Navier-Stokes (RANS) equations for unsteady, three-dimensional turbulent flows.

3 NUMERICAL MODEL

3.1 Introduction

This chapter presents the finite different scheme for both the level set equation and the RANS equations. The third order essentially non-oscillatory (ENO) scheme and the total variation diminishing (TVD) Runge-Kutta scheme are used to discretize the level set equation. The finite analytic solution is applied for the RANS equations.

3.2 Level Set Equation

We further introduce the contravariant velocity components (Chen and Patel, 1989)

$$U^i = JV^i = \sum_{j=1}^{3} b_j^i U_j \tag{3.1}$$

The level set evolution equation is written in the transformed coordinates (ξ^i, t)

$$\frac{\partial \phi}{\partial t} + \sum_{i=1}^{3} \frac{\partial (U^i \phi)}{\partial \xi^i} = 0 \tag{3.2}$$

Shu and Osher (1989) discussed the r^{th} order TVD Runger-Kutta time discretization in details. In the present study, Equation 3.2 is advanced using the 3$^{\text{rd}}$-order TVD Runge-Kutta scheme which is total variation stable:

$$\begin{aligned}
\phi^{(1)} &= \phi^n - \Delta t \cdot R(\phi^n) \\
\phi^{(2)} &= \frac{3}{4}\phi^{(n)} + \frac{1}{4}\phi^{(1)} - \frac{\Delta t}{4} R(\phi^{(1)}) \\
\phi^{(n+1)} &= \frac{1}{3}\phi^{(n)} + \frac{2}{3}\phi^{(2)} - \frac{2\Delta t}{3} R(\phi^{(2)})
\end{aligned} \tag{3.3}$$

where $R(\phi) = \dfrac{\partial(U^i\phi)}{\partial\xi^i}$.

There are two ways to discretize the spatial operator *R*: the ENO scheme (Shu 1997) and the Hamilton-Jacobi ENO scheme (Osher and Fedkiw, 2003). The former evaluates ϕ values at cell faces, while the latter evaluates the flux values directly at grid points.

For the ENO scheme, the spatial operator *R* is discretized in the transformed plane (ξ,η,ζ) in a conservative manner.

$$\begin{aligned}\frac{\partial(U^i\phi)}{\partial\xi^i} = (U^1\phi)_{i+\frac{1}{2},j,k} - (U^1\phi)_{i-\frac{1}{2},j,k} + (U^2\phi)_{i,j+\frac{1}{2},k} \\ - (U^2\phi)_{i,j-\frac{1}{2},k} + (U^3\phi)_{i,j,k+\frac{1}{2}} - (U^3\phi)_{i,j,k-\frac{1}{2}}\end{aligned} \tag{3.4}$$

The cell-face values of ϕ are constructed based on the left-shift parameters r_1, r_2, r_3 which are representing different orders. The first order ENO scheme is the same as the first order upwind scheme which is described as follows:

$$\phi_{i+\frac{1}{2}} = \begin{cases} \phi_{i+1} & if\ r_1 = 0 \\ \phi_i & if\ r_1 = 1 \end{cases} \tag{3.5}$$

with r_1 defined as follows:

$$r_1 = \begin{cases} 1 & if\ U_{i+1/2} \geq 0 \\ 0 & if\ U_{i+1/2} < 0 \end{cases} \tag{3.6}$$

The 2nd-order ENO scheme is introduced as follows:

$$\phi_{i+\frac{1}{2}} = \begin{cases} \frac{3}{2}\phi_{i+1} - \frac{1}{2}\phi_{i+2} & if \ r_2 = -1 \\ \frac{1}{2}\phi_i + \frac{1}{2}\phi_{i+1} & if \ r_2 = 0 \\ -\frac{1}{2}\phi_{i-1} + \frac{3}{2}\phi_i & if \ r_2 = 1 \end{cases} \tag{3.7}$$

with r_2 defined in terms of r_1 as follows:

$$r_2 = \begin{cases} r_1 & if \ \left| \delta\phi_i^{-r_1+1} \right| \geq \left| \delta\phi_i^{-r_1} \right| \\ r_1 - 1 & if \ \left| \delta\phi_i^{-r_1+1} \right| < \left| \delta\phi_i^{-r_1} \right| \end{cases} \tag{3.8}$$

The 3rd-order ENO scheme is introduced as follows:

$$\phi_{i+1/2} = \begin{cases} \frac{11}{6}\phi_{i+1} - \frac{7}{6}\phi_{i+2} + \frac{1}{3}\phi_{i+3} & if \ r_3 = -1 \\ \frac{1}{3}\phi_i + \frac{5}{6}\phi_{i+1} - \frac{1}{6}\phi_{i+2} & if \ r_3 = 0 \\ -\frac{1}{6}\phi_{i-1} + \frac{5}{6}\phi_i + \frac{1}{3}\phi_{i+1} & if \ r_3 = 1 \\ \frac{1}{3}\phi_{i-2} - \frac{7}{6}\phi_{i-1} + \frac{11}{6}\phi_i & if \ r_3 = 2 \end{cases} \tag{3.9}$$

with r_3 defined in terms of r_2 as follows:

$$r_3 = \begin{cases} r_2 & if \ \left| \delta\phi_i^{-r_2+1} \right| < \left| \delta\phi_i^{-r_2} \right| \\ r_2 + 1 & if \ \left| \delta\phi_i^{-r_2+1} \right| \geq \left| \delta\phi_i^{-r_2} \right| \end{cases} \tag{3.10}$$

Denoting

$$\begin{cases} \delta\phi_i^{-1} = \phi_i - \phi_{i-1} \\ \delta\phi_i^{0} = \phi_{i+1} - \phi_i \\ \delta\phi_i^{1} = \phi_{i+2} - \phi_{i+1} \end{cases} \qquad \begin{cases} \delta^2\phi_i^{-1} = \phi_{i-2} - 2\phi_{i-1} + \phi_i \\ \delta^2\phi_i^{0} = \phi_{i-1} - 2\phi_i + \phi_{i+1} \\ \delta^2\phi_i^{1} = \phi_i - 2\phi_{i+1} + \phi_{i+2} \\ \delta^2\phi_i^{2} = \phi_{i+1} - 2\phi_{i+2} + \phi_{i+3} \end{cases} \tag{3.11}$$

the same definitions for subscripts (j,k) apply in the (η,ζ) directions.

In order to avoid the logical structures to distinguish whether a given stencil is completely inside the computational domain, one could set all the ghost values outside the computational domain to be very large with large variations. This way the ENO choosing procedure will automatically avoid choosing any stencil containing ghost points.

For the Hamilton-Jacobi ENO scheme, the flux values $\dfrac{\partial\phi}{\partial\xi^i}$ are constructed directly at each grid point (i,j,k) in the transformed plane (ξ,η,ζ). Here, we again demonstrate the discretizations in the ξ direction as an example. Note that $\Delta\xi = \Delta\eta = \Delta\zeta = 1$. The algorithm is described as follows:

1. Construct the divided difference tables D^0, D^1, D^2, D^3 as follows:

$$\begin{cases} D_k^0 = \phi_k \\ D_{k+1/2}^1 = D_{k+1}^0 - D_k^0 \\ D_k^2 = \left(D_{k+1/2}^1 - D_{k-1/2}^1\right)/2 \\ D_{k+1/2}^3 = \left(D_{k+1/2}^2 - D_k^2\right)/3 \end{cases}$$

2. To find $\left(\dfrac{\partial\phi}{\partial\xi}\bigg|_i\right)^-$, start with $k = i-1$, and to find $\left(\dfrac{\partial\phi}{\partial\xi}\bigg|_i\right)^+$, start with $k = i$.

3. Define $\left.\frac{\partial \phi}{\partial \xi}\right|_i = D^1_{k+1/2}$

4. If $\left|D^2_k\right| < \left|D^2_{k+1}\right|$ then set $c = D^2_k$ and $k^* = k-1$, else set $c = D^2_{k+1}$ and $k^* = k$.

   Then $\left.\frac{\partial \phi}{\partial \xi}\right|_i = c\left(2(i-k)-1\right)$

5. If $\left|D^3_{k^*+1/2}\right| < \left|D^3_{k^*+3/2}\right|$ then set $c^* = D^3_{k^*+1/2}$, else set $c^* = D^3_{k^*+3/2}$

   Then $\left.\frac{\partial \phi}{\partial \xi}\right|_i = c^*\left(3(i-k^*)^2 - 6(i-k^*) + 2\right)$

6. If $U^1_i \geq 0$ discretize $\left.\frac{\partial \phi}{\partial \xi}\right|_i$ by $\left(\left.\frac{\partial \phi}{\partial \xi}\right|_i\right)^-$. If $U^1_i < 0$ discretize $\left.\frac{\partial \phi}{\partial \xi}\right|_i$ by $\left(\left.\frac{\partial \phi}{\partial \xi}\right|_i\right)^+$.

The same procedures are used for evaluating $\left.\frac{\partial \phi}{\partial \eta}\right|_j$ and $\left.\frac{\partial \phi}{\partial \zeta}\right|_k$.

3.3 RANS Equations

The momentum equations are solved by the 12-point finite analytic scheme of Chen et al. (1990). In the finite analytic approach, Equation 2.23 is locally linearized in each rectangular numerical element. After that, a 12-point finite analytic formula for the unsteady, three-dimensional, elliptic equations can be obtained in the form:

$$\varphi_P = \frac{1}{1 + C_P\left(C_U + C_D + \frac{R}{\Delta\tau}\right)}\left[\sum_1^8 C_{nb}\varphi_{nb} + C_P\left(C_U\varphi_U + C_D\varphi_D + \frac{R}{\Delta\tau}\varphi_P^{n-1}\right) - C_P\left(S_\varphi\right)_P\right] \tag{3.12}$$

The subscripts 'U' and 'D' represent points in the stencil, upstream and downstream of 'P' and the subscript 'nb' denotes neighboring nodes. The finite-analytic coefficients (C_P, C_U, C_D, C_{nb}) can be found in Chen et al.(1990).

The velocities U_i in Equation 3.12 are solved by the PISO/SIMPLER algorithm. The velocities and pressure are defined at the grid nodes while the contravariant pseudo-velocities are at staggered locations. The velocities U_i are decomposed into a pseudo-velocity field $\hat{U}_i$ plus the pressure-gradient terms contained in the source function and can be found as follows:

$$U_{i,P} = \hat{U}_i - \frac{\frac{1}{J} C_P R}{1 + C_P \left(C_U + C_D + \frac{R}{\Delta \tau} \right)} \frac{1}{\rho(\phi)} \sum_j b_i^j \frac{\partial p}{\partial \xi^j} \tag{3.13}$$

where the pseudo-velocities are defined by:

$$\hat{U}_i = \frac{1}{1 + C_P \left(C_U + C_D + \frac{R}{\Delta \tau} \right)} \left[\sum_1^8 C_{nb} U_{i,nb} + C_P \left(C_U U_{i,U} + C_D U_{i,D} + \frac{R}{\Delta \tau} U_{i,P}^{n-1} \right) - C_P R \left(S_{U_i} + \frac{1}{Fr^2} \right) \right] \tag{3.14}$$

A resulting equation for pressure is derived by requiring the contravariant velocity field $\hat{U}_i$ to satisfy the equation of continuity.

$$\begin{aligned} \left(E_d^{11} + E_u^{11} + E_n^{22} + E_s^{22} + E_e^{33} + E_w^{33} \right) p_P = {} & E_d^{11} p_D + E_u^{11} p_U + E_n^{22} p_{NC} \\ & + E_s^{22} p_{SC} + E_e^{33} p_{EC} + E_w^{33} p_{WC} - \hat{D} \end{aligned} \tag{3.15}$$

where

$$\begin{aligned} \hat{D} &= \hat{D}_d^1 - \hat{D}_u^1 + \hat{D}_n^2 - \hat{D}_s^2 + \hat{D}_e^3 - \hat{D}_w^3 \\ &= \frac{1}{2} \left(\hat{D}_D^1 - \hat{D}_U^1 + \hat{D}_{NC}^2 - \hat{D}_{SC}^2 + \hat{D}_{EC}^3 - \hat{D}_{WC}^3 \right) \end{aligned} \tag{3.16}$$

3.4 General Solution Procedure

In the current Level-Set RANS method, the fixed numerical grid is used to cover both air and water. The grid can be decomposed into a number of computational blocks. The grid near the structure can be refined in order to get accurate solutions. The PEGSUS program (Suhs and Tramel 1991) is employed to determine the interpolation information for linking grids before calculations.

The overall solution procedure consists of one loop for pressure, velocity and turbulence quantities and another loop for the level set function ϕ. The former loop solves a system of tri-diagonal matrices by using an iterative ADI scheme while the later solves ϕ by using ENO and TVD schemes.

For the simulations of LNG tank sloshing flow and green water, the solution procedure can be summarized as follows:

1. Construct the grids for each component in the simulation.
2. Determine interpolation information for linking grids using the PEGSUS program.
3. Construct a boundary condition table for velocity, pressure, turbulence quantities and level set function ϕ on each face of the blocks.
4. Specify the initial conditions for $u, v, w, p, k, \varepsilon, \phi$.
5. Calculate the geometric coefficients b_i^j, g^{ij}, etc.
6. Calculate the source function s_φ and solve for the finite analytic coefficients C_U, C_D, C_P etc.
7. Solve the discretization formulae for the RANS equations to obtain the velocity and turbulence quantities using the iterative ADI scheme.

8. Calculate the pseudo-velocities $\hat{U}_i$, $\hat{U}^i$, and pressure p using the iterative ADI scheme.
9. Repeat steps 7 and 8
10. Calculate the level set function ϕ, using ENO and TVD schemes.
11. Do the re-distancing procedure to ensure that ϕ is the physical distance from the interface.
12. Repeat steps 10 and 11.
13. Return to step 5 for the next time step.

4 TEST CASES AND VALIDATIONS

4.1 Re-distancing Test

In order to test the re-distancing procedure in the level set method, we initialize a discontinuous level set function in a non-uniform rectangular grid with 101×101 grid points. The domain size is 1.0×1.0 and the interface is a circle centered at (0.5, 0.5) with a radius of 0.25. The level set function is initially assigned a value of –0.1 outside the circle and +0.1 inside the circle as shown in Figure 4.1. We choose the artificial time increment to be the smallest grid size, i.e., $\Delta t = 0.005$. It can be shown in this test case that we need only to recalculate the level set ϕ for $L/\Delta t$ time steps to obtain the correct distance up to L.

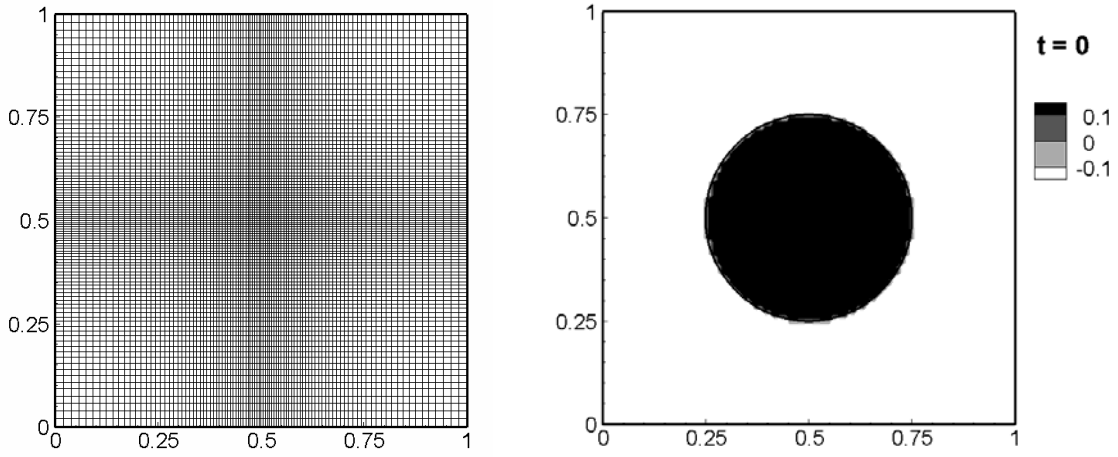

Figure 4.1 Grid and initial ϕ in re-distancing procedure

Figure 4.2 shows the contours of ϕ at different artificial times t = 0.1, 0.2, 0.3, 0.4. It is seen that the devolution of ϕ starts from the interface where the zero level set is, and propagates on both sides of the interface. Theoretically, ϕ is the physical

distance (i.e., $|\nabla\phi| = 1$) from the zero level set in the circle whose radius is equal to the artificial time *t*. It is clearly seen from Figure 4.2 that the zero level set does not change during the calculation. If we continue the calculations for more time steps until the steady state is reached, then ϕ will represent the physical distance from the interface over the entire domain as shown in the last image at *t* = 0.4.

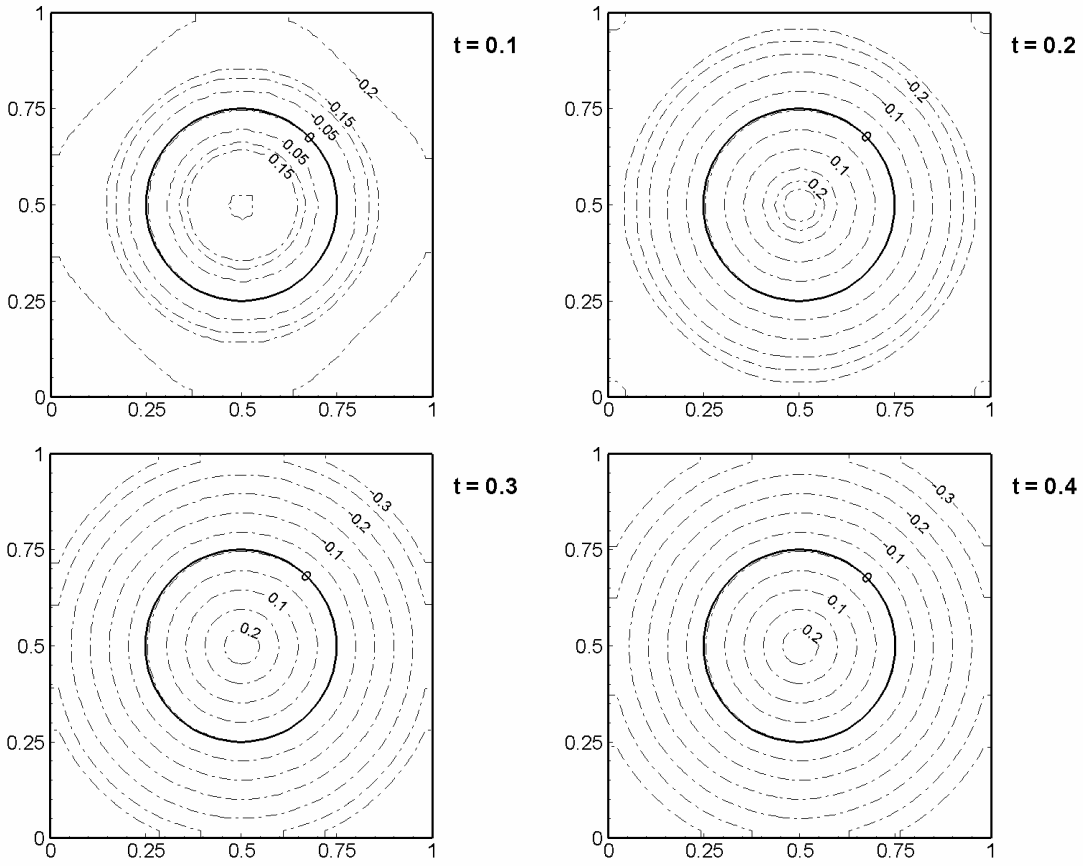

Figure 4.2 The ϕ evolution in the re-distancing procedure

We also repeated the same calculation with uniform grid spacing and obtained exactly the same result. This test case provided a good indication of the number of time steps needed for the re-distance procedure. In our numerical simulations, the initial level

set is typically very close to the physical distance. Therefore, very few time steps are needed to obtain the steady state solution in the re-distancing procedure. More specifically, we have chosen a transition zone width of two times the grid size and a time increment of one grid size. Therefore, only two iterations are needed in the present simulations for re-distancing the level set function.

4.2 Zalesak's Problem

Zalesak's problem of a rotating slotted disk is a benchmark case for testing an advection scheme. Consider a slotted solid disk that rotates around a center with a constant angular velocity. The slotted disk has a radius of 15 and a slot width of 6. It is initially located at (50, 75) in the domain of size (100, 100). The angular velocity Ω is set to 0.01 so that the disk returns to its original position at every 200π (≈ 628) time units.

Figure 4.3 shows the numerical grids and the computed slotted disk edges (solid lines) at t = 0, 157, 314, 471 and 628. The dotted line is the initial geometry of the disk. The dashed line is the final result without mass constraint in the re-distancing procedure. It can be seen that the slotted disk matches its original shape well after a circle rotation except at the sharp corners. And compared with the rotation without the mass constraint, it has good mass conservation during the rotation. This test proves that it is necessary to add the mass constraint term in the re-distancing scheme.

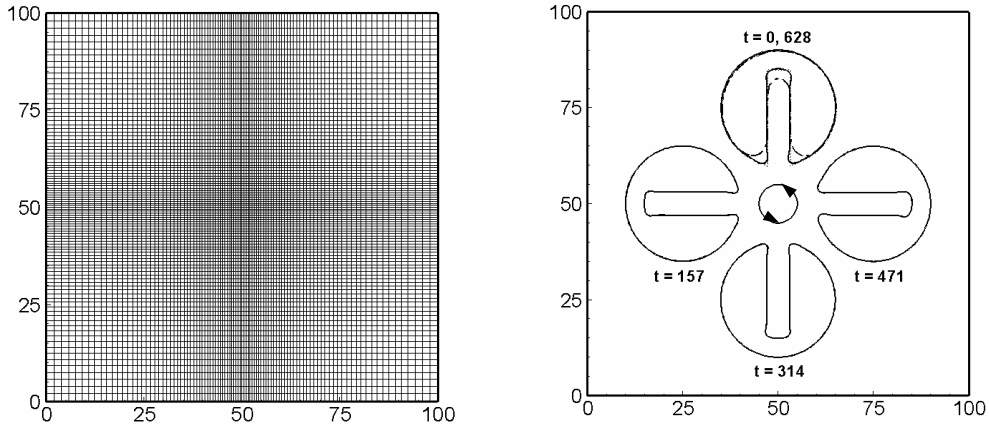

Figure 4.3 Zalesak's problem

4.3 Stretching of a Circular Fluid Element

In the third test case, a circular fluid element is placed in a swirling shear flow field within a unit square. The flow field is prescribed in terms of a two-dimensional stream function φ:

$$\varphi = \frac{1}{\pi} \sin^2(\pi y) \sin^2(\pi z) \tag{4.1}$$

This corresponds to a solenoidal velocity field with the following velocity components:

$$\begin{aligned} v &= -\sin^2\left(\frac{\pi y}{100}\right) \sin\left(\frac{\pi z}{50}\right) \\ w &= \sin^2\left(\frac{\pi z}{100}\right) \sin\left(\frac{\pi y}{50}\right) \end{aligned} \tag{4.2}$$

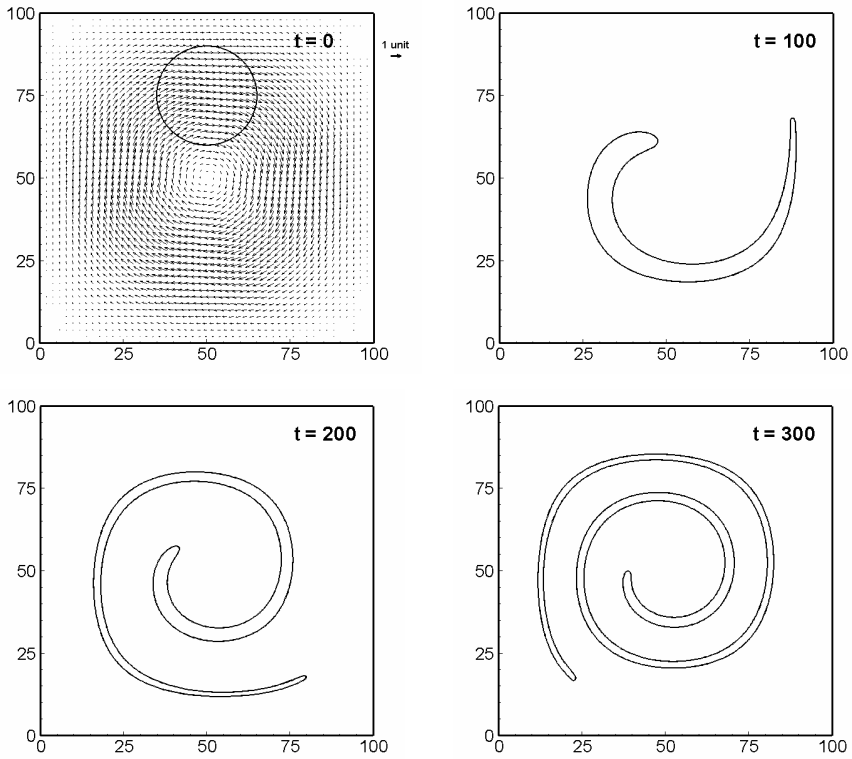

Figure 4.4 Stretching of a circular fluid element in swirling flow

The circular fluid element is stretched into a thin filament by the shearing velocity field as shown in Figure 4.4. This case provides a challenging test for surface-tracking and surface-capturing methods. The circle is initially centered at (50, 75) with a radius of 15. The total mass $M(t) = \int_{\Omega} H(\phi) d\Omega$ is evaluated at every time step to monitor the performance of the mass constraint term. As shown in Figure 4.5, the total mass decreases slightly from 706.858 to 704.694 (i.e., 0.3%). Therefore, the mass constraint term is very effective in maintaining global mass conservation during the advection of interfaces.

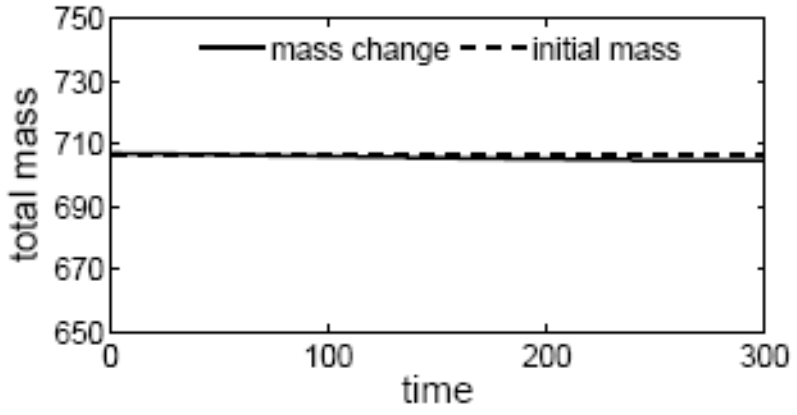

Figure 4.5 Mass change in a circular fluid element stretching

4.4 Stretching and Restoration of a Circular Fluid Element

The last test case of the interface-capturing and re-distancing procedures involves the stretching and restoration (shrinking) of a circular fluid element. In this case, the circular fluid element is subjected to a swirling flow with oscillatory velocity components given by:

$$v = -\sin^2\left(\frac{\pi y}{100}\right)\sin\left(\frac{\pi z}{50}\right)\cos\left(\frac{\pi t}{T}\right)$$
$$w = \sin^2\left(\frac{\pi z}{100}\right)\sin\left(\frac{\pi y}{50}\right)\cos\left(\frac{\pi t}{T}\right) \qquad (4.3)$$

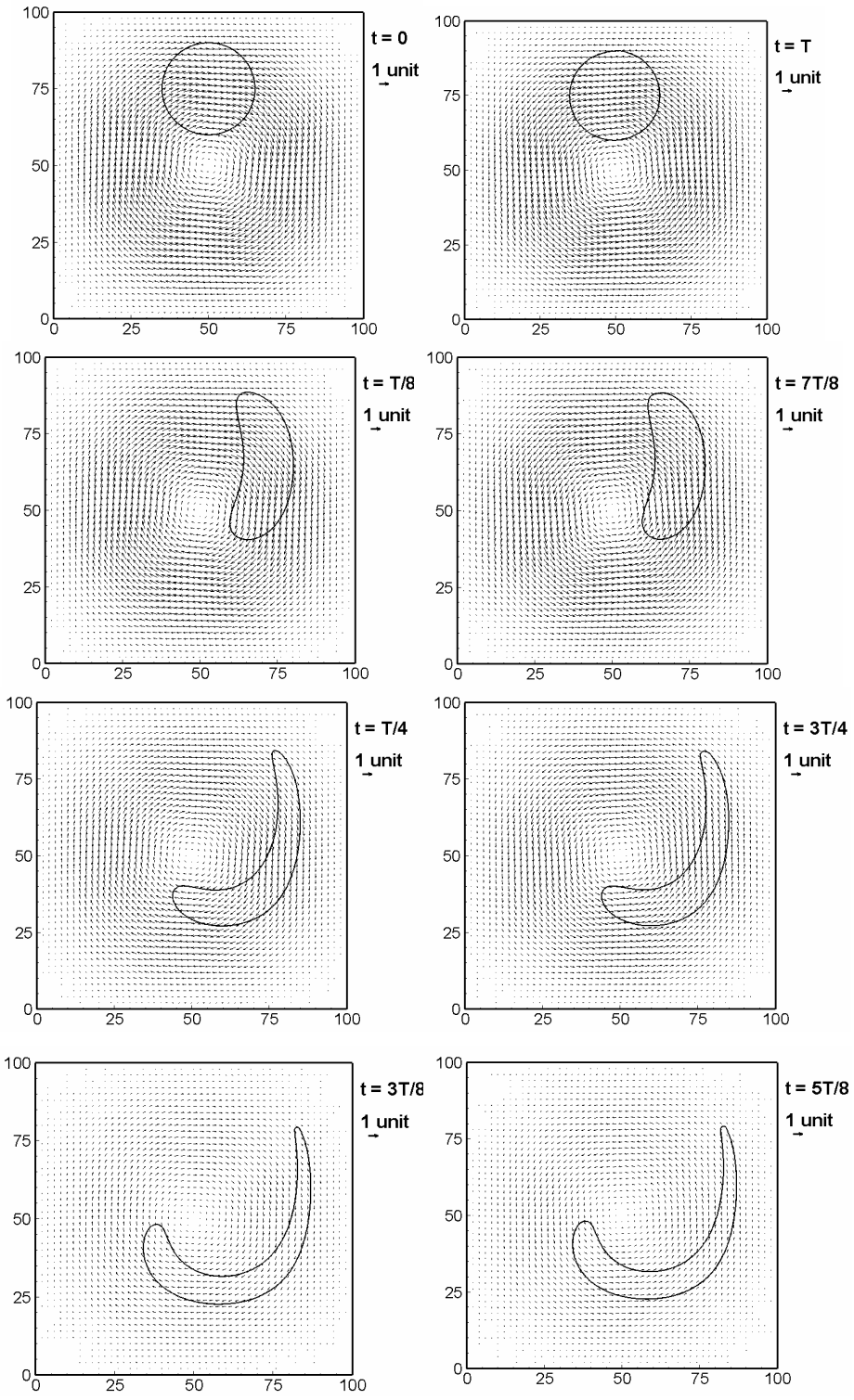

Figure 4.6 The level-set evolution during stretching and shrinking

It is worthwhile to note that the initial velocity field for the present swirling flow is identical to that considered in the previous test case. However, the swirling velocity decreases gradually as the circular fluid element is stretched out during $0 < t < T/2$. At $t = T/2$, the flow comes to a complete stop and begins to reverse its direction. During $T/2 < t < T$, the stretched fluid element shrinks back gradually due to the reversal of the swirling flow direction. The fluid element is expected to recover its initial circular shape at $t = T$ for a perfect interface-capturing scheme. It is seen from Figure 4.6 that the present interface-capturing technique successfully restored the original shape of the circular fluid element. As noted in Figure 4.7 there is a very slight reduction of the total mass $M(t) = \int_{\Omega} H(\phi) d\Omega$ from 706.858 to 701.845 (i.e., 0.7%) after one complete cycle.

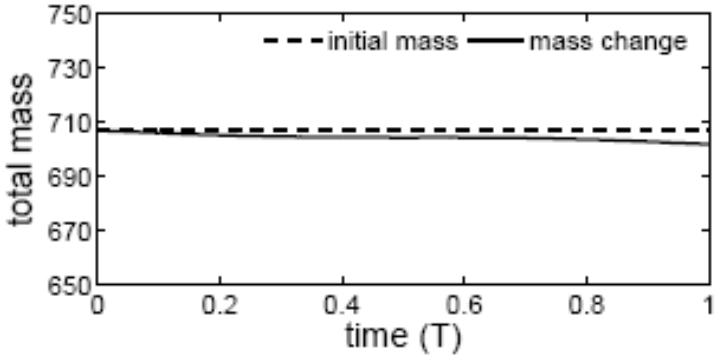

Figure 4.7 Mass change in stretching and shrinking

4.5 Propagation of a Solitary Wave

Propagation of a solitary wave is a simple and practical free surface problem that has been studied experimentally and numerically. To generate a solitary wave, one can make use of Laitone's analytical approximation. Here we release from the left vertical

wall an initially still water surface with a Boussinesq profile which is in hydrostatic balance,

$$A(y,0) = A_0 / \cosh^2\left(\frac{\sqrt{3A_0}\cdot y}{2}\right) \tag{4.4}$$

Figure 4.8 shows the wave profile at different times for the $A_0 = 0.4$ case. The corresponding velocity profile at t = 10 s is shown in Figure 4.9. It is seen that the wave amplitude decays slightly during propagation as a result of the viscous effects.

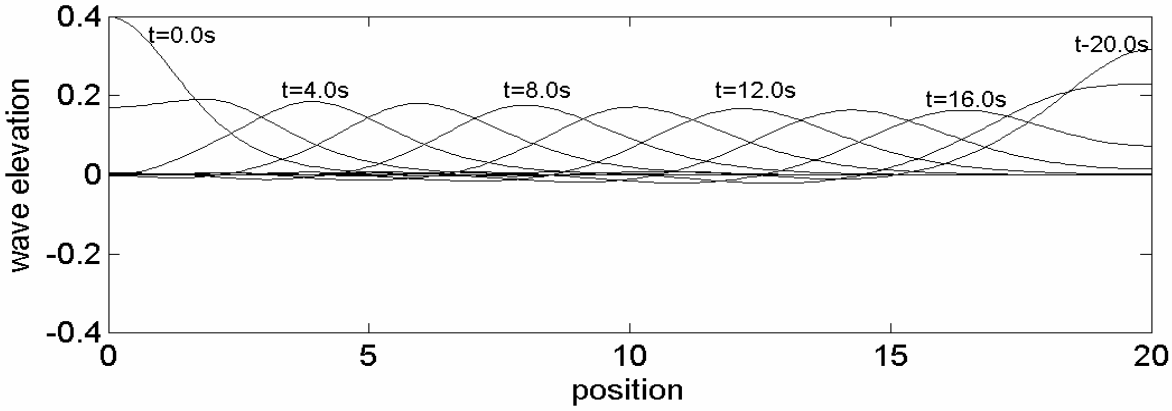

Figure 4.8 Propagation of solitary wave; A_0 = 0.4

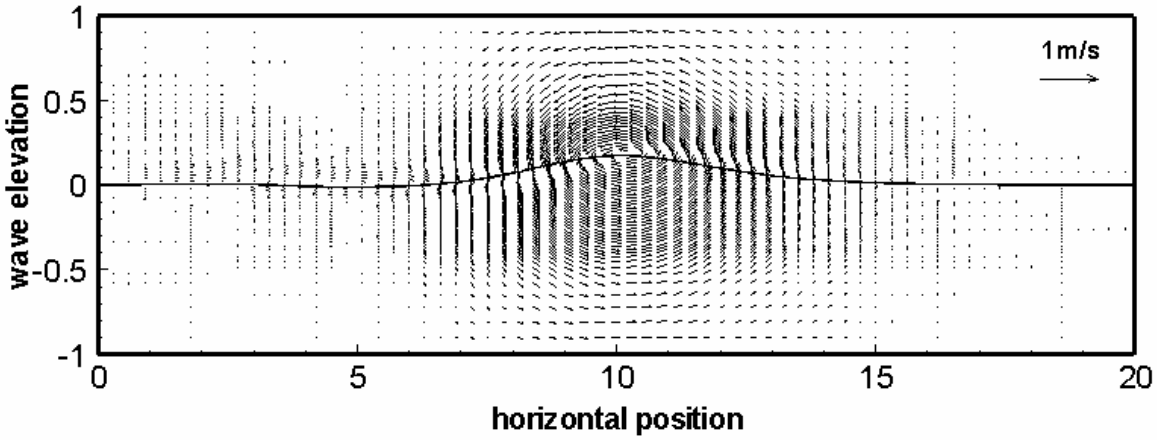

Figure 4.9 Typical velocity field of a solitary wave

To quantify the viscous damping characteristics of the wave, we compute three waves with different initial amplitude, and compare the results with those predicted by the perturbation theory of Mei (1989):

$$A^{-1/4} = A_0^{-1/4} + 0.08356\left(\frac{\nu}{(gh)^{1/2}\,h^{3/2}}\right)^{1/2}\frac{Ct}{h} \tag{4.5}$$

where *Ct* is essentially the distance traveled by the solitary wave. This formula has been verified against the measurements of Russell. In this study, we set the theoretical wave velocity $C = \sqrt{gh}$ = 1 m/s and the water dynamic viscosity $\nu = 2.0\times10^{-6}$ m^2/s. This gives a Reynolds number $\mathrm{Re} = \frac{Ch}{\nu} = 5\times10^4$. It is seen from Figure 4.10 that the present simulation result is in close agreement with the perturbation theory in the middle section of the tank. The discrepancies on the right hand side of the tank are due to the reflection of the solitary wave by the tank wall.

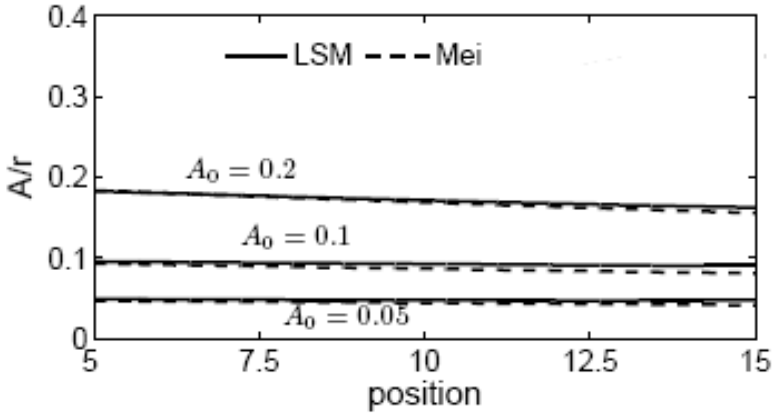

Figure 4.10 Comparison in solitary wave propagation

4.6 Dam-Breaking

The collapse of a water column on a rigid horizontal plane is also called a broken-dam problem. It is used to simulate the abrupt failure of a dam, in which an initially blocked still water column starts to spread out after the barrier is removed. The dam-breaking problem has been the subject of many previous numerical and experimental investigations. In our simulation, the computational domain size is 2.0×5.0, and the parameters used in this study are the same as those used earlier in the solitary wave simulation. The half-thickness of the air-water interface ε is fixed at two times the grid spacing, and the time step size used in the re-distancing procedure is equal to one grid spacing.

Figure 4.11 shows snapshots of water surface profiles and the associated velocity fields for air and water in the entire computational domain at selected time instants. Initially, the water column is in hydrostatic balance with pressure linearly proportional to the water depth. When the vertical barrier is removed at $t = 0$, the water column collapses and flushes to the right due to the large pressure difference between the water and air at the interface. When the front of the water column hits the tank wall, it is pushed upward against the wall by the momentum of the water flow. As the water climbs up the tank wall, the front velocity decreases gradually as the fluid momentum is being converted to potential energy. After the water front comes to a complete stop on the tank wall, it begins to fall back into the bottom water pool due to the gravitational force. The collision of falling water mass with the water in the pool produces a splash wave traveling to the left with a thin and elongated surge front. Several air pockets are observed when the simulation is terminated at $t = 8.0$. It is also clearly seen from the velocity vector plots that the violent free surface motions also induce very strong vortices at the surge front.

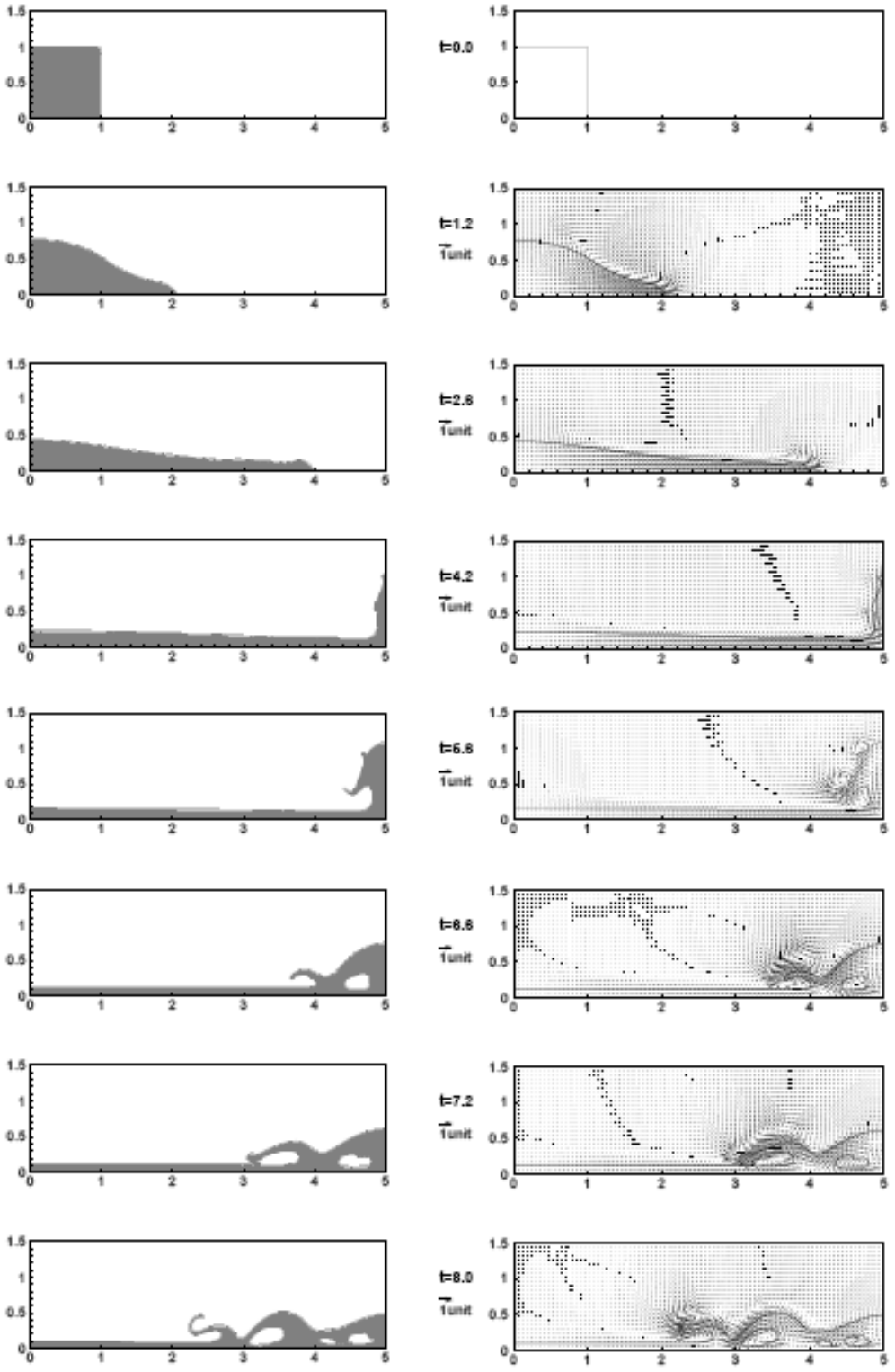

Figure 4.11 Free surface and velocity vectors in dam-breaking

Figure 4.12 shows the comparison between the numerical simulation and experimental results (Martin and Jouce, 1952). The water column is 1×1 initially. So the surge front position and remaining water column height at t = 0 are equal to 1. The maximum surge front position is 5 which is the tank length. The water front has already hit the right side wall at the moment when the surge front position equals to 5. After the surge front hits the wall and bounces back, there is still some water remaining at the left side wall. Both comparisons are in excellent agreements. This confirms that the Level Set RANS method could be used to accurately model free surface flow.

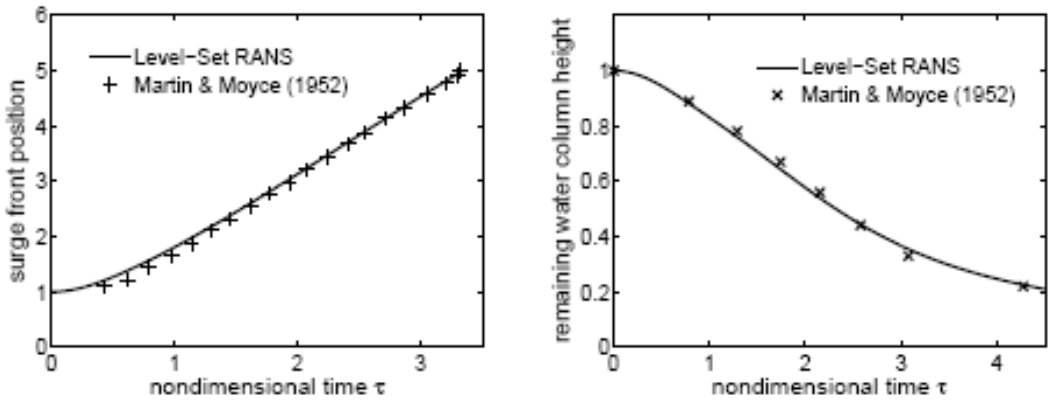

Figure 4.12 2D dam-breaking problem

It has been demonstrated in previous studies by Chen (2005) that the chimera domain decomposition approach provides an effective means to deal with complex geometry and flow conditions by allowing the judicial use of grid overlapping or embedding techniques to simplify the grid generation process. The chimera grid system also allows for selective refinement of the numerical grids in areas of high gradient without significant increase on the overall computing cost. In the present study, the feasibility of using the chimera domain decomposition approach in conjunction with the level set function was demonstrated for the dam-breaking problem using two composite

grid systems shown in Figure 4.13. In both cases, we made a hole in our computational domain first, and then patched the hole with two different grids, a rectangular grid and a semi-circular grid. In the chimera domain decomposition approach, the PEGSUS program of Suhs and Tramel (1991) was employed to identify the hole points and provide interpolation information for the hole fringe points as well as the outer boundary points for the embedded grid blocks.

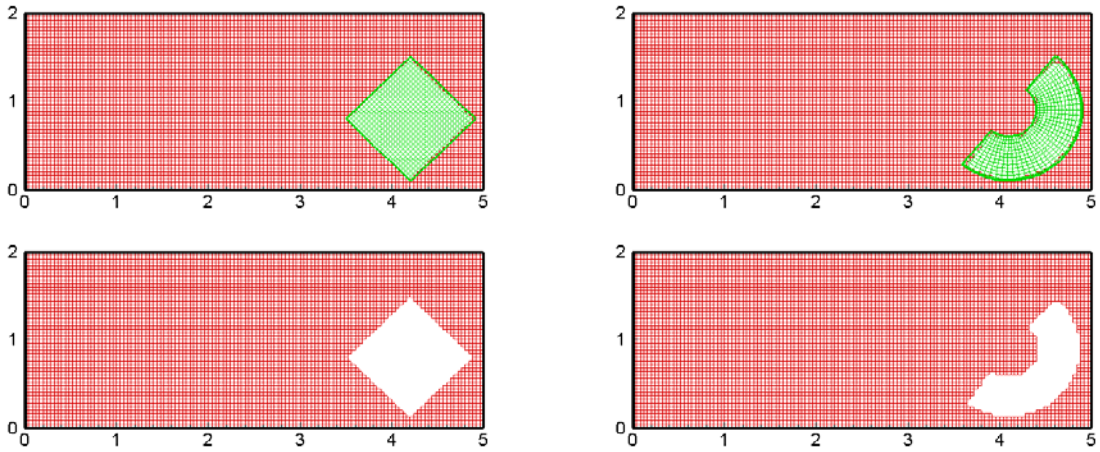

Figure 4.13 Chimera grids for dam-breaking problems

Figure 4.14 shows the simulation results for two different grid embedding systems. It is clearly seen that the air-water interface remains smooth across the overlap region between different computational blocks. This indicates that the interpolation of velocity, pressure, turbulence quantities, and level-set function is robust and accurate for arbitrary grid systems. A detailed comparison of the water surfaces and velocity vector plots in Figure 4.13 and Figure 4.14, however, indicates that the air-water interface is somewhat affected by different implementations of the grid-capturing technique in different computational blocks.

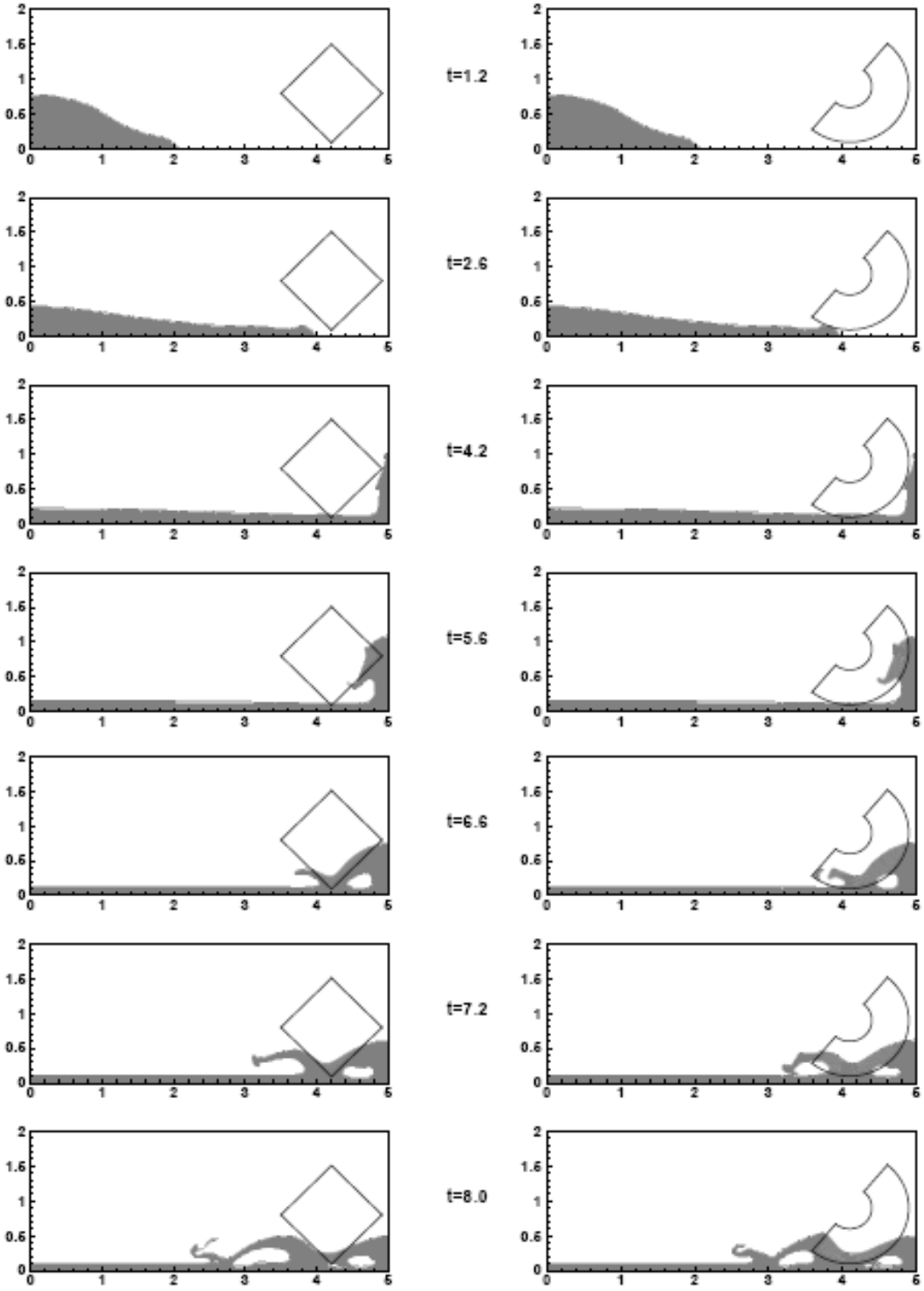

Figure 4.14 2D dam-breaking with two different embedded grids

More specifically, the half thickness of the interface was chosen to be equal to two grid spacing in all three cases. Since the grid sizes are significantly different for two different grid patches, the predicted water surface profiles and air bubble sizes were found to change slightly at later stages of the simulation beyond $t > 6$ s. There is a slight phase lag of the surge front for the semi-circular grid case. Nevertheless, the velocity fields induced by the violent free surface motion are quite similar for all three test grids as seen in Figure 4.15.

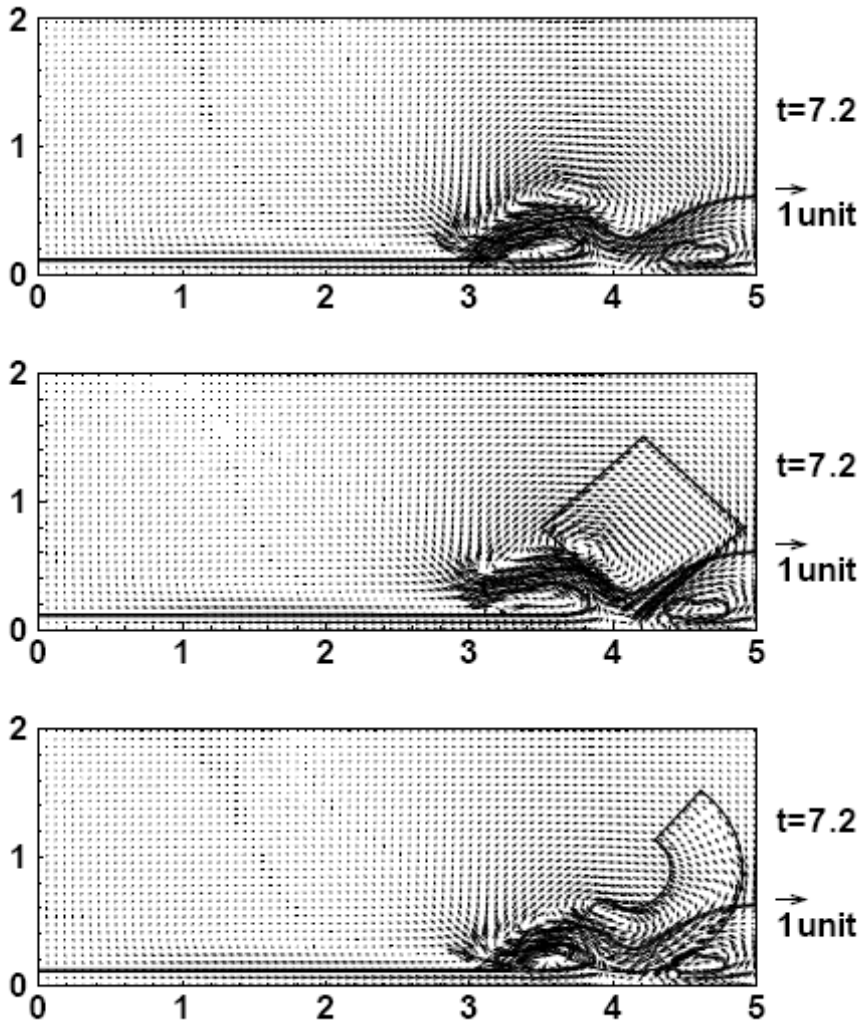

Figure 4.15 Velocity comparison for three different grids

Calculations were also performed for the dam breaking problem in a three-dimensional rectangular tank as shown in Figure 4.16. During the initial stage of the simulation, the flow remains two-dimensional when running up the opposite wall and falling back to the water pool. However, the splash wave produced by the falling water mass quickly develops into a complex 3D breaking wave pattern with the presence of small water droplets and trapped air bubbles. It is quite clear that the level-set method is capable of resolving violent free surface flow with complex three-dimensional air-water interfaces.

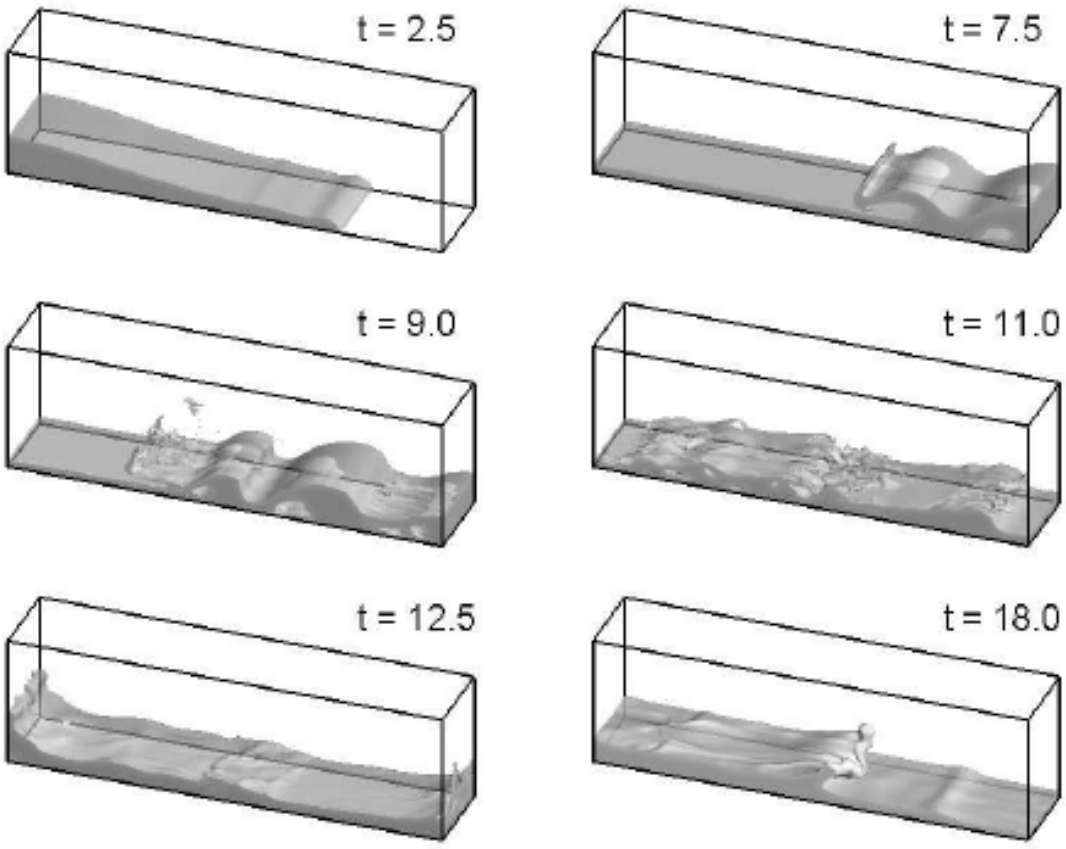

Figure 4.16 Free surface profiles for 3d dam-breaking

4.7 Dam Breaking with an Obstacle

A more interesting test case of a collapsing water column occurs when a small obstacle is placed downstream of the propagating water front. The test geometry used in the experimental investigation of Koshizuka et al. (1995) is illustrated in Figure 4.17. The height and width of the still water column are 2a and a (i.e., 0.292m × 0.146 m), respectively. The width of the tank is 4a (= 0.584 m) and the obstacle is located on the bottom wall at a distance of 2a (= 0.292 m) from the left wall. The size of the obstacle is 2d × d (0.048 m × 0.024 m). In the present study, we choose a = 0.146 m as the characteristic length. The computational domain after normalization is shown in Figure 4.18.

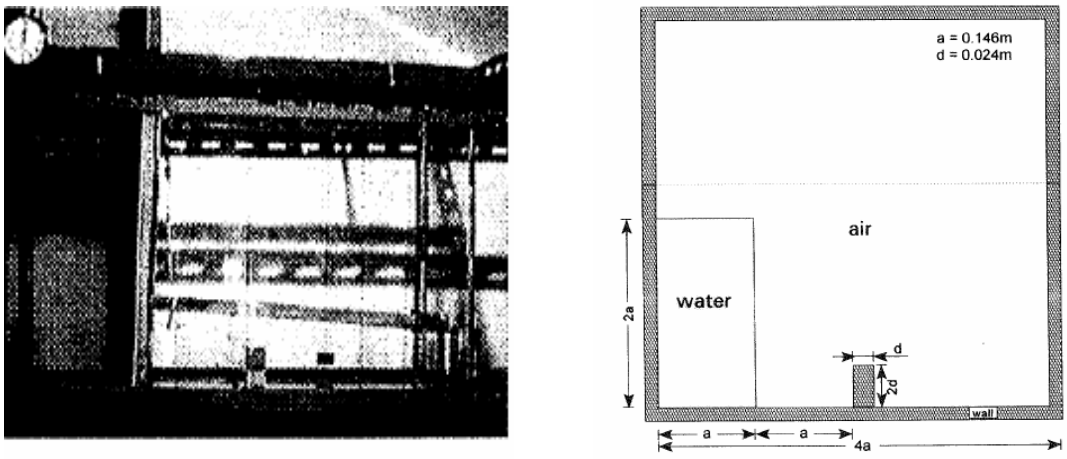

Figure 4.17 Experiment setup of dam-breaking with an obstacle

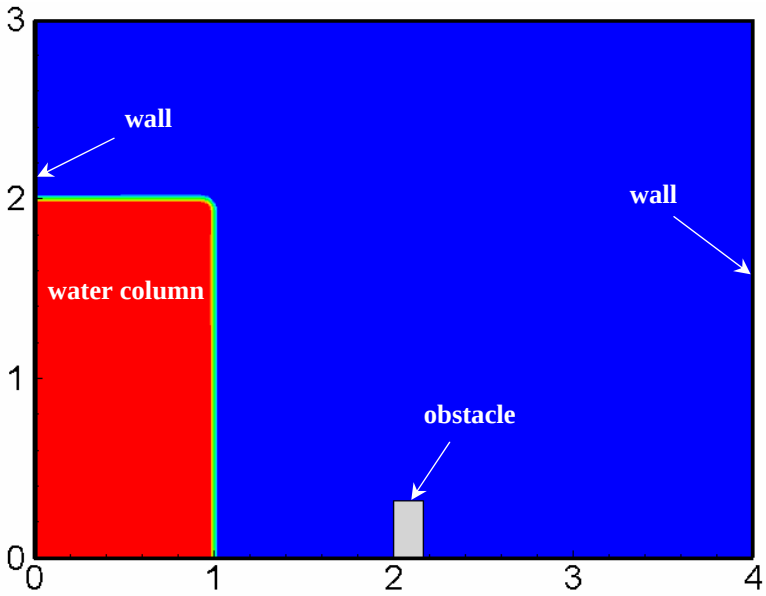

Figure 4.18 Numerical model of dam-breaking with an obstacle

Figure 4.19 shows a comparison between the experimental data and simulation results. At t = 0, the barrier holding the still water column is suddenly removed. The collapsing water column crashes upon the obstacle and produces a free jet with strong upward flow velocity. The jet continues to move to the right and eventually impinges on the vertical wall on the right hand side of the tank. As the water moves towards the right side of the tank, the jet trajectory becomes considerably flatter due to the gradual decrease of the upward jet velocity under its own weight. After impingement against the vertical wall, the jet is split into two streams moving vertically upward and downward along the tank wall. As the water level drops on the left hand side of the tank, the fluid momentum reduces gradually and the jet trajectory is deflated further downward under the gravitational force. In general, the numerical results are in close agreement with the corresponding experimental data of Koshizuka et al. (1995). This test case clearly illustrates the capability of the level set method in capturing violent free surface motions encountered in dam breaking problems. The same method can also be used for the simulation of vigorous sloshing in tanks and slamming of bodies onto a liquid surface.

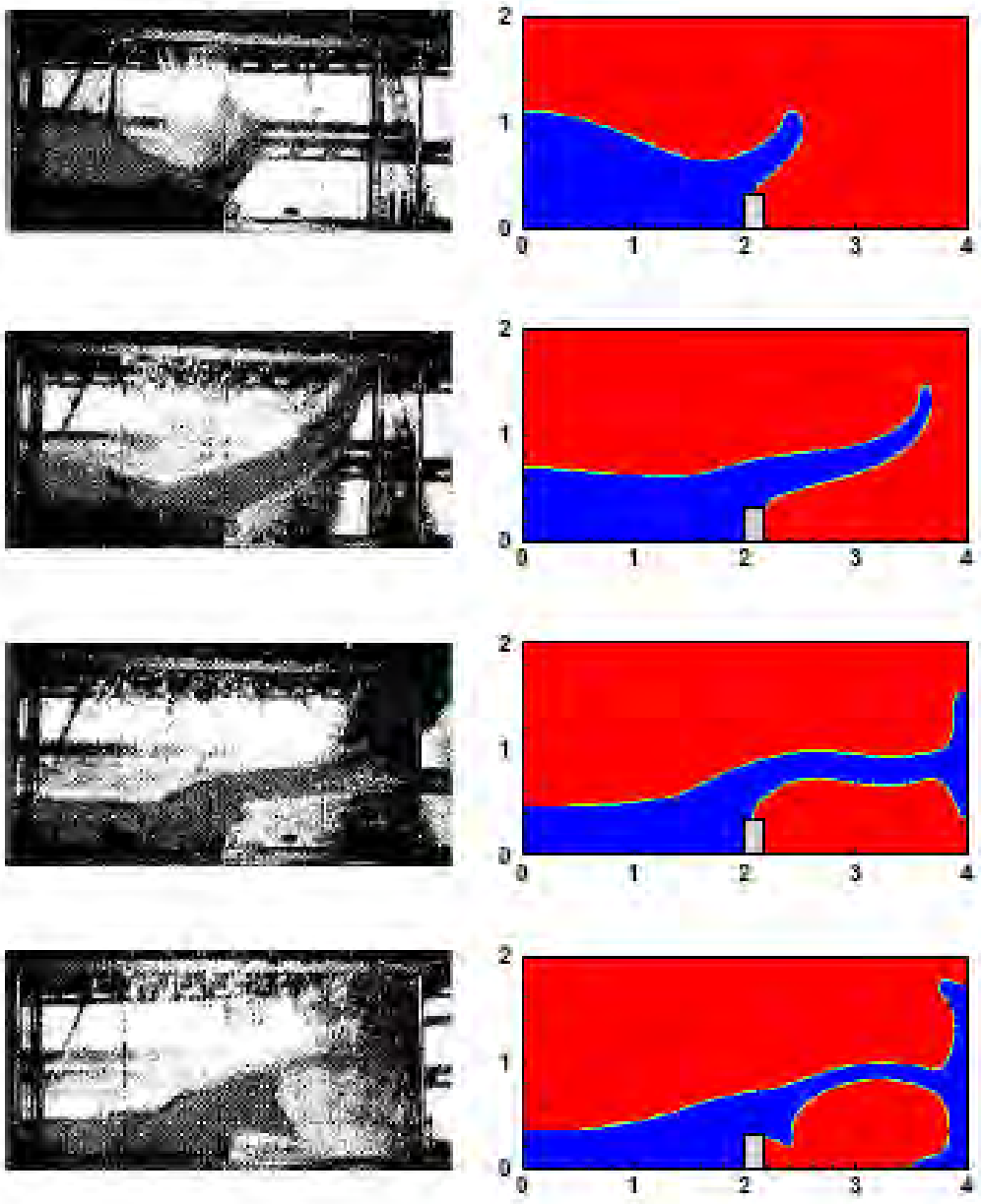

Figure 4.19 Free surface comparison

4.8 Free Jet Simulation

In this test case, we consider a water jet that enters horizontally from the left hand side of the computational domain on top of a platform at a constant velocity of 1.0. The dimension of the platform is 2.0 × 1.0, and the height of the water jet is 0.5 as shown in Figure 4.20. This is similar to a water fall caused by a sudden drop of the streambed elevation in a river.

During the initial stage of the simulation, the water jet experiences a free fall under the action of the gravitational force. As the jet impinges on the tank bottom, it spreads across the tank in both directions and induces strong vortices along the front of the air-water interface. It should be noted that the horizontal velocity of the surge front is faster than the inlet velocity of the jet due to the conversion of potential energy into kinetic energy as the water flows into the tank. After the split water jets reach the tank walls, they continue to climb up vertically against the walls by converting the fluid kinetic energy back into potential energy. It is interesting to note that the water runup on the right tank wall is considerably higher than the water level at the jet inlet during the initial stage of the simulation. This is clearly due to the combined effects of the horizontal and vertical momentum and energy while the jet was deflected upward against the vertical tank wall. As the water level continues to rise inside the tank, however, the water level on the right tank wall begins to drop since a significant part of the energy is dissipated due to strong turbulent eddy motions resulting from water splash in the pool.

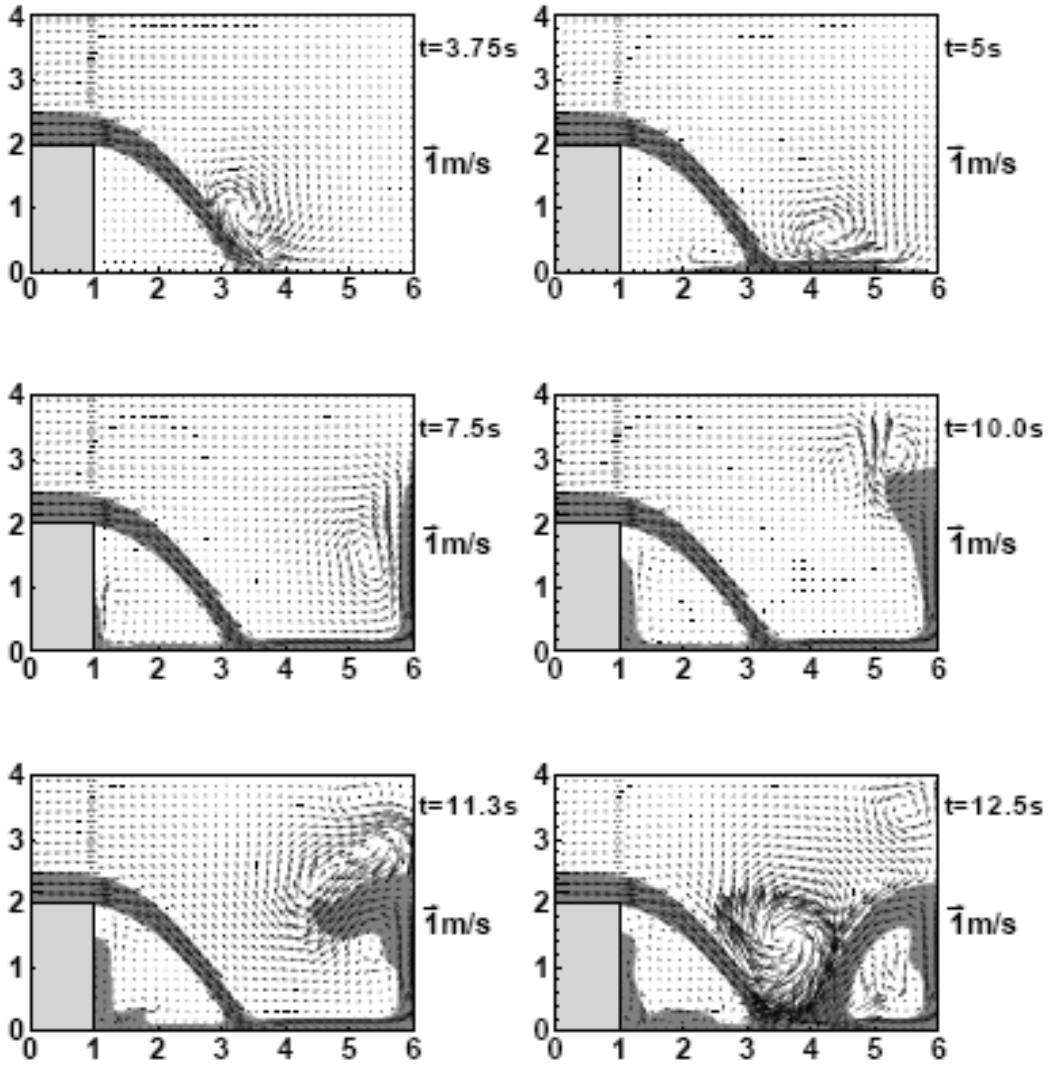

Figure 4.20 Free surface profiles and velocities, 2D free jet

Calculations were also performed for a 3D free jet problem as shown in Figure 4.21. The dimension of the tank is 1.5 × 6.0 × 3.6 while the platform size is 1.5 × 1.0 × 2.0. The height of the water jet is 0.5 and the inlet velocity is 1.0. It is seen that the free jet quickly becomes three-dimensional after impinging on the tank bottom. Compared to the 2D simulations shown earlier in Figure 4.20, the flow is strongly three-dimensional with numerous air bubbles trapped beneath the free surface when the free jet collides with the sliding water in the pool.

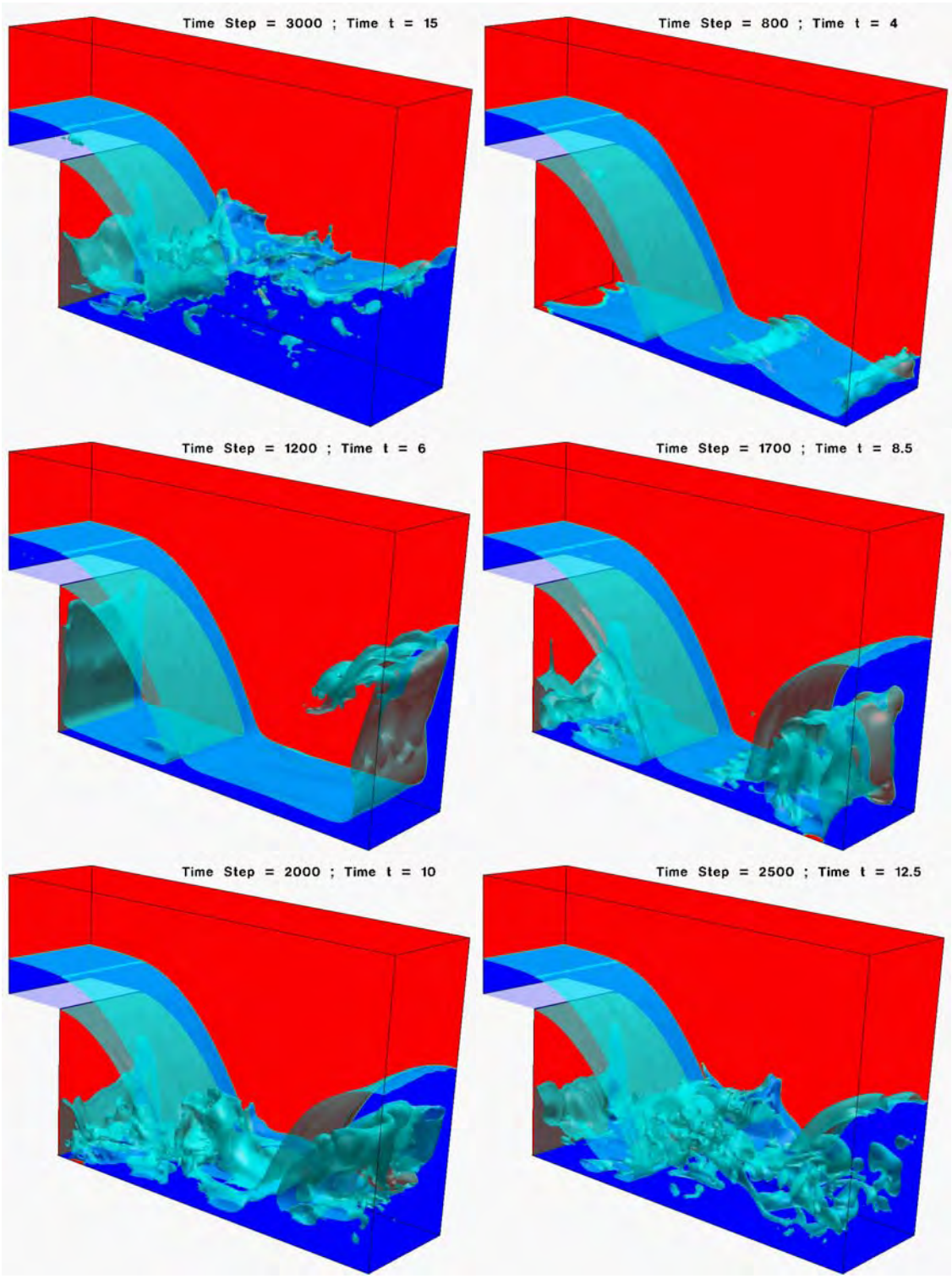

Figure 4.21 Free surface profiles, 3D free jet

5 SLOSHING SIMULATIONS

5.1 Introduction

Due to the growing LNG market, there is a strong demand for new LNG carriers with significantly larger cargo capacity. The safety of the new LNG liquid cargo hold and containment system for the membrane-type LNG carriers has to be evaluated for a wide range of filling levels. Sloshing model tests have been performed by, among others, Faltinsen et al. (2000), Lee et al. (2005b), Hwang (2006), Lee et al. (2006a) and Lee et al. (2006b) to simulate six degrees of freedom ship motions and determine the critical sloshing load. In these experiments, the Froude scaling law is adopted to scale down the geometry, tank motion, and gravitational effects. Impact pressures obtained from the model tests are then scaled up to prototype using Euler scaling with the full-scale pressure proportional to the liquid density and length dimensions. The model test is considered to be the most reliable method in predicting the maximum impact pressure, especially for violent sloshing. However, the true impact load in the full scale LNG tank is still unknown due to the scale effects associated with other unmatched parameters such as fluid viscosity, gas/liquid density ratio, gas compressibility, ullage pressure, and wall elasticity.

Numerical simulations have also been used extensively for the simulation of sloshing flow in LNG tanks. Considering the sloshing flows as free surfaces flows, there are two major approaches, namely interface-tracking and interface-capturing methods, to find the shape of the free surface. Because of the complexity of the free surface phenomena in sloshing, the interface-capturing method is more often used for sloshing flow simulations. The interface-capturing methods can be categorized into three different approaches, Marker-And-Cell (MAC), Volume of Fluid (VOF) and Level Set Method. The smoothed particle hydrodynamics (SPH) method which is developed from MAC was used by Iglesias et al. (2004) and Nam and Kim (2006) for simulating violent sloshing flows in two-dimensional tanks. Kim (2001, 2004) used SOLA-SURF to solve

the sloshing problem in rectangular and prismatic tanks. Lee et al. (2005a) employed the commercial code FLOW3D with the VOF method for a parametric sensitivity study on LNG tank sloshing load. Loots et al. (2004) presented an improved VOF (iVOF) method to account for mass conservation in cut cells and eliminate numerical spikes in pressure signals from the sloshing tank simulation. Wemmenhove et al. (2005) extended iVOF to incorporate a two-phase flow model for more accurate simulation of LNG tank sloshing. Rhee (2004) used the FLUENT commercial code for the simulation of a generic membrane type LNG carrier tank with a simplified pump tower. In addition to viscous flow methods, a potential flow finite element method has also been employed by Kim et al. (2002, 2003) for the simulation of sloshing impact pressure in a LNG tank.

In the present study, the level set method has been incorporated into the chimera RANS method of Chen and Chen (1998) for the prediction of sloshing impact load on membrane-type LNG tanks. The governing equations are formulated in curvilinear coordinate system and discretized using the finite-analytic method of Chen et al. (1990) on a non-staggered grid. For the additional level set equations of evolution and re-initialization, we use the 3rd-order TVD (total variation diminishing) Runge-Kutta scheme (Yue et al., 2003) for time derivatives, and the 3rd-order ENO (essentially non-oscillatory) scheme for spatial derivatives. The present interface-capturing method was validated earlier in Chen and Yu (2006) for several benchmark cases including a stationary circle, Zalesak's problem, and the stretching of a circular fluid element under prescribed free motion. The level set method was then incorporated into the chimera RANS method of Chen and Chen (1998) for complex free surface flow simulations. Calculations were performed for both a two-dimensional and a three-dimensional membrane-type LNG tank under prescribed transverse and longitudinal sloshing motions. The simulation results clearly demonstrate the capability of the level-set FANS method for accurate prediction of violent free surface flows and the associated impact load induced by the sloshing motion of LNG tanks.

5.2 Geometry and Motions

Figure 5.1 shows the geometry of the LNG tank used in the present simulations. The dimension of the tank in full scale is 37.9m × 43.72m × 26.75m, (tank breadth) × (tank length) × (tank height). The lower and upper chamfer angles (γ_l, γ_u) are both equal to135°. The lower chamfer height h_l is 3.77m, while the upper chamfer height h_u is 8.63m. For all the computations, the filling level is specified in terms of *d/h* (%H).

Model tests were conducted by Lee et al. (2006b) on a 1/70 scale model with dimensions of 541.36mm × 624.50mm × 382.20mm. The model was instrumented with 17 pressure gages to measure the impact pressure on the LNG tank walls. Figure 5.2 shows the positions of all 17 sensors in the model test. The dimensions in this figure are in model scale mm. The pressure gages were sampled at a frequency of about 20,000 Hz.

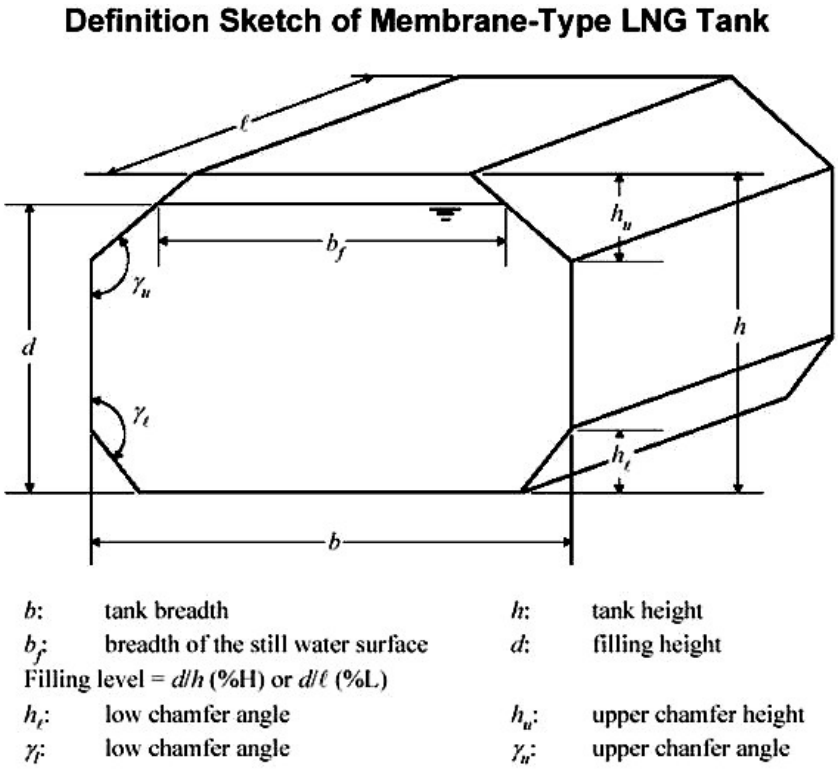

Figure 5.1 Membrane-type LNG tank geometry.

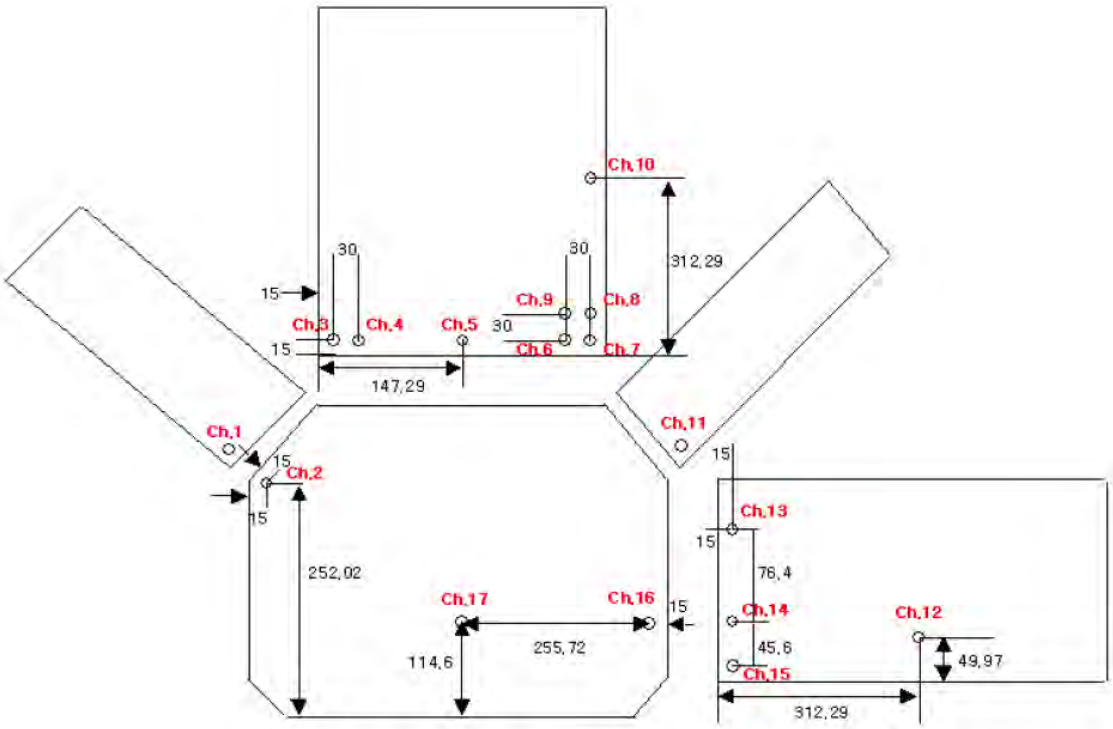

Figure 5.2 Sensor positions on LNG model tank

In the present study, we consider both the transverse and longitudinal sloshing modes with various combinations of horizontal, vertical and rotational motions. The transverse motion is in the *xz*-plane while the longitudinal motion is in the *yz*-plane as shown in Figure 5.3. The horizontal direction is along the *x*-axis for transverse motion, and along the *y*-axis for longitudinal motion. Tables 5.1 and 5.2 show the full scale motion parameters for the three transverse (Cases 1-3) and three longitudinal (Cases 4-6) motion cases considered in the present study. The horizontal, vertical, and rotational motions are defined as follows:

$$\text{motion(t)} = \text{amplitude} \times \sin\left(\frac{2\pi}{\text{period}} + \text{phase}\right) \tag{5.1}$$

Note that the positive values in Table 5.2 represent motions from left to right, bottom to top, and counterclockwise rotation.

A 1/70 scale model tank was used in the experiments. The tank motion parameters were scaled down based on the Froude scaling law, while the measured impact pressures were scaled up based on the Euler scaling law. The characteristic time and pressure are given by

$$\begin{aligned} \text{time} &= \sqrt{\text{length} / \text{gravity}} \\ \text{pressure} &= \text{density} \times \text{gravity} \times \text{length} \end{aligned} \tag{5.2}$$

Therefore, the horizontal and vertical motion amplitudes in model scale are 1/70 of the corresponding full scale values, while the motion period is scaled down by $\sqrt{1/70}$. The measured impact pressures reported in the experimental study were scaled up by 70 times.

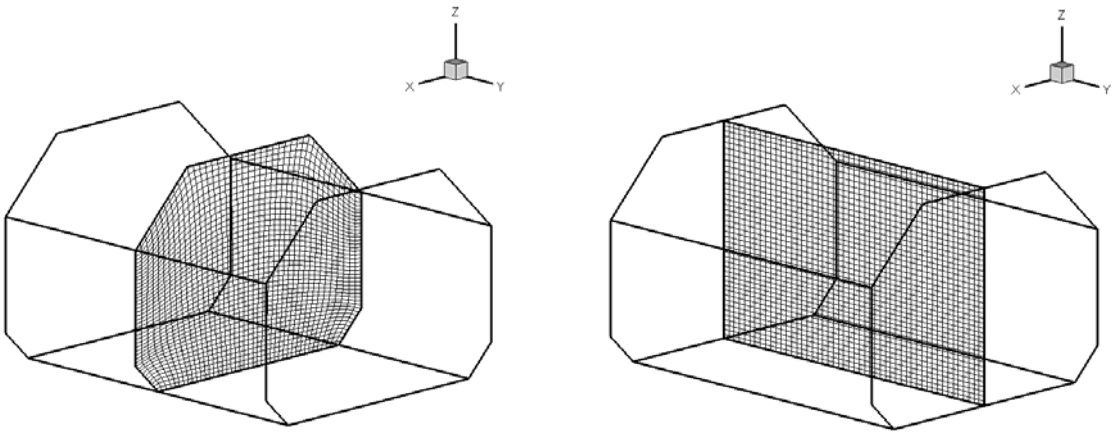

Figure 5.3 2D grids for transverse and longitudinal motions

Table 5.1 LNG tank motion periods

Case	FLVL(%H)	Direction	Period(s)
1	16.3	Transverse	10.5
2	30	Transverse	9.67
3	50	Transverse	8.98
4	50	Longitudinal	8.37
5	80	Longitudinal	7.17
6	92.5	Longitudinal	9.08

Table 5.2 LNG tank motion amplitudes

Case No.	Horizontal Motion		Vertical Motion		Rotational Motion	
	Amplitude (m)	Phase (rad)	Amplitude (m)	Phase (rad)	Amplitude (rad)	Phase (rad)
1	4.75	3.13	9.13	-2.09	0.0190	0.00
2	4.05	-2.96	7.78	-2.18	0.00600	0.00
3	3.38	-0.214	5.89	0.307	0.00248	0.00
4	0.366	-1.89	4.51	-0.412	0.0837	0.00
5	0.584	-4.47	1.72	-1.89	0.0121	0.00
6	0.181	-1.26	6.80	-0.495	0.0952	0.00

5.3 Time Step Size and Grid Refinement

Numerical simulations were performed using the level-set RANS code for all six cases listed in Table 5.1 and Table 5.2. Both the air and water flows were assumed to be incompressible, and the surface tension was ignored in the present simulations. The reference pressure was specified as the atmospheric pressure at the air-water interface along the vertical axis passing through the geometric center of the LNG tank. In the

following, we will present both 2D and 3D simulation results to illustrate the general performance of the present numerical method.

In order to determine the influence of time step size and grid spacing on the predicted impact pressure, two-dimensional numerical simulations were performed for Case 3 (transverse motion at 50% filling level) using three different time increments and two different grid sizes. Figure 5.4 shows the two-dimensional simulation results with a $85\times3\times85$ grid and three different time increments τ = 0.01T, 0.002T, and 0.001T, where T is the motion period. Figure 5.4 indicates that the predicted pressure histories at the location of sensor 11 (Ch. 11) are nearly identical for all three time increments, but the predicted peak impact pressures are somewhat sharper for the τ =0.001 case. To ensure accurate resolution of the short duration impact pressure forces, all 2D and 3D simulations were performed using 1,000 time steps per period (i.e., τ =0.001).

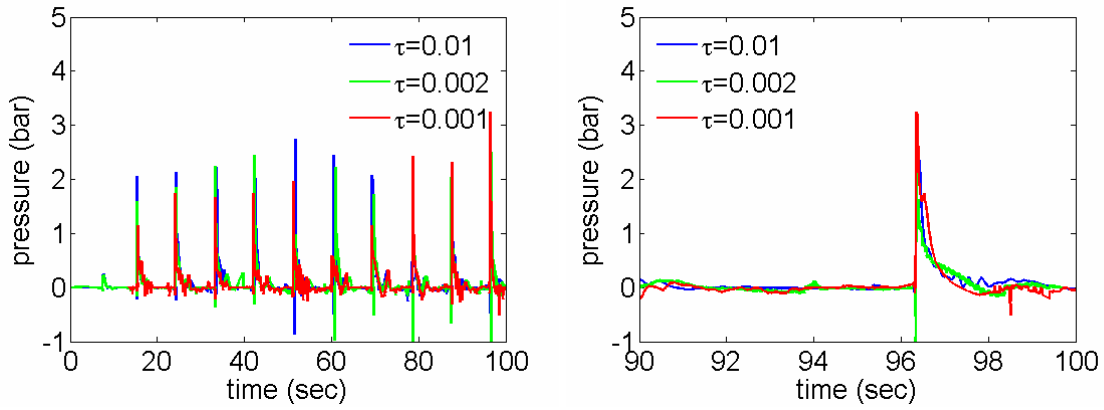

Figure 5.4 Influence of time increment, Ch.11 in Case 3

A grid refinement study was also performed by doubling the grid points in the transverse cross sections from $85\times3\times85$ to $169\times3\times169$. For the coarse grid case, the cell sizes in *x*-, *y*-, and *z*-directions are approximately (0.45 m, 0.43 m, 0.32 m) in full-scale units, and (6.4 mm, 6.2 mm, 4.5 mm) in the model-scale tank units. The grid sizes are reduced to 1/2 in all three directions for the fine grid case. Figure 5.5 shows a

comparison of the coarse $(85\times3\times85)$ and fine $(169\times3\times169)$ grid results over 10 periods. It is quite clear that the coarse and fine grid simulations predict about the same level of impact pressures, although the peak pressures obtained by fine grid simulations are somewhat higher at certain instants. For optimal usage of the available computer resource, all 2D and 3D simulations presented in this report were performed using $85\times3\times85$ and $85\times101\times85$ grid points, respectively.

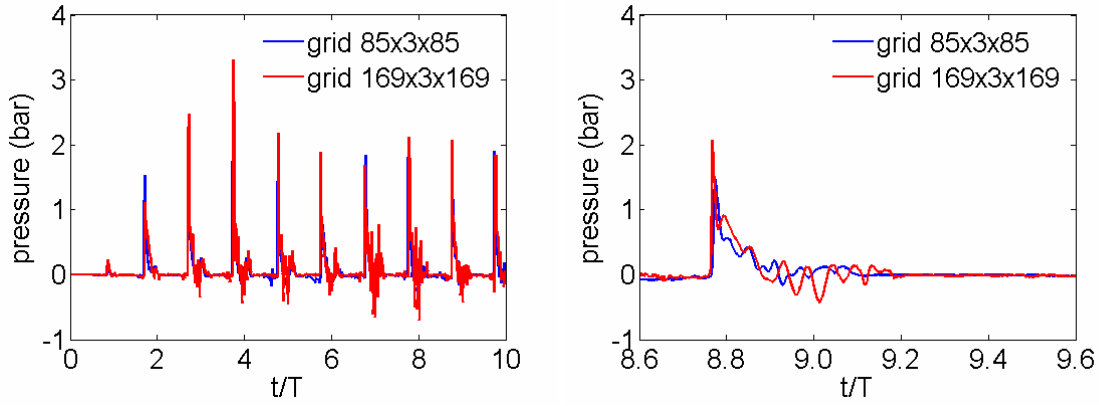

Figure 5.5 Grid refinement study, Case 3, Ch.11

5.4 Scale Effects

As noted earlier, the impact pressures reported in Lee et al. (2006b) were measured in a 1/70 scale model tank based on the Froude scaling law, and scaled up to full scale using the Euler scaling law. According to the Froude scaling law, the Reynolds number in the model test is $(1/70)^{1.5} = 0.01707$ times that of the prototype. In order to ascertain the scale effects, simulations were performed at both the full-scale and model-scale Reynolds numbers for Case 3 using the same $85\times3\times85$ numerical grid and the same dimensionless time increment τ =0.001. To facilitate a direct comparison of the simulation results, the impact pressures obtained for the model-scale tank were scaled up by 70 times based on the Euler scaling law. It is seen from Figure 5.6 that the peak impact pressures observed in the model-scale tank are comparable to those obtained at

the full-scale flow condition. For convenience, all simulations reported in the following sections were performed for the prototype LNG tank using the full-scale motion amplitudes and motion periods.

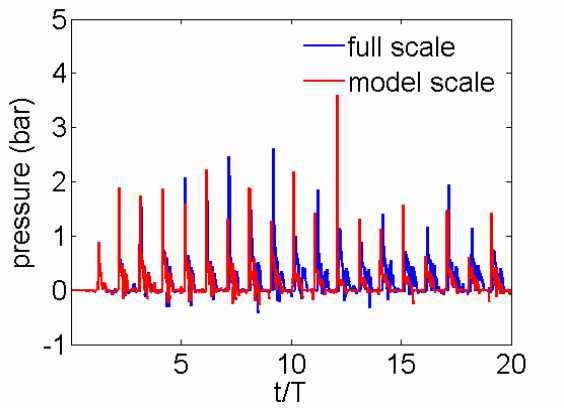

Figure 5.6 Scale effects, Ch.11, Case 3

5.5 Results and Discussions

Both 2D and 3D full-scale simulations were performed for all six cases listed in Tables 5.1 and 5.2 using a constant time increment of 0.001T (1,000 time steps per period) to provide accurate resolution of the peak impact pressures. For two-dimensional simulations, a one-block grid with $85\times3\times85$ nodes was used for the transverse motion cases (Cases 1-3), while a $3\times101\times85$ rectangular grid was used for longitudinal motion cases (Cases 4-6). All 2D simulations were performed for 20 periods and the wall pressures at selected sensor locations shown in Figure 5.7 were recorded every time step to facilitate a direct comparison with the experimental data of Lee et al. (2006b). The total CPU time for 20 periods (20,000 time steps) is about 3 hours on a single-processor Dell Optiplex GX620 computer with 3.2 GHz CPU and 3.5 GB of RAM.

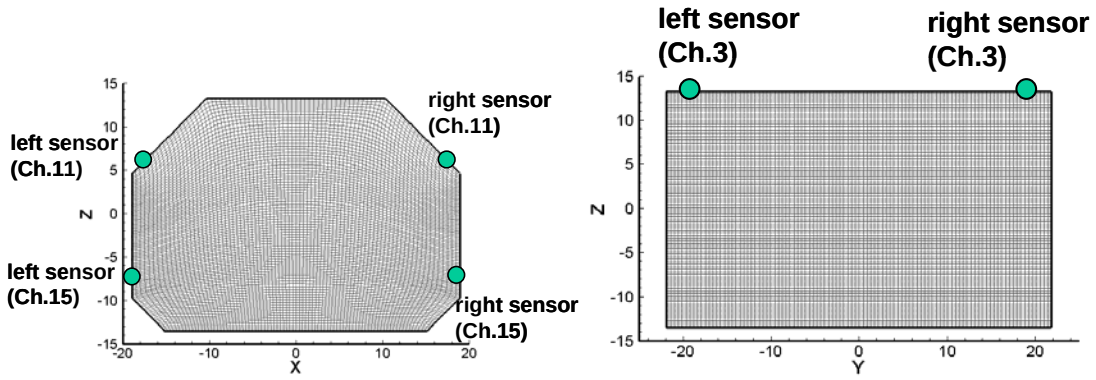

Figure 5.7 Grid and sensor locations for 2D simulations

All three-dimensional simulations were performed using a one-block grid with $85\times101\times85$ nodes. The grid size for 3D simulations was adjusted near the top wall for high filling ratio longitudinal motion cases to ensure appropriate resolution of the high velocity and pressure gradient regions. A Large Eddy Simulation (LES) approach was employed in conjunction with Smagorinsky subgrid scale model to provide appropriate resolution of the flow turbulence induced by violent free surface motions. The three-dimensional simulations were performed initially for 20 periods and the wall pressures at selected sensor locations were recorded every time step. The 3D velocity and pressure fields for the entire tank were also saved every 50 time steps to provide more detailed descriptions of the complex three-dimensional flow induced by the sloshing tank. The total CPU time for 20 periods (20,000 time steps) is about 120 hours for 3D simulations on a single-processor Dell Optiplex GX620 computer with 3.2 GHz CPU and 3.5 GB of RAM.

A detailed examination of the 3D simulation results indicated that the sloshing flow is highly three-dimensional even though the prescribed transverse or longitudinal motions are strictly two-dimensional. Due to the three-dimensional instability, the impact pressures at the mirror image locations on opposite walls were found to be drastically different under certain flow conditions. Since the wall pressures were recorded only at a small number of sensor locations for the first 20 periods of the present

3D simulations, it was not possible to quantify the three-dimensional effects. In order to provide a more detailed understanding of the violent three-dimensional free surface flows, all 3D simulations were continued for three additional periods to obtain the impact pressure histories at 48 different locations as shown in Figure 5.8. These 48 sensor locations include not only the original 17 pressure sensors in the model tank, but also their mirror images in both *x* and *y* directions. This enables us to capture the most critical impact pressures which may occur on the opposite walls of any given pressure sensor locations in the model tank.

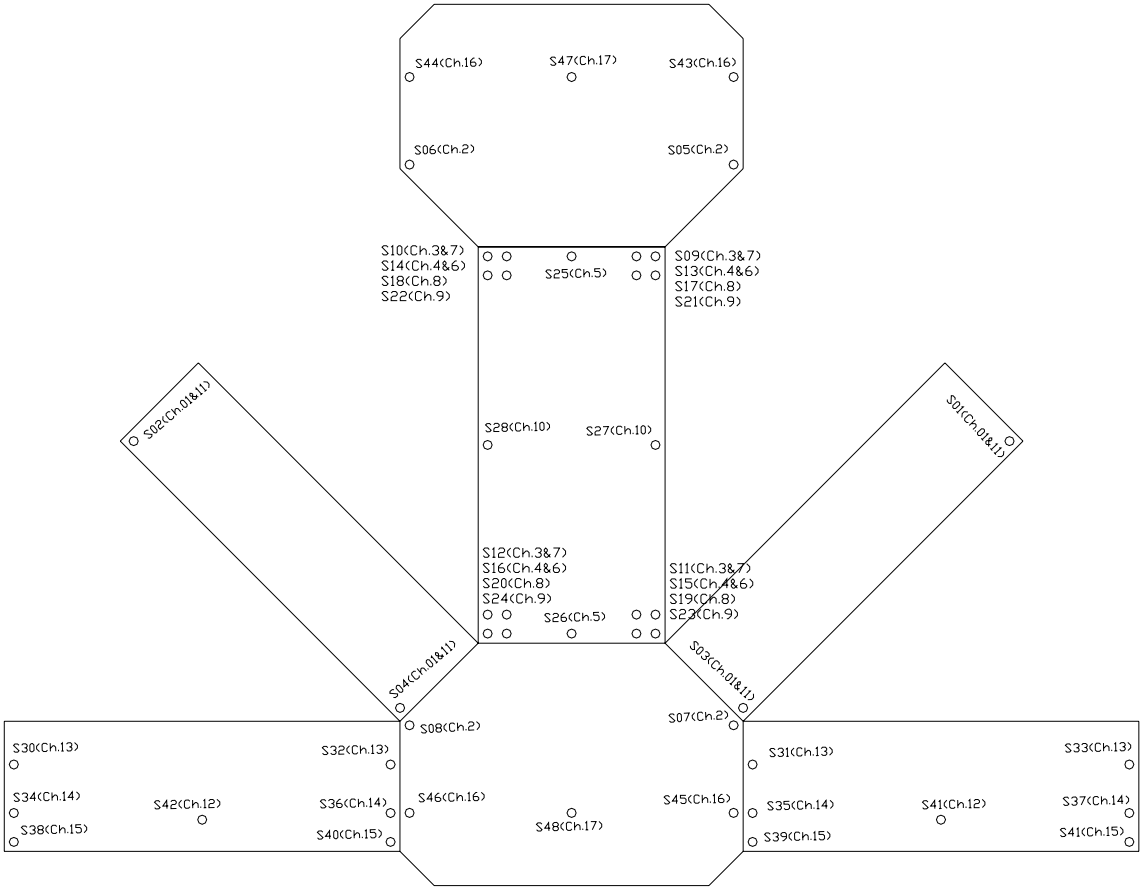

Figure 5.8 Grid and sensor locations for 3D simulations

It should be remarked also that the impact pressure on tank walls is highly localized with significant variations between two adjacent grid points. Therefore, the highest impact pressure may not occur precisely at the sensor locations unless long-duration simulations are performed for several thousand periods to capture the true peak pressure. In view of this, we have recorded the impact pressures on a 3×3 grid around each sensor location as shown in Figure 5.9, where (ξ,η,ζ) represent the grid indices of the curvilinear coordinate system and the center node (i.e., Point 5) is closest to the actual pressure sensor location in the model tank. This enables us to determine the local maximum impact pressure in the vicinity of each pressure sensor. For the sake of brevity, the predicted pressure history at Point 5 will be used for comparison with the corresponding pressure measurements in the following sections.

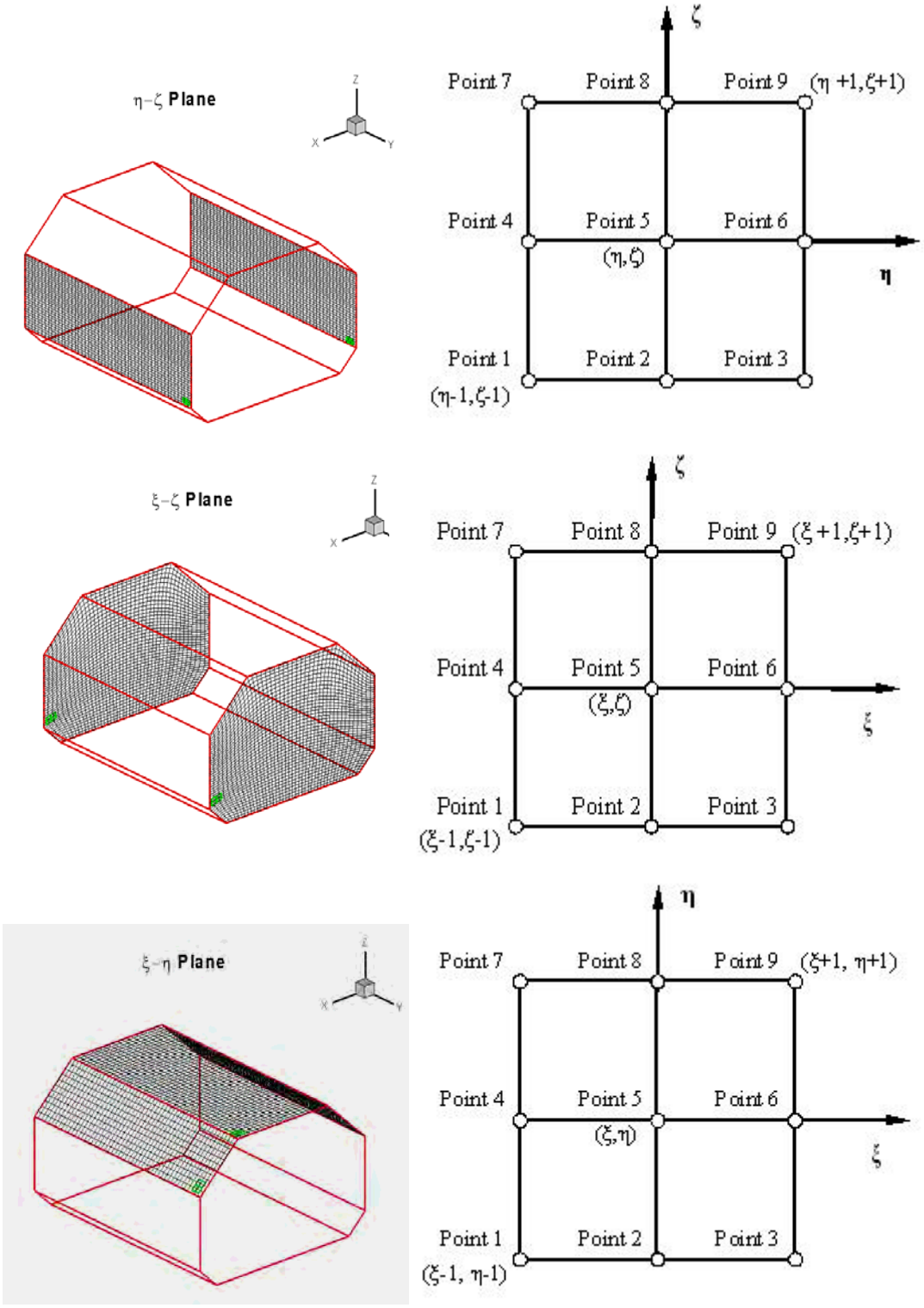

Figure 5.9 Nine-point stencils adjacent to pressure sensor

5.5.1 Case 1 – Transverse motion with 16.3% Filling Level

Figure 5.10 shows the transverse motion trajectory of the LNG tank for Case 1 with the initial tank position at the origin (0,0). The trajectory of the prescribed tank motion is elliptic and asymmetrical with respect to the *x* and *z* axes because of different phase shifts and motion amplitudes in the horizontal and vertical directions. The tank experiences a small amplitude roll motion with a maximum roll angle of ±1.09°.

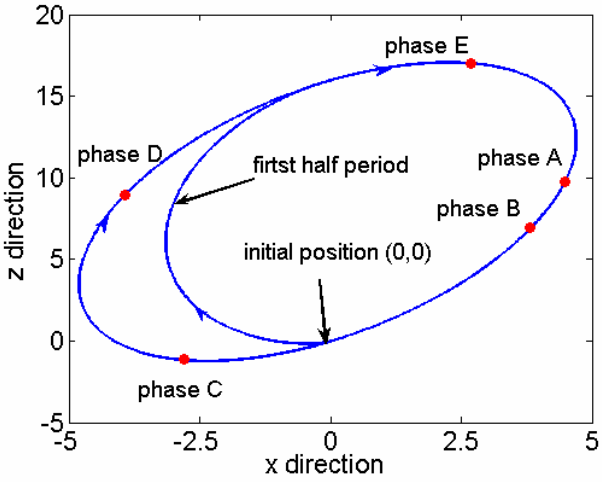

Figure 5.10 Tank motion trajectory, Case 1

Figure 5.11 shows the 2D simulation results of impact pressures for both the left and right pressure sensors corresponding to Ch.15 as shown in Figure 5.7. It is seen that there is a half-period phase difference between the left and right sensor locations. Due to the asymmetric tank motion, the predicted pressure patterns are also quite different for the left and right sensors. It is interesting to note that the pressure at the right sensor location exhibits a distinct double-peak pattern, while a single-peak pattern is observed at the left sensor location.

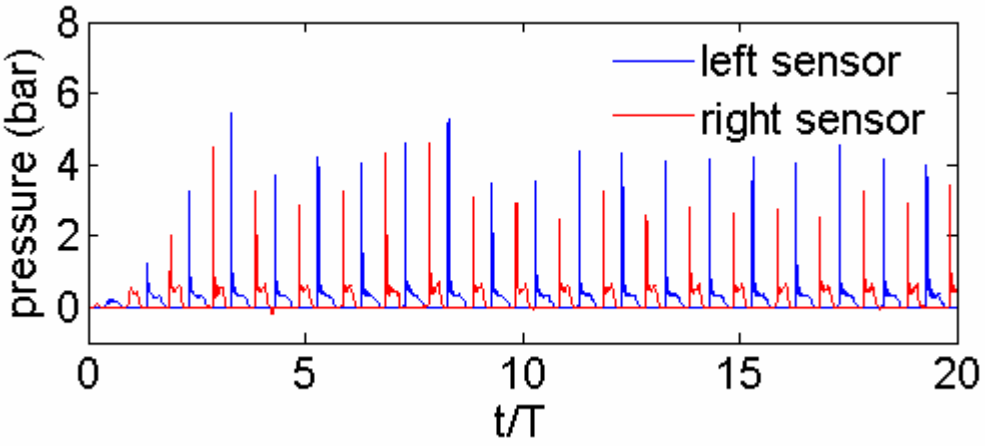

Figure 5.11 2D pressure history, Ch.15, Case 1

Figure 5.12 and Figure 5.13 show the comparisons of measured and predicted pressure histories at Ch.15 over 10 periods for the 2D and 3D simulations, respectively. It is seen that the pressure rises sharply due to water impact on the tank wall and decays rapidly following the impact. However, the pressure does not return immediately to zero but exhibits a distinct double-peak pattern after the impact. In general, both the pressure pattern and peak pressure values are accurately predicted. It is also noted that the 3D simulation gives a somewhat lower peak pressure than the 2D case since the fluid impact is highly localized in the 3D tank and may not occur at the exact sensor location.

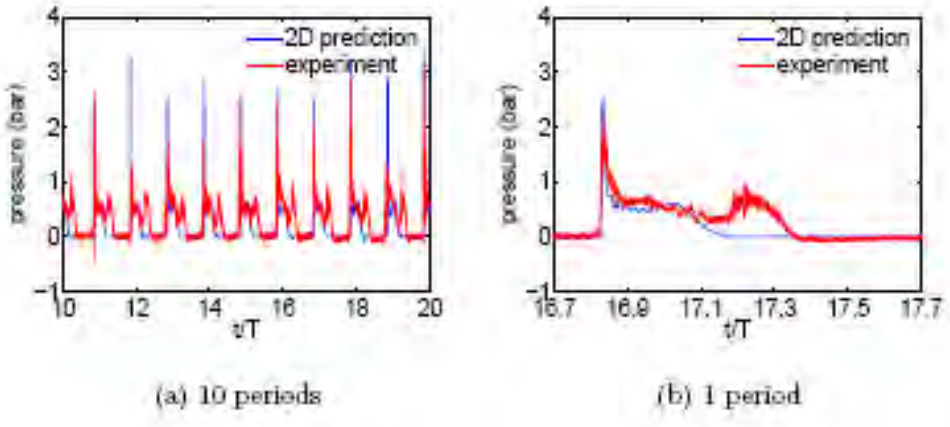

Figure 5.12 2D Impact pressure, Ch. 15 (right sensor), Case 1

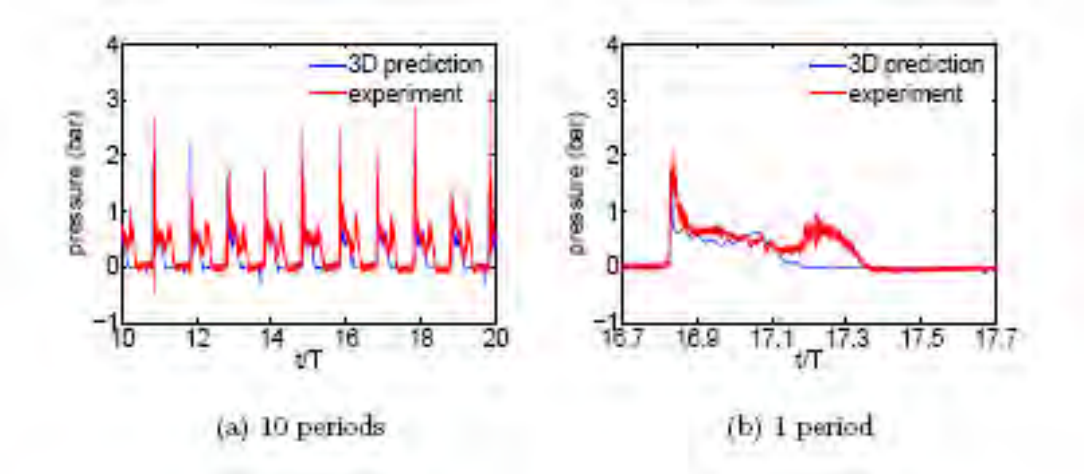

Figure 5.13 3D impact pressure, Ch.15 (S40), Case 1

The three-dimensional variations of the impact pressure in the vicinity of the Ch.15 pressure sensor can be clearly observed in Figure 5.14. A detailed examination of the pressure history over a single period shown in Figure 5.13(b) indicates that the peak impact pressure occurs between t/T = 16.80 and 16.85 over this specific period.

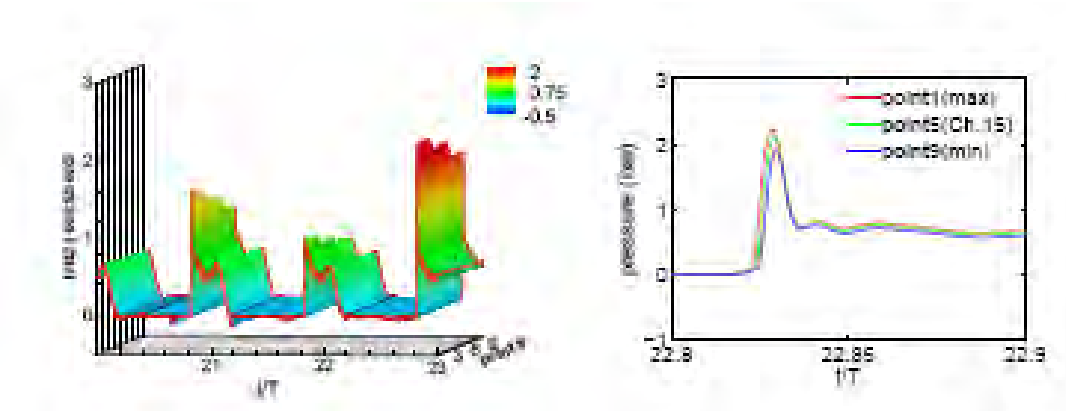

Figure 5.14 Impact pressures, the vicinity of Ch.15 (S40), Case 1

In order to facilitate a more detailed understanding of the observed impact pressure pattern, it is desirable to examine the detailed velocity and pressure fields

induced by the sloshing tank motions immediately before and after the peak impact corresponding to Phase A (t/T=16.80) and Phase B (t/T=16.85) in the motion trajectory shown in Figure 5.10. For completeness, the 2D and 3D flow and pressure fields will also be presented at three other time instants t/T = 17.10, 17.35 and 17.60 which are denoted by Phases C, D, and E in Figure 5.10. Note that Phases B, C, D, and E were chosen to be T/4 apart to illustrate the general flow patterns over one sloshing period.

Figure 5.15 shows the 2D free surface patterns, velocity vectors, and pressure contours at five time instants t/T = 16.80, 16.85, 17.10, 17.35 and 17.60, which are denoted by Phases A-E in the motion trajectory plot shown earlier in Figure 5.10. As noted earlier, the maximum impact pressure at Ch.15 (lower-right sensor) occurs between Phases A and B when the LNG tank is descending from the upper-right corner towards the lower-left corner along the elliptic motion trajectory. It is seen that the sloshing water moves rapidly from left to right between Phases A (t/T=16.80) and B (t/T=16.85) and produces a sudden impact on the right tank wall where Ch.15 is located.

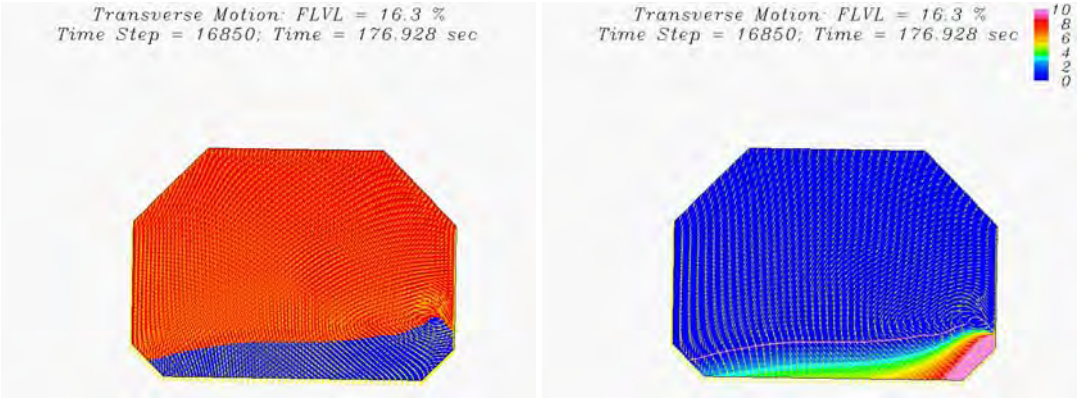

(a) Phase B: t/T = 16.85

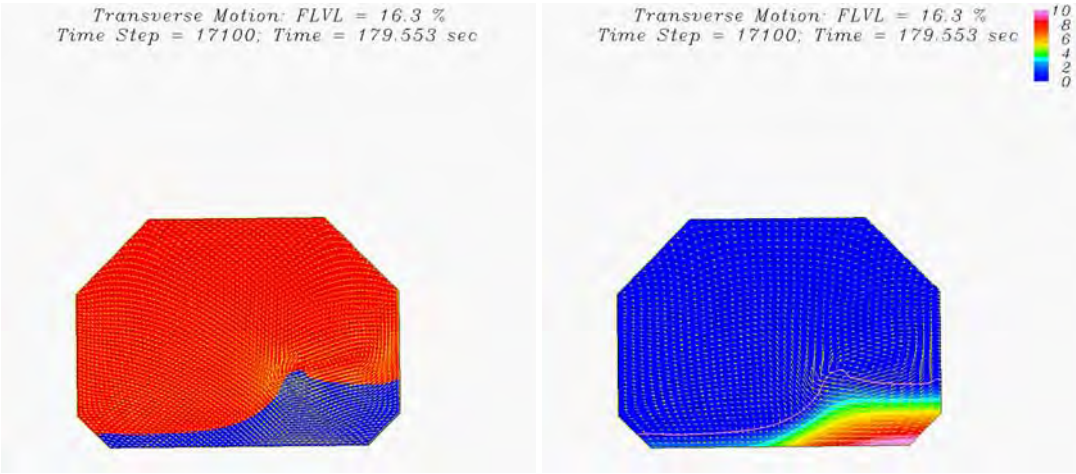

(b) Phase C: t/T = 17.10

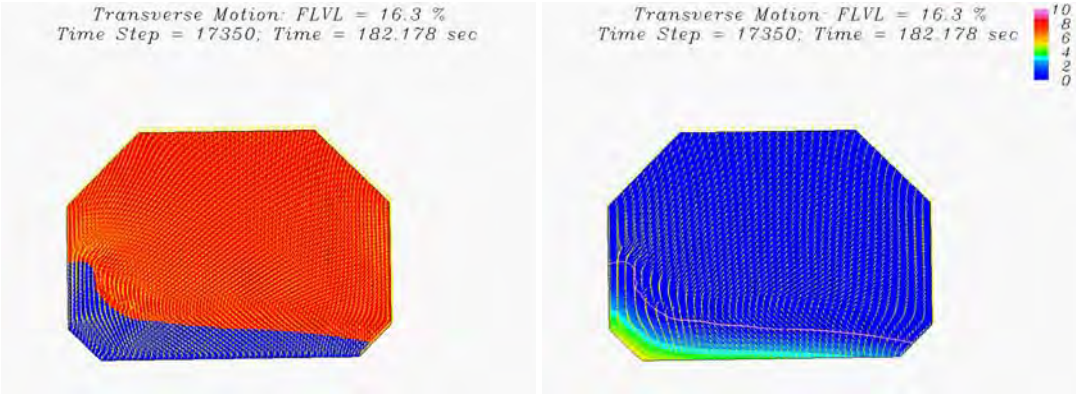

(c) Phase D: t/T = 17.35

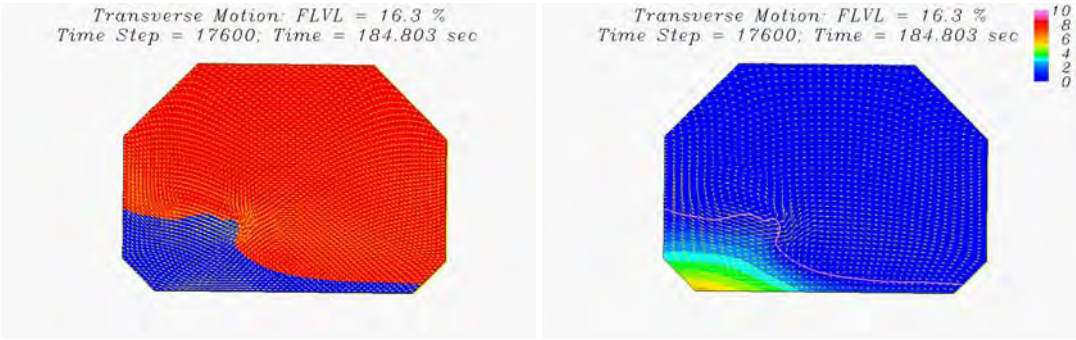

(d) Phase E: t/T = 17.60

Figure 5.15 2D free surface patterns and pressure contours

After the primary impact, the water continues to rush up the tank side wall. This leads to a double-peak pressure pattern since the pressure sensor No.15 is submerged under increasing water depth between Phases B and C when the LNG tank continues to move along the lower half of the elliptic motion trajectory towards the lower-left corner. Between Phases C and D, the tank reaches the lower-left corner and begins to ascend along the upper half of the elliptic motion trajectory towards the upper-right corner. Due to the change of motion direction, the sloshing water is moving towards the left wall. At Phases D and E, the sloshing water piles up on the tank left wall while the right wall is completely exposed in air with zero pressure reading on Ch.15.

In the present two-phase flow approach, both the water and air flows were computed simultaneously as seen from the velocity vector plots in Figure 5.15. This enables us to capture the interaction between the sloshing fluid and the gas in ullage space of the sloshing tank.

Figure 5.16 shows the predicted three dimensional free surface motions and the corresponding pressure contours on tank walls for the same five phases shown in Figure 5.10. The sharp wave fronts induced by sloshing motion can be clearly seen at Phases A, C, and E. At Phase A, the tank right wall is completely exposed with zero pressure reading at Ch.15. Between Phases A and B, the sharp front of the sloshing water impinges directly on the right wall and produces a large impact pressure at Ch.15. It is seen that the impact pressure is strongly three-dimensional at Phase B even though the free surface pattern remains nearly two-dimensional.

Since the impact pressure is highly localized and varies from one sloshing period to another, it is difficult to capture the true maximum impact pressure unless the numerical simulations can be performed for hundreds or thousands of sloshing periods. For short-duration simulations, it is desirable to record the maximum impact pressure over the entire tank wall since the peak pressure may not occur precisely at any specific sensor locations. This will provide a more reasonable prediction of the maximum

impact pressure on the LNG tank walls. It should also be remarked that the three-dimensional sloshing motion tends to reduce the risk of tank damage since the maximum impact force is less likely to occur at the same location when comparing to purely two-dimensional impacts.

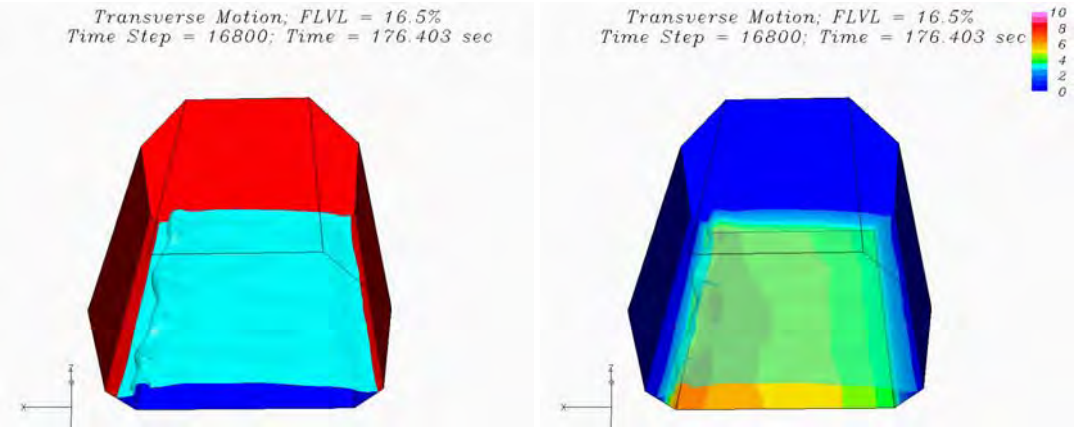

(a) Phase A: t/T = 16.80

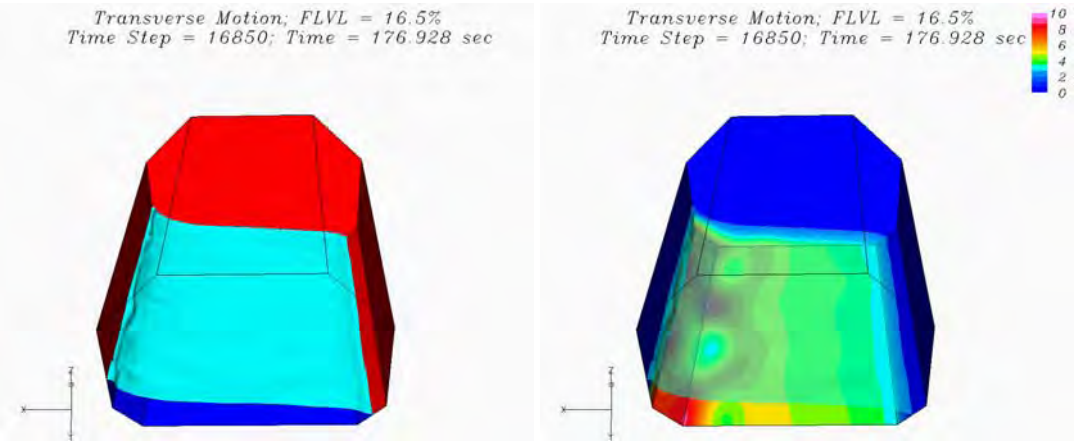

(b) Phase B: t/T = 16.85

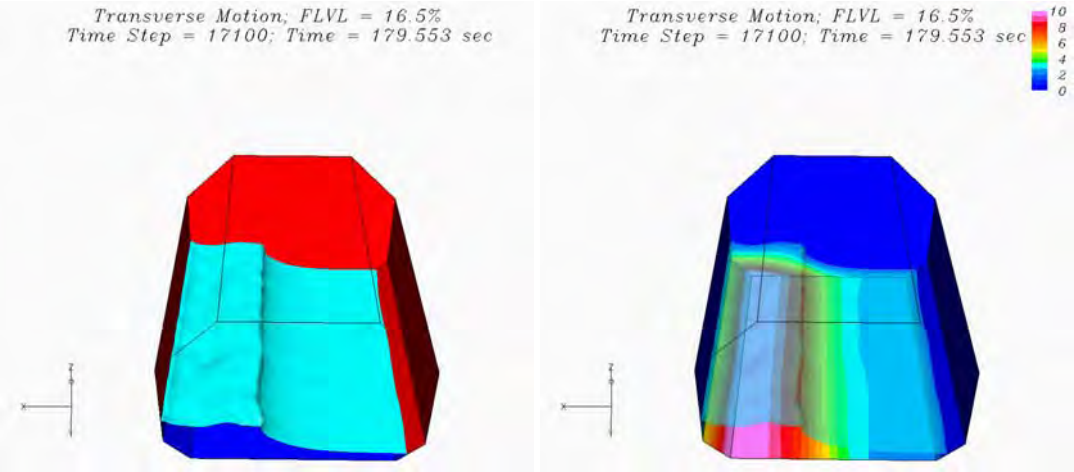

(c) Phase C: t/T = 17.10

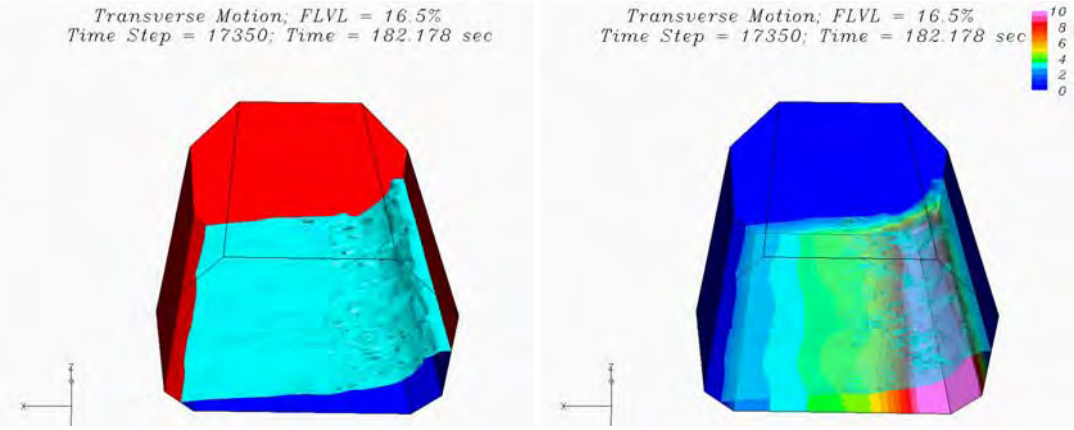

(d) Phase D: t/T = 17.35

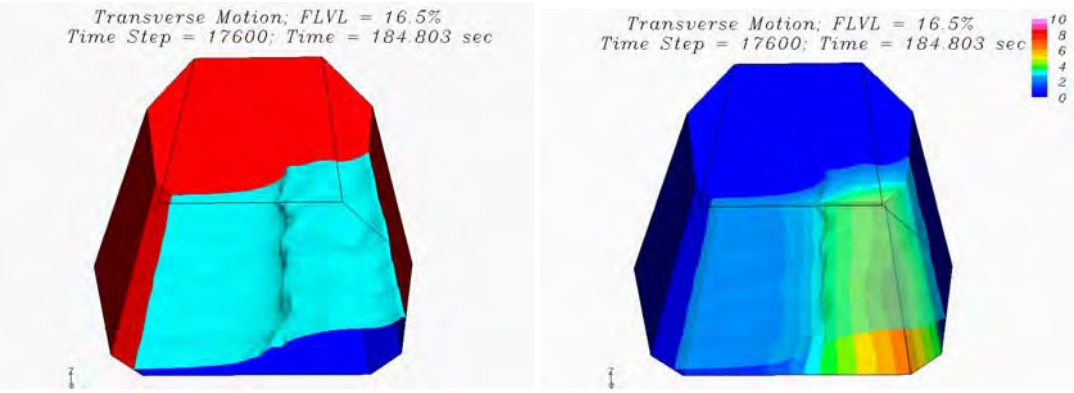

(e) Phase E: t/T = 17.60

Figure 5.16 3D free surface and pressure contours, Case 1

5.5.2 Case 2 – Transverse motion with 30% Filling Level

Figure 5.17 shows the transverse motion trajectory of the LNG tank for Case 2 with the initial tank position at the origin (0,0). Due to different phase shifts and motion amplitudes in the horizontal and vertical directions, the trajectory of the prescribed tank motion is elliptic and asymmetric with respect to the *x* and *z* axes. In addition to the large amplitude translational motions, the tank also experiences a small amplitude roll motion with a maximum roll angle of ±0.344°.

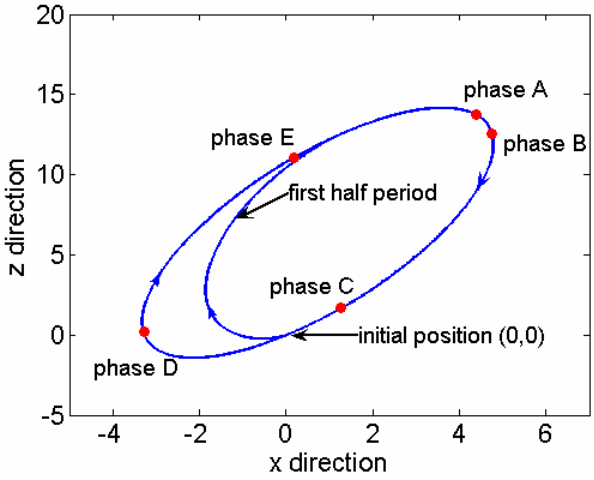

Figure 5.17 Tank motion trajectory, Case 2

Figure 5.18 shows the 2D simulation results of impact pressures for both the left and right pressure sensors corresponding to Ch.15. The predicted pressure histories are similar to those shown earlier for Case 1. Due to the asymmetric tank motion, the pressure at the right sensor location exhibits a distinct double-peak pattern, while a single-peak pattern is observed at the left sensor location.

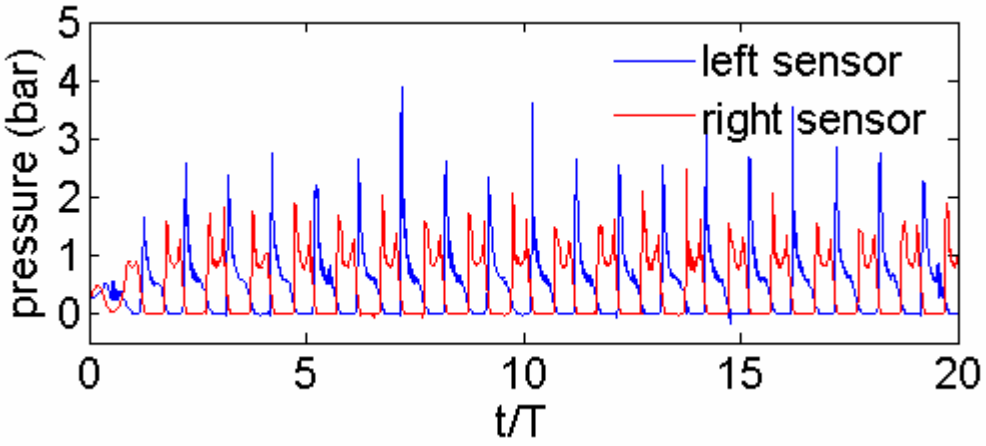

Figure 5.18 2D pressure history, Ch.15, Case 2

Figure 5.19 and Figure 5.20 show the comparisons of measured and predicted pressure histories at Ch.15 over 10 periods for the 2D and 3D simulations, respectively. It is seen that the pressure rises sharply due to water impact on the tank wall and decays rapidly following the impact. Similar to Case 1, the impact pressure at Ch.15 also exhibits a distinct double-peak pattern after the impact. In general, both the pressure pattern and peak pressure values are accurately predicted in 3D simulations. It should be noted that the pressure history shown in Figure 5.20 was recorded at sensor position S38 which is located at the mirror image position of S40. Due to the three-dimensional effects, the impact pressure at sensor location S38 is significantly higher than that at S40, and in closer agreement with the measured pressure at Ch.15.

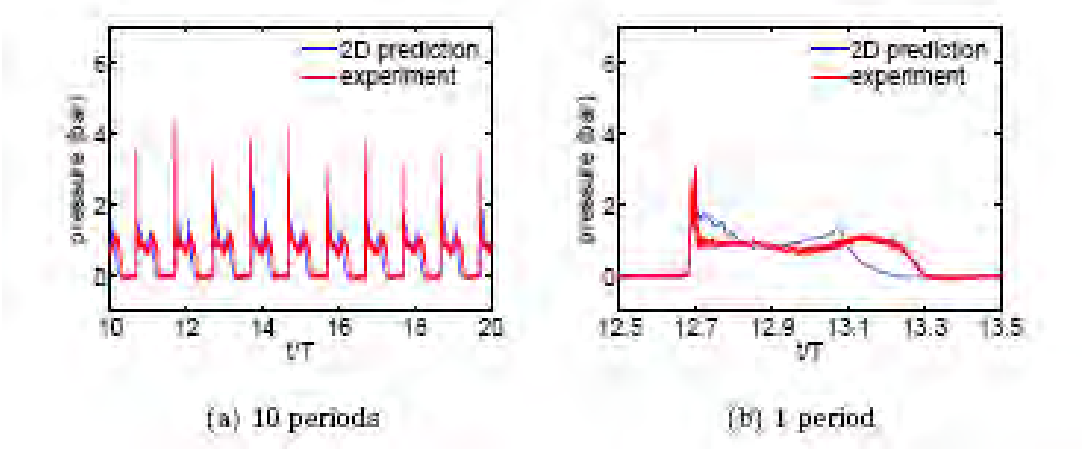

Figure 5.19 2D Impact pressure, Ch. 15 (right sensor), Case 2

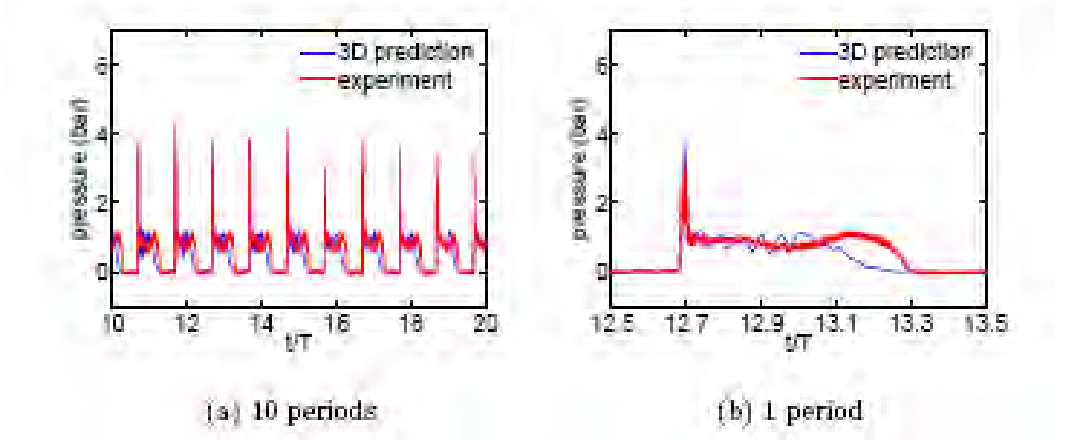

Figure 5.20 3D impact pressure, Ch.15 (S38), Case 2

Figure 5.21 shows the three-dimensional variations of the impact pressure in the vicinity of the Ch.15 (S38) pressure sensor location. It is seen that the impact pressure is fairly uniform at this location, so the pressure at Point 5 is a good representation of the pressure at Ch.15. A detailed examination of the 3D pressure history over a single sloshing period shown in Figure 5.20(b) indicates that the peak impact pressure occurs at t/T=12.695 over this specific period. On the other hand, the 2D impact occurs shortly after t/T=12.70.

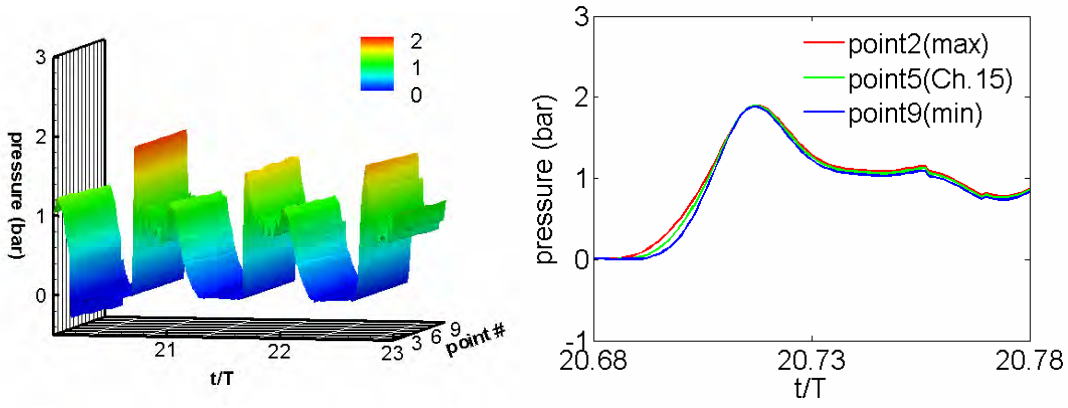

Figure 5.21 Impact pressures, the vicinity of Ch. 15 (S38), Case 2

In order to facilitate a more detailed understanding of the observed impact pressure pattern, it is desirable to examine the detailed velocity and pressure fields induced by the sloshing tank motions immediately before and after the peak impact corresponding to Phase A (t/T=12.65) and Phase B (t/T=12.70) in the motion trajectory shown in Figure 5.17. For completeness, the 2D and 3D flow and pressure fields will also be presented at three other times instants t/T=12.95,13.20 and 13.45 which are denoted by Phases C, D, and E in Figure 5.17. Note that Phases B, C, D, and E were chosen to be T/4 apart to illustrate the general flow patterns over one sloshing period.

Figure 5.22 shows the 2D free surface patterns, velocity vectors, and pressure contours at five time instants t/T = 12.65, 12.70, 12.95, 13.20 and 13.45, which are denoted by Phases A-E in the motion trajectory plot shown earlier in Figure 5.17. As noted earlier, the maximum 3D impact pressure at sensor location S37 occurs at t/T=12.695 just prior to Phase B (t/T=12.70) for the 3D case when the LNG tank reaches the upper-right corner and begins to descend towards the lower-left corner along the elliptic motion trajectory. In the present two-dimensional simulations, however, the sloshing water has not yet reached the tank right wall at Phase B. As noted earlier, the 2D impact on the left wall occurs shortly after t/T=12.70. In view of this, we will focus on the three-dimensional flow patterns in the following discussions.

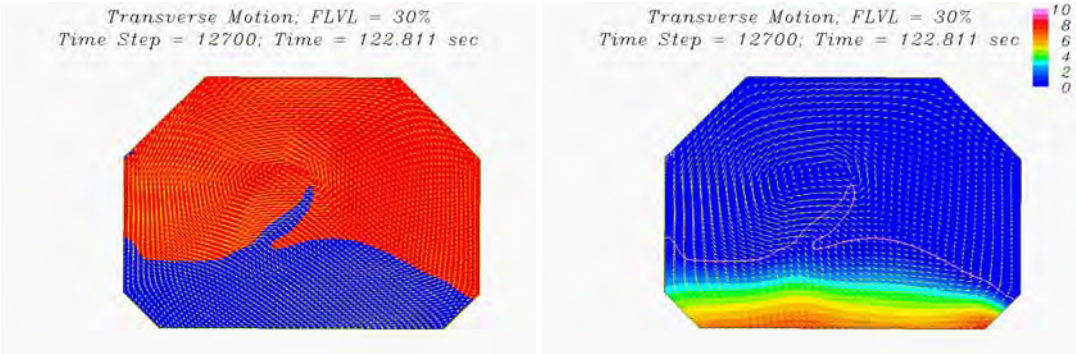

(a) Phase B: t/T = 12.70

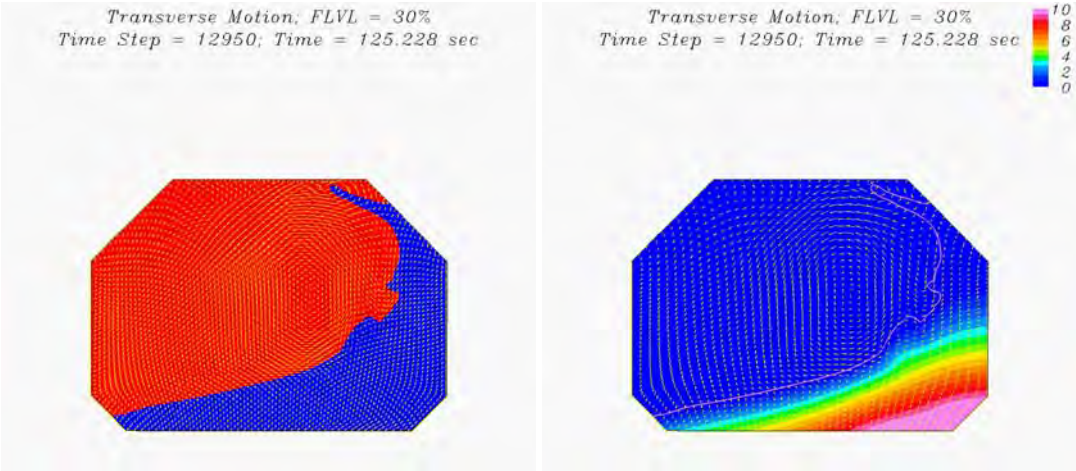

(b) Phase C: t/T = 12.95

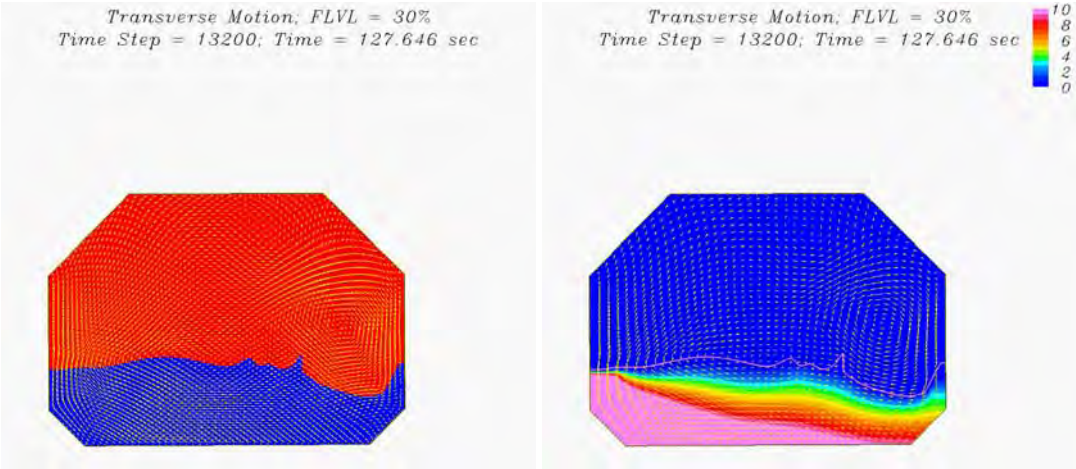

(c) Phase D: t/T = 13.20

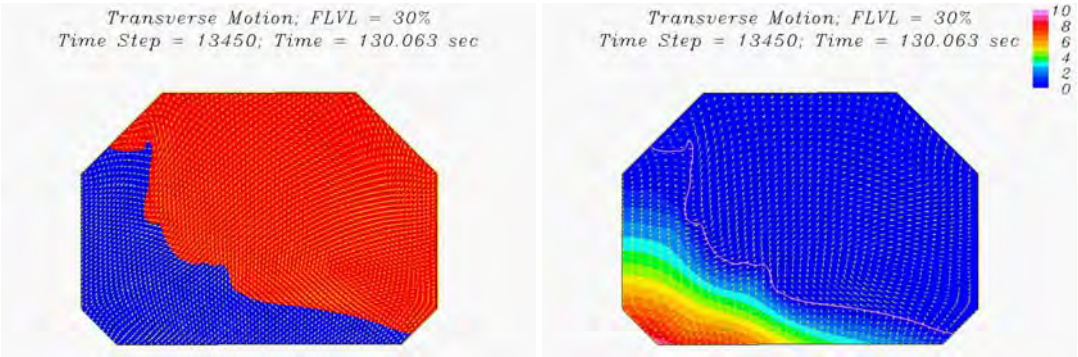

(d) Phase E: t/T = 13.45

Figure 5.22 2D free surface patterns and pressure contours, Case 2

Figure 5.23 shows the predicted 3D free surface motions and the corresponding pressure contours on tank walls at five different time instants for Case 2. As noted earlier, the maximum impact pressure at pressure sensor location S38 (mirror image of Ch.15 in model tank) occurs at t/T=12.695 when the LNG tank reaches the upper-right corner of the motion trajectory and begins to descend towards the lower-left corner. It is seen that the sloshing water moves rapidly from left to right between Phases A (t/T=12.65) and B (t/T=12.70) and produces a very high impact pressure on the right tank wall where the S38 pressure sensor is located.

After the primary impact, the water continues to rush up the tank side wall. This leads to a double-peak pressure pattern since the pressure sensor S37 (Ch.15) is submerged under increasing water depth between Phases B and C. At Phase D (t/T=13.20), the tank just passes the lower-left corner of the motion trajectory and begins to ascend along the upper half of the elliptic motion trajectory. At this instant, the tank acceleration is close to maximum and acts in the opposite direction of the gravity acceleration. The combined effects of fluid momentum change (i.e., hydrodynamics pressure) and gravity (i.e., hydrostatic pressure) produce very high surface pressures around the lower-left corner of the LNG tank as shown in Figure 5.23 (d). Between

Phases D and E, the water continues to move up the left tank wall while the tank right wall is completely exposed with zero pressure reading on Ch.15.

The experimental data in Figure 5.20 (b) indicates a somewhat slower decay of pressure at Ch.15 during this stage. The observed discrepancy may be due to the surface tension effects at model scale, which is ignored in the present full scale simulations. It is also worthwhile to note that the flow pattern is highly three-dimensional even though the excitation force due to the prescribed transverse motion is strictly two dimensional. The three-dimensional instability of the sloshing flow was also confirmed by the experimental observations.

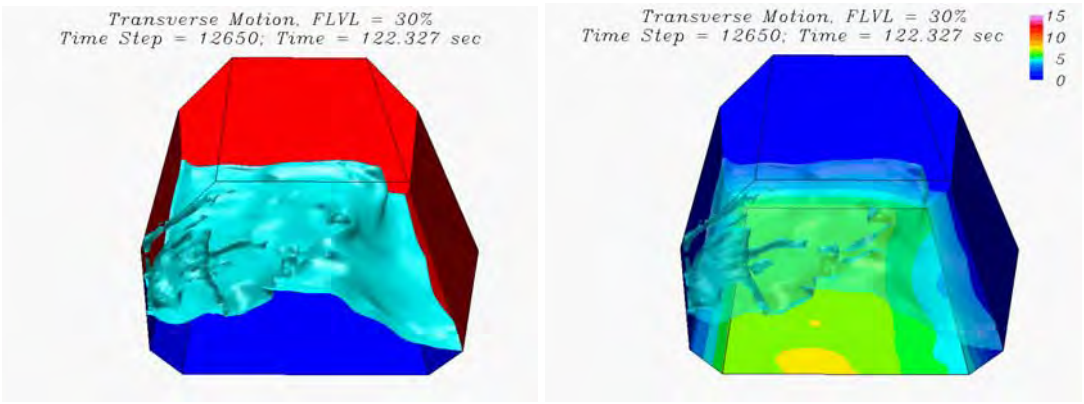

(a) Phase A: t/T = 12.65

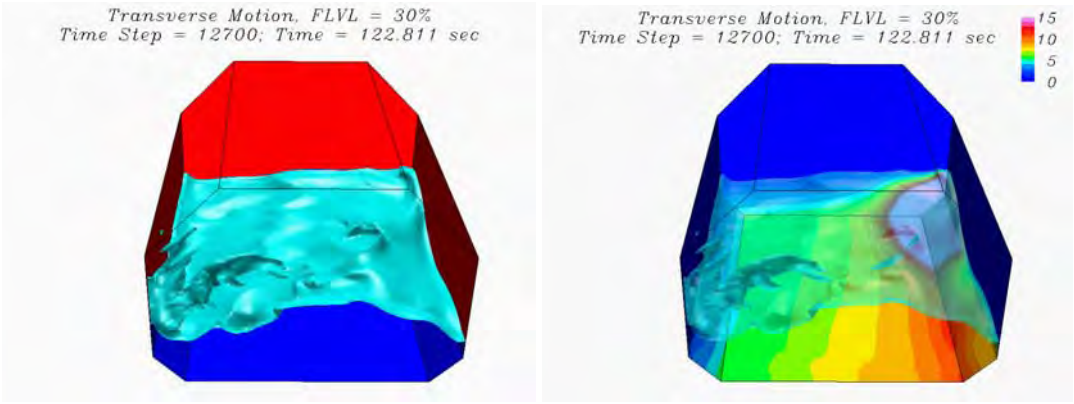

(b) Phase B: t/T = 12.70

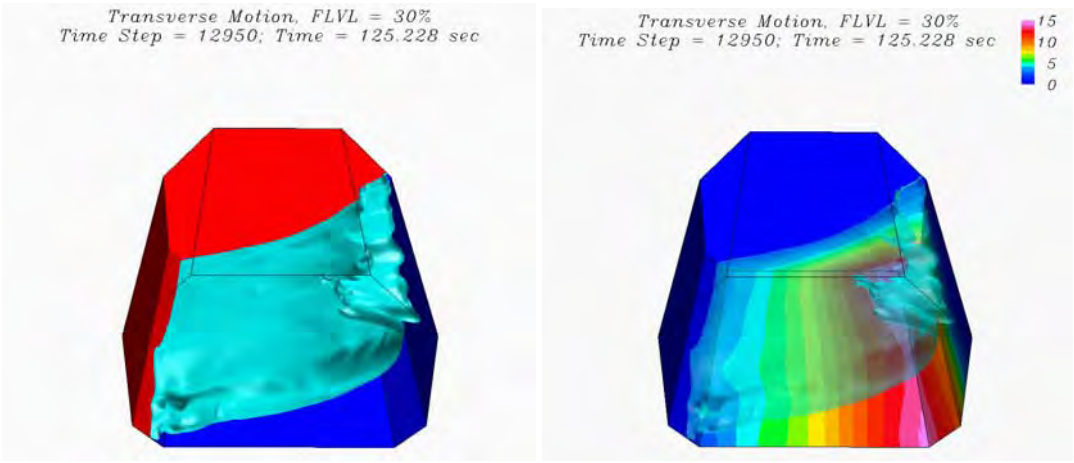

(c) Phase C: t/T = 12.95

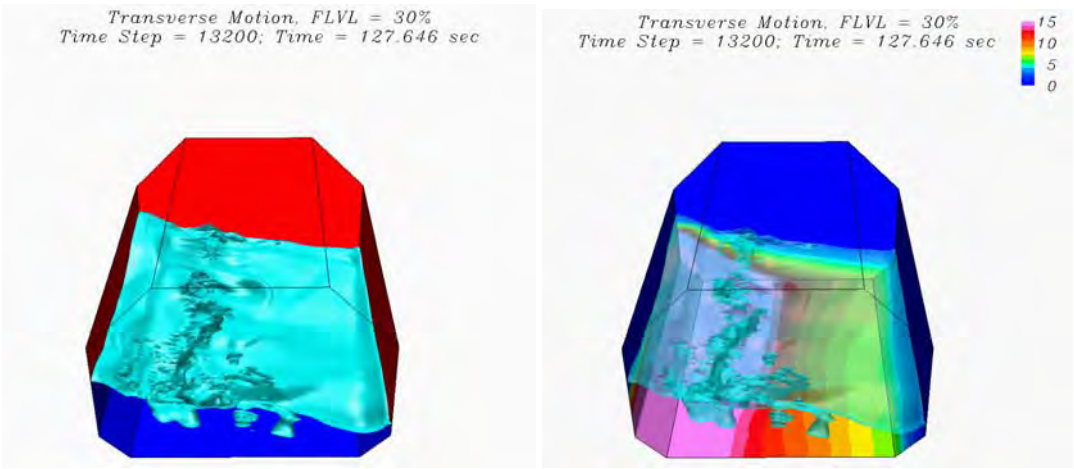

(d) Phase D: t/T = 13.2

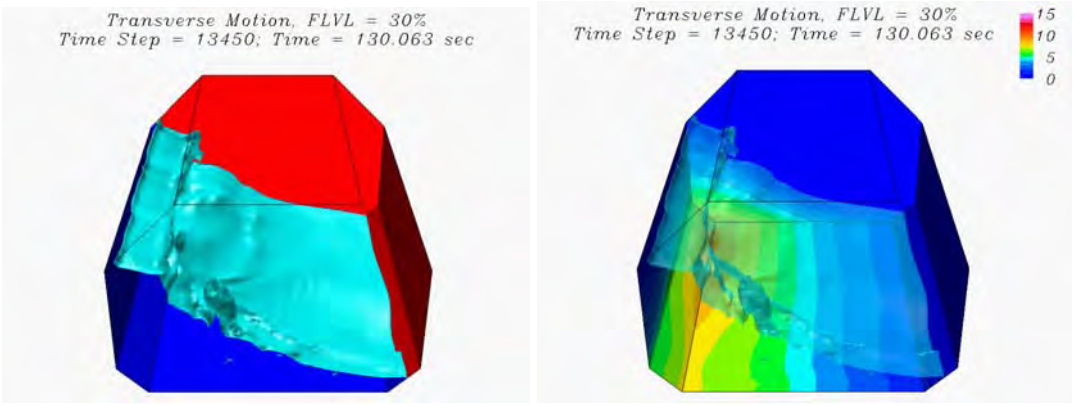

(e) Phase E: t/T = 13.45

Figure 5.23 3D Free surface and pressure contours, Case 2

5.5.3 Case 3 – Transverse motion with 50% Filling Level

Figure 5.24 shows the trajectory of the LNG tank center for Case 3 in prescribed transverse motion. It is worthwhile to note that the initial tank position for Cases 1 and 2 is located on the lower half of their corresponding motion trajectories. On the other hand, the tank motion for Case 3 is initiated on the upper half of the motion trajectory. Consequently, the sloshing flow patterns for Case 3 are also out of phase with those observed earlier for Cases 1 and 2. As shown in Table 5.2, the horizontal and vertical motion amplitudes for Case 3 are somewhat smaller than those experienced by Case 2. The maximum roll angle ($\pm 0.142^{\circ}$) is also smaller for Case 3. A modulation function was again applied for the first half period of the simulation to eliminate excessive fluid motion due to the impulsive start. Simulations were performed for 50 periods with a time increment of 0.001T. The wall pressures at selected sensor locations were recorded every time step, while the 3D velocity and pressure fields for the entire tank were saved every 50 time steps.

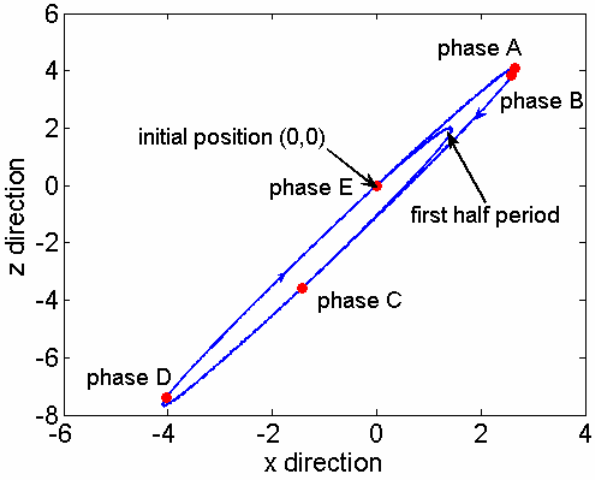

Figure 5.24 Tank motion trajectory, Case 3.

Figure 5.25 shows the 2D simulation results of impact pressures for the left and right pressure sensors corresponding to Ch.11 and its mirror image. Note that Ch.11 is located on the inclined surface slightly above the lower knuckle point of the upper chamfer as shown in Figure 5.2. Under the transverse tank motion, the pressure patterns are again shifted by a half-period between the left and right sensors. However, the impact pressures on the upper chamfer exhibit similar single-peak patterns at both the left and right sensor locations since Ch.11 is located on the upper chamfer.

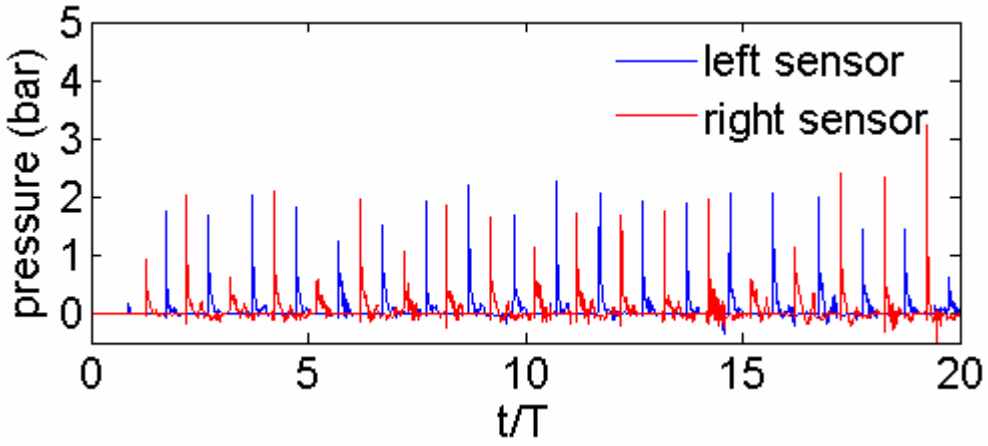

Figure 5.25 2D pressure history, Ch.11, Case 3

Figure 5.26 and Figure 5.27 show the comparisons of measured and predicted pressure histories at Ch.11 over 10 periods for the 2D and 3D simulations, respectively. It is seen that the pressure rises sharply due to water impact on the tank wall and decays rapidly immediately after the impact. Unlike the double-peak patterns observed earlier for Cases 1 and 2, the pressure decays monotonically to zero following the impact. In general, the 3D pressure pattern at sensor location S04 is in closer agreement with the experimental data than the corresponding 2D simulation result. It is also seen from Figure 5.28 that the peak impact pressure is highly localized in the vicinity of the pressure sensor with very sharp variations between two adjacent grid points.

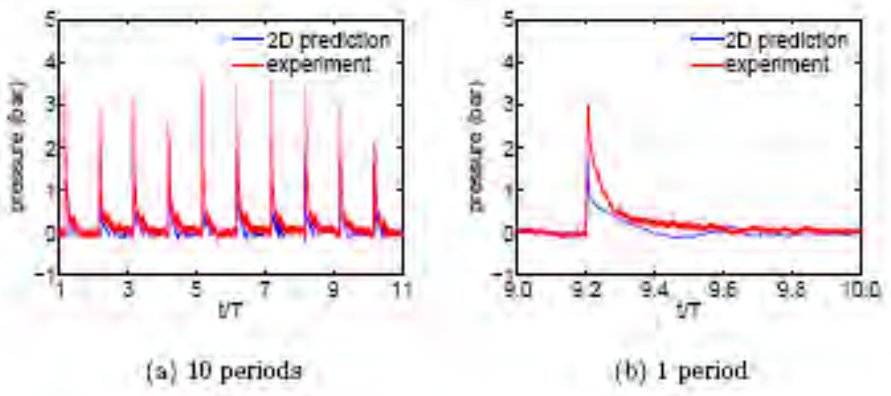

Figure 5.26 2D Impact pressure, Ch. 11 (right sensor), Case 3

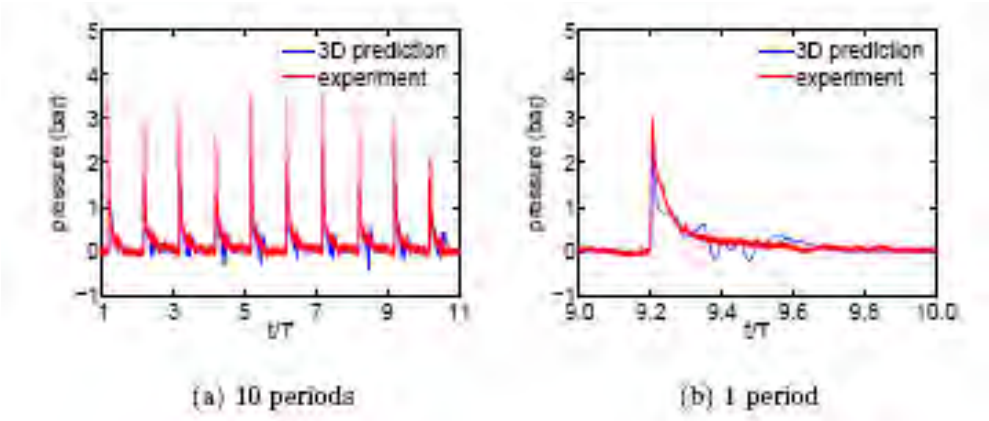

Figure 5.27 3D impact pressure, Ch. 11 (S04), Case 3

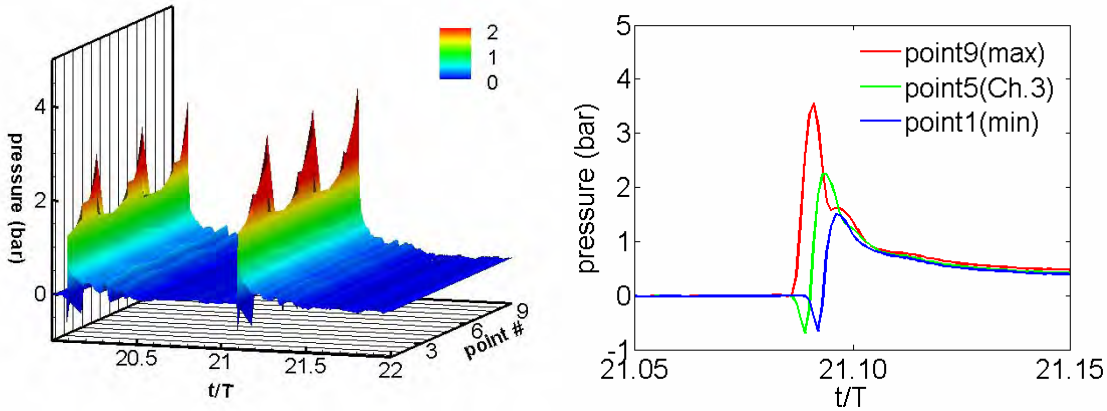

Figure 5.28 Impact pressures of 9 points around Ch. 11

A detailed examination of the 3D pressure history over a single period shown in Figure 5.27 (b) indicates that the maximum impact pressure occurs at t/T=9.207 over this specific period. In the following, we will examine the 2D and 3D velocity and pressure fields at t/T = 9.20, 9.25, 9.50, 9.75 and 10.00. These five time instants are denoted by Phases A, B, C, D, and E, respectively, along the motion trajectory shown in Figure 5.24. Note that Phases B, C, D, and E were chosen to be T/4 apart to illustrate the general flow patterns over one sloshing period.

In order to facilitate a more detailed understanding of the observed impact pressure pattern for Case 3, it is desirable to examine the 2D and 3D velocity and pressure fields induced by the sloshing tank motions as shown in Figure 5.29 and Figure 5.30, respectively. A comparison of Figure 5.29(a) and Figure 5.30(a) for Phase A (t/T=9.20) indicates that the 2D simulation predict a somewhat earlier impact at Ch.11 than the corresponding 3D simulation. This can be attributed to the three-dimensional effects which delayed the impact at pressure sensor location S04, even though a significant section of the inclined wall on the upper right chamfer was already inundated by sloshing water at t/T=9.20.

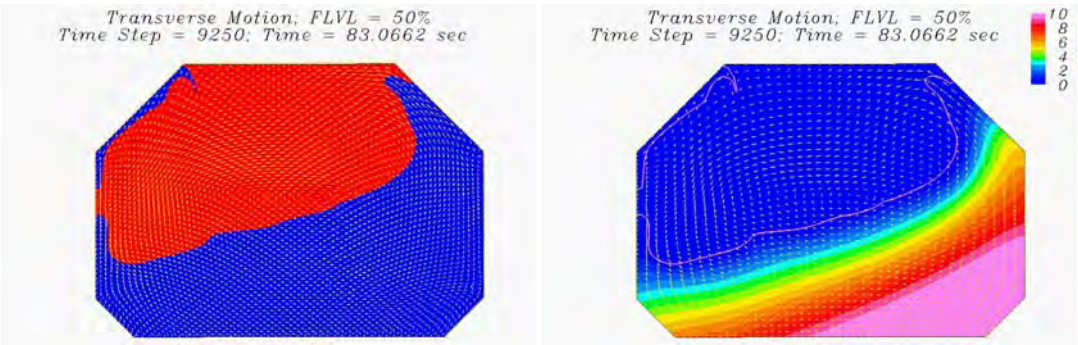

(a) Phase B: t/T = 9.25

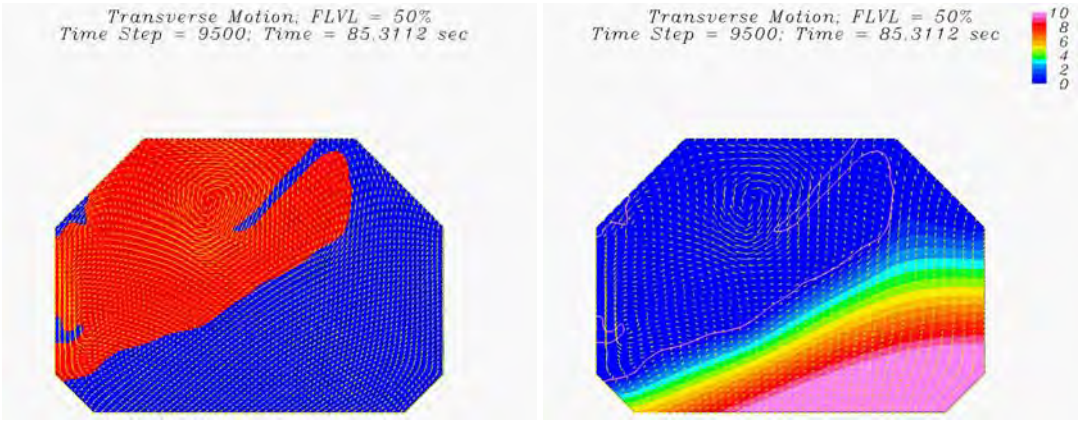

(b) Phase C: t/T = 9.50

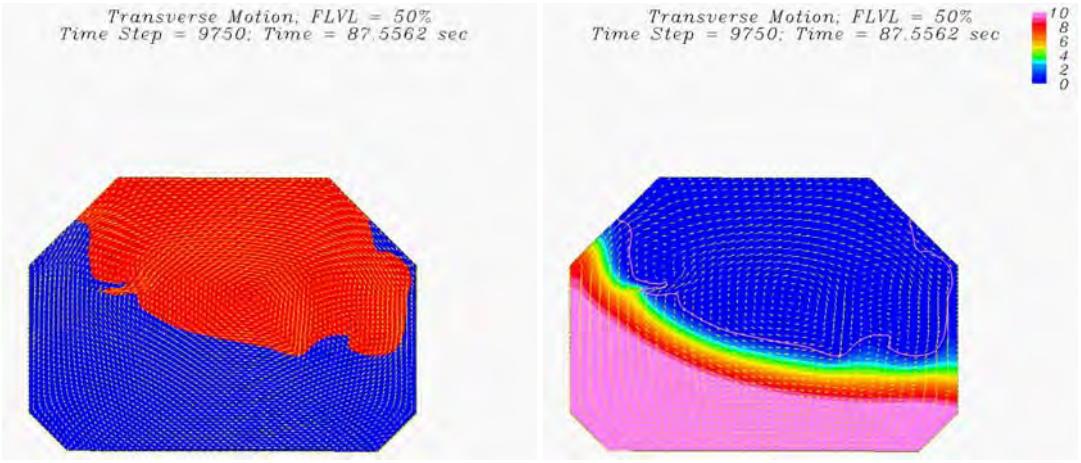

(c) Phase D: t/T = 9.75

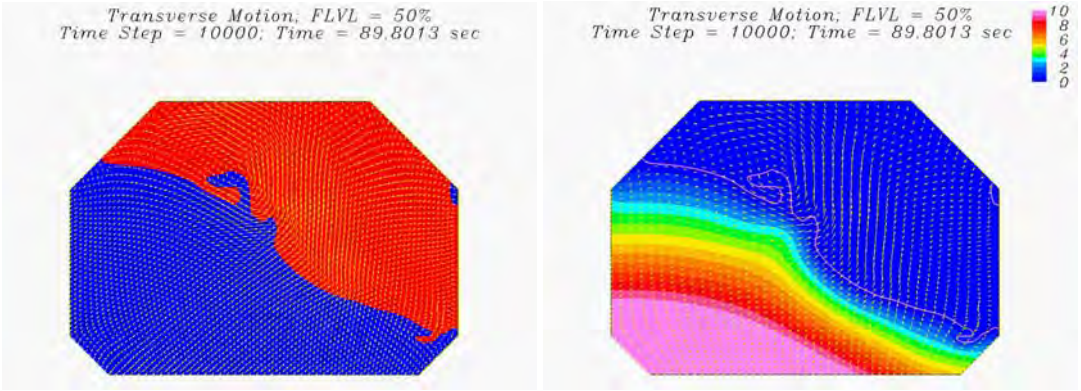

(d) Phase E: t/T = 10.00

Figure 5.29 2D free surface and pressure contours, Case 3

In the 3D simulations, the maximum impact pressure at Ch.11 occurs between Phases A and B when the LNG tank reaches the upper-right corner of the motion trajectory (see Figure 5.24) and begins to descend back to the equilibrium position. At Phase A (t/T=9.20), the free surface around the Ch.11 pressure sensor is slightly below the lower knuckle point of the upper chamfer. As noted earlier, the maximum impact pressure was observed at t/T=9.207 when the sloshing water rises rapidly over the lower knuckle point of the upper chamfer as seen at Phase B.

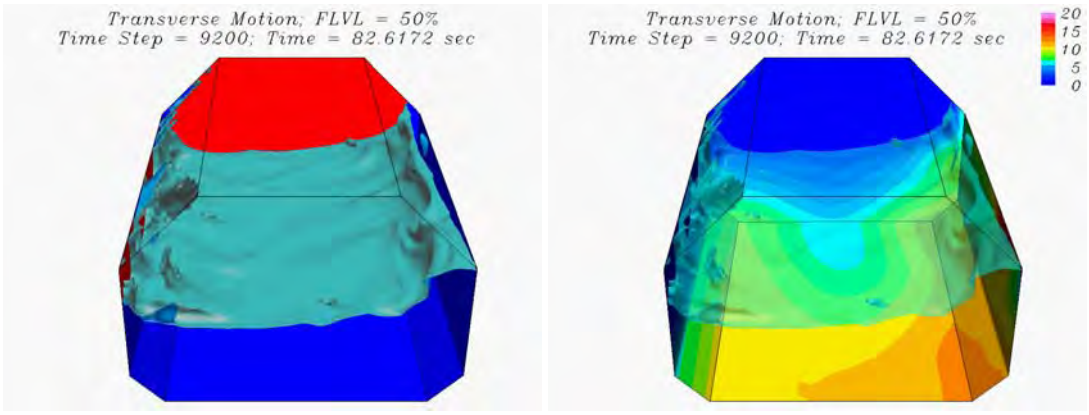

Phase A: t/T = 9.20

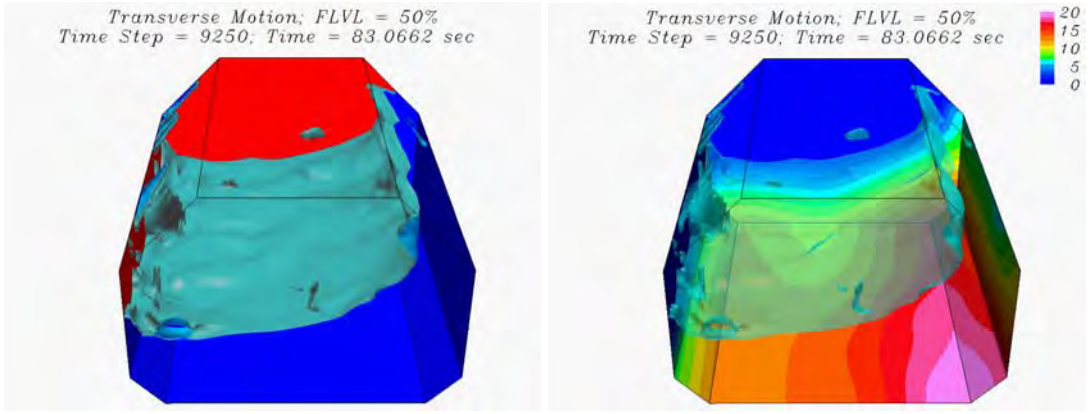

Phase B: t/T = 9.25

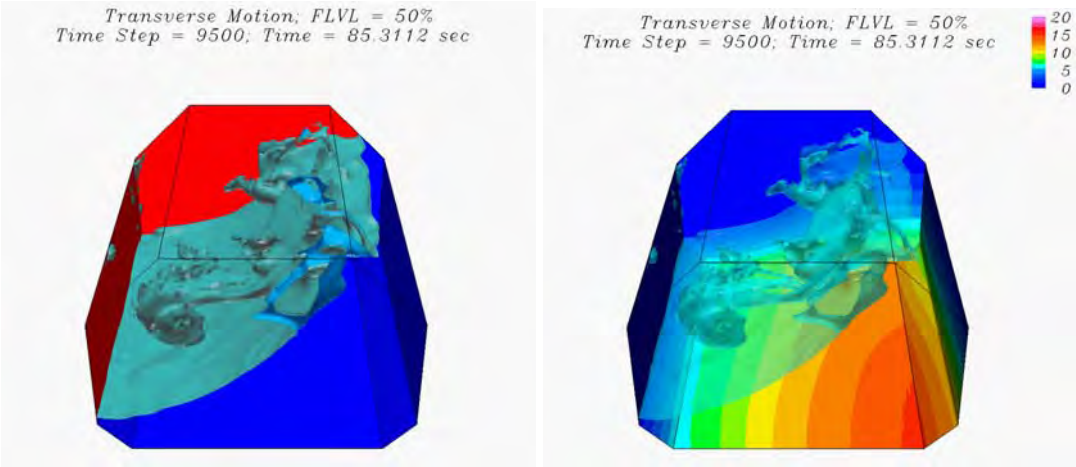

Phase C: t/T = 9.50

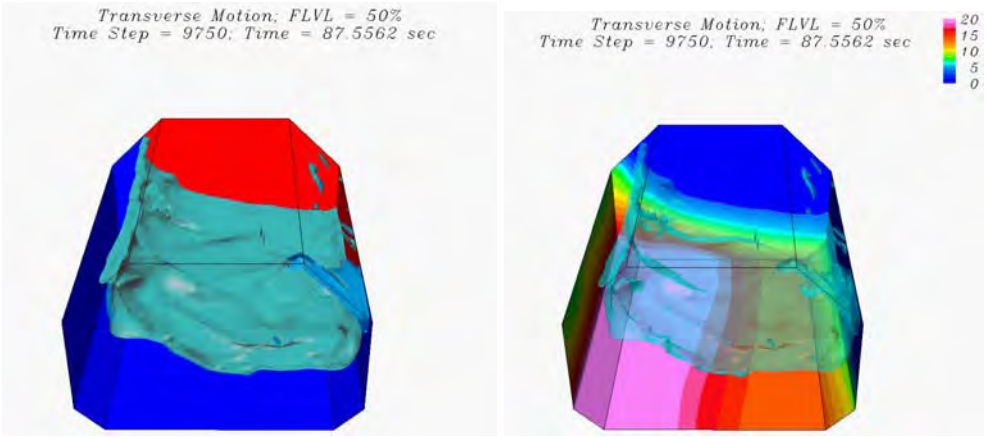

Phase D: t/T = 9.75

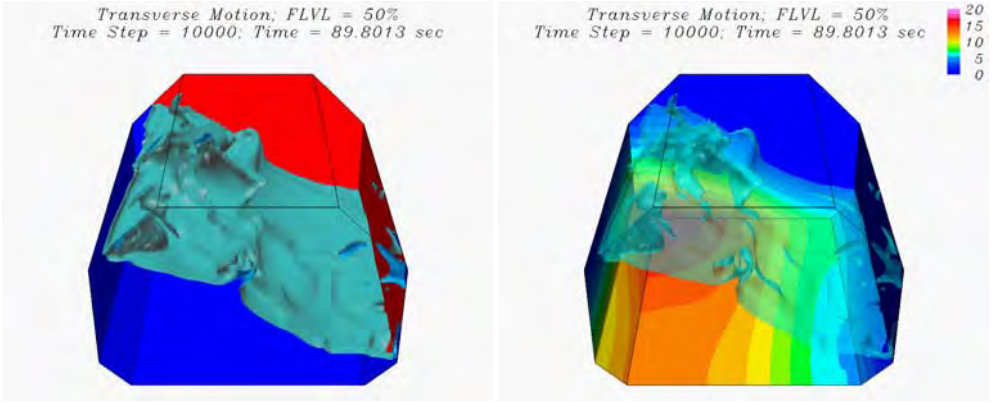

(e) t/T = 10.00

Figure 5.30 3D free surface and pressure contours, Case 3

At 50% filling level, the violent free surface flow slams on the top wall of the LNG tank as seen in Figure 5.29(c) and Figure 5.30(c) at t/T=9.50. As the LNG tank continues to move downward along the lower half of the elliptic motion trajectory between Phases C and D, the standing wave moves towards the left wall and the water on the upper chamfer of the right tank wall recedes quickly. Consequently, the pressure at Ch.11 decays monotonically to zero without the presence of a double-peak pattern.

It is clearly seen from Figure 5.30 that the free surface and pressure patterns are highly three-dimensional even though the excitation force is strictly two-dimensional. Furthermore, it was observed in the experiments that the sloshing flow for Case 3 also developed a distinct swirling flow pattern in the LNG tank which was not present in the lower filling level cases (i.e., Cases 1 and 2). In view of this, we have continued the Case 3 simulation for 30 more periods in addition to the standard 20-period simulation. A detailed examination of the simulation results clearly indicates that the three-dimensional flow instability eventually leads to the development of a swirling flow pattern after about 25 sloshing periods similar to those observed in the experiment.

Figure 5.31 shows the predicted swirling flow pattern over one sloshing period. It should be remarked that the swirling motion is not symmetric with respect to the tank center due to asymmetric tank motion. Moreover, the highest free surface elevation on four different corners does not occur exactly at T/4 interval since the LNG tank has a rectangular cross section with variable tank breadth in the lower and upper chamfers. The simulation results clearly illustrate the capability of the present method in predicting the three-dimensional instability induced by large amplitude motions in a partially filled LNG tank.

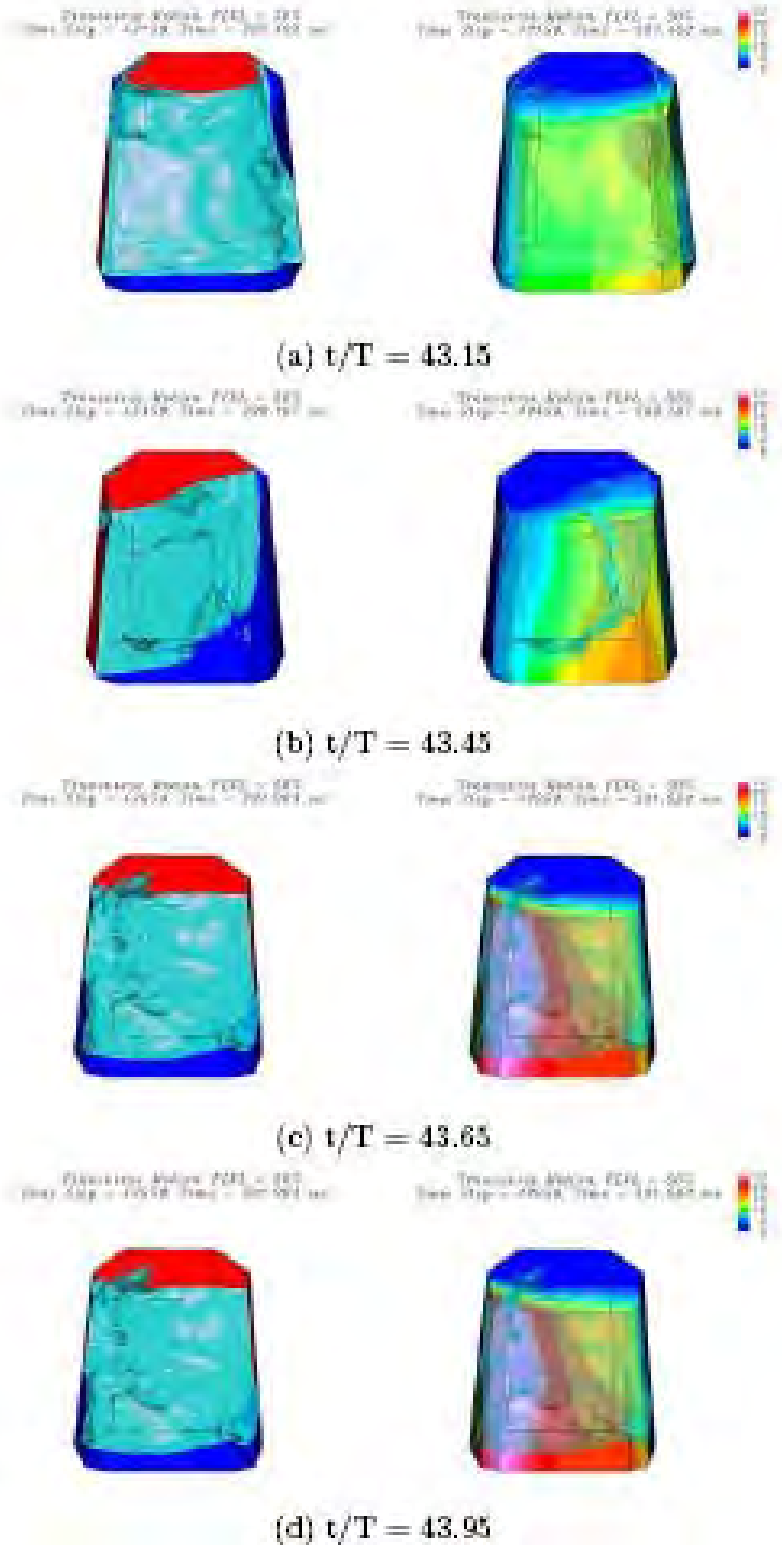

(a) t/T = 43.15

(b) t/T = 43.45

(c) t/T = 43.65

(d) t/T = 43.95

Figure 5.31 The swirling flow, Case 3

5.5.4 Case 4 – Longitudinal Motion with 50% Filling Level

Figure 5.32 shows the longitudinal motion trajectory (in the *yz*-plane) of the LNG tank for Case 4 with the initial tank position at the origin (0,0). Note that the amplitude of horizontal motion is much smaller than the vertical motion amplitude. In addition to the large amplitude vertical motions, the tank also experiences a large amplitude roll motion with a maximum pitch angle of ±4.80°. A modulation function was again applied for the first half cycle to eliminate the pressure oscillations caused by the impulsive start of the LNG tank motion. Simulations were performed for 20 periods and the wall pressures at selected sensor locations were recorded every time step to facilitate a direct comparison with the experimental data.

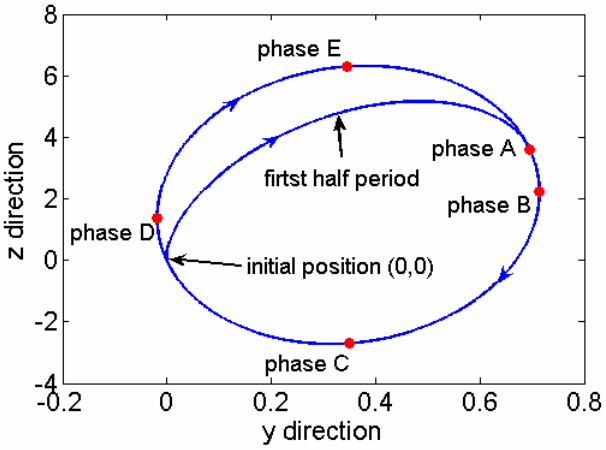

Figure 5.32 Tank motion trajectory, Case 4

Figure 5.33 shows the 2D impact pressures for both the left and right pressure sensors corresponding to Ch.3 on the top wall of the LNG tank as shown in Figure 5.7. It is quite clear that the sloshing water did not hit the top wall in the present two-dimensional simulations. The three-dimensional simulation result also indicates that the sloshing water did not reach the top wall even though the predicted water level is significantly higher than that observed in the 2D simulation.

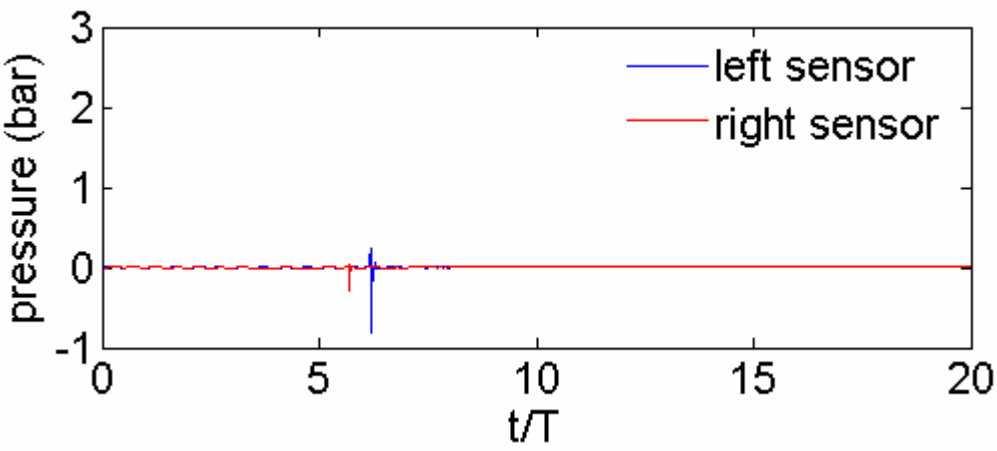

Figure 5.33 2D pressure history, Case 4

Figure 5.34 shows a comparison of the measured impact pressure history at Ch.1 (see Figure 5.2) with that obtained from the 3D simulations. As shown in Figure 5.2, Ch.1 is located on the inclined surface slightly above the lower knuckle point of the upper chamfer. It coincides with the pressure sensor S04 in Figure 5.8, and is symmetric with Ch.11 on the opposite wall. It is seen from Figure 5.34 that the pressure at Ch.1 rises sharply due to water impact on the tank wall and decays monotonically after the impact. In general, the pressure pattern is in reasonable agreement with the experimental data although the peak pressures are somewhat underpredicted. Also, the peak impact pressure is highly localized in the vicinity of the pressure sensor location as shown in Figure 5.35. A detailed examination of the pressure history over a single period shown in Figure 5.34(b) indicates that the maximum impact pressure occurs at t/T=5.505 over this specific period. For completeness, we will examine the detailed velocity and pressure fields at t/T = 5.50, 5.55, 5.80, 6.05 and 6.30, which are denoted by Phases A, B, C, D, and E, respectively, on the motion trajectory shown in Figure 5.32.

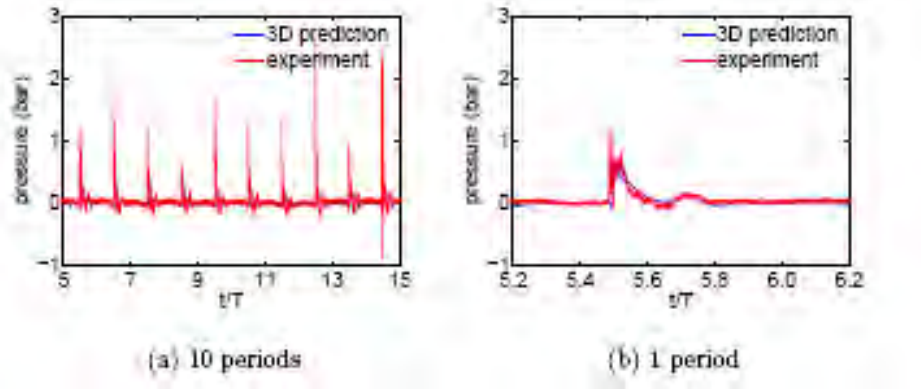

Figure 5.34 3D impact pressure, Ch.1 (S04), Case 4

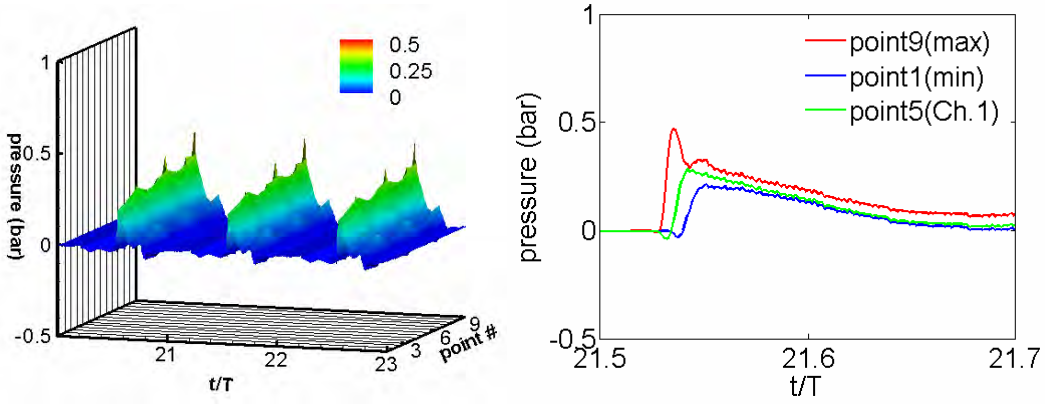

Figure 5.35 Impact pressures, the vicinity of Ch.1 (S04), Case 4

Figure 5.36 shows the predicted 2D free surface flow patterns and the corresponding pressure contours for Case 4 at five different phases A-E which were marked in the trajectory plot shown earlier in Figure 5.32. It should be remarked that the two-dimensional simulation results obtained here cannot properly account for the reduction of tank cross section area in the upper or lower chamfers of the three-dimensional LNG tank shown in Figure 5.. Consequently, the predicted free surface elevation tends to be lower than the corresponding three-dimensional simulation results shown in Figure 5.37.

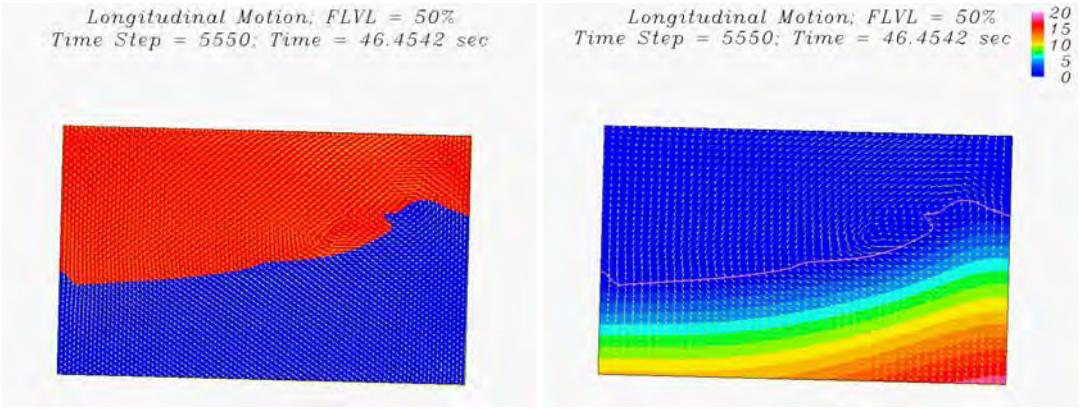

(a) Phase B: t/T = 5.55

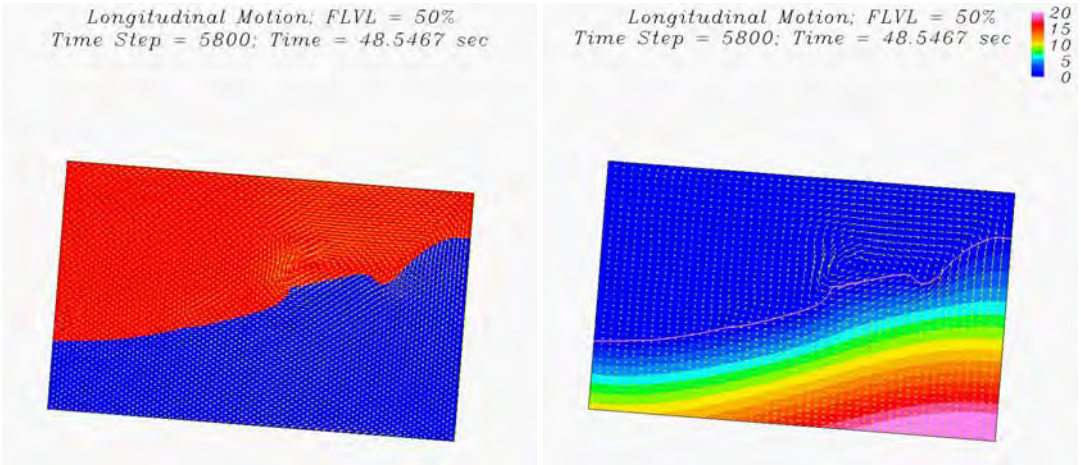

(b) Phase C: t/T = 5.80

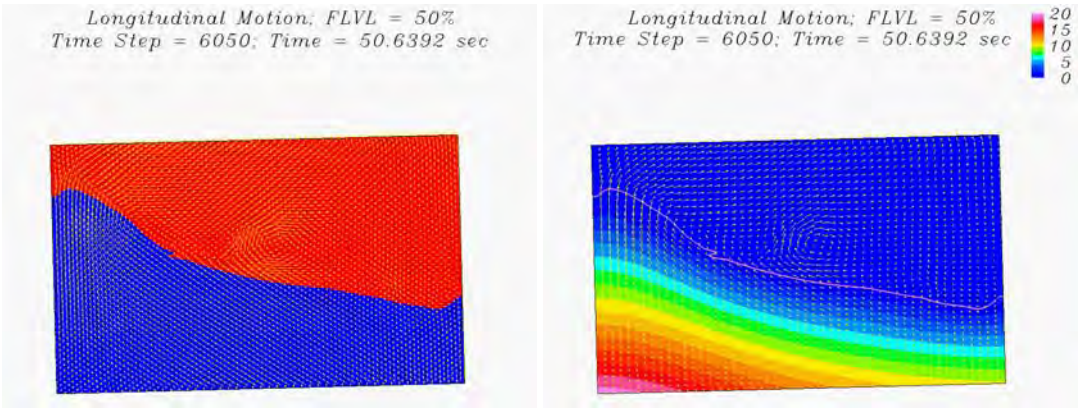

(c) Phase D: t/T = 6.05

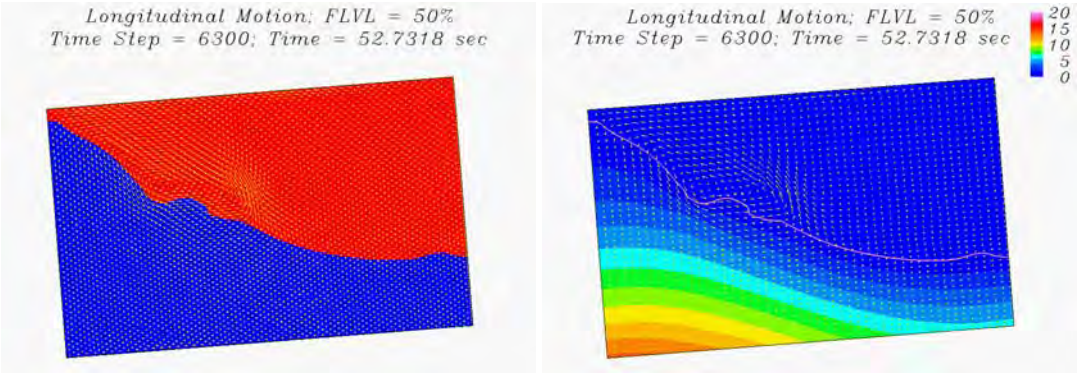

(d) Phase E: t/T = 6.30

Figure 5.36 2D free surface and pressure contours, Case 4

As noted earlier, the maximum impact pressure at Ch.1 occurs at t/T = 5.505 in the present 3D simulation. At Phase A (t/T = 5.50), the free surface level is just below the Ch.1 pressure sensor location. After impact, the water level continues to rise along the inclined wall of the upper chamfer as seen in Figure 5.37(b). However, the sloshing water never hits the top wall of the tank in the present simulation. On the other hand, experimental observation in the model tank clearly indicates the presence of violent free surface motions with numerous water droplets impinging on the tank top. It is quite clear that the present $85\times101\times85$ grid is too coarse to resolve the water droplets and their impacts on the top surface of the LNG tank. In spite of the observed discrepancy on the tank top wall, the impact pressure at Ch.1 on the upper chamfer is in fairly good agreement with the corresponding experimental data as shown earlier in Figure 5.34.

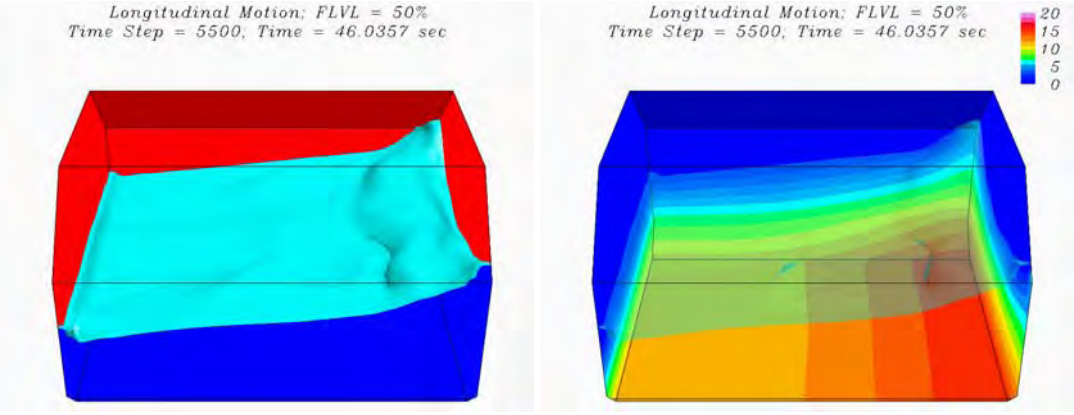

(a) Phase A: t/T = 5.50

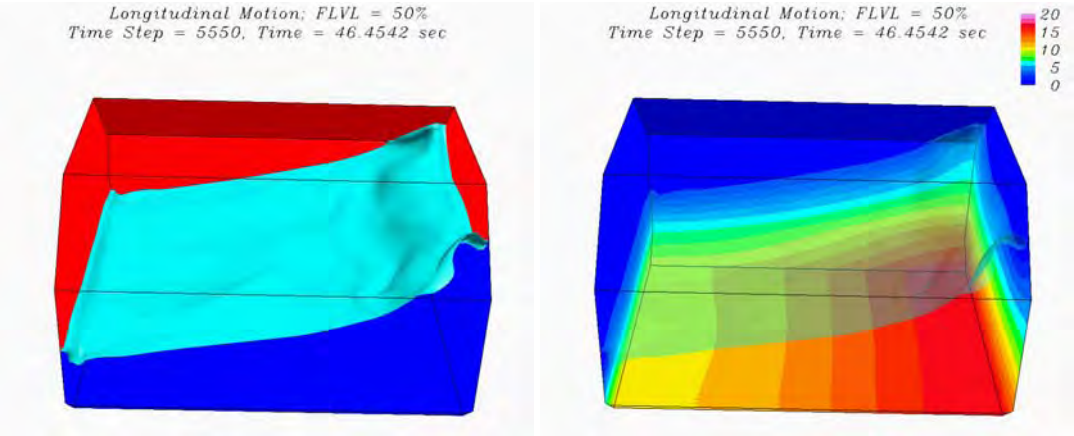

(b) Phase B: t/T = 5.55

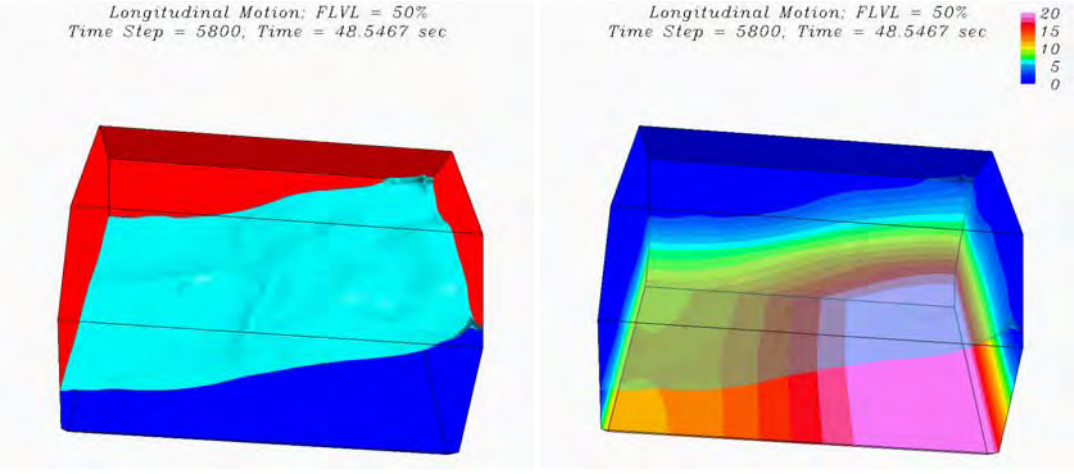

(c) Phase C: t/T = 5.80

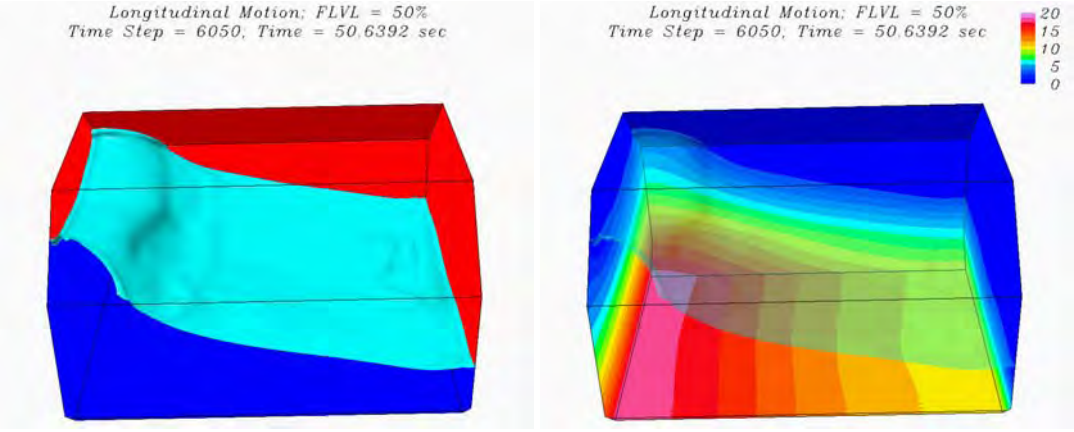

(d) Phase D: t/T = 6.05

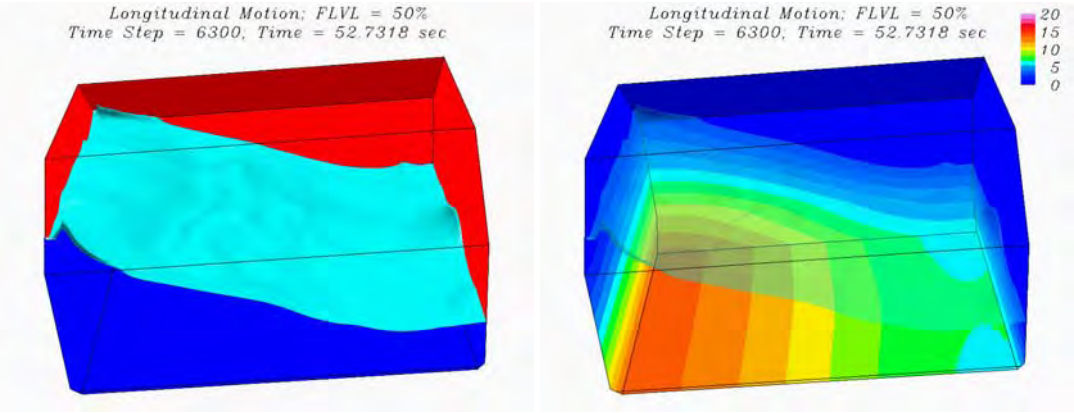

(e) Phase E: t/T = 6.30

Figure 5.37 3D free surface and pressure contours, Case 4

5.5.5 Case 5 – Longitudinal Motion with 80% Filling Level

Figure 5.38 shows the trajectory of the LNG tank center for Case 5 in prescribed transverse motion with 80% fluid filling level. Compared to Case 4, the horizontal motion amplitude is somewhat larger but the vertical motion amplitude is reduced by more than 60%. The maximum pitch angle (±0.693°) for Case 5 is also much smaller than that experienced by Case 4. A modulation function was again applied for the first half period of the simulation to eliminate excessive fluid motion due to the impulsive

start. It is worthwhile to note that the orientation of the elliptic motion trajectory for Case 5 is different from the previous four cases with the LNG tank oscillating between the lower-right and top-left corners.

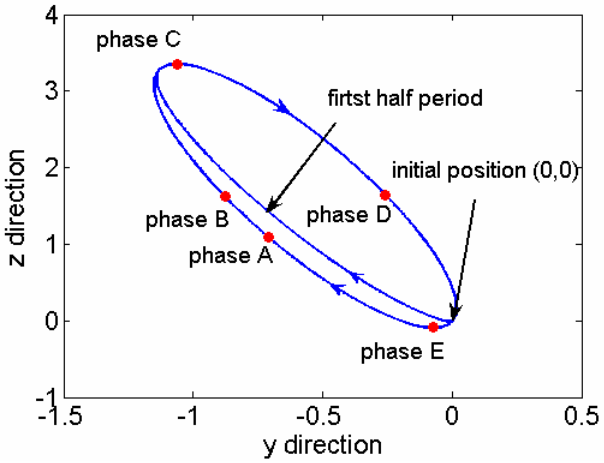

Figure 5.38 Tank motion trajectory, Case 5

Figure 5.39 shows the predicted 2D impact pressure history for both the left and right sensors on the tank top. The 2D simulation again fails to predict the impact of sloshing water on the top surface of the LNG tank even though the fluid filling level has been increased from 50% to 80%. On the other hand, the 3D simulation results shown in Figure 5.40 accurately predict the impact pressure at Ch.7 (Senor S11) on the top wall of the LNG tank. It is also seen from Figure 5.41 that the impact pressure is highly localized with huge pressure variations within the 3×3 numerical element surrounding Ch.7. A detailed examination of the pressure history over a single period shown in Figure 5.40(b) indicates that the maximum impact pressure occurs at t/T = 13.262 over this specific period. To facilitate a more detailed understanding of the observed impact pressure pattern, we will examine both the 2D and 3D flow fields at t/T = 13.25, 13.30, 13.55, 13.80 and 14.05, which are denoted by Phases A-E in Figure 5.38.

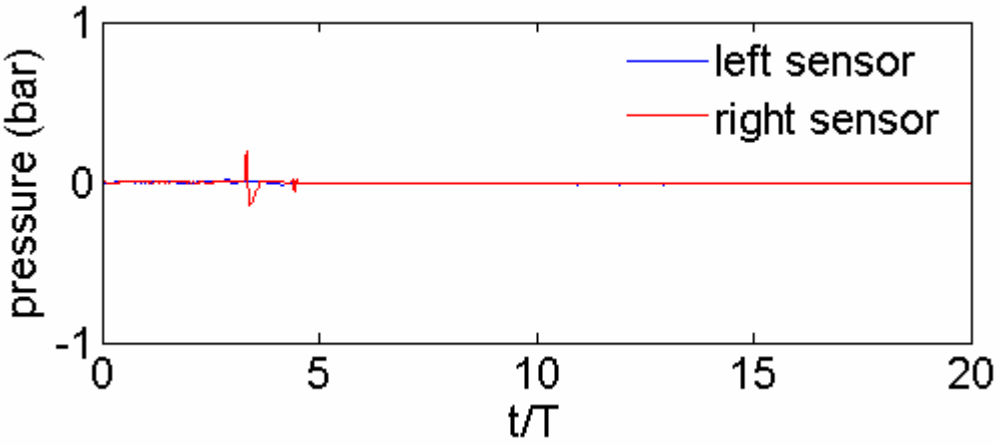

Figure 5.39 2D pressure history, Case 5

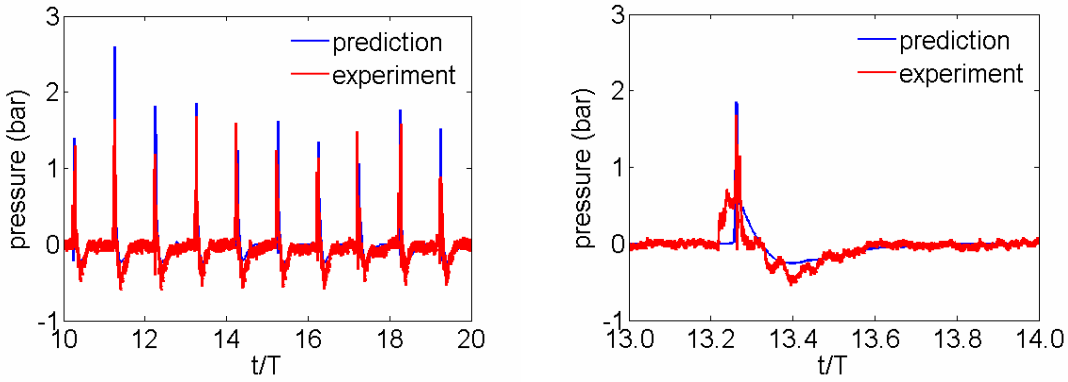

(a) 10 periods (b) 1 period

Figure 5.40 3D impact pressure, Ch.7 (S11), Case 5

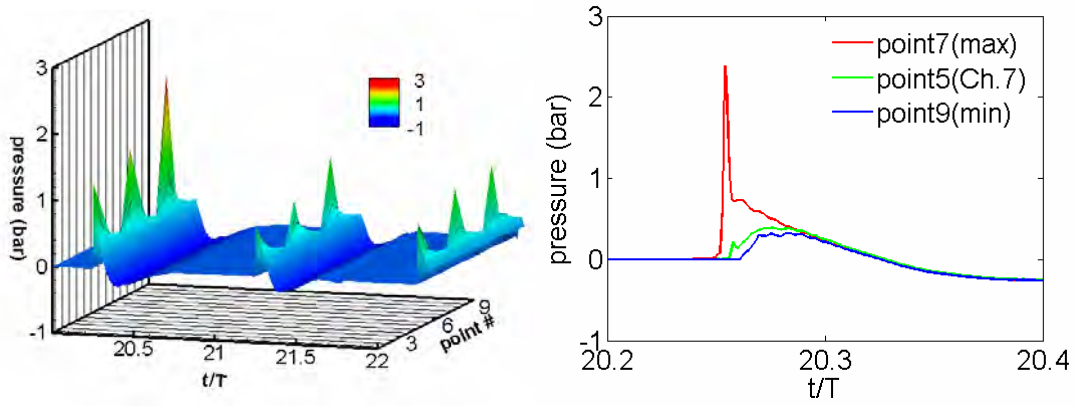

Figure 5.41 Impact pressures, the vicinity of Ch. 7 (S11), Case 5

Figure 5.42 shows the predicted two-dimensional free surface motions and the corresponding pressure contours in the sloshing LNG tank. Due to incorrect representation of the tank geometry, the sloshing water was not able to hit the tank top in the present 2D simulation. More specifically, the two-dimensional rectangular grid cannot account for the reduction of tank cross sectional area in the upper chamfer. In order to facilitate a more detailed understanding of the three-dimensional effects for sloshing flow in the upper chamfer, it is desirable to compare the 2D flow patterns to the corresponding 3D simulation results shown in Figure 5.43.

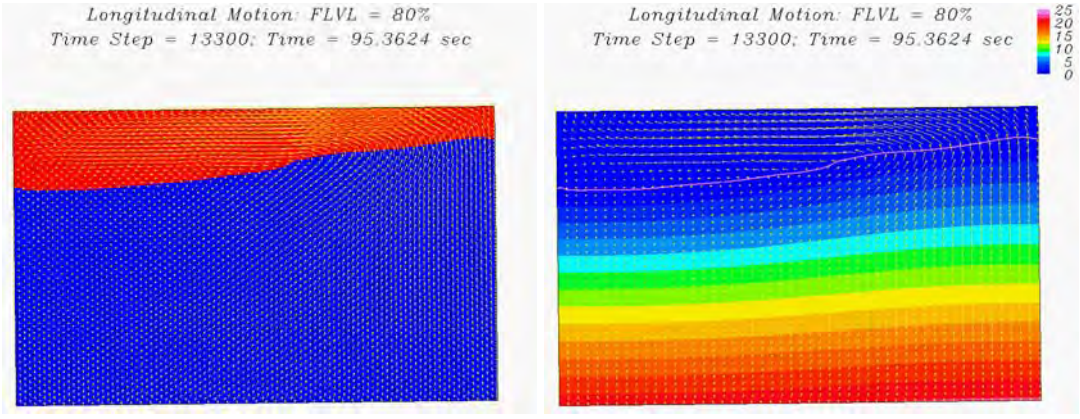

(a) Phase B: t/T = 13.30

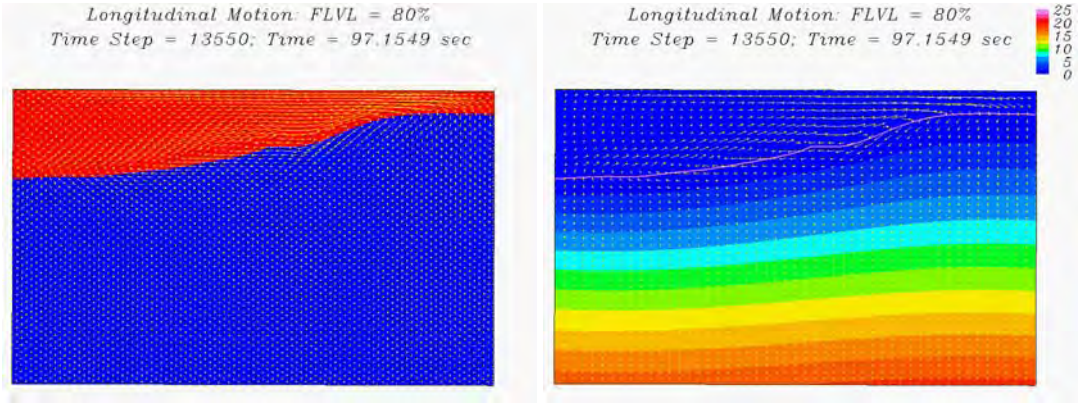

(b) Phase C: t/T = 13.55

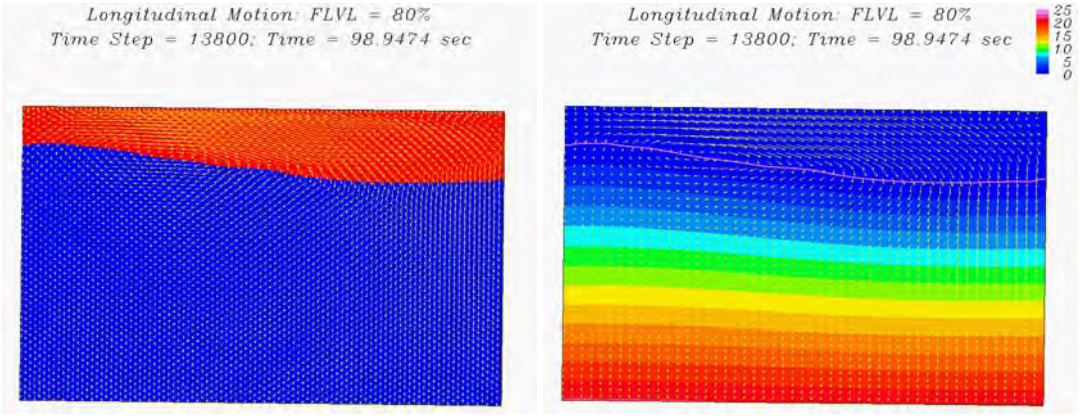

(c) Phase D: t/T = 13.80

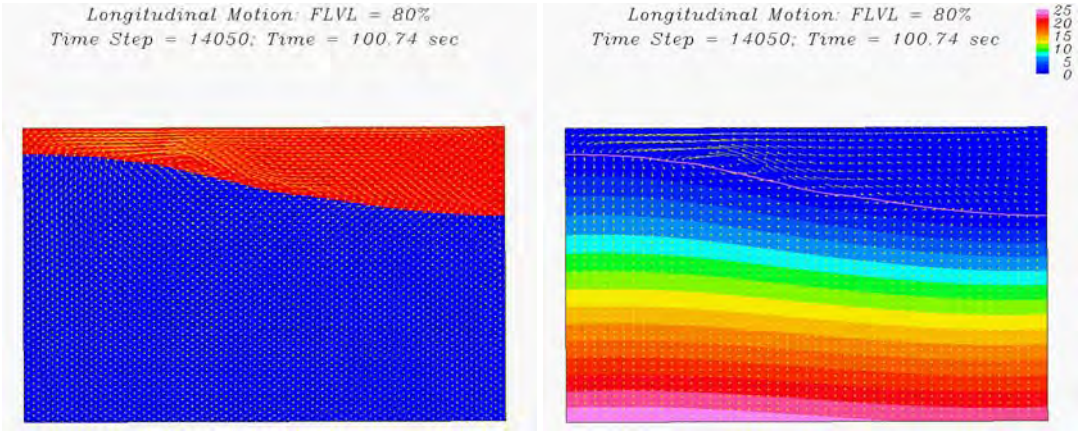

(d) Phase E: t/T = 14.05

Figure 5.42 2D free surface and pressure contours, Case 5

Figure 5.43 shows the predicted free surface motions and the corresponding pressure contours for Case 5 in the three-dimensional LNG tank. Compared to the two-dimensional rectangular tank geometry shown in Figure 5.42, it is quite obvious that the sloshing flow near the tank top wall is greatly affected by the inclined surfaces of the upper chamfer. Due to the narrowing of the tank cross section near the top wall, the sloshing flow is forced to converge towards the top surface with stronger acceleration and increasing water elevation than that encountered in a rectangular tank.

During the selected period $13 < t/T < 14$ shown in Figure 5.40(b), the peak impact occurs at $t/T = 13.262$ between Phases A and B. It is seen from Figure 5.43(a) that the free surface level near Ch.7 is slightly below the tank top at Phase A ($t/T = 13.25$). When the LNG tank continues to move towards the upper-left corner from Phases A to Phase B, the combined translational and rotational motion of the tank produces a rapid rise of the water level and a sharp impact on the tank top wall at the sensor location Ch.7. Due to the three-dimensional instability, the flow becomes asymmetric after the 7th sloshing period with sloshing water impinging upon only one corner of the top wall as shown in Figure 5.43 (b) and Figure 5.43(c).

It is also worthwhile to note from Figure 5.40 that both the measurement and numerical simulation clearly indicate the presence of small negative pressures following each impact. These negative pressure signals are very different from the pure hydrodynamic impacts observed in low filling level cases, and are due to the strong air-water interactions in the confined ullage space.

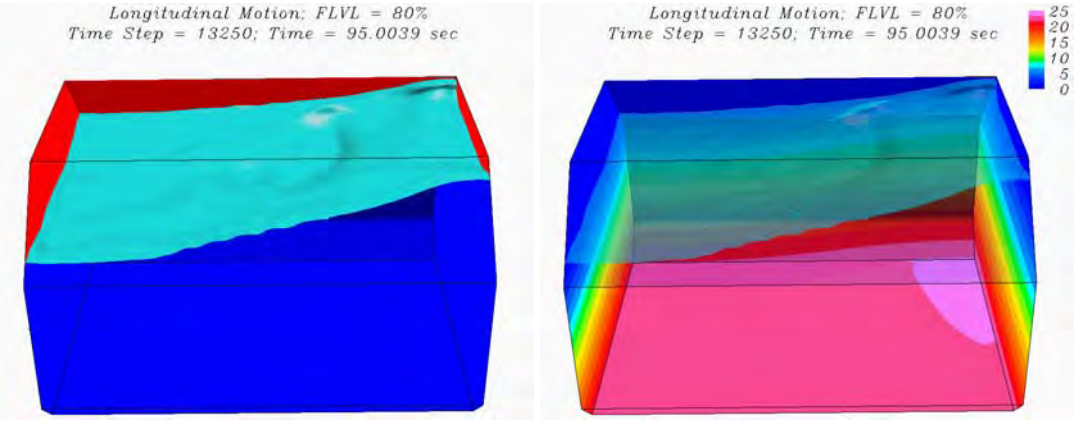

(a) Phase A: t/T = 13.25

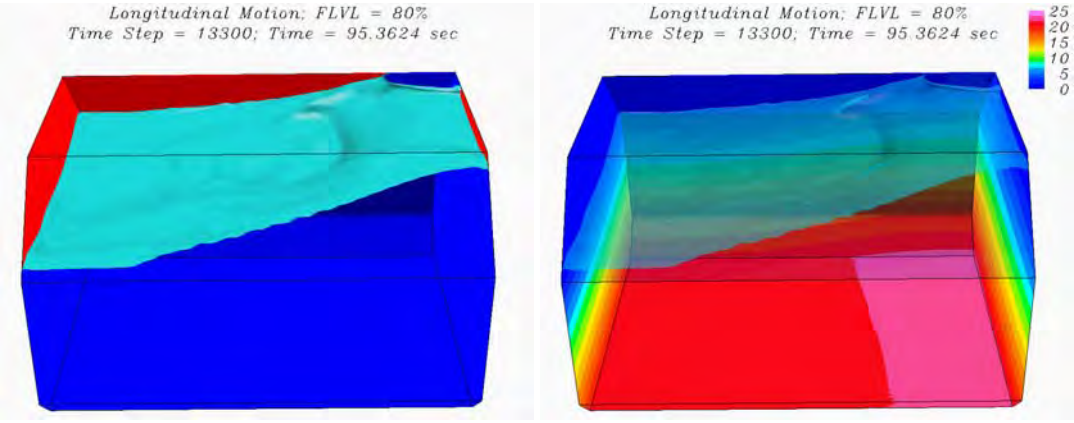

(b) Phase B: t/T = 13.30

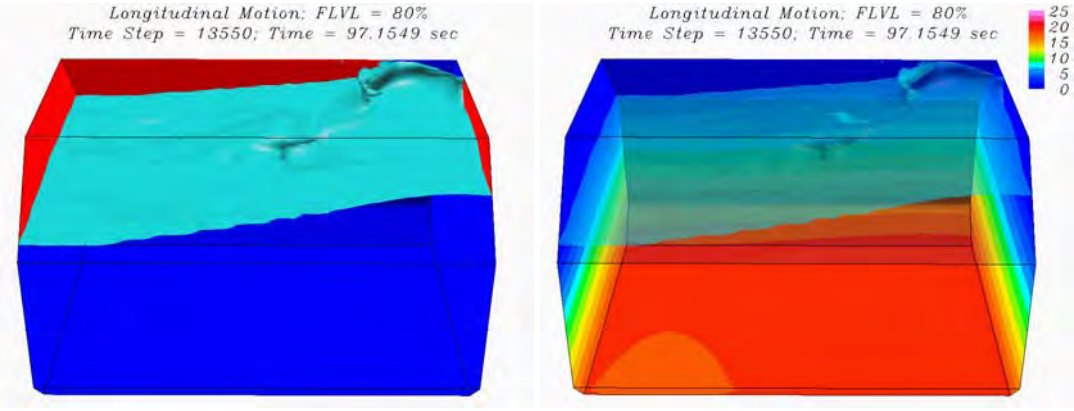

(c) Phase C: t/T = 13.55

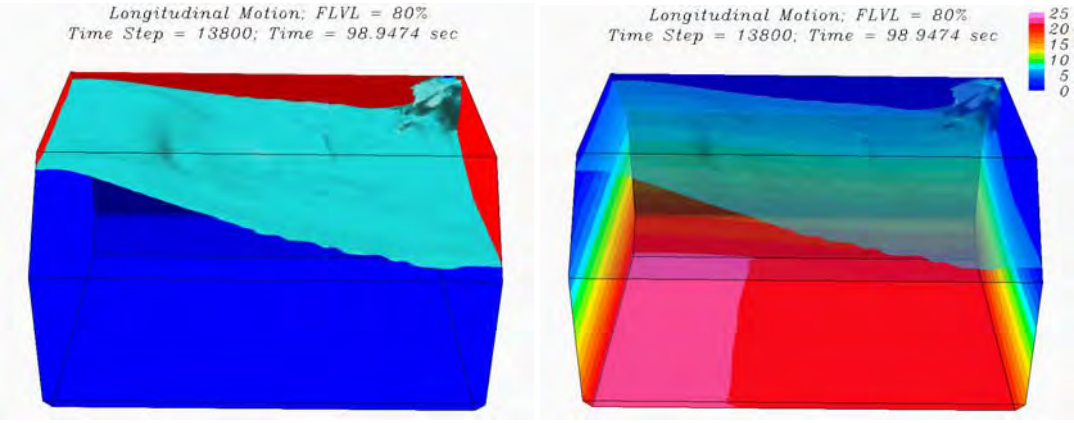

(d) Phase D: t/T = 13.80

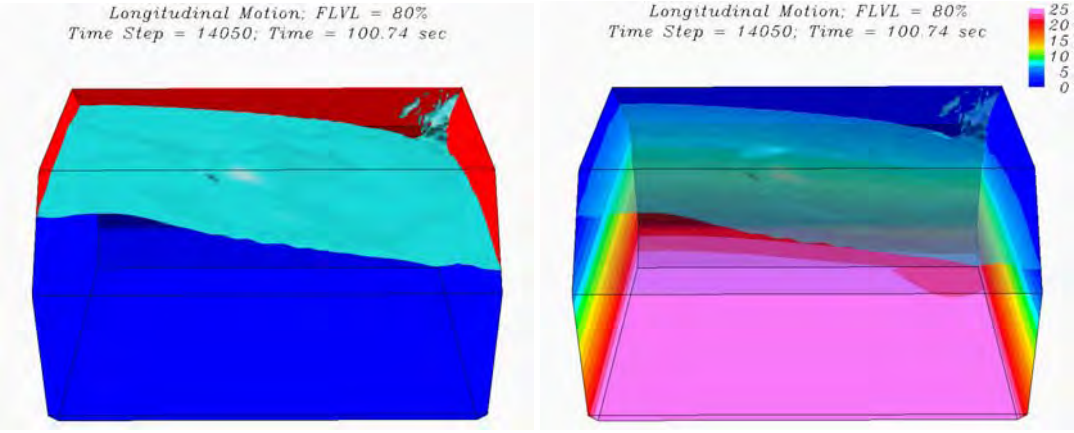

(e) Phase E: t/T = 14.05

Figure 5.43 3D free surface and pressure contours, Case 5

5.5.6 Case 6 – Longitudinal Motion with 92.5% Filling Level

Figure 5.44 shows the longitudinal motion trajectory (in the *yz*-plane) of the LNG tank for Case 6 with the initial tank position at the origin (0,0). Note that the amplitude of horizontal motion is much smaller than the vertical motion amplitude. In addition to the large amplitude vertical motions, the tank also experienced a large amplitude roll motion with a maximum roll angle of ±5.45°. A modulation function was again applied for the first half cycle to eliminate the pressure oscillations caused by the impulsive start

of the LNG tank motion. Simulations were performed for 22 periods and the wall pressures at selected sensor locations were recorded every time step to facilitate a direct comparison with the experimental data. At the 92.5% filling level, the free surface motion and high impact pressure regions are confined to the upper chamfer near the tank top. In view of this, the numerical grid was redistributed in the vertical direction to provide more accurate resolution of the impact pressures in the upper chamfer.

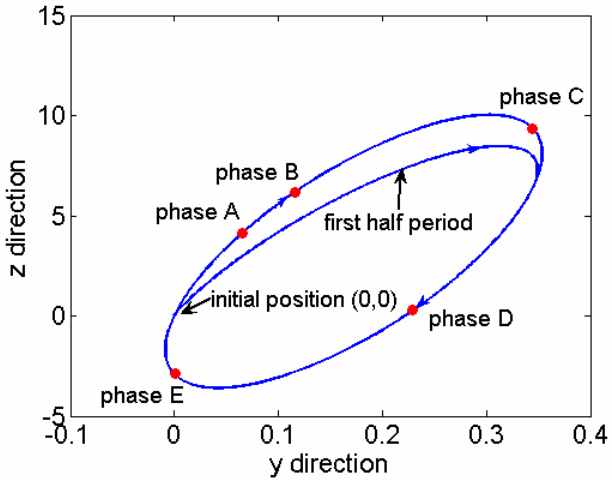

Figure 5.44 Tank motion trajectory, Case 6

Figure 5.45 shows the 2D simulation results of impact pressures for the left and right pressure sensors corresponding to Ch. 3 on the top wall. Due to asymmetric tank motion, the pressure on the right sensor location is significantly higher than that on the left sensor location.

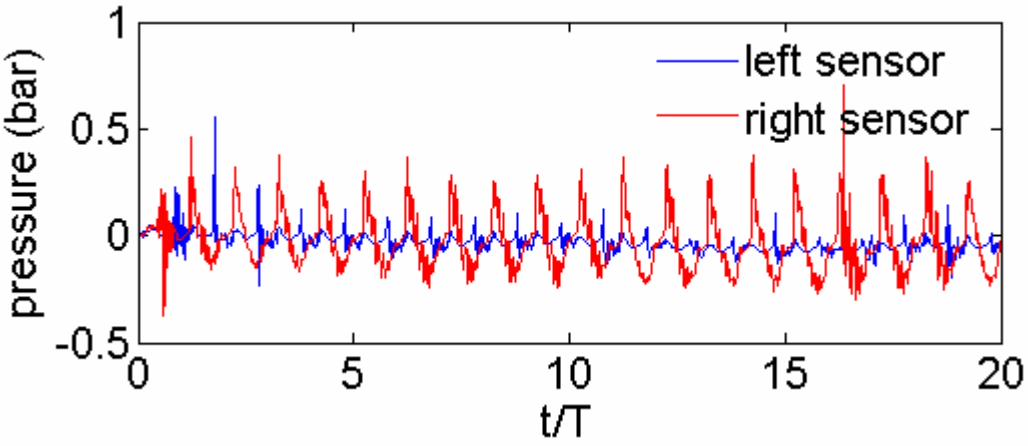

Figure 5.45 2D impact pressure, Ch. 3, Case 6

Figure 5.46 and Figure 5.47 show the time histories of the measured and predicted pressures at Ch.3 on the top surface of the LNG tank for the 2D and 3D simulations, respectively. Note that Ch.3 and Ch.7 are mirror images on opposite sides of the tank top wall. In general, the predicted impact pressures are in good agreement with the corresponding measurements. The 2D simulation gives less satisfactory predictions due to incorrect representation of the tank geometry, but the result is still reasonable because the change of tank cross section is relatively small at the 92.5% fluid filling level.

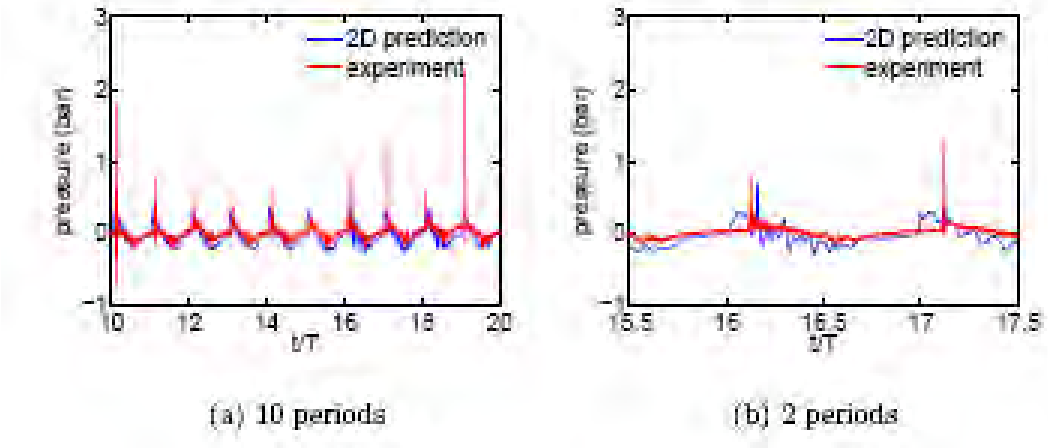

Figure 5.46 2D impact pressure, Ch.3, Case 6

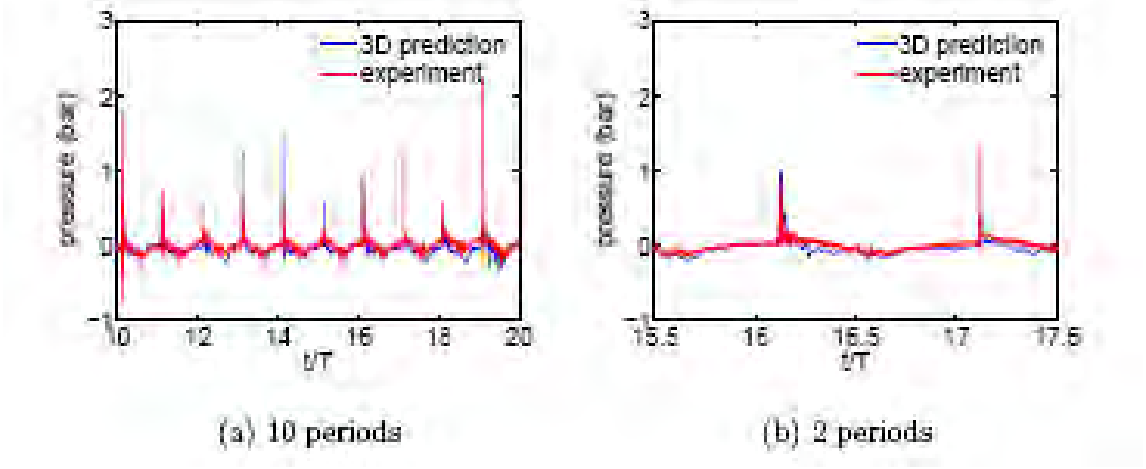

Figure 5.47 3D impact pressure, Ch.3 (S12), Case 6

It is clearly seen that the peak impact pressure on the top wall is relatively low for this high filling case since the free surface motion is less violent in the confined ullage space. It is also interesting to note that the measured and predicted pressure histories exhibit a nearly symmetric pattern between two peak impacts. Furthermore, the wall pressure at Ch.3 is slightly below the atmospheric pressure between sharp pressure impacts. These pressure signals are caused by the combined hydrodynamic impact and air trapping effects which are very different from the pure hydrodynamic impacts observed in Cases 1-4 for the lower filling level cases. In the 3D simulations, the impact pressure is again highly localized as seen in Figure 5.48 with very strong variations between two adjacent grid points at the time of peak impact.

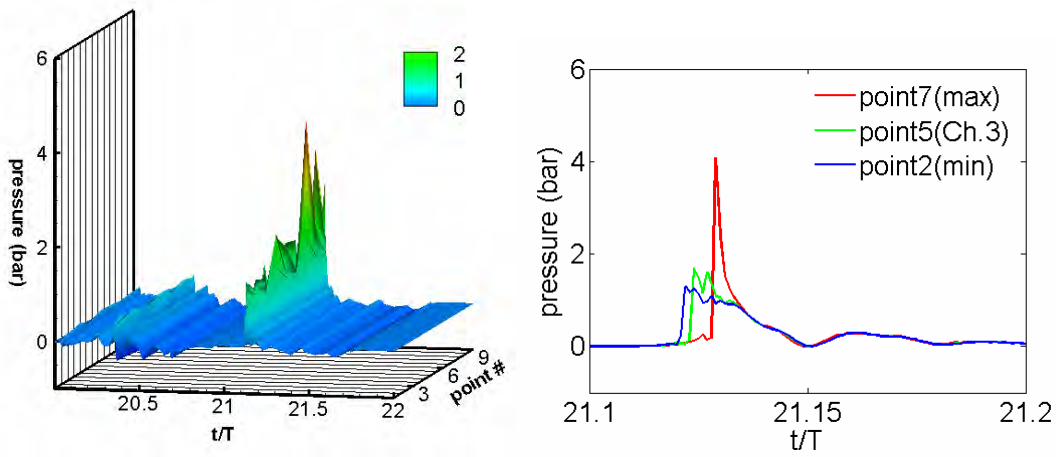

Figure 5.48 Impact pressures, the vicinity of Ch. 3, Case 6

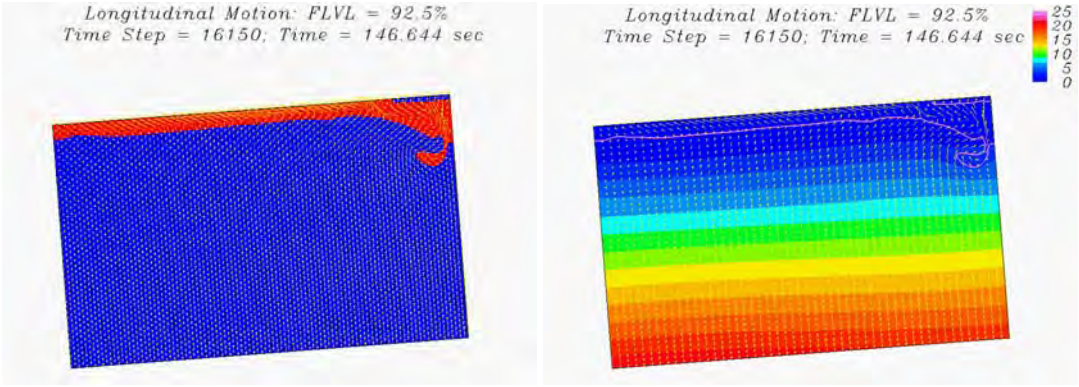

(a) Phase B: t/T = 16.15

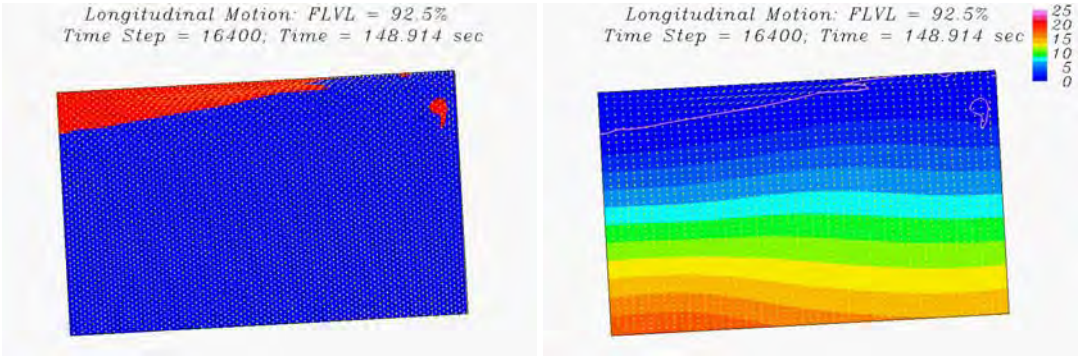

(b) Phase C: t/T = 16.40

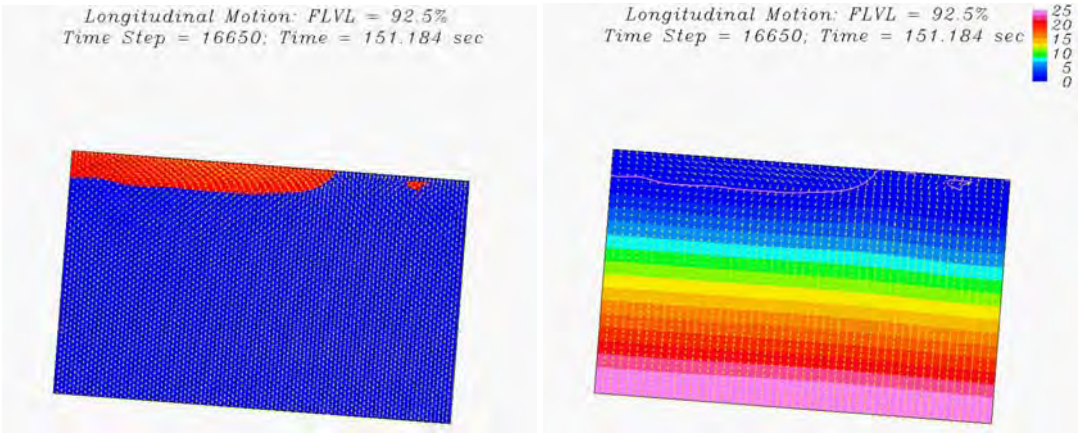

(c) Phase D: t/T = 16.65

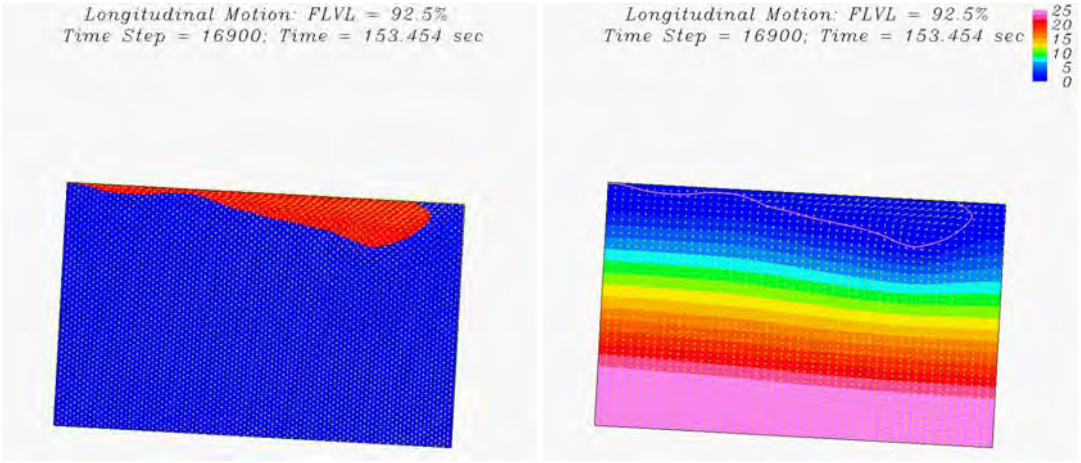

(d) Phase E: t/T = 16.90

Figure 5.49 2D free surface and pressure contours, Case 6

Figure 5.49 shows the predicted two-dimensional velocity field and pressure contours in the LNG tank at five different time instants t/T = 16.10, 16.15, 16.40, 16.65, and 16.90. The corresponding free surface patterns and wall pressure contours for the three-dimensional case are shown in Figure 5.50 to facilitate a detailed understanding of the three-dimensional effects. For clarity, the five times are denoted by Phases A, B, C, D and E in the motion trajectory plots shown earlier in Figure 5.44. These five time phases were chosen based on the 3D impact pressure history in Figure 5.47(b) which shows that the maximum impact occurs between Phases A and B.

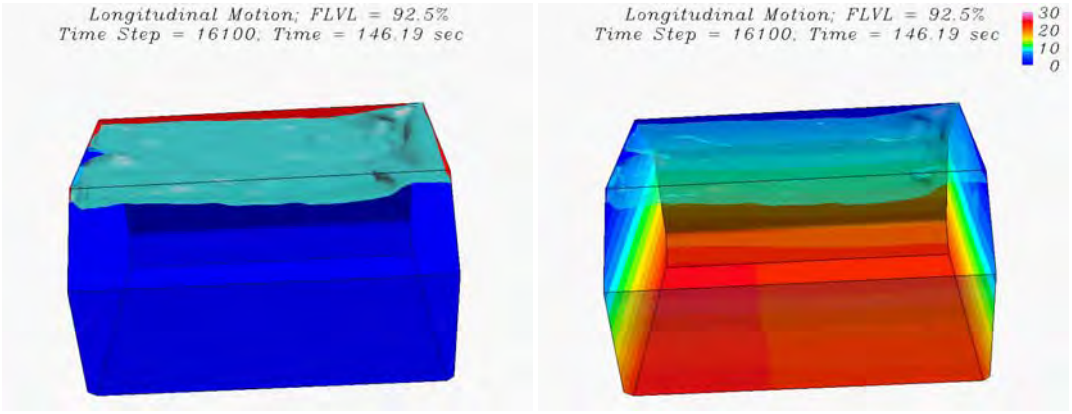

(a) Phase A: t/T = 16.10

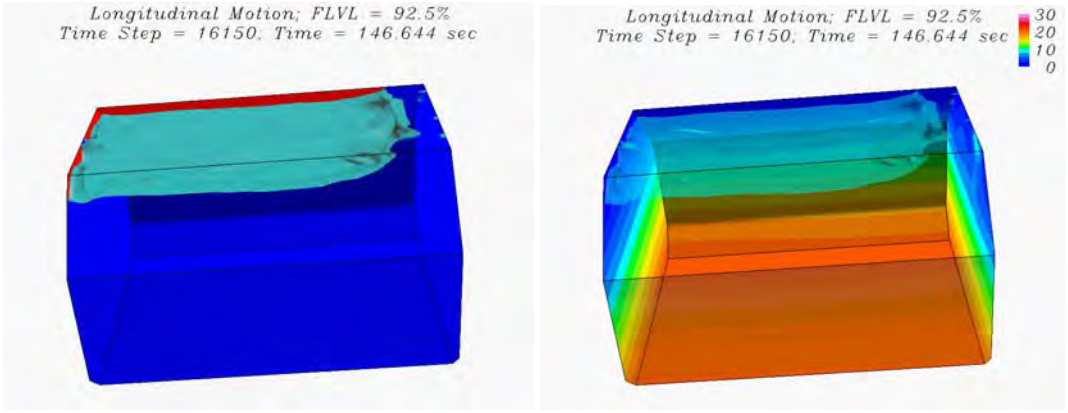

(b) Phase B: t/T = 16.15

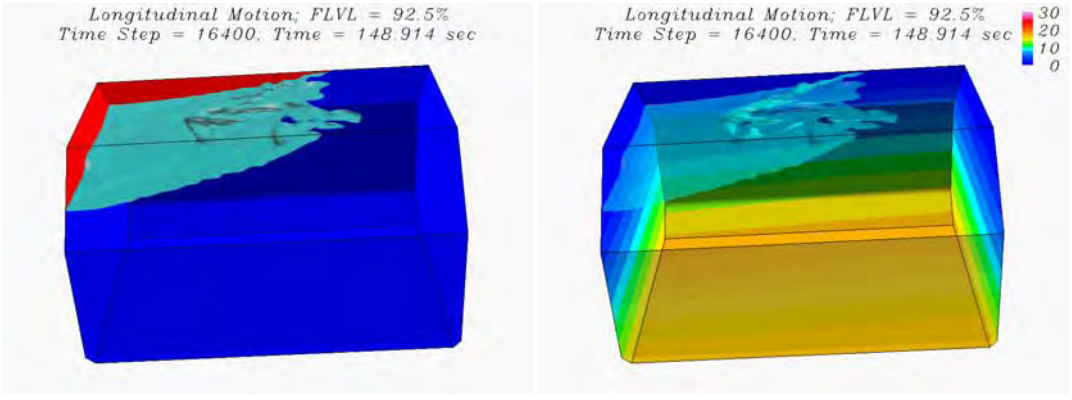

(c) Phase C: t/T = 16.40

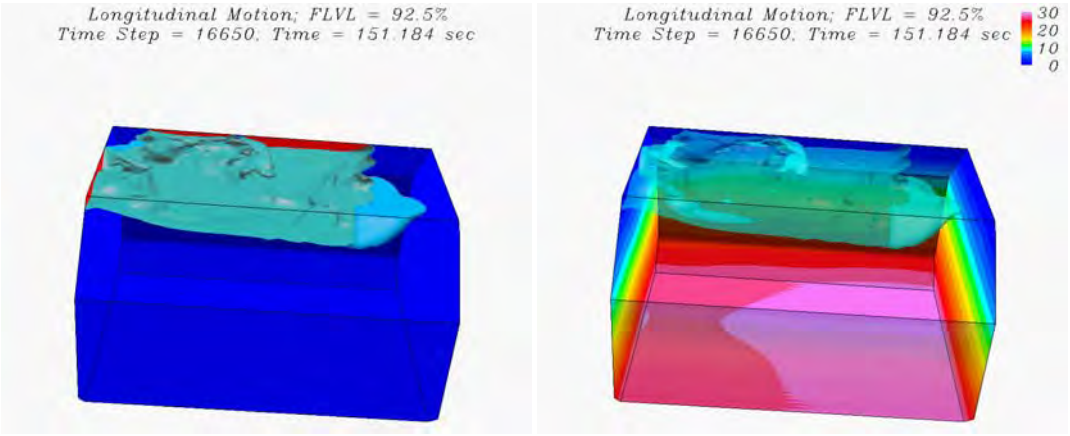

(d) Phase D: t/T = 16.65

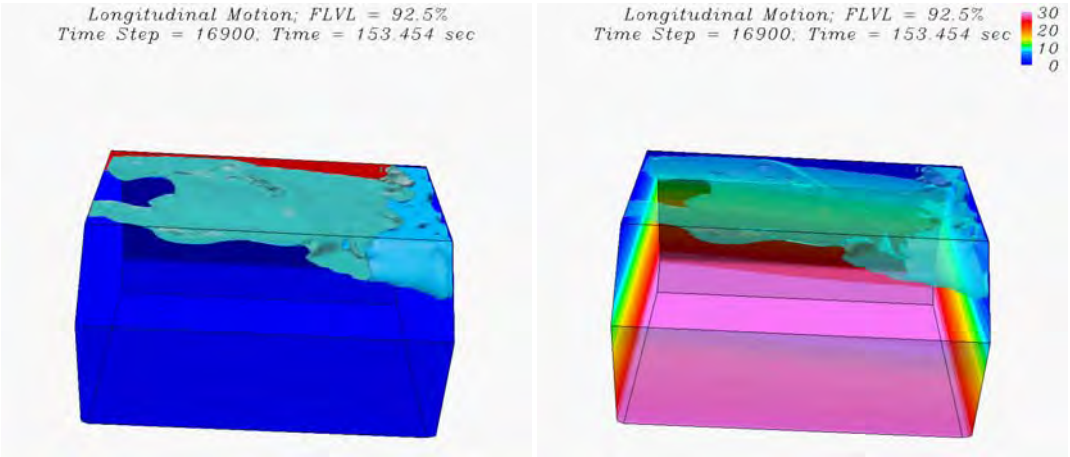

(e) Phase E: t/T = 16.90

Figure 5.50 3D free surface and pressure contours, Case 6

It is noted that the 2D and 3D flow patterns are very different at Phases A and E because the rectangular grid used in the 2D simulation cannot account for the changing cross sectional area in the upper chamfer. It is also observed that the free surface motion for Case 6 is much less violent in comparison with the motions observed earlier for lower filling level Cases 1-4 since the ullage space is confined to a small region in the upper chamfer. During this selected period, the maximum impact pressure at Ch.3 occurs at t/T = 16.128 between Phases A and B. At Phase A (t/T = 16.10), the free

surface level near Ch.3 is slightly below the tank top. The combined translational and rotational motion produces a rapid rise of the water level below Ch.3 (pressure sensor S12) and a sharp impact on the tank top wall between Phases A and B. It is also worthwhile to note that the pressure is relatively low at t/T = 16.40 since the hydrodynamic pressure due to fluid momentum acts in the opposite direction of gravity when the tank is near the top-right position. On the other hand, the wall pressure reaches maximum due to the combined hydrodynamics and hydrostatic pressure forces at t/T=16.90 when the LNG tank reaches the lower-left position and begins to ascend to the equilibrium position.

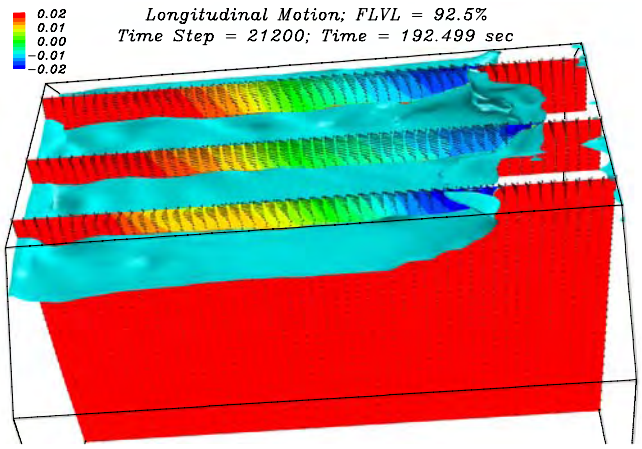

Figure 5.51 Pressure and velocity in the ullage space

In the present level-set Navier-Stokes method, both the water and air flows were solved simultaneously using a two-phase flow approach. In a single-phase model, the air pressure in the ullage space is assumed to be constant and equal to the atmospheric pressure. In the present two-phase flow simulation, however, the aerodynamic pressure in the narrow ullage space is strongly affected by the motion of the sloshing water flow. It is clearly seen from Figure 5.51 that the air velocity is much larger than the water velocity since the air is much lighter than water. The sloshing water was found to induce strong air motion which results in negative aerodynamic pressures in the ullage space. It

is also interesting to note that some of the air bubbles were trapped near the tank corner for this high filling level case. However, the air cushioning effects of the trapped air cannot be properly accounted for in the present two-phase flow simulation since the air is assumed to be incompressible. In future studies it is desirable to include the effect of ullage gas compressibility in order to determine the gas cushioning effects on the sloshing impact load of full scale LNG carriers.

5.6 Conclusions

In the present study, violent sloshing flows induced by the transverse and longitudinal motions of a membrane-type LNG tank were simulated using the level-set Navier-Stokes method. The effects of turbulence were modeled using the Smagorinsky subgrid scale model in a Large Eddy Simulation (LES) approach. Both the water and air flows were solved simultaneously in the present two-phase flow approach to resolve the strong air-water interactions in the ullage space of the LNG tank.

The predicted impact pressures for both the transverse and longitudinal motion cases are in reasonably good agreement with the corresponding experimental data although the peak pressures are somewhat under-predicted. For the 92.5% high filling level case, the free surface motion is less violent in the confined ullage space with lower impact pressures. Small negative pressures were observed for the 92.5% high filling case which can be attributed to the air trapping and strong air-water interactions in the narrow ullage space.

Three-dimensional instability of sloshing flow was observed for both the transverse and longitudinal motion cases and confirmed by the experiments even though the tank excitation forces are strictly two-dimensional.

6 GREEN WATER SIMULATIONS

6.1 Introduction

The interaction between extreme waves and floating structures is of primary concern in the design of offshore structures. Most of the earlier works employed potential flow theory without considering the viscous effects. In the past several years, however, the viscous-flow methods have been used by, among others, Park et al. (2001), and Chen et al. (2001, 2002) for the study of fully nonlinear free surface flow around coastal and offshore structures. In order to provide accurate resolution of viscous, nonlinear free surface flow around offshore structures, it is necessary to employ more sophisticated numerical methods and turbulence models capable of dealing with complex three-dimensional flow separation and fully nonlinear free surface waves.

In the wave runup simulations, we used the interface-tracking method in conjunction with a chimera Reynolds-Averaged Navier-Stokes (RANS) method for time-domain simulation of nonlinear waves around the platform. For the interface-tracking method, it is convenient to use separate body-fitted numerical grids for the structures and the ambient wave field. In the present chimera domain decomposition approach, the numerical grids around the platform remained fixed while the free surface grids are adjusted every time step to conform to the exact free surface. Since the submerged portion of the structures change continuously at different time instants, the interpolation between different chimera grid blocks were updated every time step to enforce conservation of mass and momentum across block boundaries over the entire simulation. In addition, an effective damping beach approach proposed by Chen and Huang (2004) was implemented on the wave maker boundary to prevent the reflected waves from reaching the wave maker boundary. This enabled us to perform long-duration simulations without significantly increase the size of the computational domain. In the present study, the chimera RANS method of Chen et al. (2000, 2001, 2002) was

generalized for time-domain simulation of fully nonlinear wave runup around the two-dimensional platform.

The level set method was incorporated into the chimera RANS method for the prediction of green water on offshore platforms. The governing equations were formulated in a curvilinear coordinate system and discretized using the finite-analytic method of Chen et al. (1990) on a non-staggered grid. For the additional level set equations of evolution and re-initialization, we used the 3rd-order TVD (total variation diminishing) Runge-Kutta scheme (Yu et al, 2003b) for time derivatives, and the 3rd-order ENO (essentially non-oscillatory) scheme for spatial derivatives. The final results clearly demonstrate that the level set method is capable of simulating violent free surface flows encountered in the green water simulations.

6.2 Wave Runup on 2D Platform

Ryu and Chang (2004) performed detailed velocity measurements in a laboratory flume at Texas A&M University for wave runup on a two-dimensional fixed rectangular structure based on the dimensions of a typical tension leg platform (TLP). The length and height of the model platform are 0.15 m and 0.31 m, respectively. The still water level is 0.105 m below the platform deck. Velocity fields in the vicinity of the structure were measured using the particle image velocimetry (PIV) technique for 8 phases per each wave period. Both instantaneous and phase-averaged quantities were obtained and analyzed. These PIV data provide an excellent database for the validation of the present numerical method.

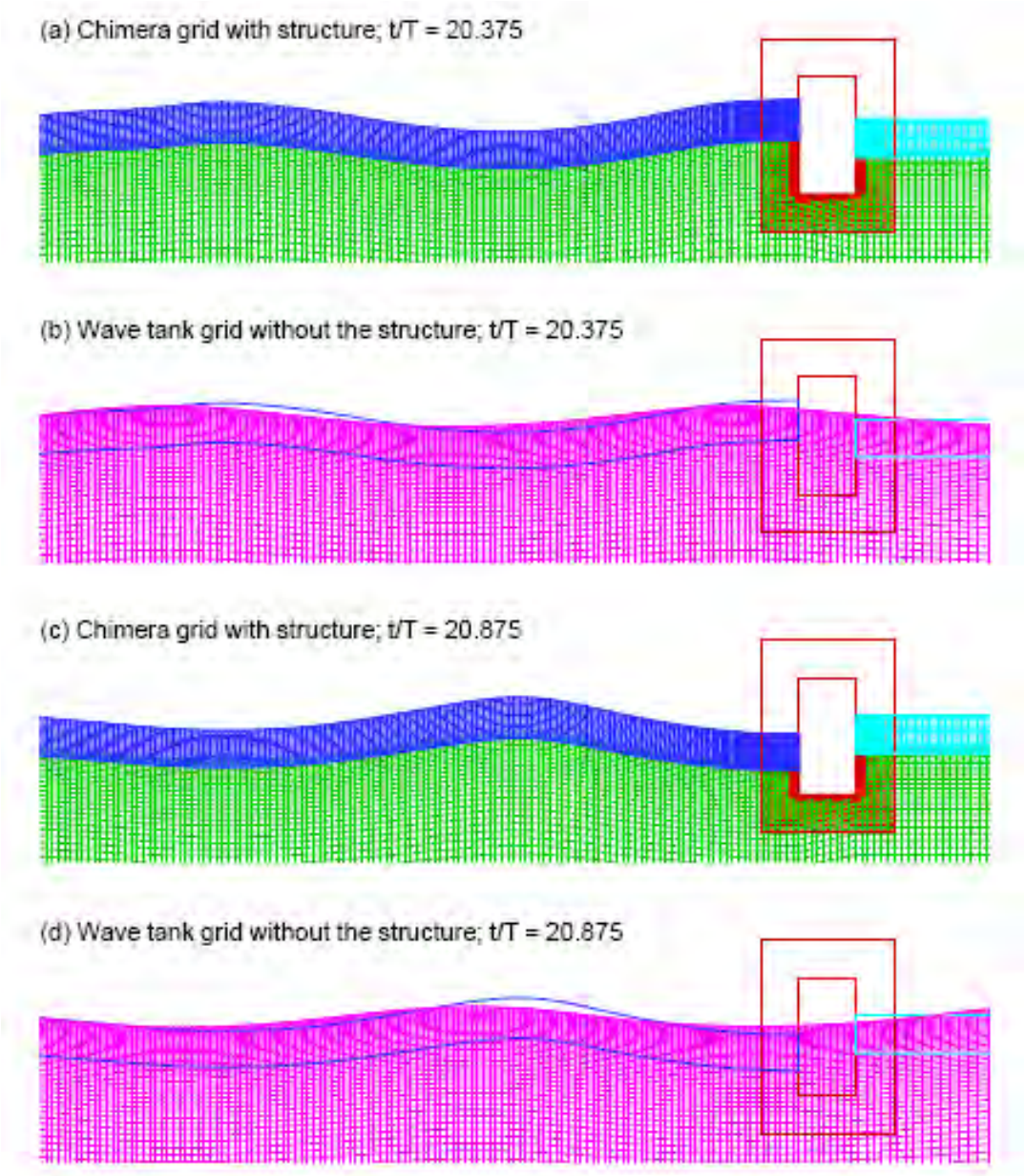

Figure 6.1 Chimera grid for wave runup simulation

In the present chimera domain decomposition approach for platform wave runup simulation, the solution domain is divided into several computational blocks as shown in Figure 6.1 to provide appropriate resolution of the platform boundary layers and wakes, as well as the nonlinear free surface waves. Figure 6.1(a) and 6.1(c) show the chimera

grid block structures around the platform at t/T = 20.375 and 20.875, respectively. For completeness, the wave tank grids at the same time instants are also shown in Figure 6.1(b) and 6.1(d). These wave tank grids are not linked to the other grid blocks and are used solely for the implementation of the absorbing beach in front of the wave maker. For long-duration simulations over many wave periods, it is well known that the wave reflected by the platform will propagate back to the wave maker boundary and interfere with the incident wave field. In the present study, a new absorbing beach approach developed recently by Chen and Huang (2004) has been implemented to prevent the reflected wave from returning to the wave maker. In this absorbing beach approach, the wave tank grids shown in Figure 6.1(b) and 6.1(d) were used to allow concurrent computation of the incident wave field without the presence of the offshore structure. This enables us to determine the exact pattern of the reflected wave since both wave fields with and without the structure were computed simultaneously at every time step. A damping function was then used to absorb the reflected waves so that the time-domain simulation can be continued for many wave periods without wave reflection from the wave maker.

In the present wave runup simulations, the incident wave field was generated using the higher order nonlinear wave theory of Cokelet (1977). The free surface grid blocks are updated at every time step to follow the instantaneous free surface wave elevation. Furthermore, the nonlinear dynamic free surface boundary condition is imposed on the exact free surface for accurate prediction of the fully nonlinear wave field. It should also be noted that the platform grid covers the entire platform surface including the dry deck area. Moreover, the platform grid remains fixed during the entire simulation even though the submerged section changes with instantaneous wave elevation. This not only simplifies the grid-generation process, but it also eliminates undesirable grid distortion which typically occurs in the simulation of large amplitude wave motions.

Simulations were performed for wave runup on the two-dimensional platform used in the experimental study of Ryu and Chang (2004) with an incident wave height of H = 0.0575 m. Figure 6.2 shows the computed free surface wave elevation and pressure contours at t/T = 20.375, 20.625, and 20.875, respectively, for the H = 0.0575 m case. The superposition and cancellation of the incident and reflected waves at different time instants can be clearly seen from this figure. The present simulation results also clearly demonstrate the effectiveness of the new absorbing beach approach as the simulation was continued for more than 20 wave periods without any distortion of the incident wave field.

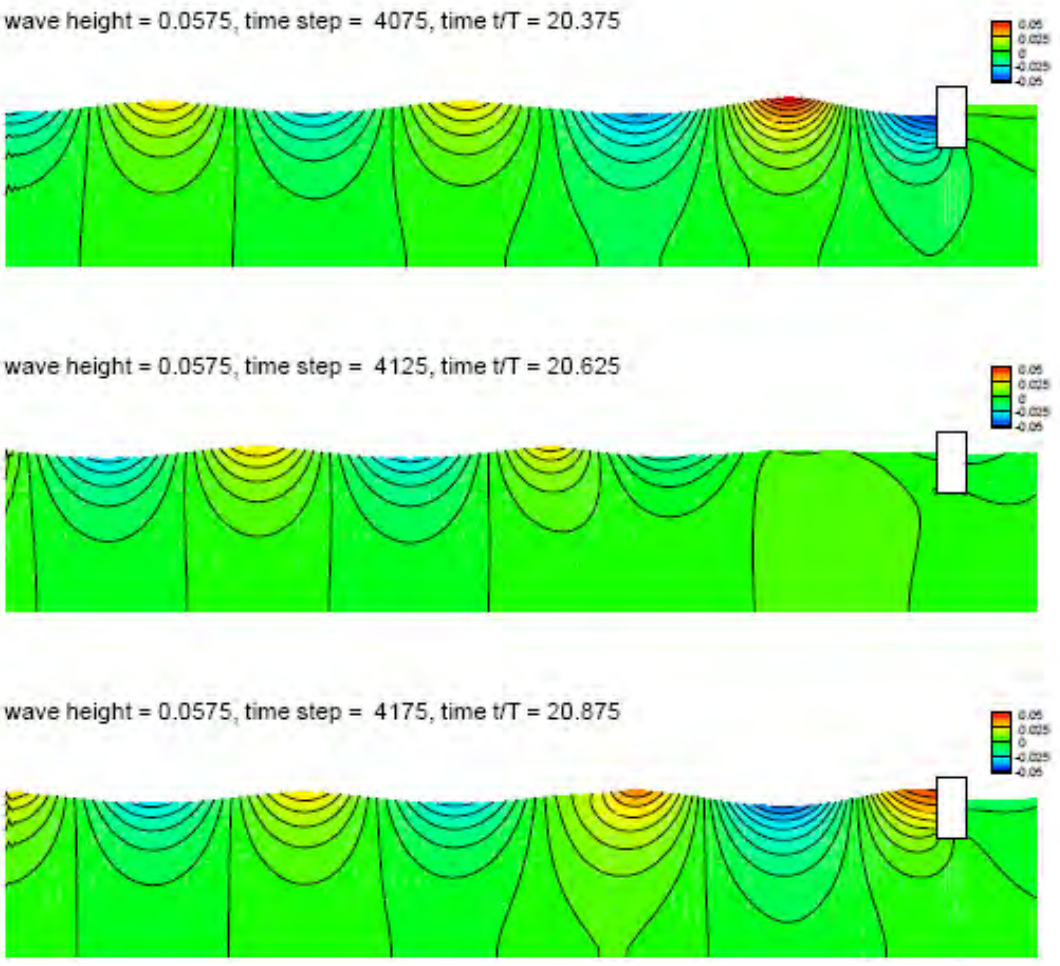

Figure 6.2 Wave elevation and pressure contours

Figure 6.3 shows the time history of the wave elevation in front of the structure. It is seen that the first wave reaches the structure after three wave periods since the wave maker is located about three wavelengths upstream of the model platform. Note that the relatively large waves occurred around the 12th-13th wave periods followed by a transition period with significant fluctuation in wave height. The flow attained a nearly periodic pattern after about 20 wave periods. It is quite clear that the absorbing beach in front of the wave maker successfully absorbed all the waves reflected from the structure so that the same incident wave can be maintained for long duration simulation with a rather small solution domain.

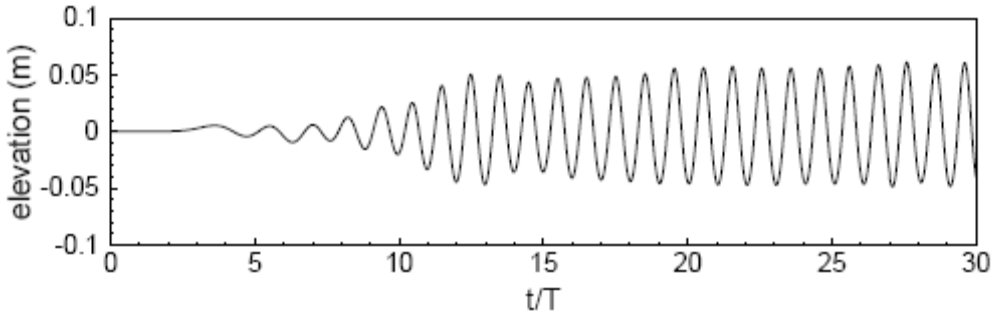

Figure 6.3 Time history of wave elevation

Figure 6.4 shows the predicted velocity vectors and the corresponding vorticity contours at t/T = 20.125, 20.375, 20.625 and 20.875, respectively. At t/T = 20.125, the wave-induced current is moving downward and produces a strong counterclockwise vortex on the platform bottom surface adjacent to the weather side corner. Another weaker counterclockwise vortex is also observed on the lee side. The wave reaches its lowest elevation and begins to move upward at around t/T = 20.375. At t/T = 20.625, the upward current velocity reaches a maximum value and a pair of clockwise vortices are induced around the sharp platform corners. The wave in front of the platform continue to move upward until the maximum runup is reached at t/T = 20.875. It is also worthwhile to note that the water elevation on the lee side of the platform changes only slightly since

the platform draft is relatively deep with negligible wave transmission. The predicted velocity vector plots are in very good agreement with the corresponding PIV measurement of Ryu and Chang (2004) at the same phases.

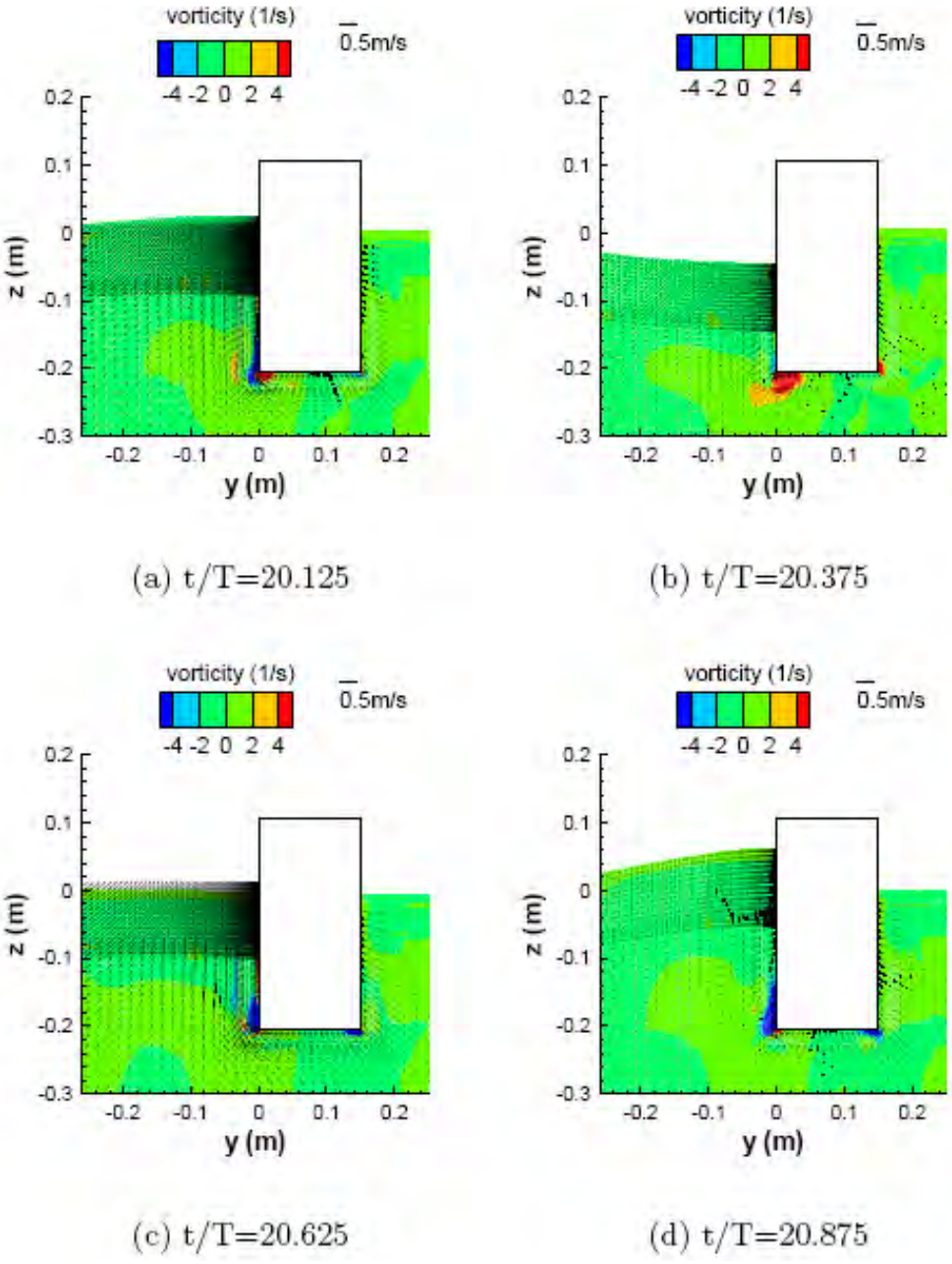

Figure 6.4 Velocity vectors and vorticity around the platform

After successful validation of the chimera RANS method for two-dimensional platform configurations, the method was further generalized for time-domain simulation of wave runup around single and multiple vertical cylinders which are common structural elements of TLPs and other types of offshore structures. Figure 6.5 shows the numerical grids around three vertical cylinders. In the chimera domain decomposition approach, it is convenient to use an overset grid system with body-fitted cylindrical grids embedded in the background rectangular grids. For the fully nonlinear waves considered here, the numerical grids are updated every time step to conform with the exact free surface.

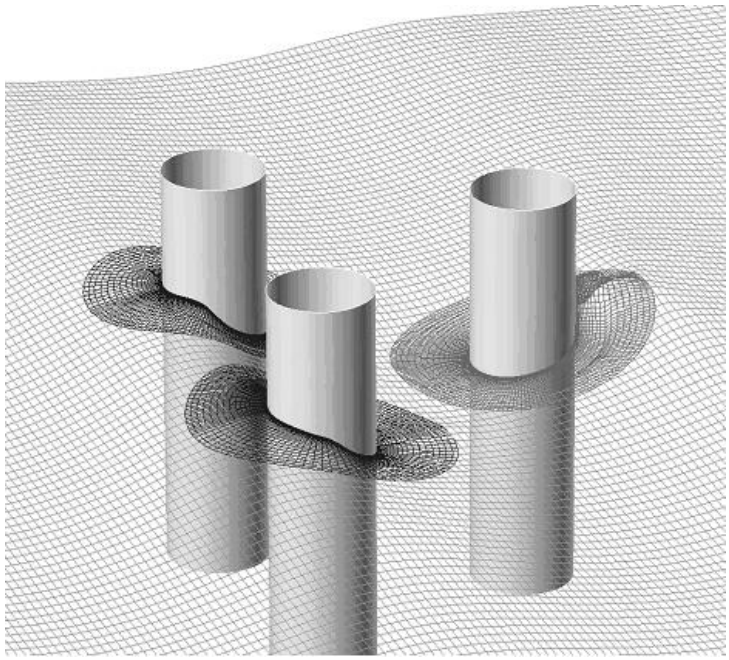

Figure 6.5 Chimera grids around vertical cylinders

Time-domain simulations were also performed for wave diffraction around three vertical cylinders. The center-to-center spacing between the two front cylinders is 2.96 D, where D is the diameter of the cylinder. The third cylinder is placed at 2.56 D (center-to-center) downstream of the two front cylinders. Figure 6.6 shows the predicted wave

patterns at t/T = 0.55, 0.60, 0.64, 0.66, 0.68 and 0.70. The incident wavelength specified in the present simulation is L/D = 5.62 and the incident wave height is H/D = 0.30.

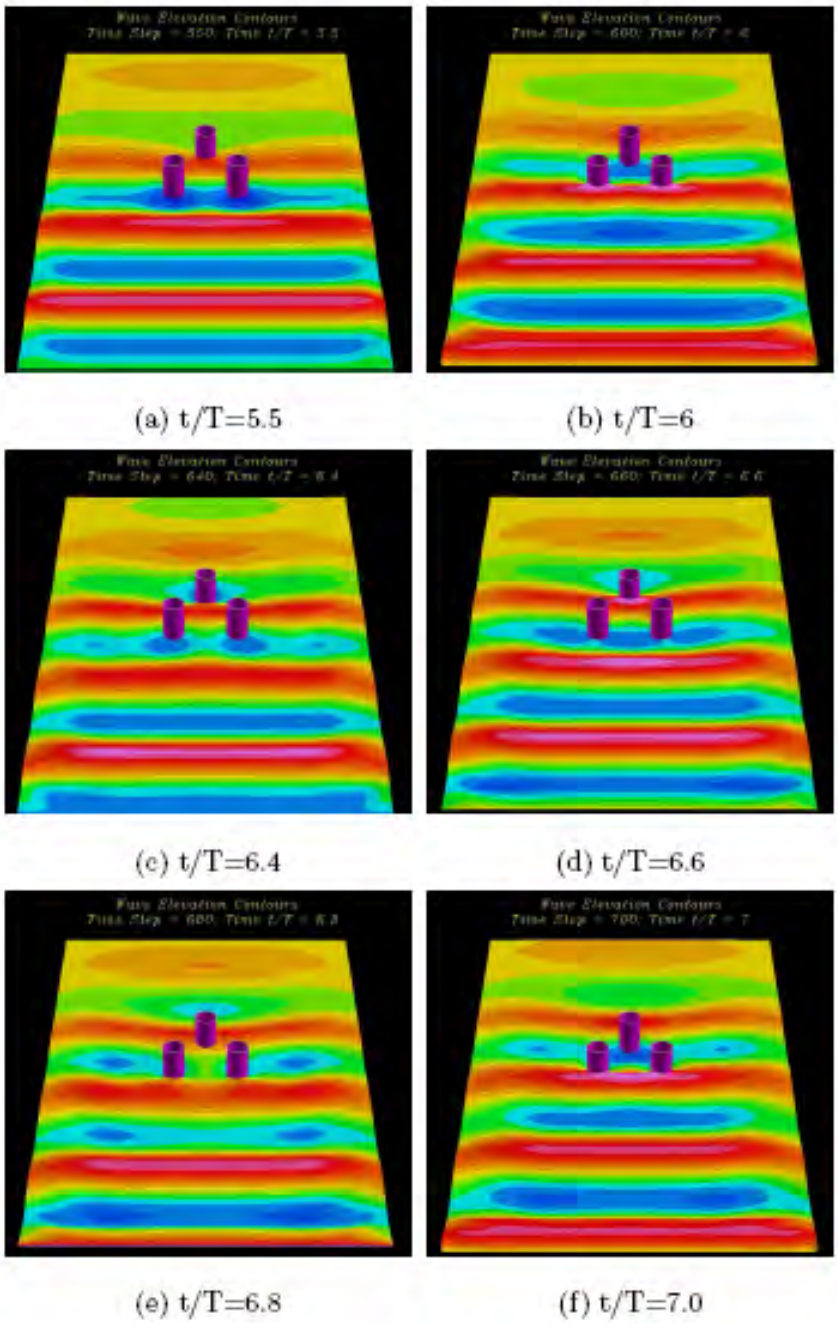

(a) t/T=5.5 (b) t/T=6

(c) t/T=6.4 (d) t/T=6.6

(e) t/T=6.8 (f) t/T=7.0

Figure 6.6 Free surface pressure contours around cylinders

The simulation results clearly indicate the presence of strong interactions between the two front cylinders in side-by-side arrangement. It is also seen that the wave runup on the downstream cylinder is almost completely out-of-phase in comparison with the front cylinders since the wavelength is about twice the cylinder spacing. Moreover, the wave diffraction pattern on the downstream cylinder is significantly different from that of the single cylinder case. This is clearly due to the strong interactions among the three vertical cylinders.

6.3 Green Water on 2D Platform

The experimental measurement of velocity fields in a plunging wave impacting on a platform was investigated recently by Ryu and Chang (2005). A new technology called bubble image velocimetry (BIV) was used to measure the velocity in the aerated region and the associated green water. The experiments were performed in a glass-walled wave tank which was described in detail in Ryu (2005). The water depth was kept constant at h = 0.8m. A flap type wave maker was installed at one end of the wave tank and a sloping beach was at the other end in order to absorb the wave energy and reduce reflection. The platform was located at 21.7m from the wave maker. A plunging breaker was generated by the wave focusing method. The wave train consisted of waves with various frequencies ranging from 0.7Hz to 1.3Hz. With the superposition of different wave frequencies and some trial and error, a plunging breaker was made to break at a desired location right in front of the structure. More details can be found in Ryu (2005). Figure 6.7 shows the sketch of the model structure, coordinate system and experimental field of view (FOV). The small window in the numerical grid is the area to be compared with the FOV1 in the experimental setup.

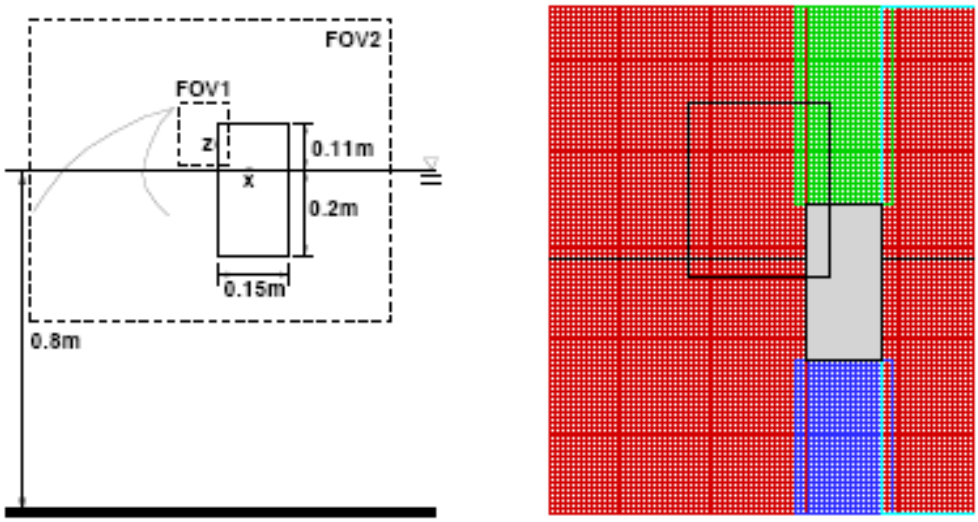

Figure 6.7 The model structure and numerical grids

Because of its high degree of nonlinearity, the plunging breaker is difficult to generate in the numerical wave tank. Longuet-Higgins and Cokelet (1976) performed the first numerical simulation of a breaking wave using the boundary integral method. Chen, Zaleski and Li (1999) described plunging breakers by solving the classical, incompressible, two-dimensional Navier-Stokes equation. They presented a plunging breaker which was developed from the initial condition based on the third order Stokes wave. The instability of this steep Stokes wave led to wave breaking. A similar initial wave is used in this study. The initial wave profile is as follows:

$$\eta(y, t=0) = \frac{1}{2\pi}\left[\varepsilon\cos(2\pi y) + \frac{1}{2}\varepsilon^2\cos(4\pi y) + \frac{3}{8}\varepsilon^3\cos(6\pi y)\right] \qquad (6.1)$$

Here, η is the wave elevation, ε $(=2\pi a/L)$ is the wave steepness, and y denotes the horizontal coordinate.

Figure 6.8 shows the snapshots of a plunging breaker in a numerical wave tank. The tank is $3\text{m}\times 2\text{m}$ with a 301×201 uniform grid. The characteristic length is set to 1m and the Froude number is set to 1. The Reynolds number is 3.17×10^6. The

simulation is performed with wave steepness $\varepsilon = 0.7$, wave length $\lambda = 1.5\text{m}$, and time step $\Delta t = 0.006$ sec. The wave steepness is much higher than $\pi/7$, the limiting steepness threshold indicated by the nonlinear Stokes wave theory.

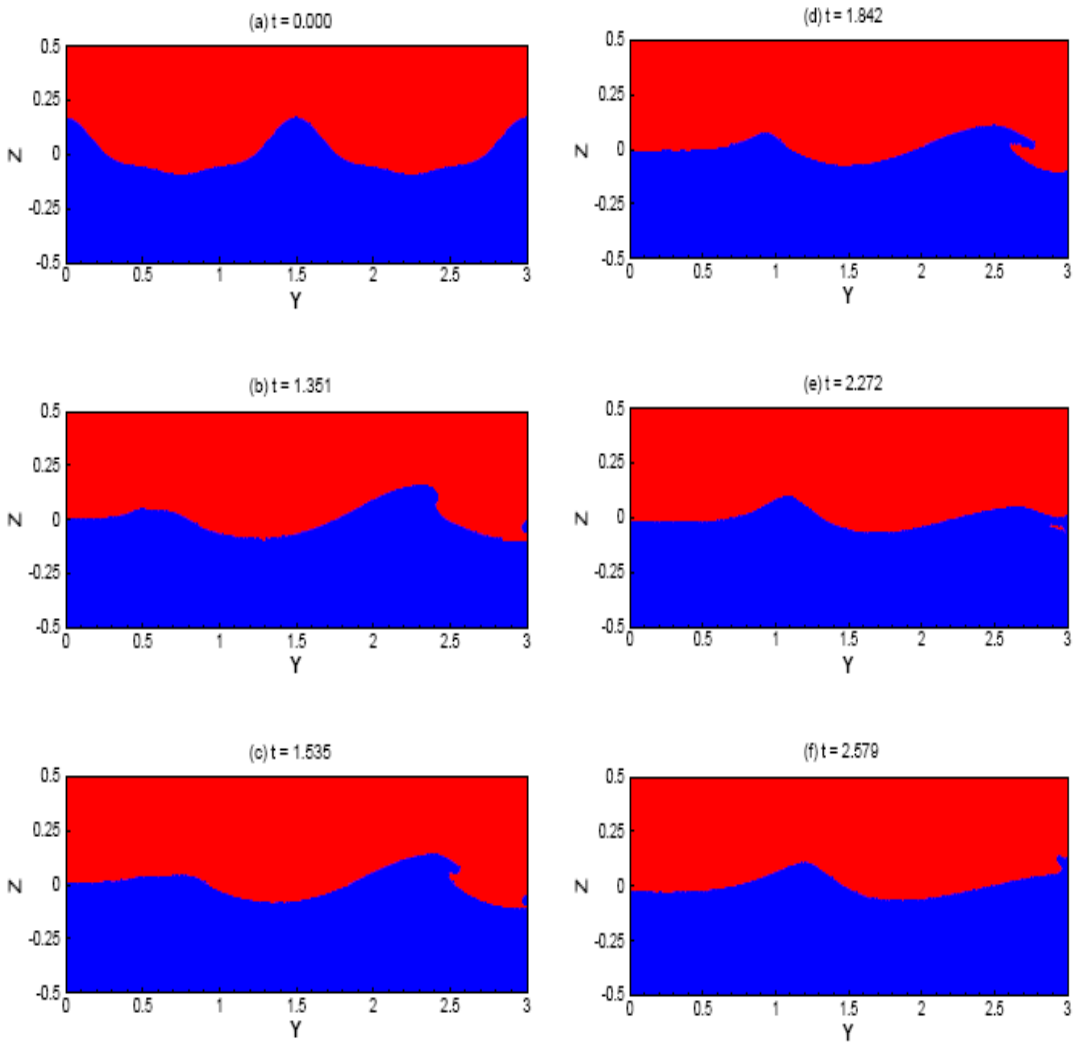

Figure 6.8 Snapshots of a plunging breaker

Chen et al. (1999) used a lower wave steepness, $\varepsilon = 0.55$, to generate plunging breakers. This steepness is too large to be generated in laboratory. We will reduce this value in the future by introducing the particle level set method, which is a hybrid method

of MAC and level set. Enright et al. (2002) discussed this method in detail. At t = 0, the initial wave has its crest at y = 1.5 and it moves from left to right. The solid wall boundary conditions are imposed on the left and right sides of tank. The velocity extrapolation boundary condition is applied at the air-water interface, i.e. $\vec{V} \cdot \nabla \phi = 0$. As the wave propagates toward the right, the crest of the wave becomes more and more asymmetric. The quick movement of the crest results in a jet curling over part of the wave trough. The jet becomes stronger along the wave propagation and eventually impinges on the right side wall. Meanwhile, air is entrapped in a big pocket. After the impingement, the jet is split into two parts. One part is splashing up and the other one is pushed to move downward. The downward flow produces a big vortex under the free surface near the wall. This vortex also appears in two-dimensional green water simulations.

After the plunging breaker is generated in the numerical wave tank, the green water simulation is performed under the same conditions by placing a platform in the middle of the wave tank. The platform is surrounded by four rectangular grids which are also shown in Figure 6.7. The horizontal black line is the initial still water level. The black frame corresponds to FOV1 in the experiment. The platform size used in the numerical simulation is identical to that of the model structure in the experiment. The initial wave is generated with a 1.5m wavelength and wave steepness of 0.7. This highly nonlinear wave breaks right in front of the structure. The horizontal position of the structure was adjusted to obtain good agreement with the measured results.

Figure 6.9 shows the comparison of the predicted and measured free surface patterns and velocity vectors at three different phases. The simulated wave breaks right in front of the structure. The first side-by-side comparison of images represents the moment when the jet front hits the leading edge of the structure. There is a big bubble entrapped by the plunging breaker which is shown in both the numerical and experimental results. After the jet impinges on the platform, the wave momentum splits the water into two parts. Some water splashes upward with strong vertical velocity on

the front face of the platform. There is also some water which moves downward along the face of the structure. This creates a vortex at around $z = 0$.

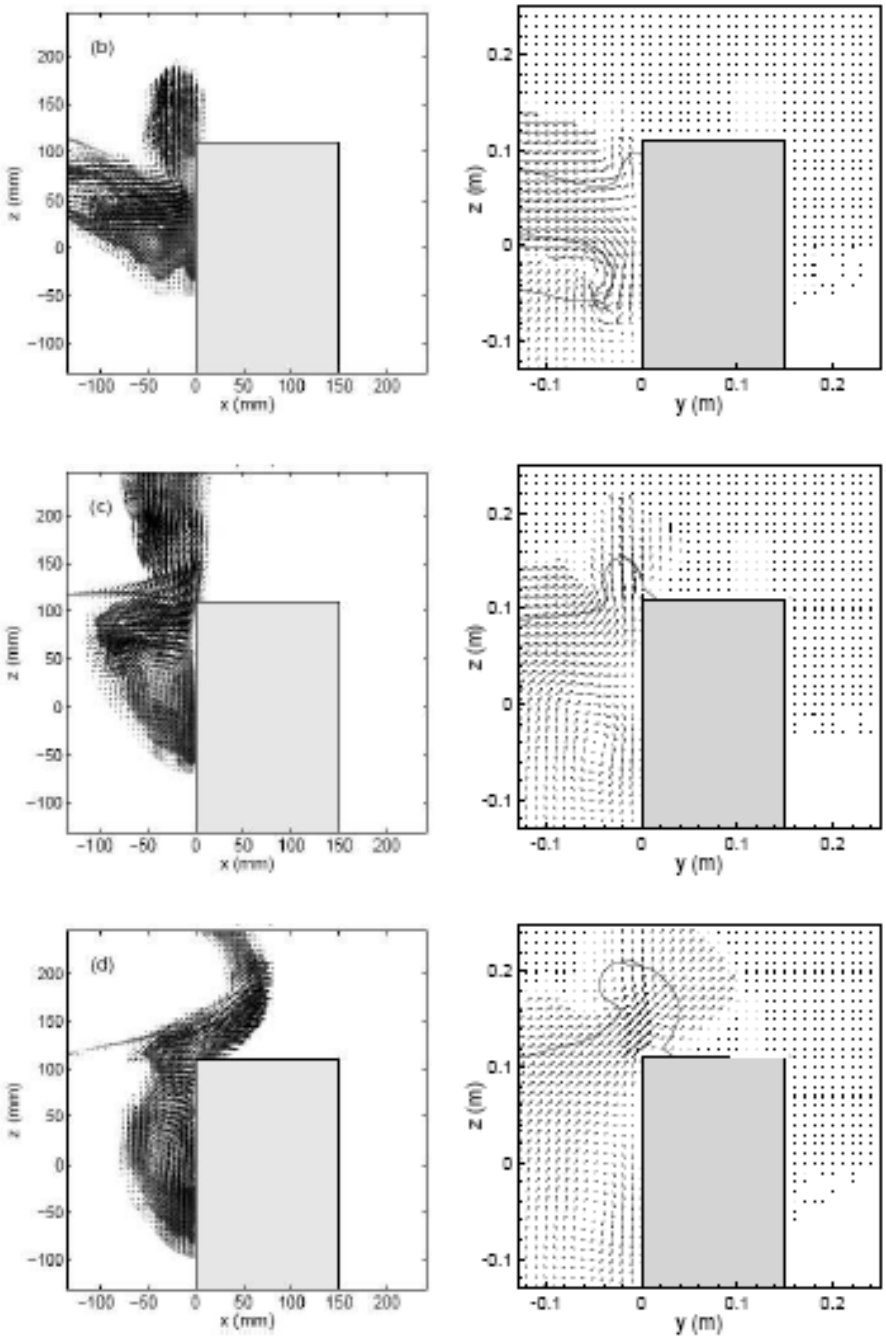

Figure 6.9 Comparison of green water effect on 2D platform

In Figure 6.9, the second comparison at a later instant indicates the vortex clearly. The vortex position is a little lower in the numerical simulation than that in the experimental measurement. After a certain duration, the wave front is pushed continuously upward onto the deck by the wave momentum. The overtopping wave rushes across the platform deck with the potential to produce a large green water load on any exposed structures. The third comparison clearly shows that the predicted free surface patterns and flow directions are in close agreement with the corresponding measurements.

Another application of the level-set RANS method is the simulation of wave impact on the deck of a large platform as shown in Figure 6.10. The center of the platform is located at (4, 0.08), and the platform deck is 1.0 wide by 0.03 high. The incident wave height is 0.15 and the wave length is 2.0. It can be seen from Figure 6.10 that the wave is about to break before hitting the platform deck. In addition to the water overtopping on the platform deck, the wave crest is also seen to slam on the bottom of the platform at certain time instants. The wave slamming is expected to produce large uplift forces which may damage the platform deck structure. It is also clearly seen that the green water on top of the platform rushes through the deck and falls back into the ocean on the lee side of the platform.

The present simulation results clearly demonstrate the capability of the level set method in dealing with violent free surface motions including both the green water and wave slamming effects. In the next phase of research, the level set method will be generalized to provide accurate resolution of the air-water interface around three-dimensional offshore platforms. In addition, a more robust numerical wave maker will be implemented to enable the generation of highly nonlinear waves as observed in the present experimental investigations.

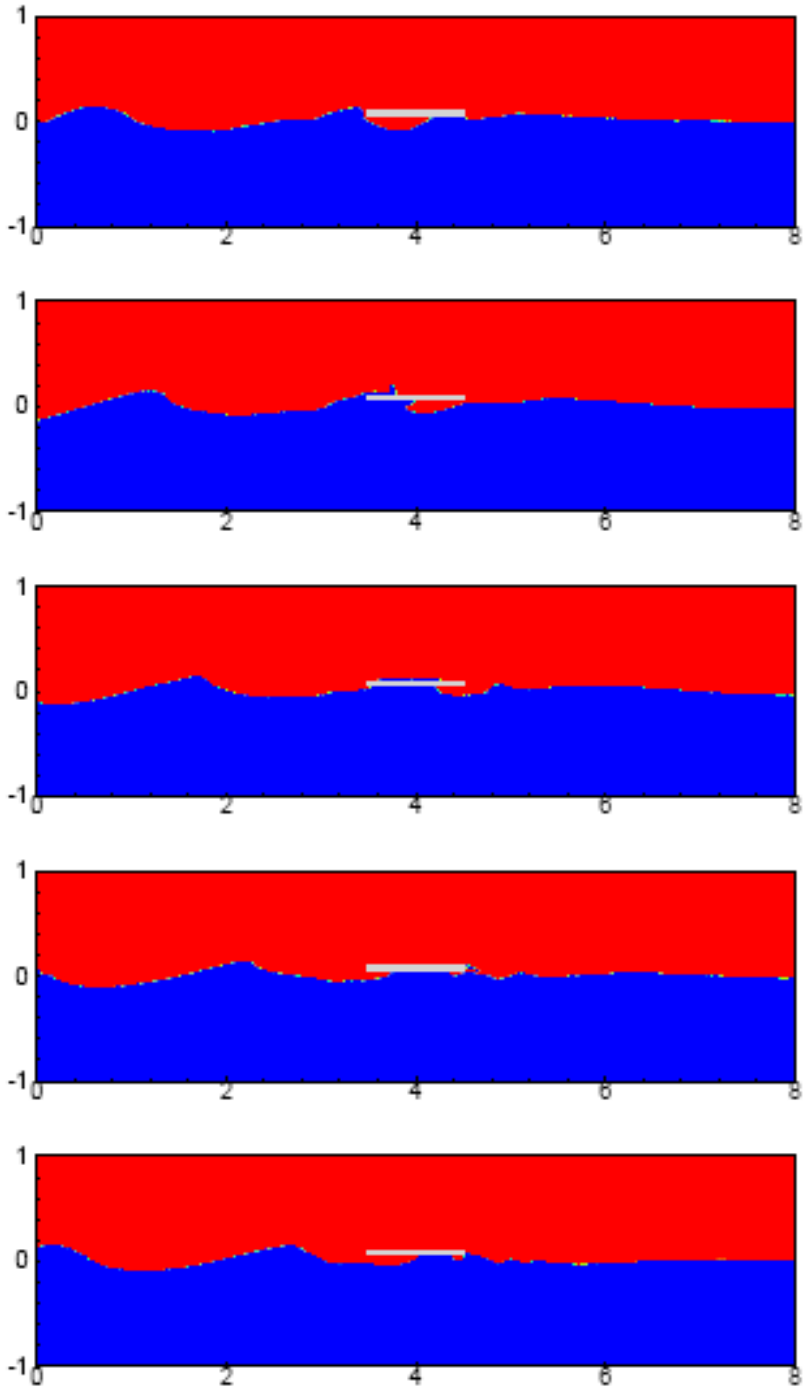

Figure 6.10 Green water around a platform deck

6.4 Green Water on 3D Platform

In addition to the two-dimensional green water simulation described above, numerical simulations were also performed for a rectangular platform to examine the edge effects around a 3D platform. The three-dimensional model test is scheduled for a later phase of the project. The following three-dimensional numerical results are a preliminary part of the project.

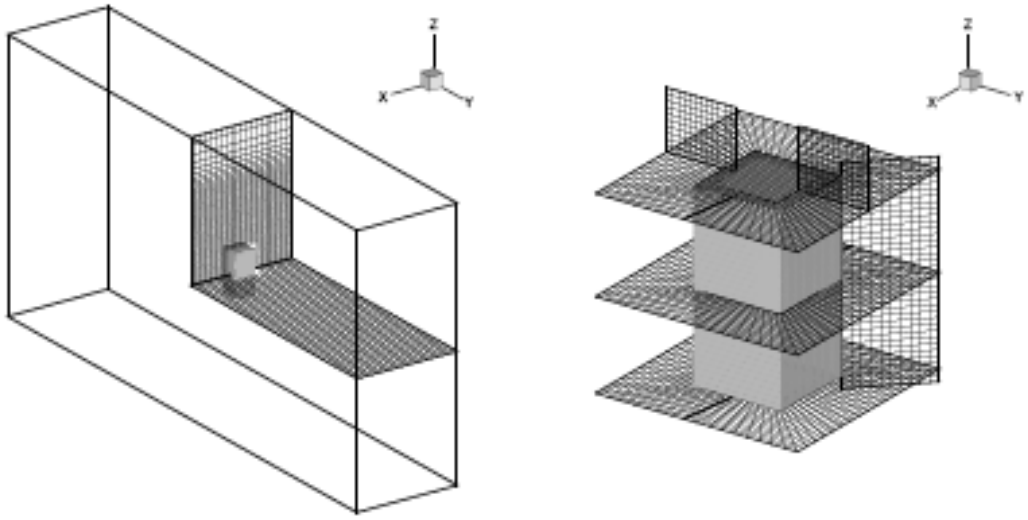

Figure 6.11 3D grid for green water simulation

Figure 6.11 shows the three-dimensional numerical grids for the 3D green water simulation. The grid consists of six computational blocks with a total of 916,057 grid points. The chimera domain decomposition technique is applied to generate appropriate grids. The structure is surrounded by five grids: two cubic grids on top and bottom and three cuboid grids with holes in middle. These near-field boundary-fitted grids are embedded in a Cartesian grid block representing the wave tank.

The tank size is $0.8\text{m} \times 4\text{m} \times 2\text{m}$. The size of the rectangular platform is $0.15\text{m} \times 0.15\text{m} \times 0.31\text{m}$, and the platform deck is located at 0.105m above the still

water level. The incident wave is generated by a flap type wave maker again using the higher order nonlinear wave theory of Cokelet (1977). The wave length is set to 1.0m and wave height is set to 0.2m, resulting in a wave steepness $\varepsilon = ka = 2\pi a / L = 0.628$. This guarantees that the incident wave will break in front of the structure. The wave period is 0.8 sec and the corresponding non-dimensional period is about 2.5. Note that the characteristic length is 1m and the Froude number is 1. The characteristic time $T = L/U = L/\sqrt{gL} \approx 0.32$ sec. The non-dimensional time step is set to 0.01. An absorption condition (numerical damping beach) is imposed at the right side of the tank to avoid wave reflections. This is implemented by the following damping function:

$$damp(y) = \left[\frac{1}{2} \left\{ 1 - \cos\left(\frac{\pi(y - s_1)}{s_2 - s_1} \right) \right\} \right]^3 \tag{6.2}$$

Figure 6.12 shows snapshots of a time series of wave impingement on a three-dimensional rectangular structure. The series shows time snapshots from 600 to 975 at e75 step intervals. Figure 6.12 also shows that the highly nonlinear incident wave evolves to break before it hits the structure. Surging breakers occur here instead of plunging breakers in the two-dimensional simulations. The surge front impinges on the front face of the platform and produces a strong upward splash. Some green water on the top is clearly shown in Figure 6.12(c) and (f). Near the platform edges, however, the incident wave is able to move around the platform with significantly less green water effect. After the front passes the structure, the wake flow is captured in Figure 6.12(d) and (e).

An experimental investigation will be conducted in the near future at Texas A&M University to provide detailed velocity measurements for the same platform configuration. The simulation results will be compared to the experimental data to provide a detailed validation of the present numerical method for the simulation of green water effects on three-dimensional offshore structures.

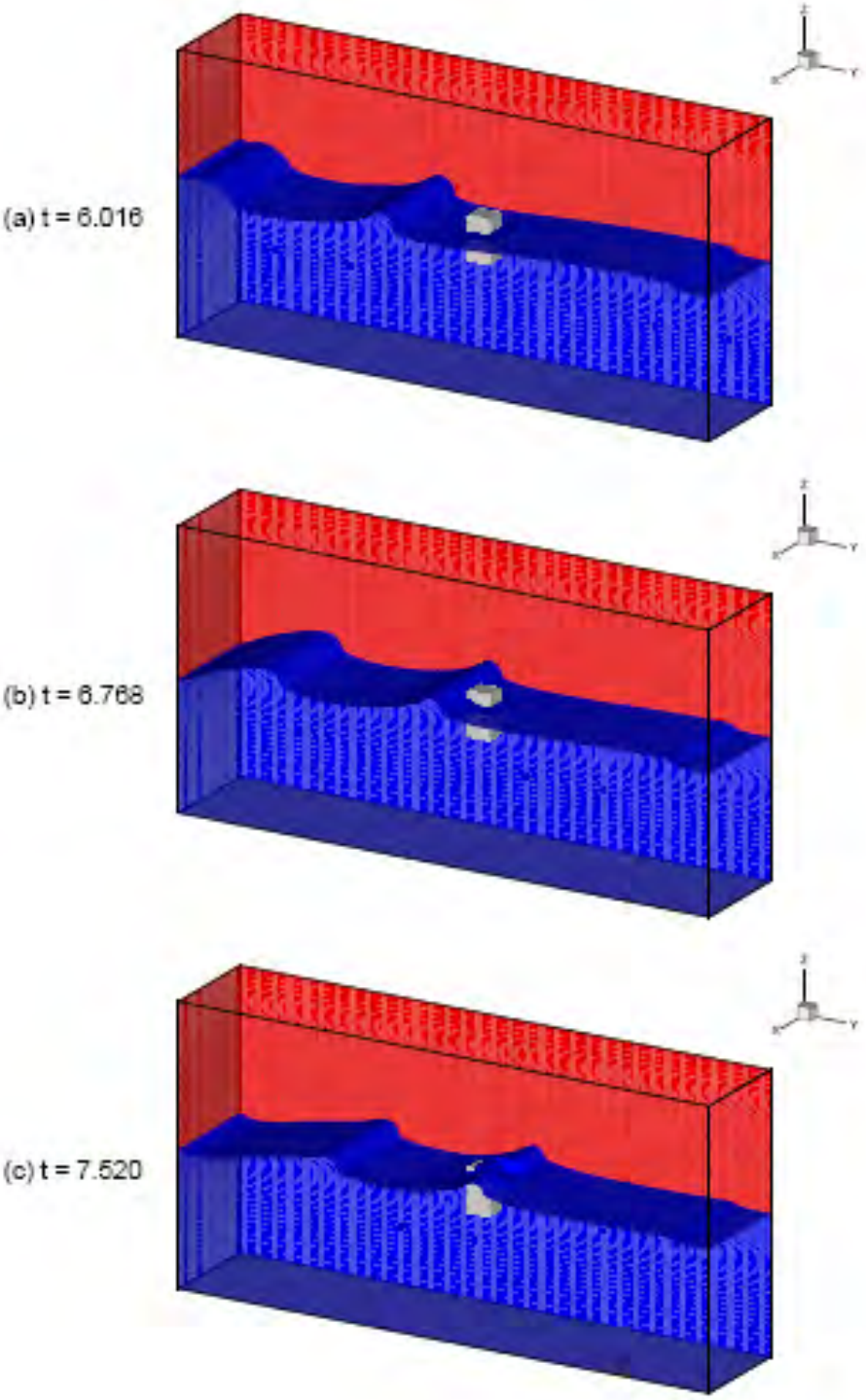
(a) t = 6.016
(b) t = 6.768
(c) t = 7.520

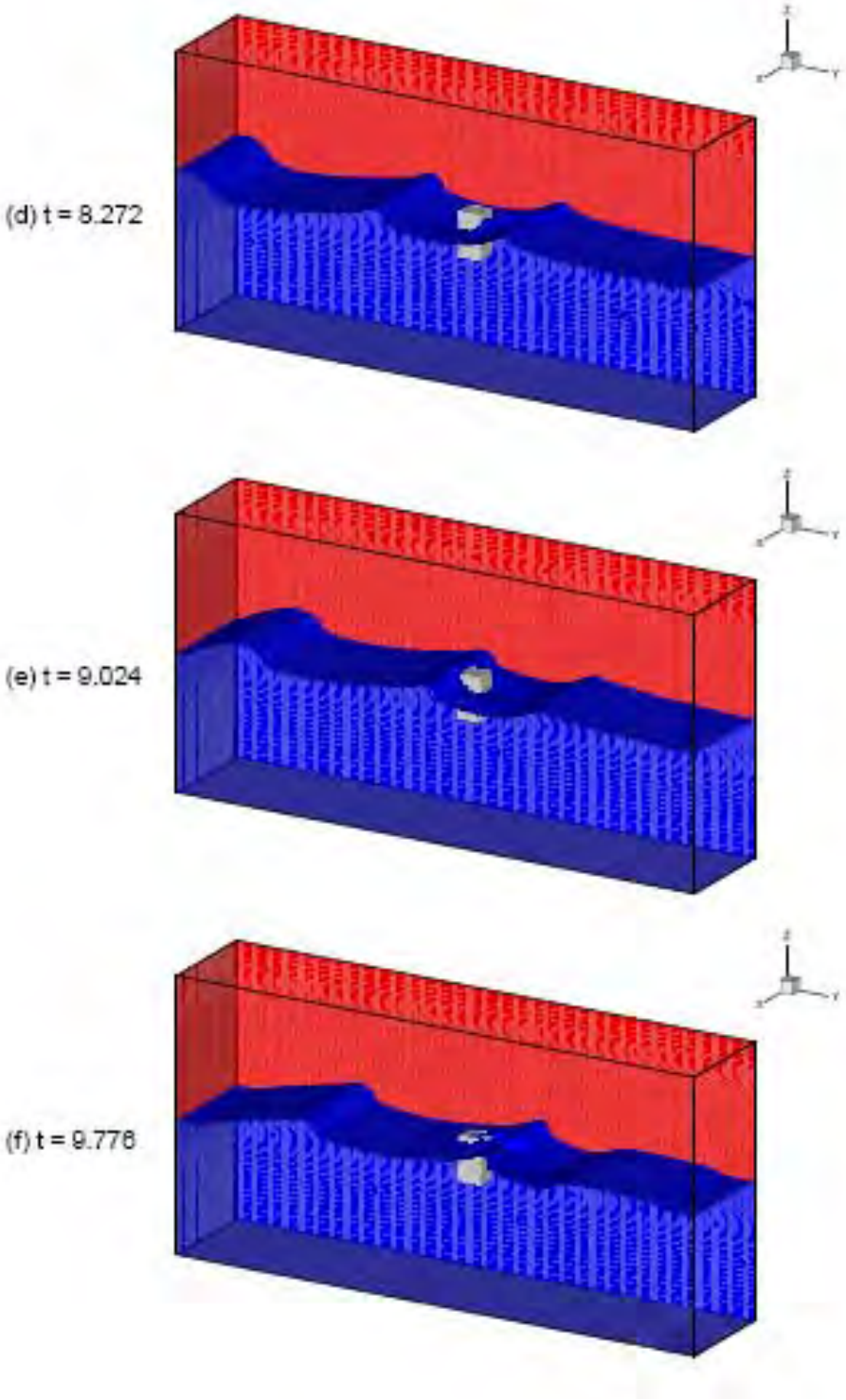

Figure 6.12 Green water on a 3D platform

7 CONCLUSIONS

7.1 Sloshing Simulations

In the present study, violent sloshing flows induced by the transverse and longitudinal motions of a membrane-type LNG tank were solved using the level-set Navier-Stokes method. The effects of turbulence were modeled using the Smagorinsky subgrid scale model in a Large Eddy Simulation (LES) approach. Both the water and air flows were solved simultaneously in the present two-phase flow approach to resolve the strong air-water interactions in the ullage space of the LNG tank. The predicted impact pressures for both the transverse and longitudinal motion cases are in reasonably good agreement with the corresponding experimental data although the peak pressures are somewhat under-predicted. For the 92.5% high filling level case, the free surface motion is less violent in the confined ullage space with lower impact pressures. Small negative pressures were observed for the 92.5% high filling case, which can be attributed to the air trapping and strong air-water interactions in the narrow ullage space. Even though the tank excitation forces are strictly two-dimensional, three-dimensional instability of sloshing flow was observed for both the transverse and longitudinal motion cases and confirmed by the experiments.

7.2 Green Water over Offshore Structure

Time-domain simulations of wave runup and green water around offshore structures were performed using a Reynolds-Averaged Navier-Stokes (RANS) numerical method in conjunction with a chimera domain decomposition approach. The wave runup simulations were performed using the interface-tracking method, while the green water on offshore platforms was simulated using the interface-capturing method based on the level set formulation. The simulation results for wave runup on a two-dimensional TLP configuration are in close agreement with the PIV measurements from

corresponding experiments. The interface-tracking method illustrates its capability for wave runup predictions including both the viscous and nonlinear wave effects.

In order to predict violent free surface flows, a Reynolds-Averaged Navier-Stokes (RANS) numerical method in conjunction with a level-set function is applied in time-domain simulations of green water around offshore structures. The new interface-capturing method is first employed to generate a plunging breaker in a numerical wave tank. Then it is used for two-dimensional green water simulations on offshore platforms. The simulation results clearly demonstrate the flexibility and accuracy of the level set method for the prediction of complex free surface motions including wave breaking and green water effects.

REFERENCES – PART I

1. Armenio, V., "An Improved MAC Method (SIMAC) for Unsteady High-reynolds Free Surface Flows," *International Journal for Numerical Methods in Fluids*, Vol.24, pp.185--214, 1997.

2. Biausser, B., Fraunie, P., Grilli, S. and Marcer, R., "Numerical Analysis of the Internal Kinematics and Dynamics of Three-dimensional Breaking Waves on Slopes," *International Journal of Offshore and Polar Engineering*, Vol.14, No.4, 2004.

3. Cariou, A. and Casella, G., "Liquid Sloshing in Ship Tanks: A Comparative Study of Numerical Simulation", *Marine Structures*, Vol.12, pp.183--198, 1999.

4. Chan, R.K.C. and Street, R.L., "A Computer Study of Finite-Amplitude Water Waves," *Journal of Computational Physics*, Vol.6, pp.68--94, 1969.

5. Chen, G., Karif, C., Zaleski, S. and Li, J., "Two-dimensional Navier-Stokes Simulation of Breaking Waves," *Physics of Fluids*, Vol.11, Number 1, pp. 121--133, 1999.

6. Chen, H.C. and Chen, M., "Chimera RANS Simulation of A Berthing DDG-51 Ship in Translational and Rotational Motions," *Int. J. of Offshore and Polar Eng.*, Vol.8, No.3, pp. 182--191, 1998.

7. Chen, H.C. and Huang, E.T., "Time-Domain Simulation of Floating Pier/Ship Interactions and Harbor Resonance," *in Proceedings of 14th International Offshore and Polar Engineering Conference*, Vol. III, pp. 772--779, 2004.

8. Chen, H.C., Liu, T., Chang, K.A., and Huang, E.T., "Time-Domain Simulation of Barge Capsizing by A Chimera Domain Decomposition Approach," *in 12th International Offshore and Polar Engineering Conference*, Vol. III, pp. 494-501, 2002.

9. Chen, H.C., Liu, T., and Huang, E.T., "Time-Domain Simulation of Large Amplitude Ship Roll Motions by A Chimera RANS Method," *in Proceedings, 11th International Offshore and Polar Engineering Conference*, Vol. III, pp. 299-306, 2001.

10. Chen, H.C., Liu, T., Huang, E.T. and Davis, D.A., "Chimera RANS Simulation of Ship and Fender Coupling for Berthing Operations," *International Journal of Offshore and Polar Engineering*, Vol. 10, No. 2, pp. 112-122, 2000.

11. Chen, H.C. and Patel, V.C., "The Flow around Wing-Body Junctions," *in Proceedings, 4th Symp. on Numerical & Physical Aspects of Aerodynamic Flows*, 1989.

12. Chen, H.C. and Patel, V.C., "Near-Wall Turbulence Models for Complex Flows Including Separation," *AIAA Journal*, Vol.26, No. 6, pp.641--648, 1988.

13. Chen, H.C., Patel, V.C. and Ju, S., "Solutions of Reynolds-averaged Navier-Stokes Equations for Three-Dimensional Incompressible Flows," *Journal of Computational Physics*, Vol. 88, pp. 305-335, 1990.

14. Chen, H.C., Yu, Kai and Chen, S.Y., "Simulation of Wave Runup Around Offshore Structures by A Chimera Domain Decomposition Approach," *in Proceedings, Civil Engineering in the Oceans VI Conference*, October 20-22, 2004.

15. Cokelet, E.D., "Steep Gravity Waves in Water of Arbitrary Uniform Depth," Philosophical Transactions of Royal Society of London, Vol, 286, pp. 183-230, 1977.

16. Dean, R.G. and Dalrymple, R.A. (1994), "Water Wave Mechanics for Engineers and Scientists," World Scientific, Singapore, 1994.

17. Dong, C.M. and Huang, C.J., "Vortex Generation in Water Waves Propagating Over A Submerged Rectangular Dike," *in Proceedings, 9th International Offshore and Polar Engineering Conference*, Vol. III, pp. 388-395, 1999.

18. Duval, M., Astruc, D. and Legendre, D., "Two-phase Flow Modeling of Breaking Waves without Interface Reconstruction," *in Proceedings, 14th International Offshore and Polar Engineering Conference*, 2004.

19. Enright, D., Fedkiw, R., Ferziger, J. and Mitchell, I., "A Hybrid Particle Level Set Method for Improved Interface Capturing," *Journal of Computational Physics*, Vol.183, pp.83--116, 2002.

20. Faltinsen, O.M., Rognebakke, O.F., Lukovski, I.A. and Timoka, A.N., "Multidimensional Modal Analysis of Nonlinear Sloshing in A Rectangular Tank with Finite Water Depth," *Journal of Fluid Mechanics*, Vol.407, pp.201--234, 2000.

21. Ferziger, J.H. and Peric, M., "Computational Methods for Fluid Dynamics," 2nd Edition, Springer-Verlag, 1999.

22. Frandsen, J.B., "Sloshing Motions in Excited Tanks," *Journal of Computational Physics*, Vol.196, pp.53--87, 2004.

23. Gibou, F., Fedkiw, R. Caflisch, R. and Osher S., "A Level Set Approach for the Numerical Simulation of Dendritic Growth," *Journal of Scientific Computing* Vol.19, pp.183--199, 2003.

24. Harlow, F.H. and Welch, J.E., "Numerical Study of Large-Amplitude Free Surface Motions," *Physics of Fluids*, Vol. 8, pp.2182-2189, 1965.

25. Hirt, C.W. and Hotchkiss, R.S., "SOLA-VOF: A Solution Algorithm for Transient Fluid Flow with Multiple Free Boundaries," Technical Report LA-8355, Los Alamos National Laboratory, 1980.

26. Hirt, C.W. and Nichols, B.D., "Volume of Fluid (VOF) Method for the Dynamics of Free Boundaries," *Journal of Computational Physics*, Vol. 39, pp. 201-225, 1981.

27. Huijsmans, R.H.M. and van Grosen, E., "Coupling Freak Wave Effects with Green Water Simulations," *in Proceeding of the 14th ISOPE*, pp.366--373, 2004.

28. Hwang, S.H., “Experimental and Numerical Investigation on Sloshing Impact Load,” *Ph.D. Dissertation*, Pusan Nation University, Korea, 2006.

29. Iglesias, A.S., Rojas, L.P. and Rodriguez, R.Z., “Simulation of Anti-roll Tanks and Sloshing Type Problems with Smoothed Particle Hydrodynamics,” *Ocean Engineering*, Vol.31, pp.1169--1192, 2004.

30. Kim, Y., “Numerical Simulation of Sloshing Flows with Impact Load,” *Applied Ocean Research*, Vol.23, pp.53--62, 2001.

31. Kim, Y., “Numerical Study on Slosh-induced Impact Pressures on Three-dimensional Prismatic Tanks,” *Applied Ocean Research*, Vol.26, pp.213--216, 2004.

32. Koshizuka, S., Tamako, H. and Oka, Y., “A Particle Method for Incompressible Viscous Flow with Fluid Fragmentation,” *Computational Fluid Dynamics Journal*, Vol. 4, No. 1, pp. 29-46, 1995.

33. Kothe, D.B. and Rider, W.J., “Comments on Modeling Interfacial Flows with Volume-of Fluid Methods,” *Los Alamos National Laboratory Reports*, 1995.

34. Lafaurie, B., Nardone, C., Scardovelli, R., Zalesaki, S. and Zanetti, G., “Modelling Merging and Fragmentation in Multiphase Flows with SURFER,” *Journal of Computational Physics*, Vol.113, pp.134--147, 1994.

35. Lee, D.H., Kim, M.H., Kwon, S.H., Kim, J.W. and Lee, Y.B., “A Parametric Sensitivity Study on LNG Tank Sloshing Loads by Numerical Simulations,” *Ocean Engineering*, Vol.34, pp.3--9, 2007.

36. Lee, Y.B., Lee, J.M., Kim, Y.S., Jung, J.H., Jung, D.W. and Kwon, S.H., “An Experimental Study of Impulsive Sloshing Load Acting on LNGC Tank,” *in Proceedings of the 16th ISOPE*, 2006.

37. Longuet-Higgins, M.S. and Cokelet, E.D., “The Deformation of Steep Surface Waves on Water. I. A Numerical Method for Computation,” *Proceedings of the Royal Society of London*, Series A, Vol.350, No.1660, pp. 1--26, 1976.

38. Loots, E., Pastoor, W., Buchner, B. and Tveitnes, T., “The Numerical Simulation of LNG Sloshing with An Improved Volume of Fluid Method,” *in Proceedings, 23rd International Conference on Offshore Mechanics and Arctic Engineering*, 2004.

39. Mei, C.C., “"The Applied Dynamics of Ocean Surface Waves,” World Scientific: Singapore. Nichols, B.D., 1989.

40. Miyata, H., “Finite-Difference Simulation of Breaking Waves,” *Journal of Computational Physics*, Vol.65, pp.179--214, 1986.

41. Nam, B.W. and Kim, Y., “Simulation of Two-Dimensional Sloshing Flows by SPH Method,” *in Proceedings of the 16th ISOPE*, pp.342--347, 2006.

42. Osher, S. and Fedkiw, R., “Level Set Methods: An Overview and Some Recent Results,” *Journal of Computational Physics*, Vol.169, pp.463--502, 2001.

43. Osher, S. and Fedkiw, R., “Level Set Methods and Dynamics Implicit Surfaces,” New York Springer-Verlag, 2003.

44. Osher, S., and Sethian, J.A., “Fronts Propagating with Curvature-dependent Speed: Algorithms Based on Hamilton-Jacobi Formulations,” *Journal of Computational Physics*, Vol. 79, No.1, pp. 12-49, 1988.

45. Park, J.C., Uno, Y., Matsuo, H., Sato, T. and Miyata, H., “Reproduction of Fully-Nonlinear Multi-Directional Waves by a 3D Viscous Numerical Wave Tank,” *in Proceedings, 11th International Offshore and Polar Engineering Conference*, Vol. III, pp. 140-147, 2001.

46. Pitsch, H. and Lageneste, L., “Large-eddy Simulation of Premixed Turbulent Combustion Using A Level-set Approach,” *Proceedings of the Combustion Institute*, Vol.29, pp.2001--2008, 2002.

47. Rocca, M.L., Sciortino, G. and Boniforti, M.A., “A Fully Nonlinear Model for Sloshing in A Rotating Container,” *Fluid Dynamics Research*, Vol.27, pp.23--52, 2000.

48. Scardovelli, R. and Zaleski, S., “Direct Numerical Simulation of Free-surface and Interfacial Flow,” *Annual Reviews of Fluid Mechanics*, Vol.31, pp.567--603, 1999.

49. Sethian, J.A., “Level Set Methods,” Cambridge Univ. Press, 1996.

50. Sethian, J.A. and Adalsteinsson, D., “An Overview of Level Set Methods for Etching, Deposition, and Lithography Development,” *IEEEE Transactions on Semiconductor Devices*, Vol.10, 167--184, 1996.

51. Shu, C.W, “Essentially Non-Oscillatory and Weighted Essentially Non-Oscillatory Schemes for Hyperbolic Conservation Laws,” ICASE Report No.97-65, NASA/CR-97-206253, 1997.

52. Shu, C.W. and Osher, S., “Efficient Implementation of Essentially Nonoscillatory Shock Capturing Schemes II,” *Journal of Computational Physics*, Vol. 83, pp. 32-78, 1989.

53. Sussman, M., Smereka, P. and Osher, S., “A Level Set Approach for Computing Solutions to Incompressible Two-Phase Flow,” *Journal of Computational Physics*, Vol. 114, pp. 146-159, 1994.

54. Sussman, M. Fatemi, E., Smereka, P. and Osher, S., “An Improved Level Set Method for Incompressible Two-phase Flows,” *Computer & Fluids*, Vol. 27, pp. 663-680, 1998.

55. Sussman, M. and Fatemi, E., “An Efficient, Interface-Preserving Level Set Redistancing Algorithm and Its Application to Interfacial Incompressible Fluid Flow,” *SIAM J. of Scientific Comput.*, Vol. 20, pp. 1165-1191, 1999.

56. Sussman, M. and Puckett, E.G., “A Coupled Level Set and Volume-of-fluid Method for Computing 3D and Axiymmetric Incompressible Two-phase Flows,” *Journal of Computational Physics*, Vol.162, pp:301--337, 2000.

57. Suhs, N.E. and Tramel, R.W., “PEGSUS 4.0 Users Manual,” *Arnold Eng Dev Center Rep AEDC-TR-91-8*, Arnold Air Force Station, TN, 1991.

58. Takahira, H., Horiuchi, T. and Banerjee, S., “An Improved Three-Dimensional Level Set Method for Gas-Liquid Two-Phase Flows,” *Journal of Fluids Engineering*, Vol.126, pp.578--585, 2004.

59. Wu, G.X., Ma, Q.W. and Taylor, R.E., “Numerical Simulation of Sloshing Waves in A 3D Tank Based on A Finite Element Method,” *Applied Ocean Research*, Vol.20, pp.337--355, 1998.

60. Yang, Chi and Lohner, Rainald, “Computation of 3D Flows with Violent Free Surface Motion,” *in Proceedings of the 15th ISOPE*, 2005.

61. Valentine, D.T. and Frandsen, J.B., “Nonlinear Free-Surface and Viscous-Internal Sloshing,” *Journal of Offshore Mechanics and Arctic Engineering*, Vol.127, pp. 141--149, 2005.

62. Van der Pijl, S.P., Segal, A., Vuik, C. and Wesseling, P., “A Mass-conserving Level-Set Method for Modelling of Multi-phase Flows,” *International Journal for Numerical Methods in Fluids*, Vol.47, pp.339--361, 2005.

63. Yue, W.S., Lin, C.L. and Patel, V.C., “Numerical Simulation of Unsteady Multidimensional Free Surface Motions by Level Set Method,” *Int. J. Numer. Meth. Fluids*, Vol. 42, pp. 853-884, 2003.

64. Zalesak, S.T., “Fully Multidimensional Flux-Corrected Transport Algorithms for Fluids,” *Journal of Computational Physics*, Vol. 31, pp. 335-362, 1979.

PART II: EXPERIMENTAL APPROACH [1]

[1] Part of the work has been published as "Green water void fraction due to breaking wave impinging and overtopping" in *Experiments in Fluids* (publisher: Springer).

8 INTRODUCTION

The impingement of a large breaking wave on an offshore structure is of great concern to the safety of the offshore structure. Green water loads were found to be responsible for damage to structures during large storms. Green water occurs when an incoming wave significantly exceeds the free board and water rushes onto the deck. In order to understand the green water flow, both the velocity field and the void fraction distribution are needed. Even though the green water problem has been studied by many researchers, direct measurements of velocity and void fraction have been rare. Not only is green water very difficult to measure in the laboratory and field, it is also very difficult to simulate numerically. The fast moving, highly aerated, and highly turbulent nature makes the problem nearly not amenable.

Breaking waves are multi-phased and turbulent. If a wave breaking event takes place near a structure, reflection, runup, overtopping, aeration, and turbulence further complicate the problem. Since aeration changes the density of the gas-liquid flow, void fraction and velocity are considered as crucial factors in the understanding of several important issues in the breaking wave-structure interaction problem. This includes the overtopping flow rate, water volume, and momentum on the deck of the structure that pertain to the integrity of the structure and equipment, and safety of personnel on the structure. In addition, void fraction is relevant to the wave impact pressure as it affects the maximum pressure (Bullock *et al*. 2001).

Most laboratory measurements of wave breaking or green water were taken outside the aerated region because of the capability of the existing measurement tools used (e.g., Ting and Kirby, 1994; Chang and Liu, 1999; Chang and Liu, 2000; Cox and Ortega, 2002; Shin and Cox, 2006). Due to the advances in measurement techniques in the past several years, progress has been made in the understanding of kinematics and flow structure of breaking waves. Shin and Cox (2006) used laser Doppler velocimetry to measure fluid velocities in the inner surf zone and swash zone and found that the bore

front velocity of the breaking wave in the zones is about 1.1 times the wave celerity. Govender *et al*. (2002) reported successful measurements of velocity and flow structure inside the highly aerated region of breaking waves using an imaging method. Ryu *et al*. (2005) introduced a technique called bubble image velocimetry (BIV) for measuring the velocity field in bubbly flows, and used the technique to obtain the velocity in the vicinity of a structure impinged by a breaking wave. Although based on different principles, both Govender *et al*. (2002) and Ryu *et al*. (2005) utilized imaging methods by correlating textures in flows for velocity determination. They opened a door for possible full-field velocity measurements in highly aerated flows such as wave breaking, wave impingement, and green water.

Unlike velocity measurements, there have been a relatively large number of studies on the void fraction of breaking waves in the aerated region, although reports relating to the void fraction in green water flows are rare. Hwung et al. (1992) carried out a laboratory investigation on void fraction and velocity of breaking waves. They related void fraction to energy dissipation based on their measurements in plunging and spilling breakers. They found the void fraction is about 20% and 16% in a plunging breaker and spilling breaker, respectively. Similar results on void fraction were also found in an experimental study by Hoque and Aoki (2005). Lamarre and Melville (1992) reported on the development and application of an impedance probe for measuring void fraction in bubble plumes generated by breaking waves in the laboratory and in the ocean. Deane (1997) used both optical and acoustical methods for void fraction measurements in breaking waves in a surf zone and found that the void fraction is between 30% and 40%. Chanson *et al*. (2002) studied the air entrainment and detrainment processes under a pseudo-plunging breaker formed by the impingement of a vertical water jet and bubble injection. They suggested a dominant time scale for bubble rise in the processes. Cox and Shin (2003) measured the temporal variation of void fraction above the still water level of a breaking wave and found the trend of a linear growth followed by an exponential decay. They also showed that the distribution of void fraction above the still water normalized by the wave period and the average void

fraction is self-similar. Blenkinsopp and Chaplin (2007) examined time varying void fraction distributions of breaking waves. They reported that there exists a similarity in void fraction of breaking waves. The similarity and the energy dissipation rate during the breaking process vary and depend on the breaker type. Besides the void fraction of breaking waves, one may also examine the void fraction of dam break flows or alike known to behave similarly to green water. The void fraction of unsteady sudden open surging flows was investigated experimentally by Chanson (2004). He concluded that the front and the free surface of the surging flows are strongly aerated.

This study presents void fraction measurements of an overtopping green water flow on top of a structure generated by breaking wave impingement. The void fraction was measured using a fiber optic reflectometer (FOR) introduced by Chang *et al*. (2003). Repeated instantaneous measurements of void fraction were ensemble-averaged to obtain mean properties. Together with the velocity measurements using BIV reported in Ryu *et al*. (2007a), the flow rate, momentum flux, and water volume of the overtopping flow were estimated. The obtained overtopping water volume was compared with the directly measured water volume using a large container for validation of the void fraction, velocity, and water level measurements. Empirical similarity equations of depth-averaged void fraction, depth-averaged velocity, and overtopping water level were obtained by applying dimensional analysis and regression of the measurement data.

9 EXPERIMENT SETUP

The experiments were carried out at the Department of Civil Engineering, Texas A&M University in a 36 m long, 0.9 m wide, and 1.5 m high glass-walled wave tank equipped with a flap-type wavemaker and a 1:5.5 sloped wave absorber. A rectangular model structure was located 21.7 m away from the wavemaker. The structure has a height of 0.31 m, a length of 0.37 m (including a 0.22 m long extended deck), and spans the width of the wave tank so it can be considered as two-dimensional. The structure is a 1:168 scaled-down simplified geometry tension leg platform (TLP) while the extension deck mimics a ship-shape platform such as a floating, production, storage, and off-loading (FPSO) platform. The wave tank was filled to a water depth d = 0.80 m throughout the experiments and the model structure has a draft of 0.20 m so the free board is 0.11 m. The model structure was rigidly fixed. It was mounted on aluminum frames and suspended from the top of the tank, thus the motion of the prototype structure was not simulated. The setup of the wave tank and model structure is sketched in Figure 9.1.

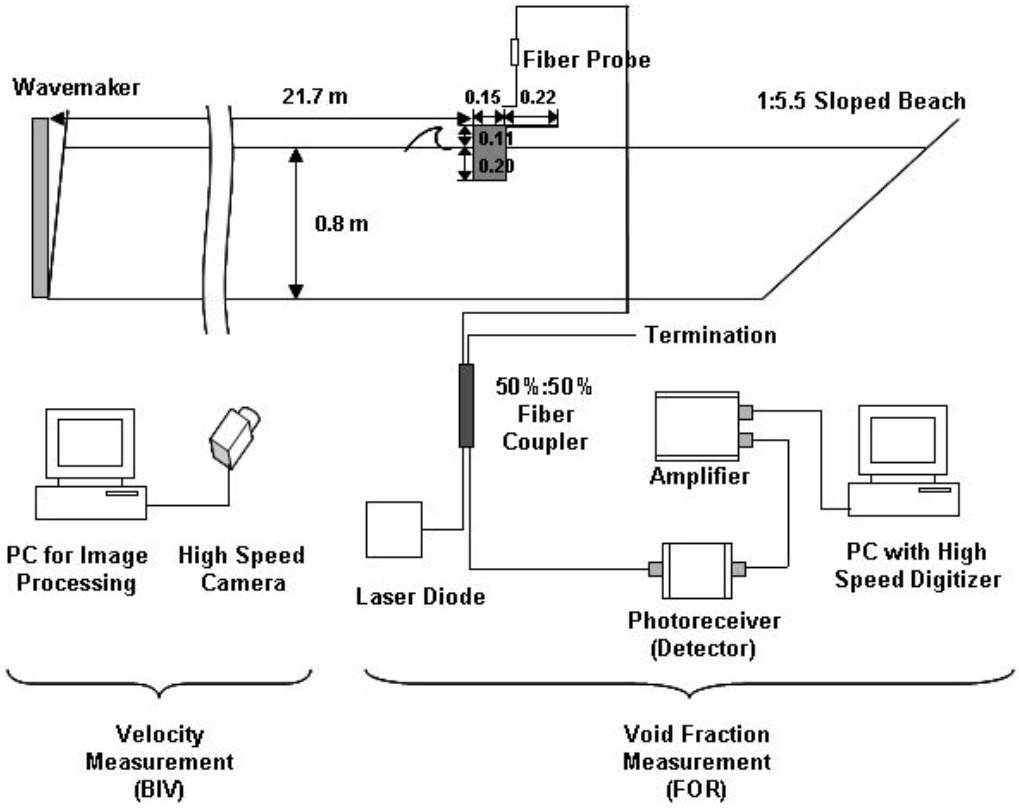

Figure 9.1 Experimental setup. Dimensions of the model structure are in meter.

Overtopping green water was created by a plunging breaking wave that impinged on the front wall of the model structure and then overtopped the structure. The plunging breaker was generated using a wave focusing method that features a wave train with frequencies ranging from 0.7 Hz to 1.3 Hz. The breaking wave follows the same Froude scaling according to the reported maximum wave height during Hurricane Ivan (Wang *et al.*, 2005). The primary wave period (T), wavelength (L), wave height (H), and phase speed (C) of the breaking wave in the deep water are T = 1.30 s, L = 2.54 m, H = 17.1 cm, and C = 1.95 m/s, respectively. The primary wave period, obtained from the zero up-crossing period of the wave, is the period of the specific wave in the wave train that has the largest wave amplitude and leads to the breaking event. The physical modeling is based on the undistorted Froude scaling except for the upstream water depth which

does not matter because of the deep water condition. The plunging breaker breaks at a desired location right in front of the model structure. The generated breaking wave is highly repeatable and the tests were repeated 20 times to obtain the mean quantity from ensemble average. Details on the plunging wave can be found in Ryu *et al.* (2007a).

Velocity fields of the overtopping green water flow were measured using bubble image velocimetry (BIV), which is a non-intrusive velocity measurement technique for multi-phased flows (Ryu *et al.*, 2005). The BIV technique measures the two-dimensional velocity field of liquid-gas flows by correlating the "texture" in consecutive images formed by bubbles and gas-liquid interfaces. Details on BIV are reported in Ryu *et al*. (2005). Since BIV uses bubbles and air-water interfaces as tracers, it is necessary to examine whether the measurements are representative of the fluid (i.e., the mixture of air and water) velocity. Whether or not bubble motion reflects the fluid motion depends on the ratio of the inertia force to the buoyancy force. In this study, the ratio is about 10 to 20, which means the measured velocity indeed represents the fluid velocity.

In the present setup, the flow was illuminated using the shadowgraphy technique with light coming from the back. A thin translucent white acrylic sheet was attached to the back glass wall of the wave tank while 600 W light bulbs behind the sheet were used as the light source. An 8-bit high speed camera with a maximum framing rate of 1200 frames per second and a resolution of 1024×1024 pixels was used to capture images for later velocity analysis. The camera was mounted with a 105 mm focal lens with the aperture set at f/1.8 and the sampling rate set at 1000 frames per second throughout the experiments. The camera was positioned at a distance of 4 m from the front glass wall of the wave tank to minimize uncertainty due to the limited thickness of the depth of field (Ryu *et al.*, 2005). The measurement plane (i.e., the center of the camera focal plane) was located about 15 cm from the front glass wall of the wave tank. The boundary effect was tested through velocity measurements from the top of the wave tank and found to be insignificant at such a location. The depth of field

was about 15 cm and the uncertainty in velocity due to the depth of field is within 2%. Note that the uncertainty was determined from the ratio between the half thickness of the depth of field and the distance between the focal plane and the camera. Velocities were calculated using commercial software from LaVision Inc. Velocity calculation using cross-correlation was performed with an interrogation window of 32×32 pixels and a 50% overlap between adjacent interrogation windows. Spurious vectors in the velocities were removed by post-processing with a median filter. The mean velocities were obtained from ensemble averaging the 20 repeated tests. Details on velocity measurements have been reported in Ryu *et al.* (2007a).

In addition to velocity measurements, void fraction in green water was also measured using a fiber optic reflectometer (FOR). Chang *et al*. (2003) introduced the FOR technique which is capable of measuring the time history of velocity and void fraction of a multiphase flow at a given point. The FOR technique is based on the coherent-mixing of a scattered signal with a Fresnel reflection signal from the tip of an optical fiber. A continuous optical signal derived from a diode laser driven by a constant current is launched into a single-mode optical fiber and transmitted through a fiber coupler to the signal fiber located at the measurement point. The coherently-mixed signal propagates back to the signal fiber and is detected by a detector. By analyzing the signal, the velocity and fraction ratio of each phase can be obtained. Details on the FOR method can be found in Chang *et al*. (2003).

The optical fiber in the FOR system is tiny with a diameter of 125 μm. Although the FOR technique is an intrusive method, the disturbance induced by the tiny probe to most flows is negligible due to its miniature size. To minimize the flow disturbance caused by the FOR probe and be able to mount the probe at a desired measurement point, the optical fiber was inserted inside a very thin but rigid hollow stainless tube with a diameter less than 1 mm. The end of the fiber protrudes out from the tube with a short length of 2 mm. The probe was located above the deck of the model structure and oriented toward the wavemaker. Signals were sampled at a relatively low frequency of

10 kHz throughout the experiments so only the void fraction is obtained but not the velocity. Note that the FOR system usually requires an *O*(10 MHz) sampling rate for velocity measurements. The FOR system used in the present study is sketched in Figure 9.1 along with the setup of the experiments.

The void fraction was measured at 7 cross sections from x = 0 mm to x = 300 mm with a separation of 50 mm. The coordinate system defined as (x, z) = (0, 0) is at the leading edge of the deck and the still water level with x being the horizontal direction and z the vertical direction. At each cross section, measurements were taken from z_d = 10 mm to z_d = 150 mm with a 10 mm increment except at the frontal edge of the deck. Note that z_d is another vertical coordinate with z_d = 0 being at the deck surface (i.e., z_d = z – 110 mm). The arrangement of the FOR measurement points is shown in Figure 9.2. Since the green water flow has a very short passing duration (less than 0.02 ms) and the void fraction is close to 1.0 (i.e., 100% air) above z_d = 100 mm at the cross sections from x = 50 mm to x = 300 mm, only the data in the region equal to or below z_d = 100 mm were analyzed. This includes a total number of 68 points. Similar to the BIV velocity measurements reported in Ryu *et al.* (2007a), at each FOR measurement point the experiments were repeated 20 times to obtain the ensemble averaged mean quantity.

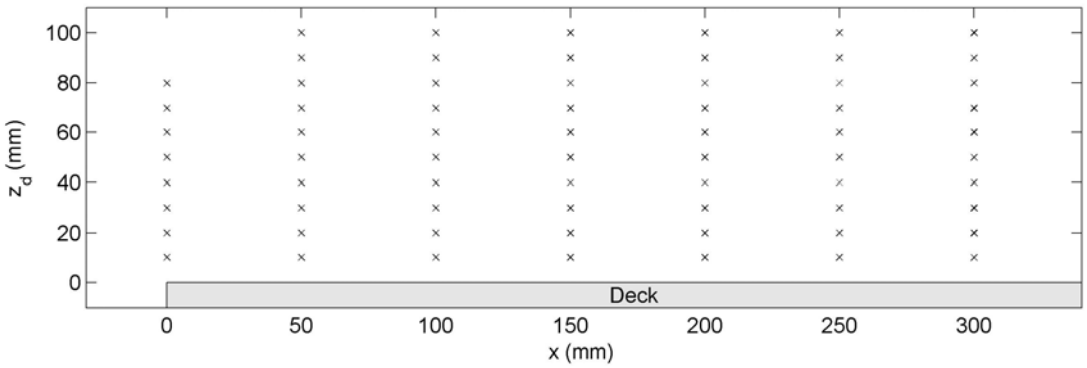

Figure 9.2 Void fraction measurement points.

10 VOID FRACTION TIME HISTORY AND SIGNAL PROCESSING

The phases (i.e., water and air) of the green water flow at each measurement point are determined based on the time-history signal acquired by the FOR probe according to the change in refractive index. A typical raw signal taken using FOR is presented in Figure 10.1. The signal registers 0 Volt when the probe is submerged and 4 Volt when the probe is in the air. In the present study, a threshold of 1.0 Volt was set to separate the phases. Typically, the FOR signal also fluctuates when the probe encounters solid particles. Since the signal fluctuation is less than 1 Volt, a signal greater than 1.0 Volt indicates air. Note that the small spike in front of the rising edge in the figure (at approximately 0.118 s) is the result of coherent beating that belongs to the liquid phase and provides velocity information if sampled at a very high frequency (see Chang *et al*., 2003).

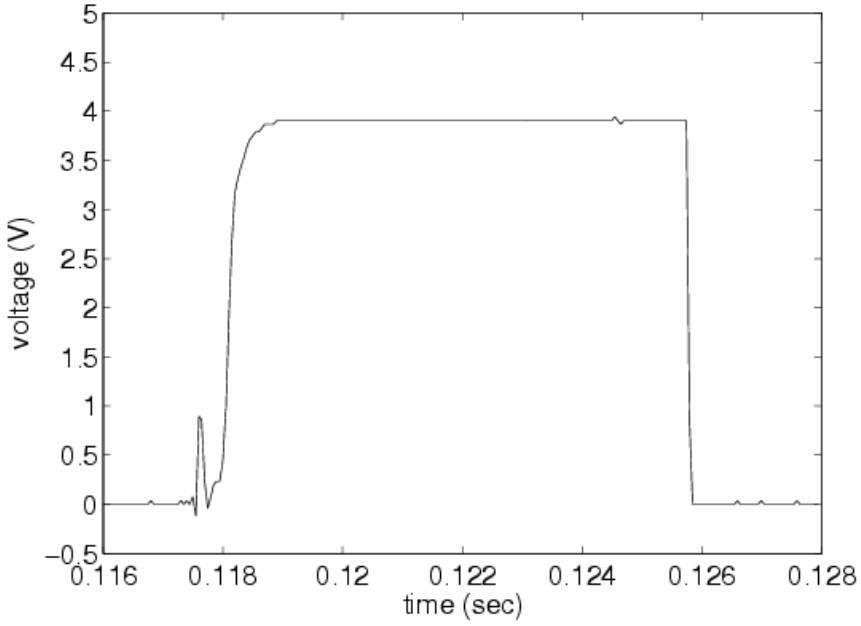

Figure 10.1 Typical raw FOR signal sampled at 10 kHz.

The void fraction is defined as the ratio of air-phase residence time (T_{air}) to the duration of air-water mixture (T_{dur}) at the point of interest. Thus, the value of the void fraction may be affected by the selection of T_{dur} in the data analysis. In this study, the void fraction was calculated by averaging the signal over a short time interval of 0.01 s (i.e., averaged over 100 data points). This way the interval is long enough so the time-averaged value of void fraction can be determined with enough samples while short enough so the temporal variation of void fraction can also be obtained.

The definition of void fraction at a given point is expressed as:

$$\alpha_i = \frac{T_{air,i}}{T_{dur,i}} \tag{10.1}$$

where α_i is the instantaneous void fraction, $T_{dur,i}$ is the time interval for void fraction binning (set as 0.01 s in this study), $T_{air,i}$ is the duration of air phase residence time during $T_{dur,i}$, and the subscript indicates the *i*th repeated measurement. For example, α_i = 1.0 means the tip of the fiber probe does not encounter water during the interval of 0.01 s, whereas α_i = 0 indicates the probe is in water during the entire 0.01 s interval. Based on the calculated void fraction, a 100 Hz time series of void fraction was obtained.

Since the green water flow is very turbulent, ensemble averaging was applied to quantify the temporal variation of the mean void fraction, expressed as follows:

$$\alpha = \frac{\sum \alpha_i}{n} \tag{10.2}$$

where α is the ensemble averaged void fraction and n is the number of repeated samples. In the present study, 20 instantaneous measurements of void fraction were taken at each point so n = 20. Convergence of the mean void fraction based on the number of samples was tested for two measurement points with the results shown in Figure 10.2. Based on the tests, 20 samples are found to be not perfect but acceptable for the convergence of void fraction averaging.

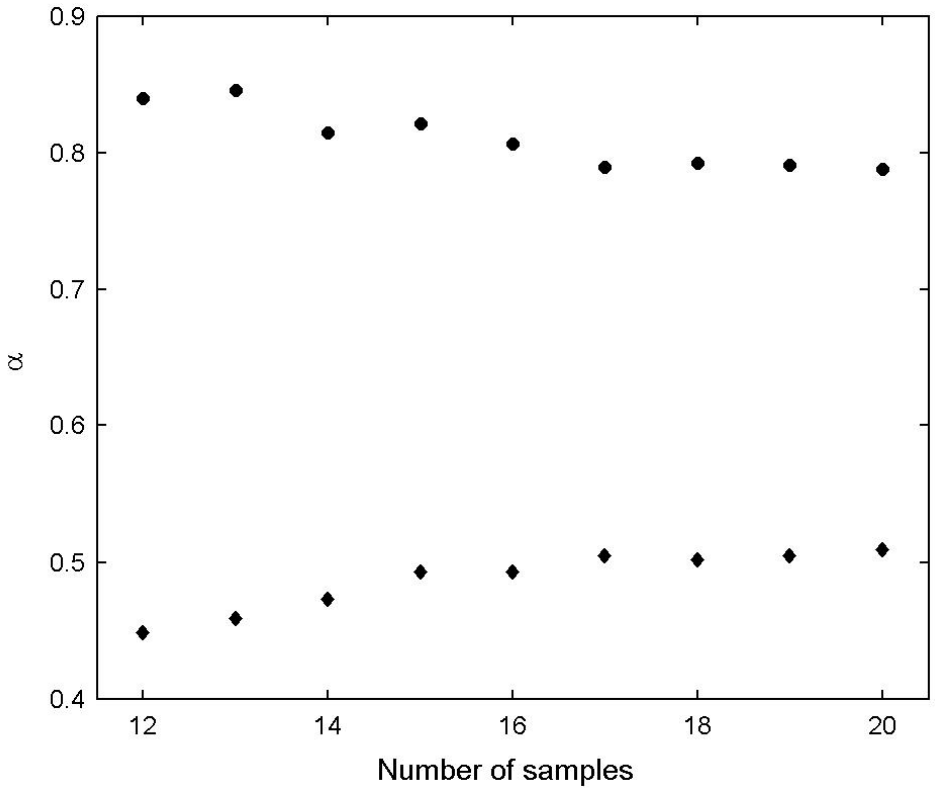

Figure 10.2 Convergence of mean void fraction against samples at two measurement points.

Void fraction in the present study was obtained by averaging over the short time interval of 0.01 s. The interval was determined with the intention of matching the time steps in the velocity measurements which have a temporal resolution the same as the time interval. Chanson (2004) presented a void fraction analysis for a time interval with 5 to 20 bubble encounters and showed the time interval is important to the determination of void fraction. In this study, the dependence of temporal variation of void fraction on various time intervals was examined to ensure the time interval used is appropriate.

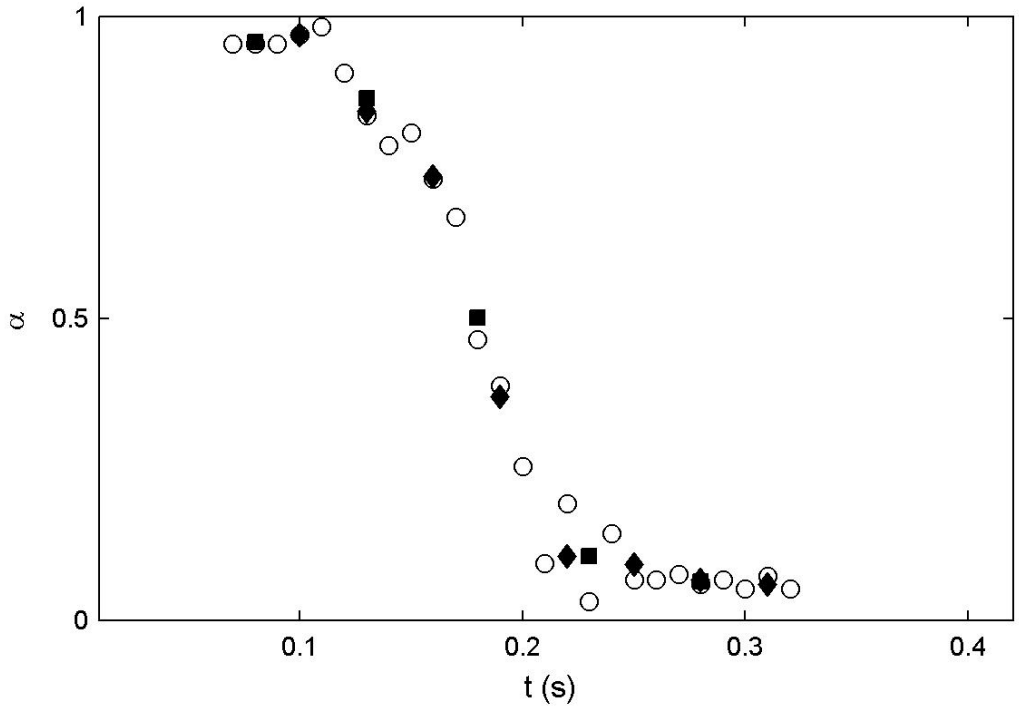

Figure 10.3 Void fraction distributions obtained using time interval T_{dur} = 0.01 s (○), 0.03 s (♦), and 0.05 s (■) at (x, z_d) = (100, 20) mm.

In the present study, convergence tests were performed with T_{dur} = 0.01 s, 0.03 s, and 0.05 s. Figure 10.3 shows the temporal distribution of void fraction at the point (x, z_d) = (100, 20) mm for the three different time intervals. Although the distribution for T_{dur} = 0.01 s is slightly fluctuating, the three distributions appear to collapse onto a single curve. Similar results were obtained at other locations. In green water with a typical velocity about 2 m/s, the horizontal travel distances corresponding to T_{dur} = 0.01 s and 0.05 s are about 2 cm and 10 cm, respectively. The negligible variation in the distributions over the different travel distances indicates that the time interval of 0.01 s is long enough to obtain an appropriate void fraction while short enough to have a high temporal resolution.

Note that the measurements of void fraction and velocity were conducted separately in the present study. Thus, it is necessary to match the time between the two

sets of measurements, and to make sure each instantaneous measurement in the 20 repeated measurements in each set is synchronized. For velocity measurements, timing of each instantaneous velocity measurement was matched at the moment when the free surface of the breaking wave is crossing the leading edge of the structure. This particular moment is set as $t = 0$. The instantaneous velocities were then ensemble-averaged after matching the time step. For void fraction measurements, the timing was matched with the velocity measurement based on the instant when the rear surface of the breaking wave was passing the FOR probe. This is because the frontal surface of the flow is highly aerated and turbulent while the rear surface is neither fluctuating nor turbulent, evidenced from ensemble-averaged images.

One of the images is shown in Figure 10.4. The ensemble-averaged image in the figure, averaged over 20 instantaneous images, shows that the frontal area of the overtopping water is blurry due to aeration while the rear free surface appears to be clean and can be easily identified by the interface line. There is no noticeable difference at the rear free surface among the instantaneous images, indicating the level of turbulence and aeration is insignificant. This means in each FOR measurement the final signal rising (i.e., encountering the air) presents the moment of encountering the rear free surface. Accordingly, the time of the void fraction measurements was matched to that of the velocity measurements by comparing the time series of the data sets at the given FOR measurement point.

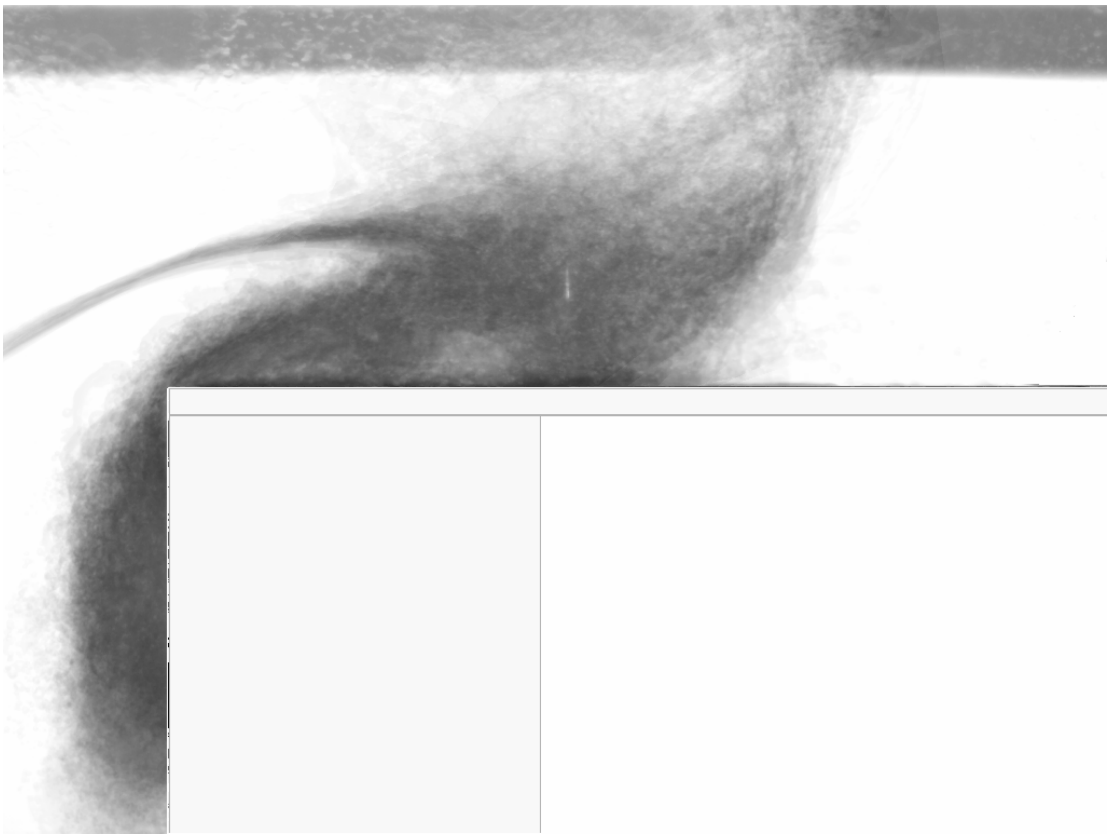

Figure 10.4 Sample ensemble averaged image of overtopping water on the deck.

11 DISTRIBUTIONS OF VOID FRACTION AND VELOCITY ALONG THE DECK

Figure 11.1 presents a series of vertical profiles of void fraction and horizontal velocity along the deck from t = 0.02 s to 0.28 s. Note that the void fraction measurements are point measurements using FOR even though they are spatially plotted every 50 mm in x along the deck and 10 mm in z. The horizontal velocity measured by BIV was plotted together with the void fraction measurements at each corresponding measurement point. Near the front of green water, as mentioned in Figure 10.4, the value of void fraction is close to unity, indicating the flow is mostly air. This is demonstrated in the cross sections at the front of green water in Figs. 11.1(a-d). The highly aerated front was indeed continuously observed during the process when the breaking wave was running up along the front wall of the structure, moving onto the deck, and passing the end of the deck. It suggests that overtopping green water induced by a breaking wave causes very high aeration near the water front. In contrast, near the rear free surface, green water shows very low aeration. At a given location on the deck, the general pattern of void fraction therefore decreases monotonically as time progresses. This is evidenced in Figs. 11.1(e-g) after the water front passed the end of the deck. At this stage the velocity profile seems to be similar to the void fraction profile.

Dam break flows have been applied to predict the green water velocity due to certain similarity in their flow patterns and the simplicity of the dam-break solution (Ryu *et al*., 2007b). In addition, the green water flow seems to have a similar pattern to the surging flow moving on a stepped bottom (Chanson, 2004). Both flows exhibit strong aeration in the wave front. After the wave front, the sudden open surging flow is highly aerated near the free surface which is similar to the vertical distribution of the green water void fraction. However, their void fractions are quite different and the water level variation in green water makes comparisons impractical.

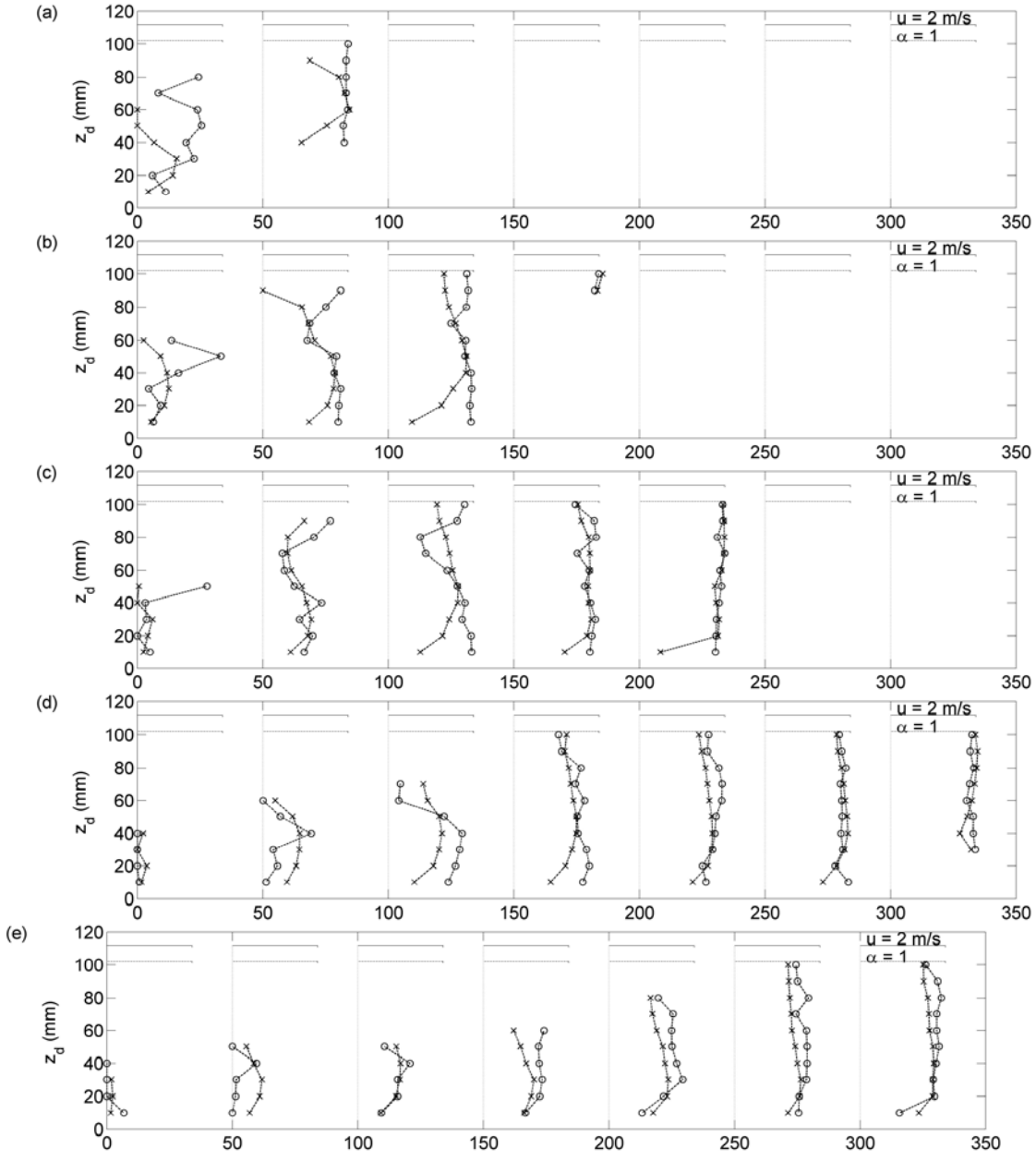

Figure 11.1 Distributions of void fraction and velocity along the deck from *t* = 0.02 s to 0.26 s with an increment of 0.04 s between panels. "○", void fraction; "×", velocity.

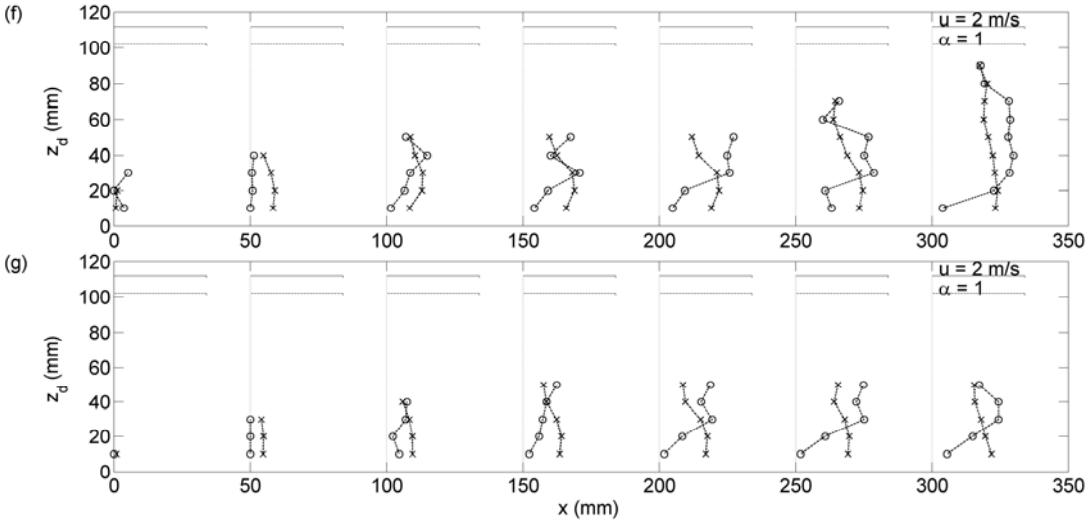

Figure 11.1 Continued.

The void fraction profiles in Figure 11.1 are a bit noisy due to the small sample number used in ensemble averaging. We time-averaged the void fraction and the result is shown in Figure 11.2. The time-averaged void fraction is defined as the total duration of air over the duration of green water from the front surface to the rear surface at a given point on the deck (i.e., averaging the time-history of void fraction at a given point). The figure reveals that the void fraction distribution changes gradually along the deck from approximately a linear distribution near the front of the deck to a profile similar to a boundary layer velocity distribution near the end of the deck. The time-averaged void fraction profiles in Figure 11.2 are categorized into three regions and shown in Figure 11.3. In the region from x = 0 mm to 50 mm, the time-averaged void fraction exhibits a nearly linear distribution against the vertical distance, as shown in Figure 11.3(a). The distribution in the region at $x \geq 200$ mm, shown in Figure 11.3(c), is close to a typical boundary-layer velocity distribution with a maximum void fraction occurring at about z_d = 40 mm and a nearly constant value around 0.86 above this level. In the transitional region from x = 100 mm to 150 mm, as shown in Figure 11.3(b), the distribution is in between Figs. 11.3(a) and 11.3(c).

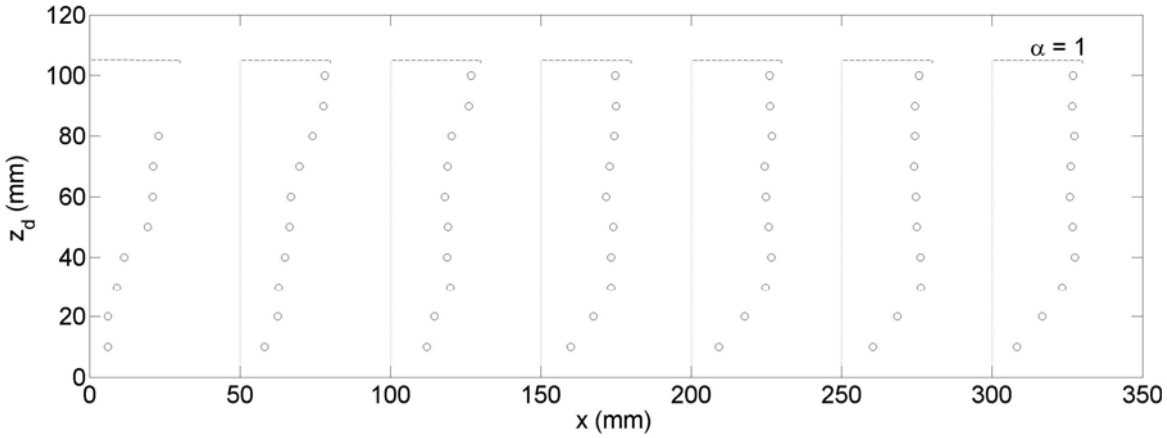

Figure 11.2 Distributions of time-averaged void fraction.

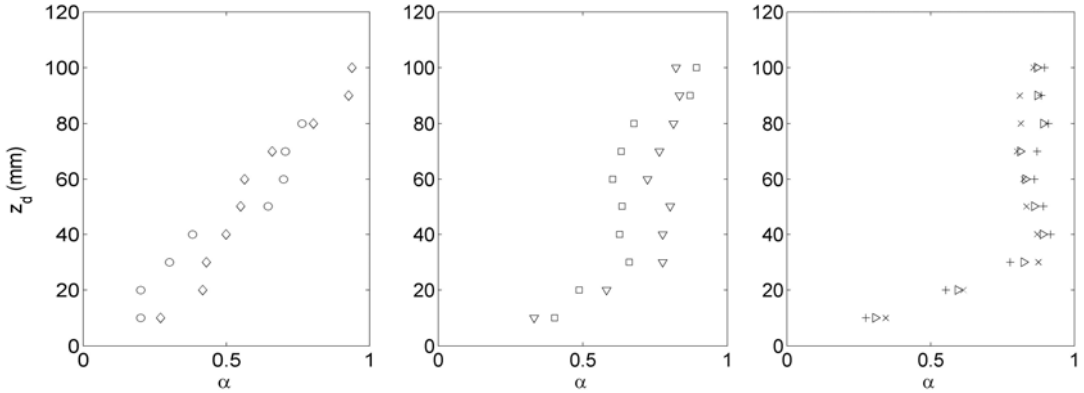

Figure 11.3 Categorization of time-averaged void fraction profiles: (a) the linearly increase region, *x* = 0 mm (o) and 50 (◊) mm; (b) the transitional region, *x* = 100 mm (□) and 150 (∇) mm; (c) the boundary layer alike region, *x* = 200 mm (×), 250 mm (▷), and 300 (+) mm.

12 FLOW RATE, VOLUME, MOMENTUM FLUX, AND VALIDATION OF MEASUREMENT

Using the measured velocity and void fraction, the time history of flow rate of the green water flow can be calculated. Knowing void fraction is necessary in the flow rate calculation since the green water is multi-phased. The volume flow rate per unit width, q, at a given cross section is expressed as follows:

$$q = \int_{h_l}^{h} (1-\alpha) U \, dz_d \tag{12.1}$$

where h is the upper water surface of green water on the deck and h_l is the lower water surface. In the calculation, only the horizontal velocity component U is considered. Note that the flow rate calculated in this study does not cover the entire green water flow field at a certain region, as mentioned in the Experimental Setup section. The flow rate is estimated by integrating vertically up to z_d = 100 mm (i.e., h = 100 mm). Although the void fraction was measured above z_d = 100 mm, the green water at the measurement points is found to be very highly aerated (mostly over 0.95) with a very short duration, implying a negligible contribution to the flow rate estimation.

The time history of flow rate of green water at six cross sections on the deck from x = 50 mm to 300 mm with a 50 mm increment is shown in Figure 12.1. The flow rate displays a similar pattern at each cross section - increasing linearly and rapidly and then, after reaching the maximum, decreasing with a slower pace. For all the cross sections, the flow rate reaches the maximum at approximately 0.10 s after the front of green water arrives at the corresponding cross section. According to the velocity measurements in Ryu *et al.* (2007a), the maximum velocity was observed at the front of green water so the velocity at each cross section decreases monotonically. If the flow rate was estimated with only the velocity information but not void fraction, the distribution would appear to have the maximum value initially and then decrease

monotonically. This emphasizes the importance of void fraction measurement in the green water flow.

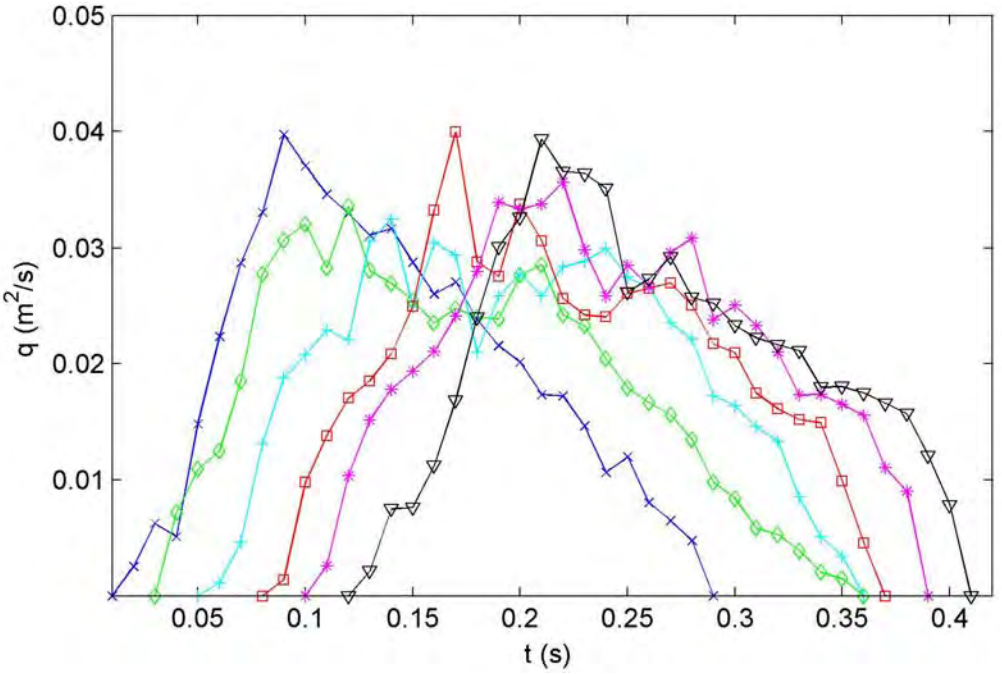

Figure 12.1 Time history of flow rate of green water at six cross-sections: x = 50 mm (×); 100 mm (◊); 150 mm (+); 200 mm (□); 250 mm (✳); and 300 mm (▽).

The momentum flux per unit width, M, divided by the water density, ρ, at a given cross section was also calculated as follows:

$$\frac{M}{\rho} = \int_{h_l}^{h} (1-\alpha) U^2 \, dz_d \tag{12.2}$$

Figure 12.2 shows the momentum flux distribution against time at the six cross sections. The distribution is similar to that of flow rate except the momentum flux skews more. It increases more rapidly and reaches the maximum value earlier than the distribution of flow rate. Near the leading edge of the deck, the momentum flux reaches the maximum value at about 0.05 s after the arrival of the water front, in comparison to the 0.10 s

arrival time of the maximum flow rate. Near the end of the deck, the momentum flux researches the maximum value at about 0.08 s after the arrival of the water front. The momentum flux decays monotonically after reaching the maximum value. Although the maximum velocity was found to be at the front of the green water, the maximum momentum arrives with a short delay. Note that the total momentum flux obtained by integrating the distribution does not fluctuate much.

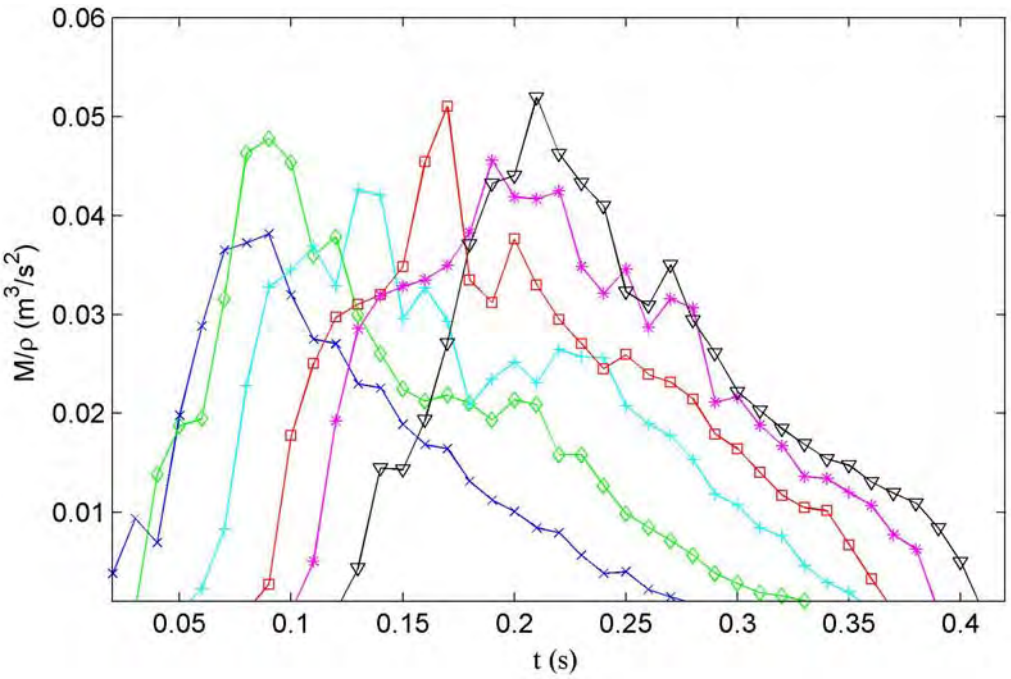

Figure 12.2 Time history of momentum flux of green water at six cross-sections corresponding to Figure 11.3.

The total volume per unit width of the overtopping water, *V*, was calculated by integrating the flow rate with respect to time as follows:

$$V = \int_{T_s}^{T_e} q\,dt = \int_{T_s}^{T_e} \int_{h_l}^{h} (1-\alpha) U\,dz_d\,dt \tag{12.3}$$

where T_s is the starting time of the green water flow at a given cross section and T_e is the ending time. The calculated volume using Eq. (12.3) is compared with a directly measured water volume. The overtopping water was collected behind the structure using a large container so the water volume could be directly measured. The section behind the model structure was screened and sealed with a sheet of vinyl for the collection of overtopping water. The water volume measurement was repeated 10 times to obtain the mean value for comparison.

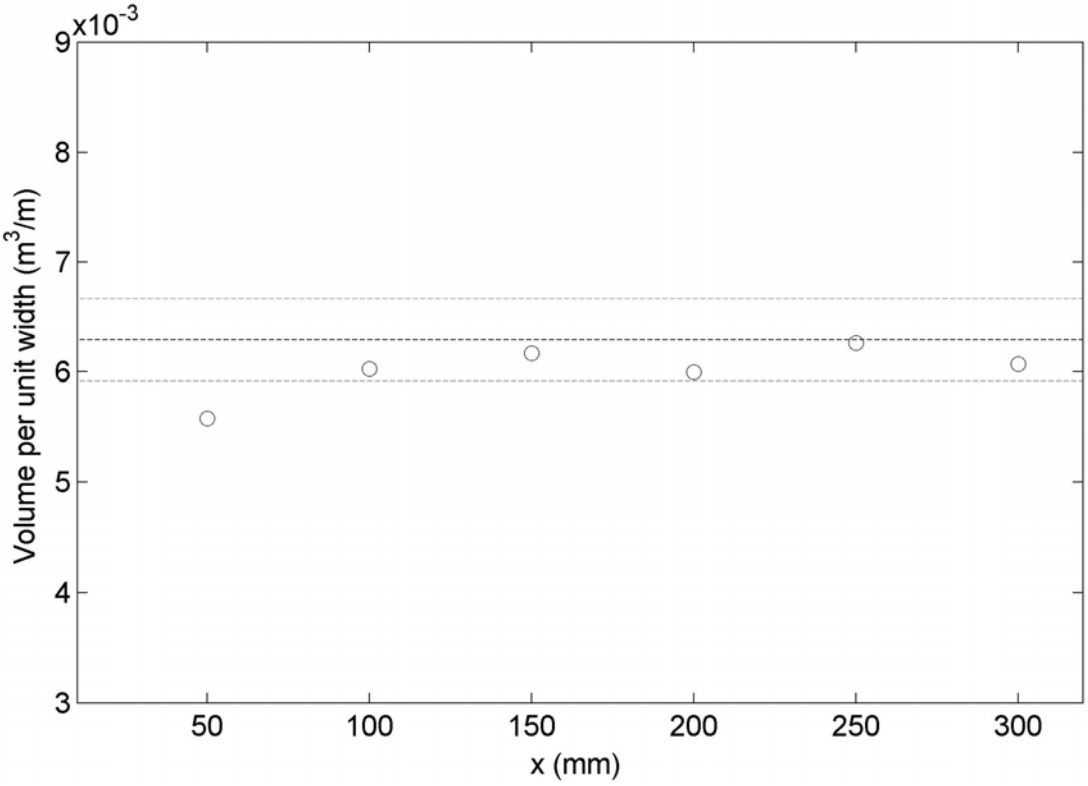

Figure 12.3 Comparison of overtopping water volume per unit width. "○", calculated water volume using Eq. (12.3) with measured void fraction and velocity; lines, mean and standard deviation of directly measured water volume using a container.

Figure 12.3 shows the comparison of volume of overtopping water over the deck between the calculated value using Eq. (12.3) and the directly measured value using the container. The calculated volumes using Eq. (12.3) at six cross sections are quite constant. The only relatively large deviation occurring at x = 50 mm may be due to the large vertical motion of the water particle and the large spatial variation of void fraction near the front of the structure right after wave impingement that results in a relatively larger error. The directly measured mean water volume per unit width using the container of 5.60×10^{-3} m^3/m is in good agreement with the corresponding mean water volume of 6.33×10^{-3} m^3/m obtained using Eq. (12.3). The overall comparison confirms that the water volume is conserved and the velocity and void fraction measurements are reliable.

13 DEPTH-AVERAGED VOID FRACTION AND HORIZONTAL VELOCITY

The depth-averaged void fraction and horizontal velocity were calculated using the measurement data to simplify the two-dimensional problem to one dimension for possible and easier engineering use. The depth-averaged properties were computed by integrating along a vertical cross section as follows:

$$\alpha_D = \frac{1}{h - h_l} \int_{h_l}^{h} \alpha \, dz_d \tag{13.1}$$

$$U_D = \frac{1}{h - h_l} \int_{h_l}^{h} U \, dz_d \tag{13.2}$$

where α_D is the depth-averaged void fraction and U_D is the depth-averaged horizontal velocity. Figure 13.1 shows the distributions of the depth-averaged void fraction and velocity along the deck from t = 0.02 s to 0.26 s. Both distributions display a similar pattern that has a roughly logarithmic increase along the downstream distance. The maximum value of each distribution is observed near the front of green water. The distributions confirm that strong aeration occurs in the frontal region of green water and the highly aerated front has the highest velocity.

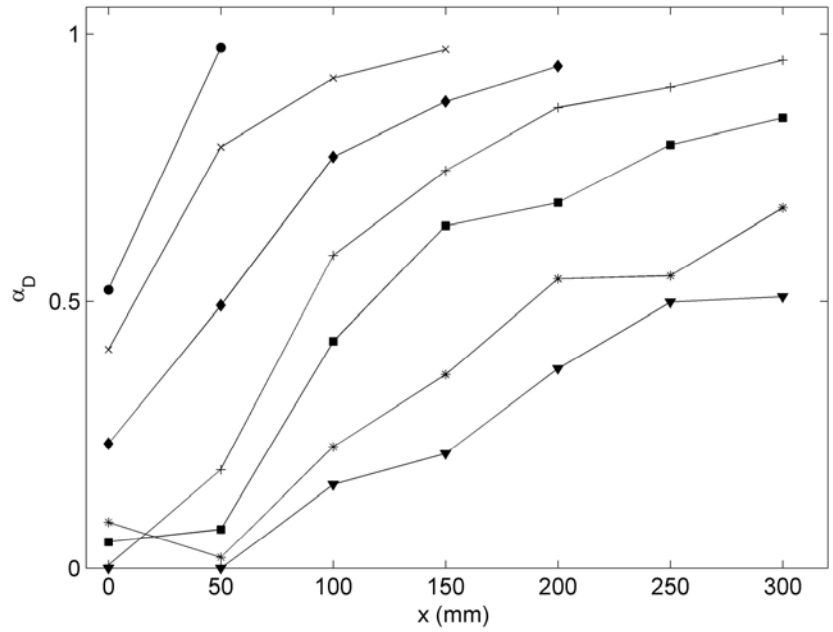

(a)

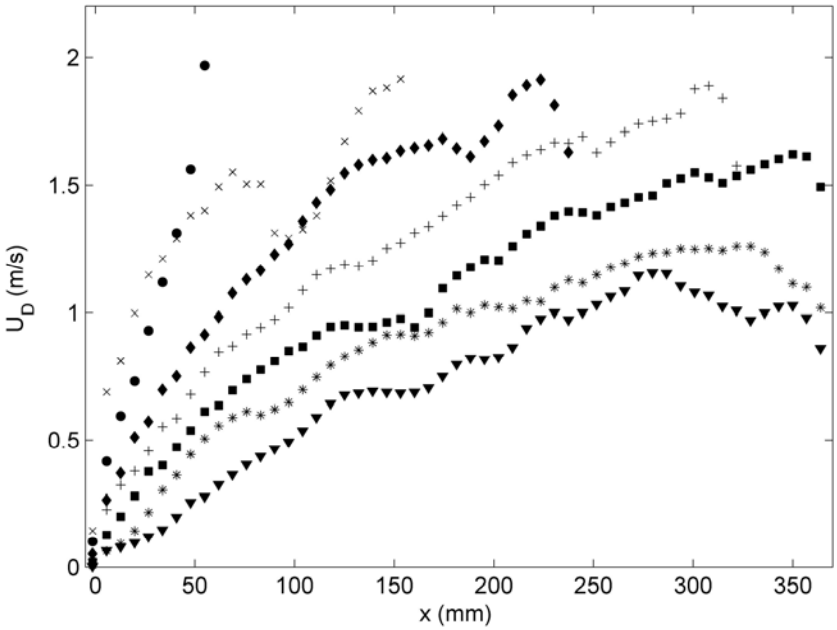

(b)

Figure 13.1 Distributions of depth-averaged (a) void fraction and (b) velocity at *t* = 0.02 s (●), 0.06 s (×), 0.10 s (♦), 0.14 s (+), 0.18 s (■), 0.22 (✳), and 0.26 s (▼).

The depth-averaged properties were empirically formulated to find possible similarities. For void fraction, it was found that there exists a similarity relationship among three non-dimensional parameters: the depth averaged void fraction α_D, the non-dimensional arrival time of green water front $x/(U_{FG}T)$, and the non-dimensional time t/T. Note that T is the wave period and U_{FG} is the front velocity of green water that was found to be constant and equal to $1.15C$ (Ryu *et al.*, 2007a). The similarity relationship using data at the six cross sections is plotted in Figure 13.2(a). The solid line in the figure is the result obtained by least-square curve-fitting. The regression equation for the self-similar depth-averaged void fraction can be expressed as:

$$\alpha_D = 0.92\exp\left[-60\left(\frac{t - x/U_{FG}}{T}\right)^2\right] \qquad \text{for } 0 \le \alpha_D < 1 \tag{13.3}$$

The coefficient of determination, R^2, of the fit is 0.89.

An empirical self-similar equation for depth-averaged velocity was also obtained applying the same similarity analysis to the data. The similarity profile is observed between U_D/U_{DM} and $(t - x/U_{FG})/T$ as shown in Figure 13.2(b), in which U_{DM} is the maximum depth-averaged velocity at a given time t. Based on the measurements, U_{DM} is found to be constant and equal to $0.95C$ until the water front passes the end of the deck. Based on least-square regression, the self-similar equation for depth-averaged horizontal velocity can be expressed as:

$$\frac{U_D}{U_{DM}} = \exp\left[-7.0\left(\frac{t - x/U_{FG}}{T}\right)\right] \qquad \text{for } 0 < \frac{U_D}{U_{DM}} \le 1$$
$$U_{DM} = 0.95C \tag{13.4}$$

The R^2 value of the fit is 0.91. Note that in both the void fraction and velocity plots in Figure 13.2 the data at x = 50 mm do not fit well. This may be due to the same reason mentioned in volume comparisons and Figure 12.3 in which a relative large discrepancy at x = 50 mm occurs.

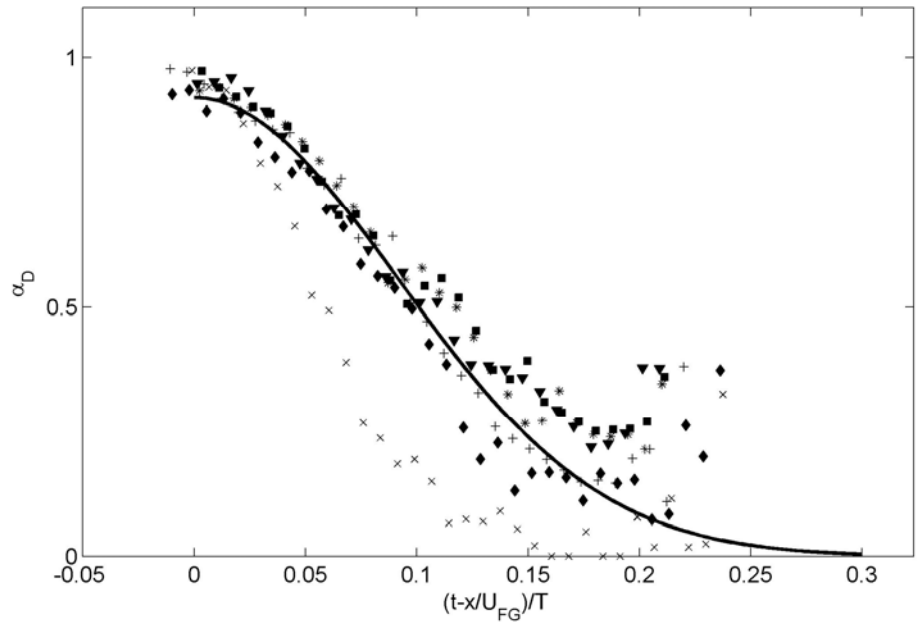

(a)

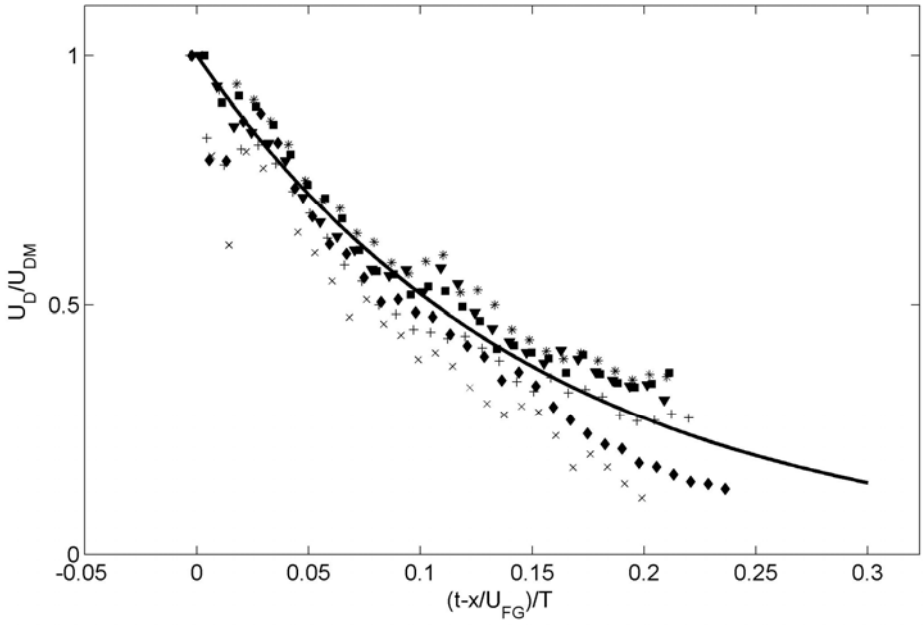

(b)

Figure 13.2 Similarity profiles of (a) depth-averaged void fraction and (b) depth-averaged velocity. Measurement data at *x* = 50 mm (×); 100 mm (♦); 150 mm (+); 200 mm (■); 250 mm (✳); and 300 mm (▼) were used in the plots. Solid lines are the fittings based on least square regression.

14 OVERTOPPING WATER LEVEL AND PREDICTIONS OF FLOW RATE AND MOMENTUM FLUX

The depth-averaged empirical equations for void fraction and velocity may be useful in terms of their simplicity. However, the flow rate and momentum flux at a give location on the deck cannot be predicted from the equations without knowing the cross-section area. Therefore we must measure the water level on the deck. Since the overtopping water may not be in contact with the deck surface, especially in the frontal region as we mentioned previously, the overtopping water height, *h'*, is defined as the vertical distance between the upper surface and the lower surface of green water. Wave gauges were not used for the water level measurement because they measure the "wet length" along the gauges, i.e., the total length in contact with water. Since the flow is aerated, wave gauges will result in incorrect measurements.

In this study, the ensemble-averaged images introduced earlier such as the one in Figure 10.4 were used to obtain the water level. The determined water level was then further checked with the void fraction measurements (that have a spatial resolution of 10 mm). The free surface profile was traced out by examining the intensity difference in the images. The approach is similar to that in Govender *et al*. (2002). Note that in the highly aerated region, the intensity difference in the images may not be very distinguishable from the background (air). In such cases, the void fraction measurements were used to determine or confirm the surface profiles. A relatively large uncertainty of ±10 mm therefore exists in those cases. Fortunately, the highly aerated region typically has a high water level, as shown near the green water front in Figure 10.4, so the ±10 mm uncertainty represents no greater than 10% of the water level.

The normalized water level h'/h_{max}, where h_{max} is the maximum water level, is plotted in Figure 14.1. Note that the maximum water level is nearly constant as h_{max} = 0.16 m, which is close to $2.6(H - z_{deck})$ with H being the deep water wave height (H = 17.1 cm) and z_{deck} the height of the free board (z_{deck} = 11.0 cm). The non-dimensional

water level shows self-similar behavior with a rapid increase followed by an exponential decay. The non-dimensional water level variation can be modeled as:

$$\frac{h'}{h_{max}} = 320\left(\frac{t - x/U_{FG}}{T}\right)\exp\left[-14\left(\frac{t - x/U_{FG}}{T}\right)^{0.5}\right] \qquad (14.1)$$

$$h_{max} = 2.6\left(H - z_{deck}\right)$$

The R^2 value of the normalized water level is 0.87. The flow rate per unit width can now be calculated using the empirical equations for depth-averaged void fraction, depth-averaged velocity, and water level as follows:

$$q = \left(1-\alpha_D\right) U_D\, h' \qquad (14.2)$$

in which α_D, U_D, and h' are expressed in Eqs. (8), (9), and (10), respectively.

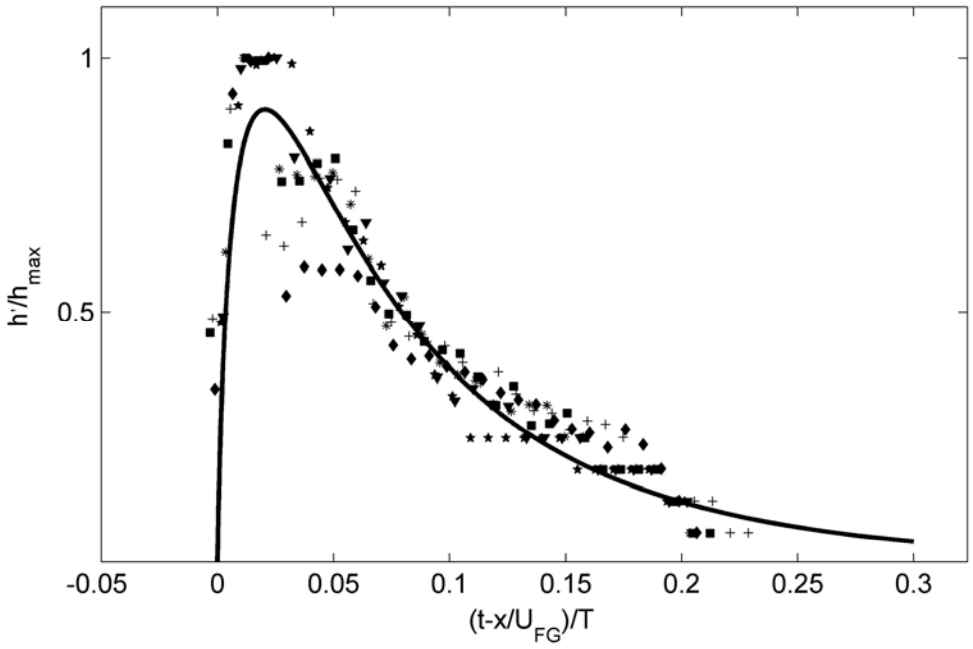

Figure 14.1 Water level of overtopping green water at x = 50 mm (×), 100 mm (♦), 150 mm (+), 200 mm (■), 250 mm (✳), and 300 mm (▼).

Although the flow rate should be calculated by integrating the data at each measurement point along a vertical column, the simplified approach using the depth-averaged one-dimensional equations along the deck provides easy-to-use advantages for engineering applications. To make sure the depth-averaged approach is valid with a reasonable accuracy, comparisons between the flow rate obtained using Eq. (14.2) and the flow rate obtained by integrating the void fraction and velocity distribution along a vertical column are shown in Figure 14.2. The figure presents comparisons for six cross sections from x = 50 mm to 300 mm. Although discrepancy is observed in the frontal region at most cross sections, the overall agreement is quite reasonable and suitable for engineering applications. This is especially true if considering the use of the simple depth-averaged one-dimensional approach and similarity profiles for void fraction, velocity, and water level. The overtopping water volume calculated by integration of Eq. (14.2) (i.e., the solid lines in Figure 14.2) is found to be 6.6×10^{-3} m^3/m which is about 7% larger than that obtained from direct measurements. The approach by Eq. (14.2) is based on the assumption that the two properties (void fraction and velocity) in the equation distribute uniformly in the vertical direction at any given point on the deck. If the distributions of the properties become less uniform, nonlinear effects increase and the depth-averaged Eq. (14.2) would result in a greater discrepancy. This may be the reason contributing to a relatively greater discrepancy near the front of green water in Figure 14.2.

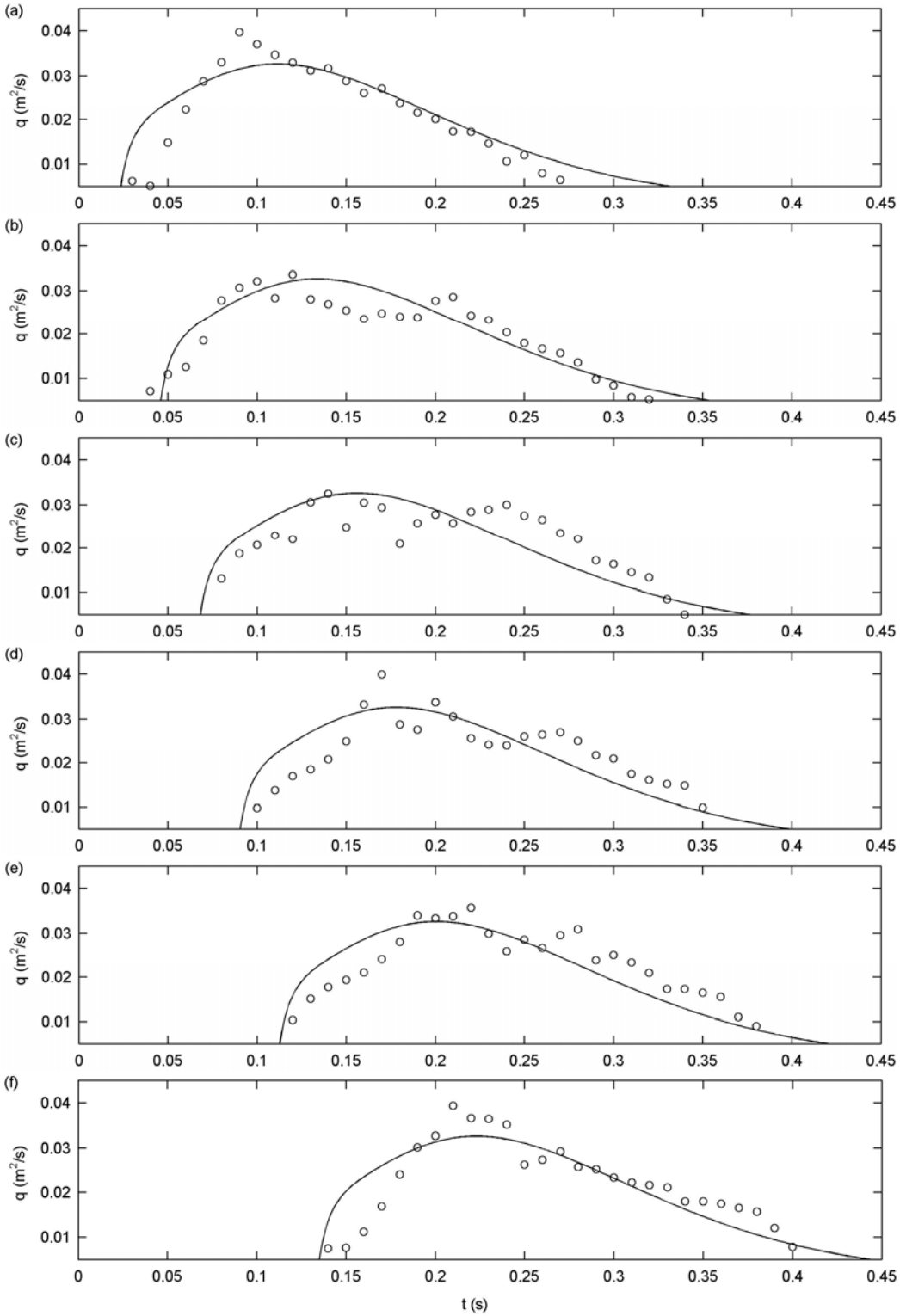

Figure 14.2 Flow rate comparisons between Eq. (14.2) and measurements at x = (a) 50 mm, (b) 100 mm, (c) 150 mm, (d) 200 mm, (e) 250 mm, and (f) 300 mm.

Similar to the depth-averaged approach for flow rate, the momentum flux per unit width (divided by the water density) is expressed as follows:

$$\frac{M}{\rho} = \left(1-\alpha_D\right) U_D{}^2 h' \tag{14.3}$$

Figure 14.3 shows the comparisons of momentum flux between the calculation using Eq. (14.3) and the measurements obtained by integrating the void fraction and velocity distribution along a vertical column. The comparisons are similar to that in Figure 14.2. Eq. (14.3) predicts that the peak momentum flux occurs at about 0.05 s after the arrival of the water front. This lag agrees well with the measurement at locations near the leading edge of the structure while it is a little too short at locations behind x = 150 mm. It takes about 0.08 s after the arrival of the water front to reach the maximum momentum at locations near the end of the deck. The overall comparisons confirm that the simple depth-averaged equations, i.e., Eqs. (13.3), (13.4), and (14.1), may be used for momentum (and therefore force) prediction.

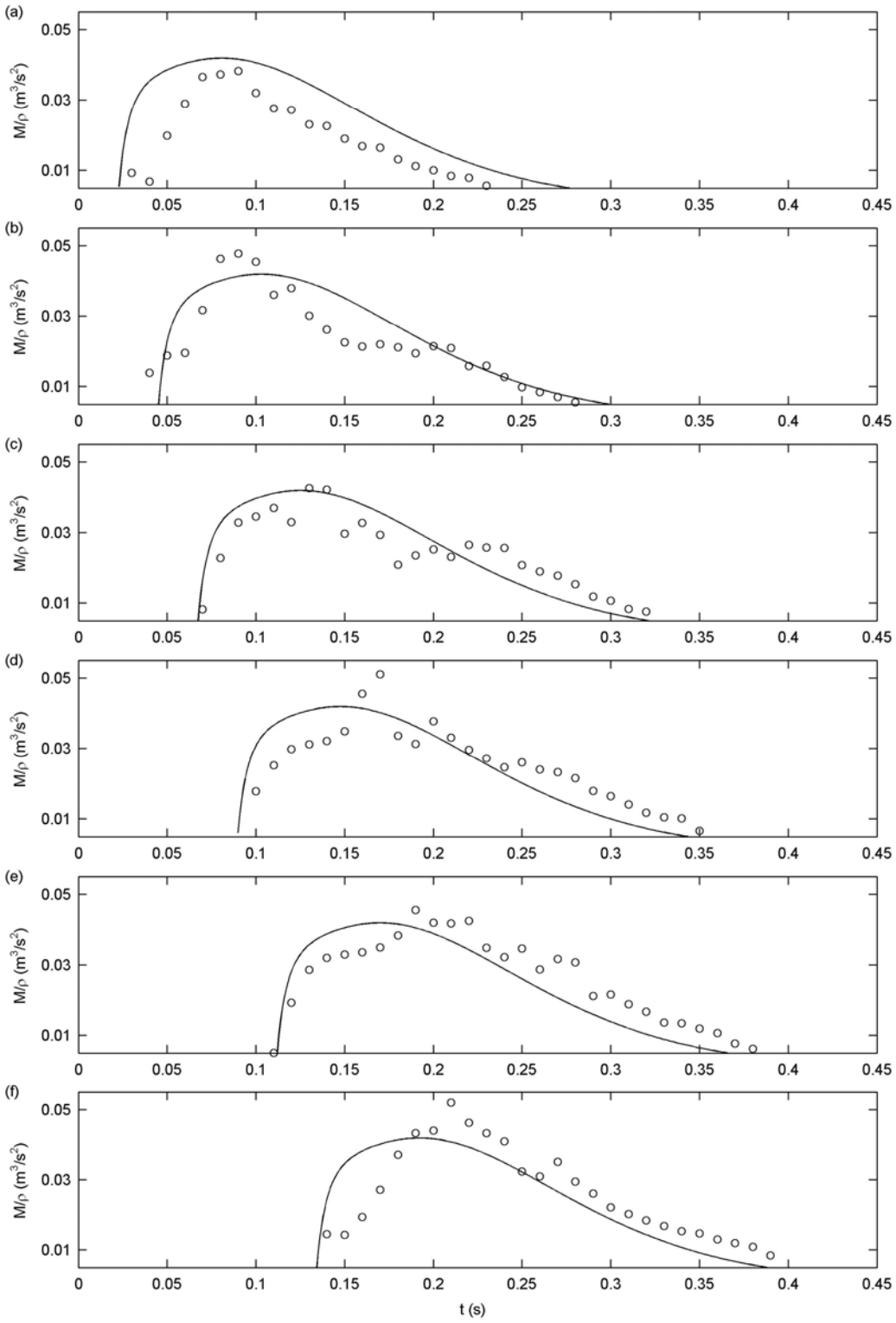

Figure 14.3 Momentum flux comparisons between Eq. (14.3) and measurements corresponding to Figure 14.2.

15 GREEN WATER ENERGY

The (total) time-averaged energy per unit surface area of the green water, E, was estimated using the measured void fractions and velocity as follows:

$$\overline{PE} = \frac{1}{t_{ge} - t_{gs}} \int_{t_{gs}}^{t_{ge}} \int_{h_l}^{h} (1-\alpha)\, \rho g\, z\; dz\; dt \tag{15.1}$$

$$\overline{KE} = \frac{1}{t_{ge} - t_{gs}} \int_{t_{gs}}^{t_{ge}} \int_{h_l}^{h} (1-\alpha)\, \rho \frac{\left(U^2 + W^2\right)}{2}\; dz\; dt \tag{15.2}$$

$$E = \overline{PE} + \overline{KE} \tag{15.3}$$

where $\overline{PE}$ is the time-averaged potential energy, $\overline{KE}$ is the time-averaged kinetic energy, t_{gs} and t_{ge} are the moments when the front and rear of the green water pass the point of interest, respectively, and U and W are the mean velocities in the x and z directions.

Figure 15.1 presents the energy variation along the deck. Note that the green water energy is normalized by the incoming wave energy, $E_w = \rho g H^2 / 8$, based on the linear wave theory and the location at the deck is normalized by the wave length, L, also based on the linear wave theory. From the figure, it is observed that, as x increases, the potential energy decreases while the kinetic energy increases. This is consistent with the observed evolution from the vertically dominant runup near the leading edge of the deck to the horizontally dominant green water near the end of the deck. Although the potential energy is greater than the kinetic energy on the deck, the difference decreases from about 5.5 times near the leading edge of the deck to about 2.0 times near the end of the deck. The ratio E/E_w is about 1.3 near the leading edge and reduces to about 1.2 after x = 150 mm (x/L = 0.06). There is no significant variation in the total energy along the deck. The greater decrease of the total energy near the leading edge of the deck indicates a higher rate of energy dissipation near the front of the structure.

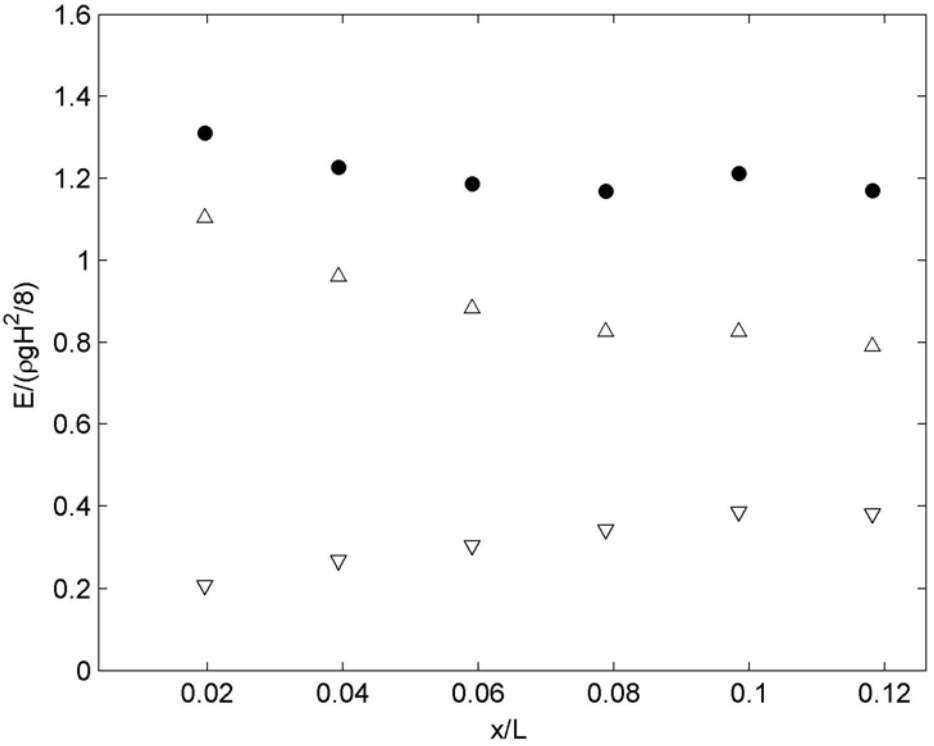

Figure 15.1 Normalized green water energy to wave energy: total energy (●), potential energy (△), kinetic energy (▽).

The reason for the large ratio of E/E_w = 1.3 above is due to the definition of E in Eqs. (15.1–15.3). The duration of green water on deck, ($t_{ge} - t_{gs}$), is about 0.26 s in the calculation of $\overline{PE}$ and $\overline{KE}$ in the equations while the wave energy is averaged over the wave period of T = 1.30 s. If we average the green water energy over the entire wave period of 1.30 s rather than the short duration of 0.26 s, the energy ratio becomes 1.3×0.26/1.30 = 0.26. This means that the energy of green water on deck is about one quarter of that of the incoming wave.

16 CONCLUDING REMARKS

The present study performed laboratory measurements of void fraction and velocity using the in-house developed fiber optic reflectometer (FOR) and bubble image velocimetry (BIV) in overtopping green water flow generated by breaking wave impingement. The wave and structure were designed following Froude scaling based on an extreme hurricane event and a simplified offshore platform. Void fraction measurements were taken at more than 10 points along each vertical column at seven cross sections along the deck. In addition, the velocity field and water level were also obtained along the deck.

The temporal and spatial distributions of void fraction show that the front of green water is highly aerated while the rear has very low aeration. The time-averaged void fraction distribution shows high aeration near the upper free surface and low aeration near the deck surface in the green water flow. The distribution is close to linear near the leading edge of the deck but rapidly transforms to a shape like a typical boundary layer velocity profile over a short distance.

Through dimensional analysis and regression, similarity profiles for depth-averaged void fraction, depth-averaged velocity, and water level on the deck were obtained, as expressed in Eqs. (13.3), (13.4), and (14.1), respectively. The depth-averaged similarity profiles may be useful in practical applications due to their simplicity. The flow rate and momentum flux of the overtopping green water flow at any given locations on deck, as shown in Eqs. (14.2) and (14.3), were predicted using the depth-averaged void fraction, depth-averaged velocity, and water level. Validations of the depth-averaged similarity profiles were performed by comparing the water volume, volume flow rate, and momentum flux of green water between predictions using the similarity profiles and integrated quantities from measurements. Good agreement was found in the comparisons.

The time-averaged energy (per unit surface area) of green water was also estimated based on the measurements and compared with the energy of the incoming wave. The time-averaged green water energy was found to be significantly greater than the wave energy. However, the green water energy is only about one quarter of the incoming wave energy.

Based on the measurements and estimates of flow rate, momentum flux, and energy, the void fraction is found to be important for the study of green water. The void fraction changes the green water density and consequently leads to changes of those properties. The present study has focused on the overtopping green water generated by a specific plunging breaker. Since the void fraction as well as other flow properties of green water may depend on the type of incoming wave causing the occurrence of a green water event, more future studies considering various incoming wave conditions may be needed. In addition, an extension of this study to account for three-dimensional effects may also be valuable.

17 PRELIMINARY STUDY AND RESULTS USING A 3D MODEL STRUCTURE

Laboratory experiments were also set up and performed using a 3D model structure with the same wave condition as that in the 2D experimental study. The experiments were performed in the same glass-walled wave tank located at the Department of Civil Engineering, Texas A&M University with the same water depth of 0.80 m. The setup is shown in Figure 17.1.

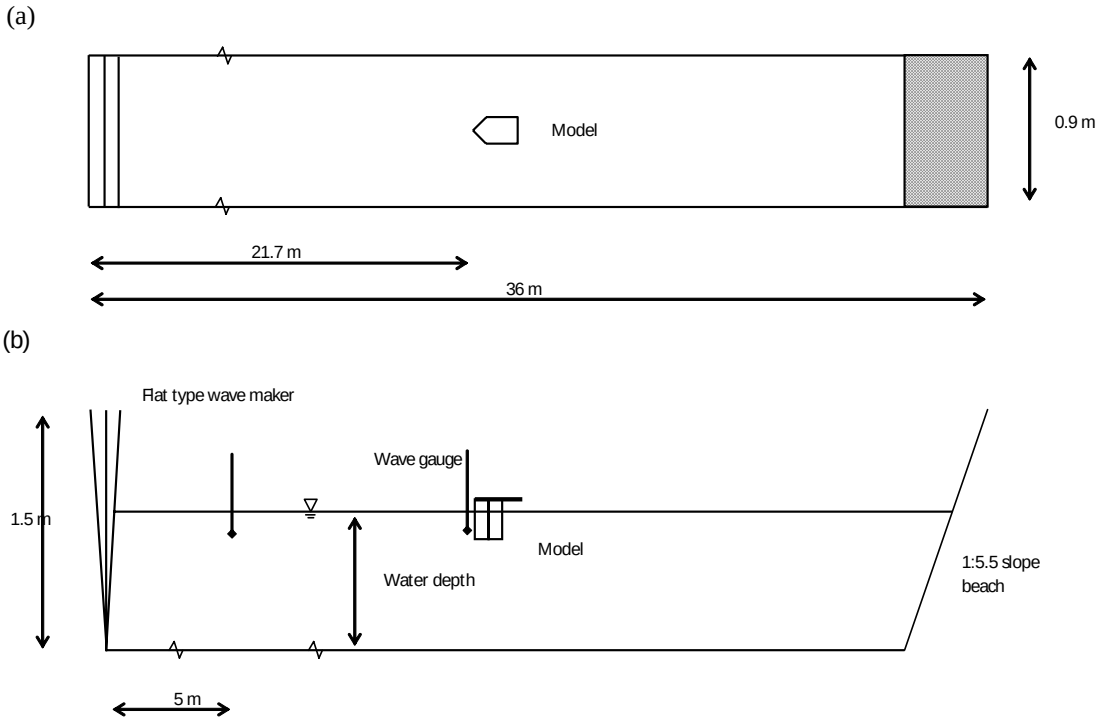

Figure 17.1 Wave tank schematic with the 3D test model. (a) Top view; (b) side view.

The model structure (mimicking a tension leg platform or the front of a ship-shape structure) was built based on a scale ratio of 1:169. It has the dimensions as

shown in Figure 17.2. The model was designed to be close to the 2D structure but account for the three dimensional effects of wave structure interaction. The model structure was supported by an aluminum frame and fixed rigidly to the bottom of the tank.

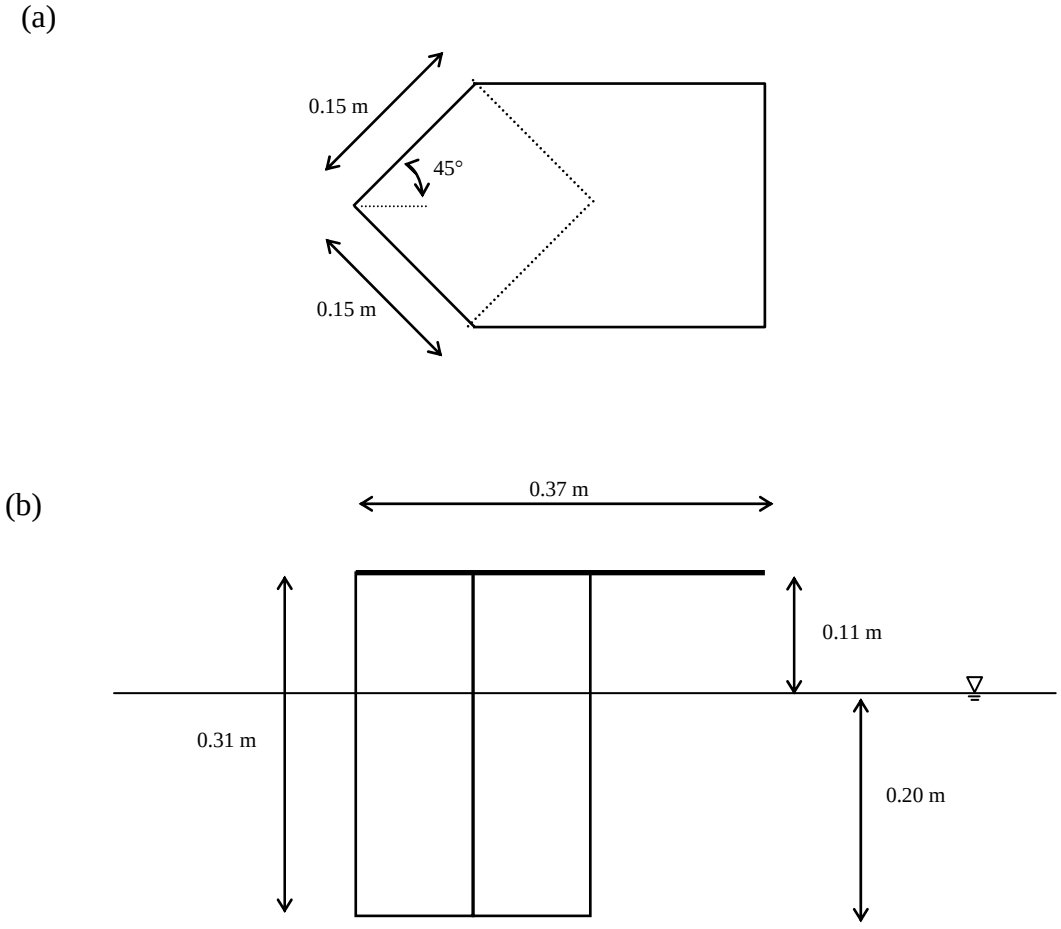

Figure 17.2 Model structure schematic. (a) Top view; (b) side view.

To investigate the difference in flow field and impact load due to the location of breaking wave impingement, two types of impingement due to breaking wave impact were tested: wave breaking on the front wall (at the interface of still water and structure) and wave breaking on the deck. The sketches are shown in Figure 17.3. To achieve this,

the wave period and wave heights were slightly varied. The breaking waves are plunging breakers generated using a wave focusing method which is the same as that in the 2D study mentioned previous sections of this report. The wave trains consist of waves with a range of frequencies from 0.7 Hz to 1.3 Hz. For the case of wave breaking on the front wall, the wave height and wave period are 17.1 cm and 1.34 s, respectively. The wave height and wave period for the case of wave breaking on the deck are 16.8 cm and 1.33 s. The tests were repeated 30 times for each type for ensemble averaging. The wave elevation was measured using double wired resistance type wave gauges. The measurements were taken at two locations that are 5.0 m and 21.5 m away from the wavemaker in order to measure the incoming wave height and the wave height at the front edge of the structure.

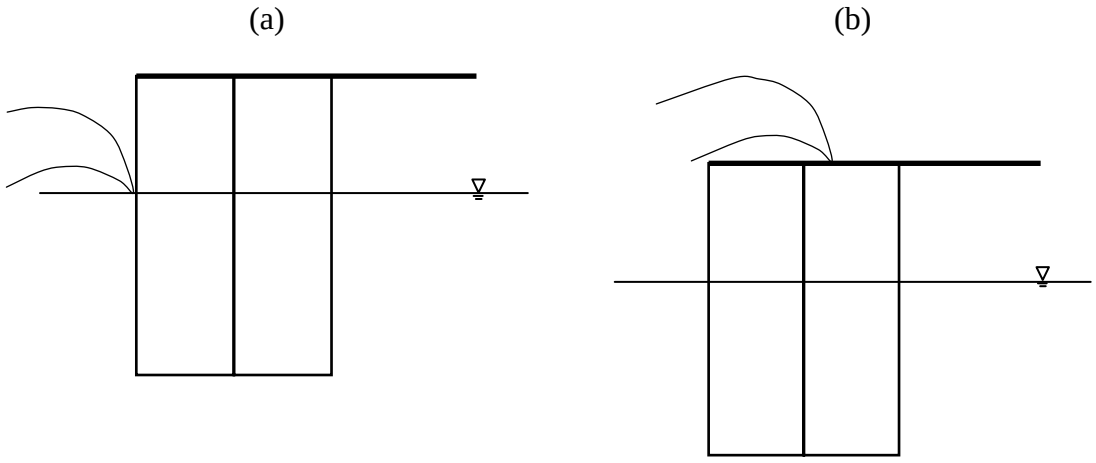

Figure 17.3 Breaking wave impingement location: (a) on wall; (b) on deck.

For the velocity field measurements, the BIV technique was employed. The method is the same as that used in the 2D velocity measurements reported earlier. The field of view (FOV) was selected as 44×44 cm^2 as shown in Figure 17.4. The control and data acquisition signals for operating the wavemaker and the BIV system were synchronized.

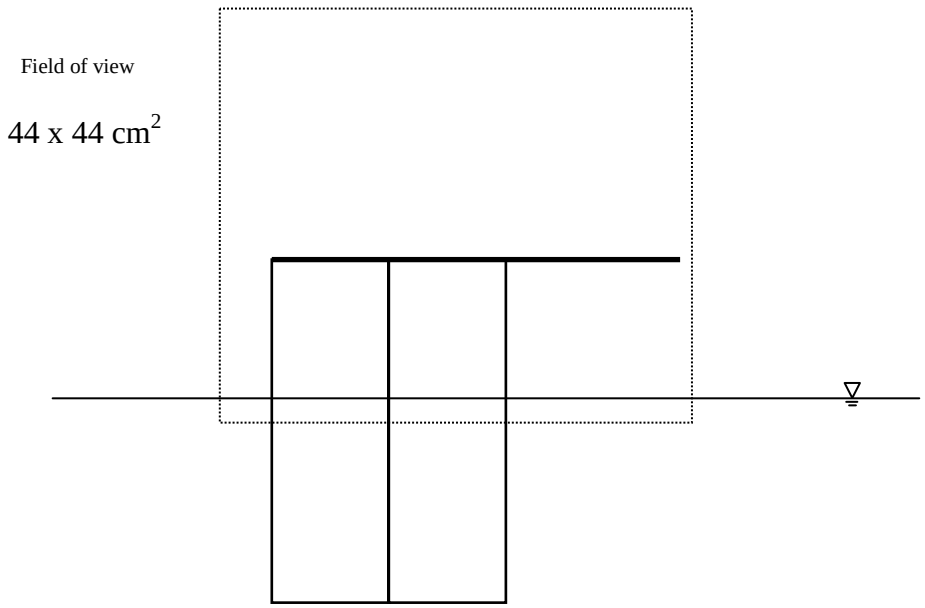

Figure 17.4 Field of view (FOV) for the BIV velocity measurements

The illumination of the flow was done by placing two 600W lights at both sides of the wave tank, as shown in Figure 17.5. The images were captured by a high speed camera mounted with a 50 mm focal lens with aperture set at f/1.4. The camera has a resolution of 1024×1024 pixels and the frame rate was set at 1000 frames per second. Since the BIV technique does not use a laser light sheet, the depth of field (DOF) of measurements was limited to about 0.06 m by adjusting the camera focal length (= 0.5 m), f-number (= 1.4), and the distance between the model and the camera (= 1.5 m). The error due to the thickness of the DOF in the obtained velocity is approximately 2%. The images were analyzed using commercial software from LaVision Inc. The interrogation area for the velocity determination was 32×32 pixels with a 50% overlap. The average velocity fields were calculated using ensemble averaging.

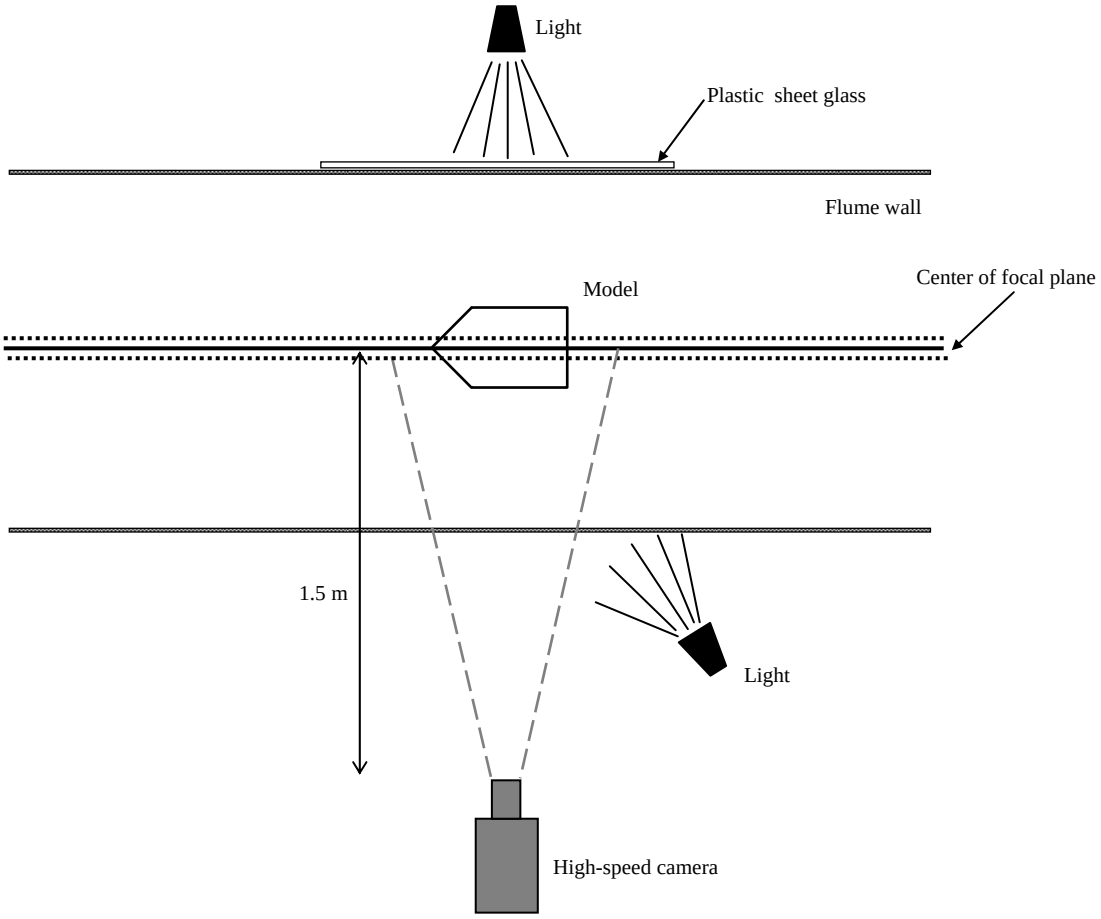

Figure 17.5 BIV Setup

Figure 17.6 shows the velocity fields for the case of wave breaking on the wall as sketched in Figure 17.3(a). Mainly the velocities at the centerline of the structure were measured for water above the deck. Since the velocities were determined by analyzing the images, the velocities for water in front of the structure were also obtained, as shown in the figure. Note that $t = 0$ represents the moment when the wave was impinging at the front wall of the model. The time duration for wave breaking and passing the deck is very short and lasts for only about 0.3 s.

(a) (b)

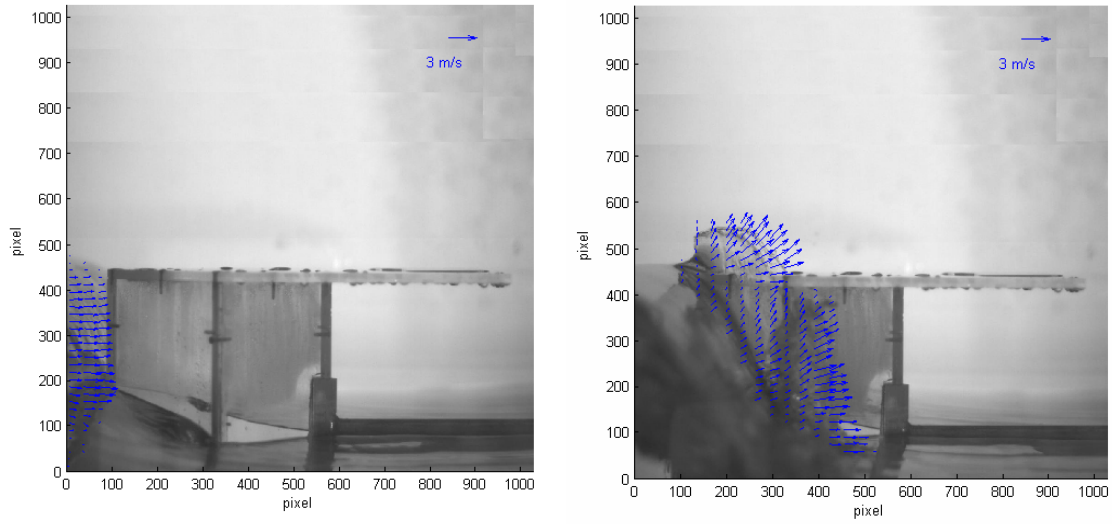

(c) (d)

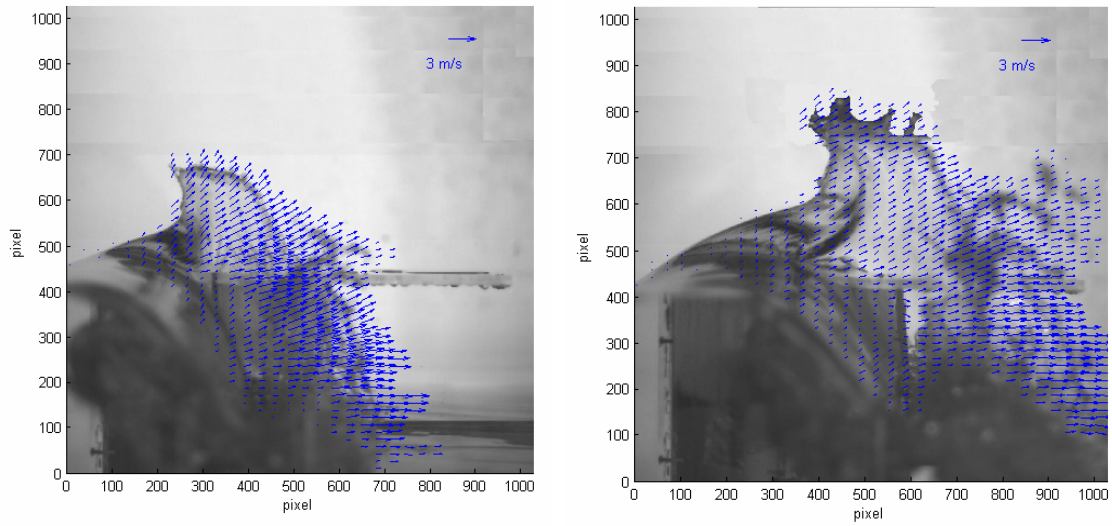

Figure 17.6 Velocity fields for the case of wave breaking on the front wall. (a) *t* = 0 s (b) *t* = 0.05 s (c) *t* = 0.08 s (d) *t* = 0.118 s (e) *t* = 0.146 s (f) *t* = 0.212 s.

(e) (f)

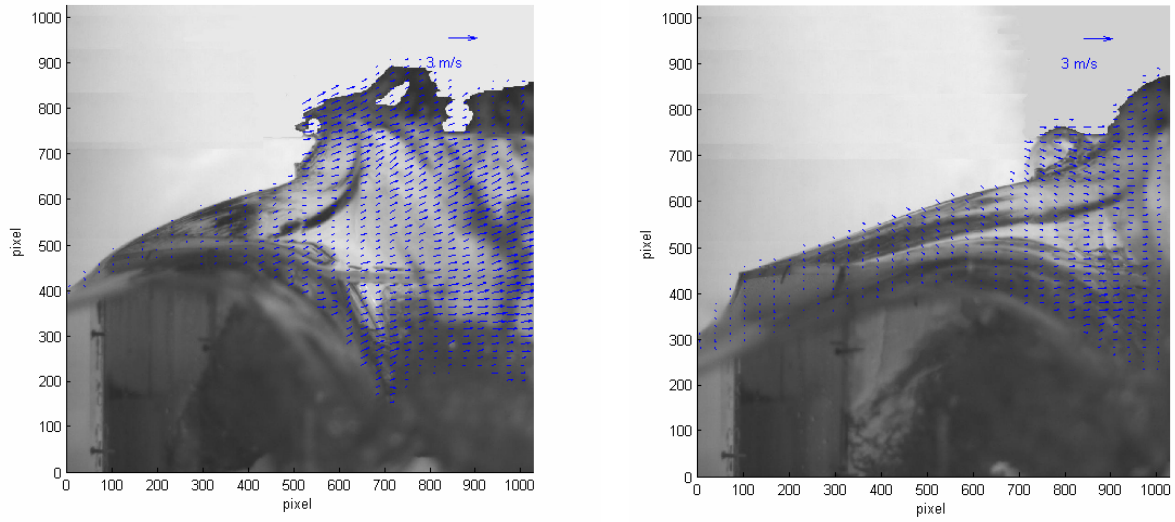

Figure 17.6 Continued.

In Figure 17.6 the velocity of the breaking wave is horizontal dominant at the moment of wave breaking on the front wall of the model. Once the wave impinges the frontal edge, the wave separates into two portions due to the shape of the model while some water moves vertically upward onto the structure. When the wave is moving forward, the magnitude of the velocity increases. The maximum horizontal velocity occurs while the wave is on deck and the magnitude is about 3.0 m/s in the measurement (about 1.5*C*). It occurs at about 0.08 s after the wave hits the structure. After the wave moves onto the deck, the vertical run up flow changes to a horizontally dominant overtopping flow, even though the vertical component is still significant. Finally, as the wave front passes the rear edge of the deck the flow becomes downward moving. The maximum vertical velocity occurs while the wave falls from the deck and the magnitude is about 1.08 m/s which is about 0.54*C*, occurring at about t = 0.336 s.

Figure 17.7 shows the velocity fields for the case of wave breaking on the deck as sketched in Figure 17.3(b). Time t =0 s represents the moment at which the wave front tip crosses the frontal edge of the model structure. The wave hits on the deck at about 6 cm from the front edge of the model. Before the wave hits the model, the flow is horizontally dominant. Once it hits the model, an up splash is created near the central portion of the deck. This upward flow continues with an increasing velocity. The maximum horizontal velocity reaches about 2.67 m/s (about 1.35C), occurring at about t = 0.102 s. This maximum velocity is close to but slightly lower than that in the other case of wave breaking on the wall. Unlike the case of wave breaking on the wall, the flow on the deck is horizontally dominant with a very small vertical component. The duration for the wave passing the deck is also about 0.3 s.

The green water flow field around the 3D structure shown in this section is preliminary. More tests are being conducted.

(a) (b)

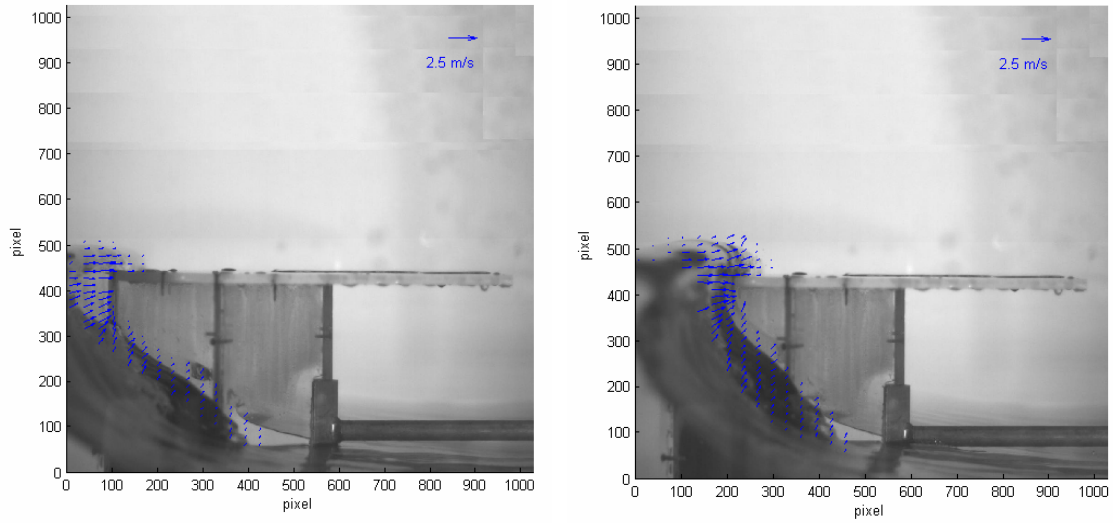

Figure 17.7 Velocity fields for the case of wave breaking on the deck. (a) t = 0.008 s (b) t = 0.036 s (c) t = 0.046 s (d) t = 0.064 s (e) t = 0.104 s (f) t = 0.166 s.

(c)

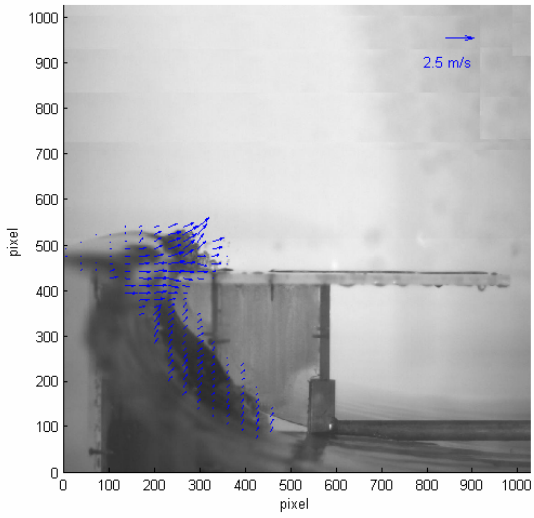

(d)

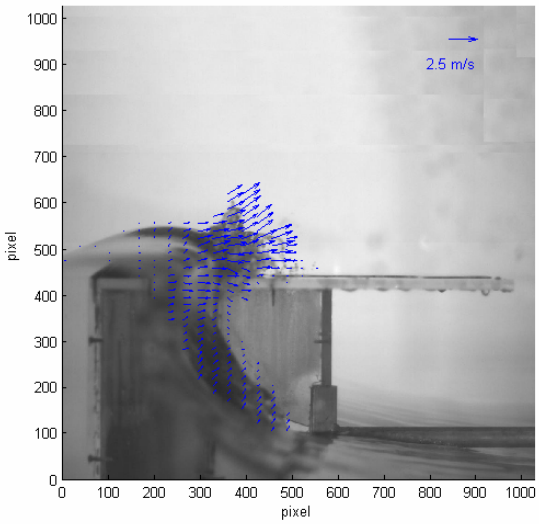

(e)

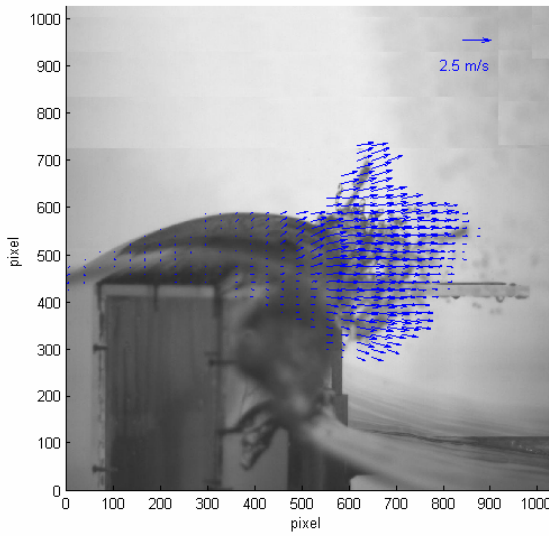

(f)

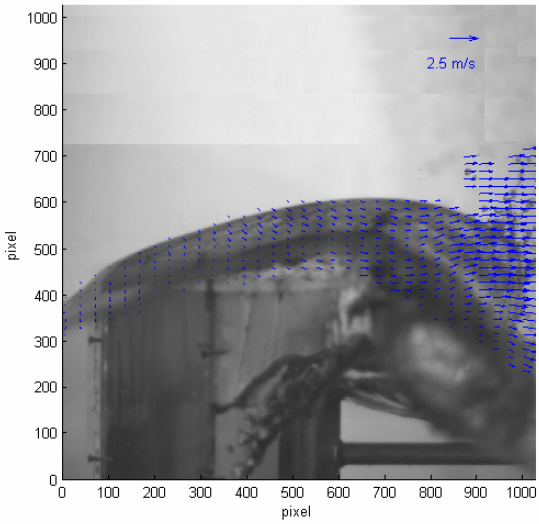

Figure 17.7 Continued.

REFERENCES - PART II

Blenkinsopp CE, Chaplin JR (2007) Void fraction measurements in breaking waves. Proc R Soc A463: 3151-3170

Bullock GN, Crawford AR, Hewson PJ, Walkden MJA, Bird PAD (2001) The influence of air and scale on wave impact pressures. Coast Eng 42:291-312

Chang K-A, Lim H-J, Su CB (2003) Fiber optic reflectometer for velocity and fraction ratio measurements in multiphase flows. Rev Sci Instrum 74:3559-3565

Chang K-A, Liu PL-F (1999) Experimental investigation of turbulence generated by breaking waves in water of intermediate depth. Phys Fluids 11:3390-3400

Chang K-A, Liu PL-F (2000) Pseudo turbulence in PIV breaking wave measurements. Exp Fluids 29:331-338

Chanson H, Aoki S, Maruyama M (2002) Unsteady air bubble entrainment and detrainment at a plunging breaker: Dominant time scales and similarity of water level variation. Coast Eng 46:139–157

Chanson H (2004) Unsteady air-water flow measurements in sudden open channel flows. Exp Fluids 37(6):899-909

Cox DT, Orgeta JA (2002) Laboratory observations of green water overtopping a fixed deck. Ocean Eng 29:1827-1840

Cox DT, Shin S (2003) Laboratory measurements of void fraction and turbulence in the bore region of surf zone waves. J Eng Mech 129(10):1197-1205

Deane GB (1997) Sound generation and air entrainment by breaking waves in the surf zone. J Acous Soc Am 102(5):2671–2689

Govender K, Mocke GP, Alport MJ (2002) Video-imaged surf zone wave and roller structures and flow fields. J Geophy Res 107C:3072

Hoque A, Aoki S (2005) Distributions of void fraction under breaking waves in the surf zone. Ocean Eng 32(14-15):1829-1840

Hwung HH, Chyan JM, Chung YC (1992) Energy dissipation and air bubbles mixing inside surf zone. Proc 23rd Int Conf Coast Eng Venice Italy 1(22):308-321

Lamarre E, Melville WK (1992) Instrumentation for the measurement of void-fraction in breaking waves: Laboratory and field results. IEEE J Ocean Eng 17:204-215

Ryu Y, Chang K-A, Lim H-J (2005) Use of bubble image velocimetry for measurement of plunging wave impinging on structure and associated greenwater. Meas Sci Technol 16:1945-1953

Ryu Y, Chang K-A, Mercier R (2007a) Runup and green water velocities due to breaking wave impinging and overtopping. Exp Fluids 43:555-567

Ryu Y, Chang K-A, Mercier R (2007b) Application of dam break flow to green water prediction. Appl Ocean Res 29:128-136

Shin S, Cox D (2006) Laboratory observations of inner surf and swash-zone hydrodynamics on a steep slope. Cont Shelf Res 26:561-573

Ting FCK, Kirby JT (1994) Observation of undertow and turbulence in a laboratory surf zone. Coast Eng 24:51–80

Wang DW, Mitchell DA, Teague WJ, Jarosz E, Hulbert MS (2005) Extreme waves under Hurricane Ivan. Sci 309:896

ACKNOWLEDGEMENTS

The authors wish to thank the financial support provided by the Offshore Technology Research Center through its cooperative agreement with the Minerals Management Service and through its Industry Consortium, under the project entitled “Loads due to extreme wave crests.”